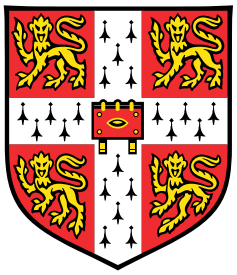

Properties and processing of direct-spun carbon nanotube mats

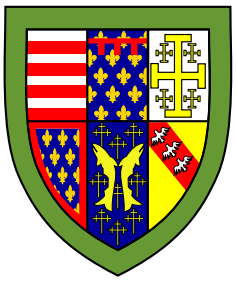

Joe C. Stallard

Supervisor: Prof. N. A. Fleck

Department of Engineering
University of Cambridge

This dissertation is submitted for the degree of
Doctor of Philosophy

Queens' College

September 2019

Declaration

This thesis is submitted for the degree of Doctor of Philosophy at the University of Cambridge.

The work presented in this thesis was carried out during the period from October 2015 to September 2019 at the Cambridge University Engineering Department, under the supervision of Professor Norman A. Fleck. The research was funded by the Engineering and Physical Sciences Research Council through a PhD Studentship in Engineering and under the grant titled *"Advanced nanotube application and manufacturing (ANAM) initative"*, No. EP/M015211/1.

The dissertation is the result of my own work, and includes nothing which is the outcome of work done in collaboration except as declared in the text and acknowledgements. It is not substantially the same as any that I have submitted, or is being currently submitted for a degree or diploma or other qualification at the University of Cambridge other than as declared here or as specified within the text. The work in Chapter 4 was done in collaboration with Dr. Wei Tan (University of Cambridge), who aided with experiments and finite element calculations.

This thesis does not exceed the word limit or maximum number of figures required by the Degree Committee in the Department of Engineering.

Joe C. Stallard
September 2019

Acknowledgements

I would like to thank my supervisor, Professor Norman Fleck, whose dedication to materials and science is matched by his passion for passing on his philosophy of thought and argument. He has been supportive and encouraging throughout my PhD, offering a combination of academic freedom, generous resources, great wisdom, and invaluable scrutiny. His broad knowledge, extensive network and enthusiasm have been of immense value, alongside his inspirational dedication to research questions of real interest, and courage in tackling the unknown.

I would also like to acknowledge the other academics who have followed my work over many talks and meetings as part of the ANAM initiative. Dr Adam Boies has provided me with so many opportunities to share my research with others, useful collaboration, and encouragement. Dr Michael De Volder and his lab offered great advice on chemistry, and exciting collaboration. Professors James Elliott and Alan Windle provided illuminating discussion and commentary on my work throughout my studies. Regular meetings with the industrial partners in the initiative were a frequent source of useful scrutiny and inspiration alike. In the closing stages of my PhD research I was also grateful for discussions with Professor Tobias Kraus of the Leibniz Institute for New Materials, whose knowledge of colloidal theory and engaged approach was most helpful in clarifying my understanding of interactions between carbon nanotubes and chlorosulfonic acid.

Upon arrival in Cambridge I was most grateful for the assistance of Dr Fiona Smail, who shared an extensive knowledge of literature and useful guidance. The fourth chapter in this thesis is the result of an extensive collaboration with Dr Wei Tan, who undertook numerous experiments and worked closely with me over many iterations of micromechanical models for the composite microstructure. I couldn't give enough thanks for the extensive experience and expertise of the technicians at Cambridge — my work on superacid processing would have been impossible without the resources provided by Len Howlett. I have relied on the skills of Simon Marshall, Stefan Savage, and Daniel Flack to manufacture equipment. Alan Heaver provided much useful guidance (personal and professional); Simon Griggs and Dr

Thurid Gspann at the Materials Science department were welcoming, supportive, and shared extensive knowledge of microscopy. Dr Xiao Zhang and Dr Hadi Modarres both assisted with Raman analysis and thermogravimetric characterisation.

The company and friendships of my fellow PhD students Frederik Van Loock, Adam Boyce and Hamsini Suresh were invaluable throughout my time at Cambridge. I will never forget the fantastic times we spent together discussing so many aspects of life and research, and the camaraderie they provided. Other researchers in the Oatley Lab — Dr Emilio Martínez-Pañeda, Dr Philipp Seiler, Dr Karthikeyan Kandan, and Dr Harika Tankasala — provided critique and shared extensive knowledge.

My college community has also been an immense source of friendship and support throughout my studies. I owe the most to my housemates, Andrea Wessendorf, Xuezi Ma, Francesca van Tartwijk, Mansoor Ahmed (and Emma Rengers), Mistral Contrastin, Avagi Stavropoulou-Tatla, and Jolly Dusabe, for their friendship. The fellows and staff at Queens' have always been friendly and inspirational. They endow the college with immense dedication to serving students, research and community alike.

Finally, I must thank my family — my parents Hugh and Tina Stallard, my sister Kim Stallard, and my grandmothers Heather Stallard and Margaret Gould, for their endless warmth, encouragement, and advice. This thesis is as much theirs as it is mine — I am so thankful for their encouragement of me throughout my life, their infectious love of learning, and example of what can be achieved through hard work.

Abstract

The mechanical and electrical properties of direct-spun carbon nanotube mats are investigated. Processing techniques which enhance their performance are developed, and their effects are characterised and understood through experiment and micromechanical modelling.

Macroscopic carbon nanotube material properties are surmised with material property charts that elucidate the relationships between processing, microstructure and properties, and identify the contribution of different carbon nanotube morphologies to material-property space.

The mechanical and electrical properties of a direct-spun carbon nanotube mat are determined. Formed from a 2D network of interconnected nanotube bundles, the measured stress-strain response is elasto-plastic, with orientation hardening. In-situ microscopy reveals foam-like deformation of the bundle network due to macroscopic strain. A micromechanical model is developed to relate the macroscopic mechanical properties to those of the nanotube bundles. Direct-spun carbon nanotube mat-epoxy composites are manufactured with varying volume fractions of air, epoxy, and nanotube bundles. Their electrical conductivity relates proportionally to the nanotube bundle volume fraction, whereas their strength and modulus depend nonlinearly upon the nanotube bundle and epoxy volume fractions. A unit cell idealisation of the composite microstructure captures the variation in modulus and strength over the compositional range.

The stress-strain response of a direct-spun mat is measured whilst immersed in organic solvents and in chlorosulfonic acid. Softening observed upon immersion in organic solvents is attributed to a reduced contact area between bundled nanotubes. Upon chlorosulfonic acid immersion nanotubes separate, resulting in ductile behaviour. A tensile drawing process based upon solutions of chlorosulfonic acid and chloroform is capable of enhancing the modulus and strength of direct-spun mat samples; the properties of the drawn mats are investigated as a function of draw strain and chosen fluid.

The thesis concludes with recommendations for future work — in furthering the understanding of the relationship between direct-spun mat microstructure and properties, and in enhancing performance.

Table of contents

List of figures

List of tables

Chapter 1

Introduction

In his 1991 paper, *"Helical microtubules of graphitic carbon"* [1], Iijima described carbon nanotubes (CNTs) which were produced with the arc-discharge method. Presenting electron micrographs, he revealed a structure of concentric seamless tubular shells spaced 0.34 nm apart, and used diffraction patterns to measure the varying orientations of the hexagonal carbon lattice which comprised them (now known as the chiral vector). Whilst Iijima may not have been first scientist to observe CNTs [2–4], his clear and unambiguous description of their structure, and suggestion of their potential as building blocks for materials with extreme properties above the nanoscale, is credited with spawning what remains a major field of materials research today. At present, the world's knowledge and interest in the properties and applications of these once enigmatic nanoscale particles and their bulk materials continues to expand apace.

1.1 The structure, properties and applications of carbon nanotubes

CNTs are hollow tubular structures comprised from seamless coaxial graphitic carbon shells (or walls), each one atom in thickness. The structure of concentric shells, with spacing of 0.34 nm between the mid-plane of each shell, is illustrated in Figure 1.1a. The diameters of the innermost shells can be as small as 0.4 nm [5]. A CNT consisting of a single graphitic shell is termed a single-walled carbon nanotube (SWNT), a CNT with two walls is known as a 'double-walled nanotube' (DWNT), thereafter a CNT with three or more shells is termed a 'multi-walled nanotube' (MWNT). The distinct feature of highly ordered tubular graphitic shells distinguishes CNTs from carbon nanofibers (CNFs), which are formed from stacked cone or cup-shaped graphitic layers [6]. The orientation of the lattice structure within a CNT

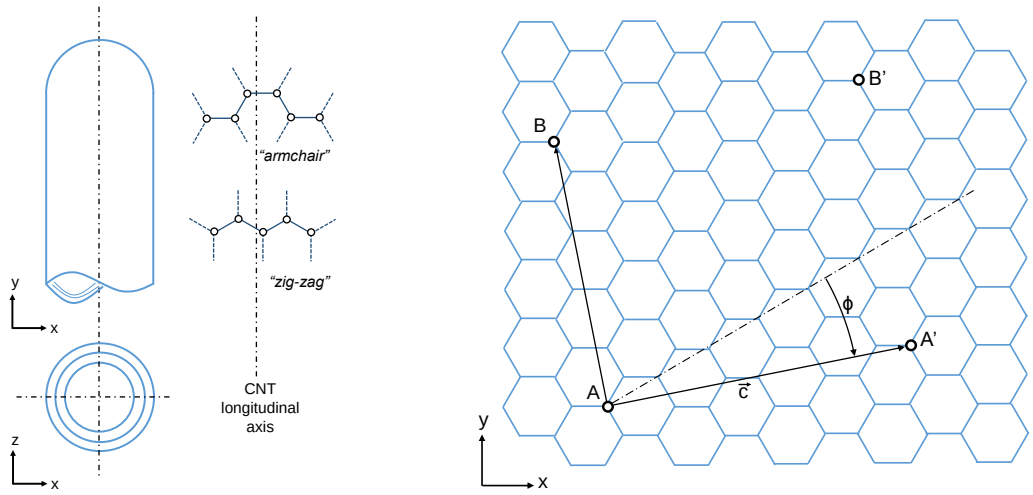

(a) CNT structure (b) Chiral angle definition

Fig. 1.1 The structure of CNTs, showing (a) the concentric structure of cylindrical carbon shells, and (b) the lattice orientation within the walls.

wall is measured relative to the so called *zig-zag* direction within the hexagonal lattice of covalently bonded carbon atoms which comprises each wall. Consider the graphitic lattice drawn in Figure 1.1b. A CNT could be constructed by joining the lattice along the two parallel lines $A-B$ and $A'-B'$. The chiral vector $\vec{c}$ drawn parallel to the hoop direction of the nanotube wall makes an angle ϕ with the *zig-zag* direction, known as the chiral angle. For a *zig-zag* nanotube, $\phi = 0°$, whereas for a so-called *armchair* CNT, $\phi = 30°$.

The measured tensile Young's modulus, ultimate tensile strength and electrical and thermal conductivity of CNT walls reported in literature and normalised by their density are plotted in the charts of Figure 1.2 and Figure 1.3, alongside those of conventional engineering materials [7–27]. The specific mechanical properties of individual CNT walls are much above those of all conventional engineering materials. Stiff covalent bonds within the walls endow them with a high in-plane modulus and ultimate strength. The specific thermal conductivity of carbon nanotube walls is much above those of conventional engineering materials, and the specific electrical conductivity of individual CNTs varies widely as a function of their diameter, chiral angle, and number of walls [19–29].

A timeline of milestones, discoveries and significant commercial events since carbon nanotubes were first reported by Iijima [1] is presented in Figure 1.4 [1, 30–47], with particular regard to the manufacture of carbon nanotube mats and fibres. Key to the mass production of

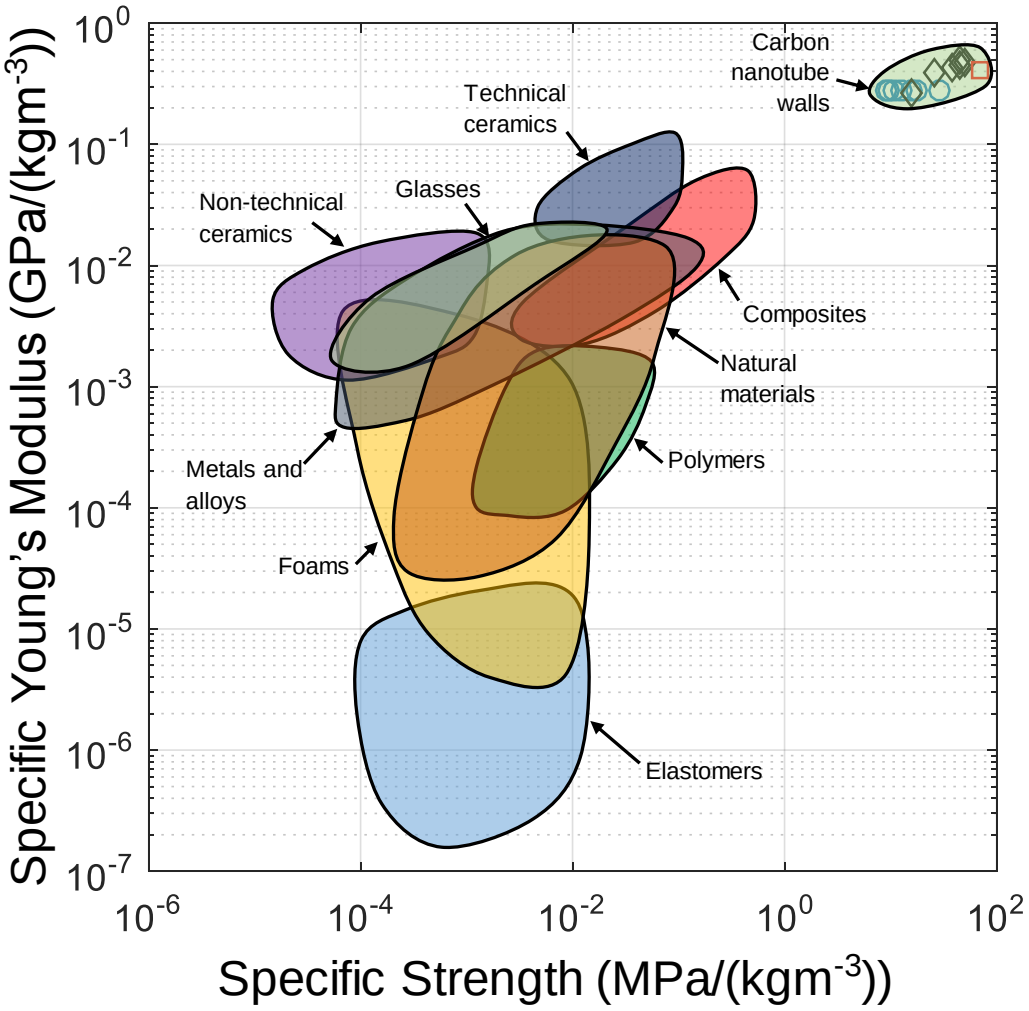

Fig. 1.2 The specific tensile Young's modulus and ultimate tensile strength of carbon nanotube walls as reported in literature, compared with those of conventional engineering materials [7–13].

CNTs has been development of chemical vapour deposition (CVD) production processes, especially with fluidised bed reactors [48, 49]. In CVD production processes, carbon nanotubes grow in a carbon-rich atmosphere from the surface of hot metal catalyst particles [50]. If the metal catalyst particles are seeded upon a substrate, CNTs grow into a vertically aligned array — a so-called *CNT forest* [51]; if catalyst particles are contained within the reactor gas (referred to as a fluidised bed), CNTs may be extracted in powder form suitable for further processing, either continuously or in batches [52]. One variant of the CVD growth process, the Cambridge direct-spinning process, involves the continuous spinning of a CNT aerogel from the gas phase to form *direct-spun* mats or fibres, and has received much attention since its description by Li *et al.* in 2004 [31]. Industrial interest in the Cambridge direct-spinning

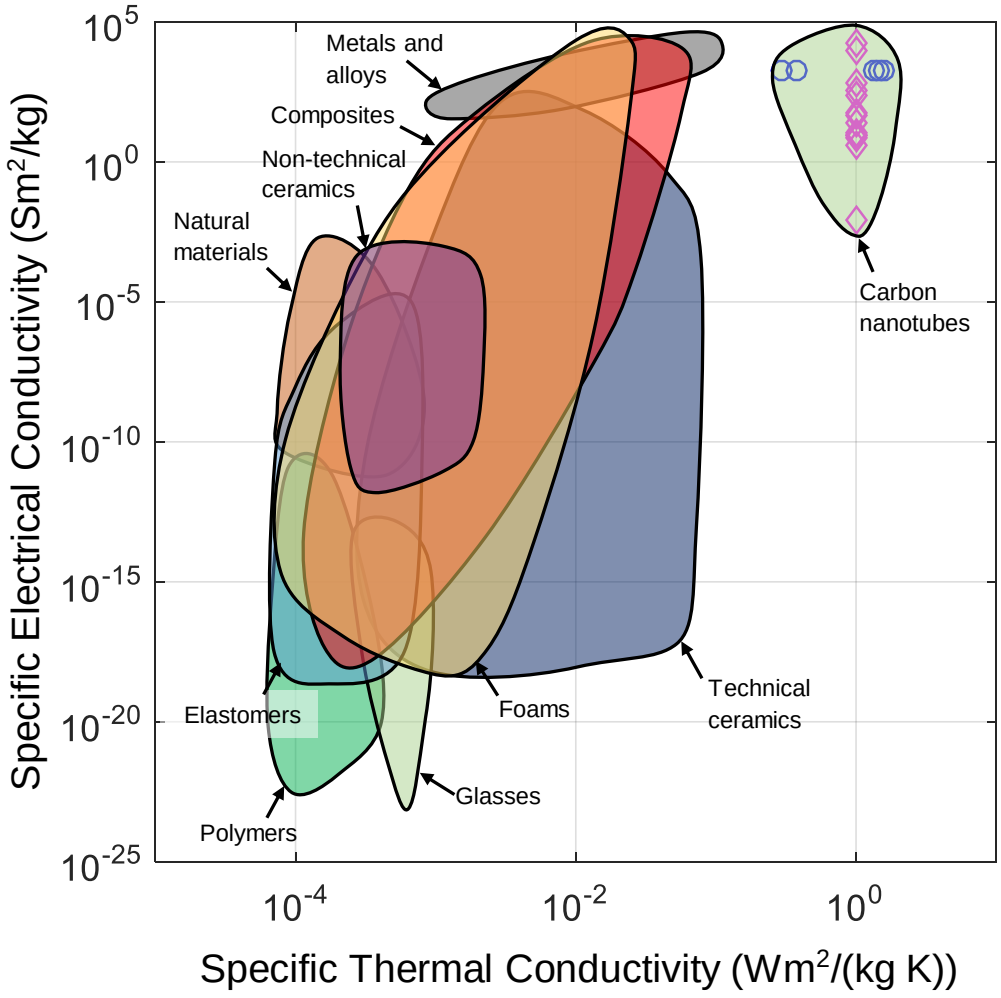

Fig. 1.3 The specific electrical and thermal conductivity of carbon nanotube walls as reported in literature, compared with those of conventional engineering materials [12–27].

process arises from its potential for continuous production [53], and because the CNTs it produces are long at up to 1 mm in length [54] and remain contained within the direct-spun mats and fibres. This eliminates the risks associated with inhalation of much shorter CNTs in powder form [55].

Macroscopic materials containing carbon nanotubes are now employed in multiple applications, and research spans a multitude of possible uses [48, 62]. The diverse list of CNT research topics includes water filtration [63], structural components [64], thermal management [65–67], and radiation shielding [68]. CNT transistor technology has also been developed to store and process data [34, 47]. Sustained industrial and academic interest

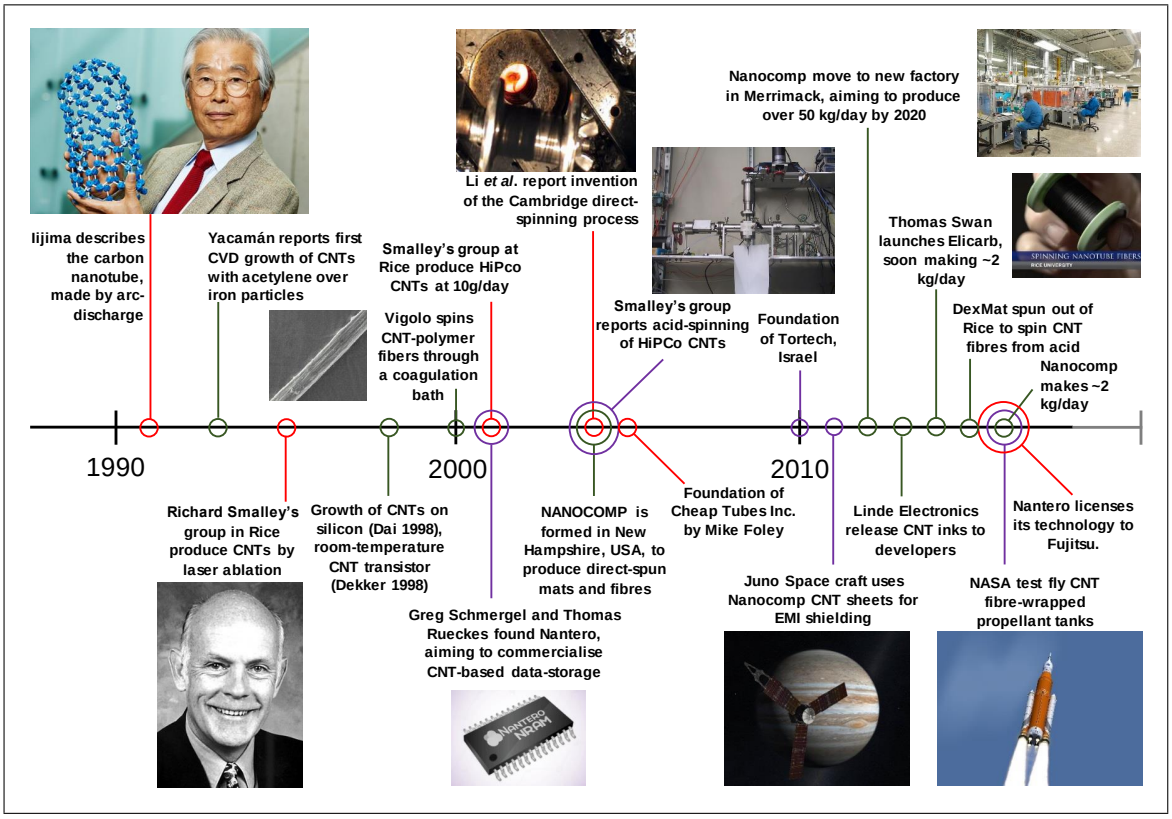

Fig. 1.4 Milestones in CNT production technology and application [1, 30–47].

in CNT technology has arisen due to the impressive mechanical, electrical and thermal properties of the tubes themselves, and because of the widely varied microstructures and properties of different macroscopic CNT materials [69]. The pace of academic research, quantified by the number of carbon nanotube-related publications per year [56], is plotted in Figure 1.5 against time, alongside the annual rate of CNT-related patent publications [57]. The number of tonnes of CNTs produced per year [48, 58] and retail cost of carbon nanotubes per unit mass [30, 59] are also included. Since 2015 over 4,000 patents have been published about carbon nanotube-related technologies each year. Alongside, the financial value of the global CNT market grew from USD 600 million in 2010 [60] to USD 4.55 billion in 2018 [61]. China has the largest national share of CNT-related scientific publications, accounting alone for 25% of the world's total; the USA follows with 22%, and Japan and South Korea have 8.5% and 7.1% respectively [56]. Annually, thousands of tonnes of CNTs are produced each year [48], and production costs for bulk grown CNT powders have fallen as low as 0.6 USD/gram at the time of writing [30]. Though much below historical costs of production [59], this cost remains much above that of most engineering materials [12].

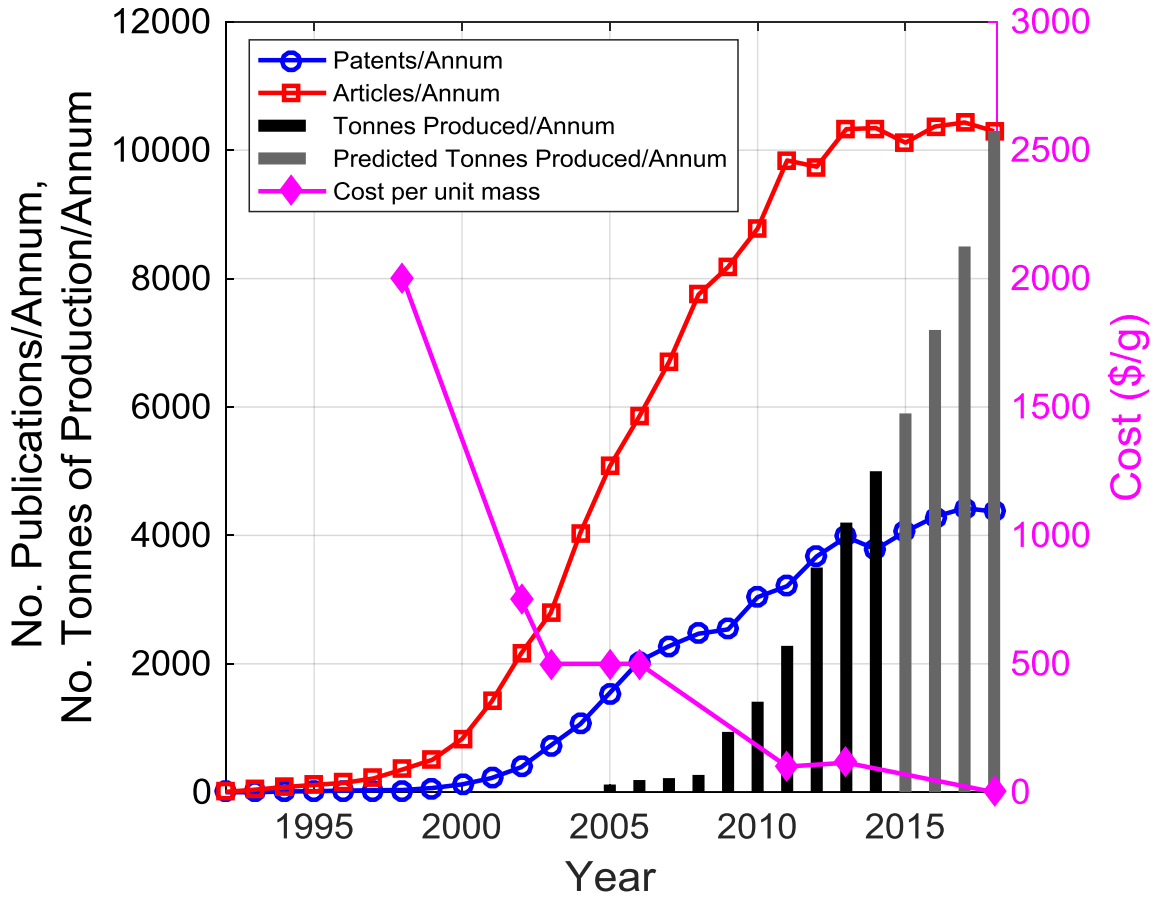

Fig. 1.5 Annual production volumes, and industrial and academic interest in CNT research [30, 48, 56–61].

1.2 Questions for research

The successful application of macroscopic carbon nanotube materials will ultimately depend upon their properties, and their cost relative to other engineering materials. Three clear research questions emerge:

- What are the properties of macroscopic carbon nanotube materials and their composites: can they exceed the properties of other engineering materials?
- How do the properties of macroscopic carbon nanotube materials and their composites relate, through micromechanical phenomena, to their microstructures? What limits their modulus and strength?

- How can the properties of carbon nanotube materials be enhanced? How can the microstructure of macroscopic carbon nanotube materials be tailored to increase their tensile strength, modulus and electrical and thermal conductivity?

In this thesis, these three questions are explored, with particular reference to a particular macroscopic CNT material: direct-spun mats, produced via the Cambridge direct-spinning process [31].

1.3 CNT materials manufactured via the Cambridge direct-spinning process

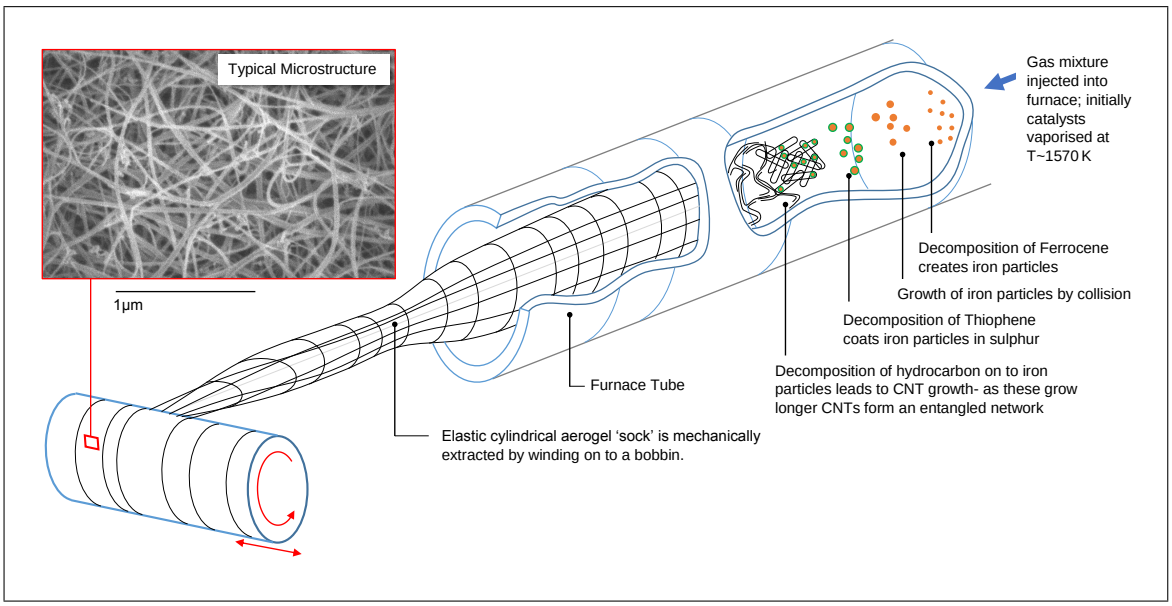

Fig. 1.6 The Cambridge direct-spinning process [31, 70–72], and image of typical direct-spun mat microstructure from scanning electron microscopy.

A schematic of the Cambridge direct-spinning process is presented in Figure 1.6. A carbon source, often methane, is mixed with iron and sulphur catalysts and a carrier gas, typically hydrogen, in a furnace at 1570 K [71]. The catalysts initially vaporise but later, as the mixture cools, iron nanoparticles re-condense out of the gas phase. The iron particles grow, and develop a sulphur coating [70]. Fullerene caps form on the surfaces of the nanoparticles, and the caps then evolve into individual CNTs [50]. The CNTs bind together into a network of CNT bundles by van der Waals attraction [70]. This forms a cylindrical aerogel 'sock', and the sock is drawn from the reactor by winding it on to a mandrel. The degree of anisotropy

in direct-spun mats and fibres is sensitive to the ratio of drawing speed and gas flow velocity [71, 72]. Many layers of drawn CNT aerogel stack to form a carbon nanotube mat. Immersion in a solvent, typically acetone, followed by evaporation, results in capillary condensation and a thinner, denser sheet [73]. Alternatively, spraying the aerogel sock with solvent as it is drawn from the reactor promotes its collapse into a direct-spun fibre.

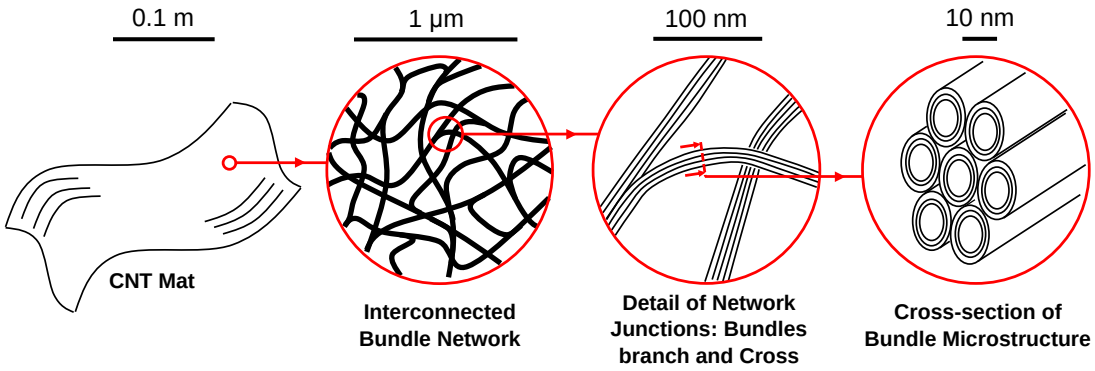

Fig. 1.7 Hierarchical microstructure of direct-spun carbon nanotube mat.

The hierarchical microstructure of direct-spun carbon nanotube mats is illustrated in Figure 1.7. The multi-layered mat microstructure is comprised of an interlinked network of carbon nanotube bundles; each bundle typically contains tens of carbon nanotubes. The modulus and tensile strength of direct-spun materials varies widely as a function of chosen manufacturing parameters and microstructure [53]; the strongest fibres reported in literature possess ultimate tensile strengths in the GPa range [54]. Direct-spun carbon nanotube materials have been processed into polymer composites [74], yet a comprehensive understanding of the origin of their properties, and their limits, remain fundamental topics for research.

1.4 Scope of thesis

In this thesis, the research questions outlined in section 1.2 are addressed, as follows:

- In chapter 2, the properties of macroscopic carbon nanotube materials and CNT-polymer composites are summarised with material property charts. The properties of the macroscopic carbon nanotube materials are compared with those of other conventional engineering materials to identify their contribution to material property space. Relevant literature regarding the mechanical behaviour of CNTs, CNT bundles,

CNT mats and fibres, and CNT-polymer composites is reviewed, alongside methods for the dispersion of CNTs in fluids.

- In chapter 3, a direct-spun carbon nanotube mat is characterised by measuring its stress-strain response under uniaxial tension, electrical conductivity, and piezoresistive behaviour. In-situ uniaxial tensile tests capable of tracking the evolution of the mat's bundle microstructure motivate the development of an analytical model, which relates the macroscopic strength and stiffness of the mat to the mechanical properties of the constituent carbon nanotube bundles.

- Chapter 4 presents a comprehensive investigation into the manufacture and properties of direct-spun carbon nanotube mat-epoxy composites. Critical experiments and models are used to characterise and infer the effect of epoxy infiltration upon the mat microstructure of interconnected CNT bundles, which leads to a synergistic increase in both modulus and strength.

- In chapter 5, the behaviour of a direct-spun carbon nanotube mat is investigated upon immersion in common solvents and chlorosulfonic acid. The dramatic increase in ductility upon chlorosulfonic acid immersion facilitates the development of a drawing process, the effect of which is to enhance the mat modulus, strength and electrical conductivity. The mechanisms behind softening in solvents and superacids are investigated with a micromechanical model of the CNT bundle microstructure and by application of colloidal theory.

- In chapter 6, the thesis concludes with a summary of key findings, and suggested directions for future research.

1.5 Published works and conference communications

The following papers have been published in scientific journals:

- Based on chapters 2 and 3:
  J. C. Stallard, W. Tan, T. S. Gspann, A. M. Boies, N. A. Fleck. "The mechanical and electrical properties of direct-spun carbon nanotube mats". *Extreme Mechanics Letters* 21 (2018), pp. 65-75. https://doi.org/10.1016/j.eml.2018.03.003

- Based on chapters 2 and 4:
  W. Tan, J. C. Stallard, F. R. Smail, A. M. Boies, N. A. Fleck. "The mechanical and electrical properties of direct-spun carbon nanotube mat-epoxy composites". *Carbon* 150 (2019), pp. 489-504. https://doi.org/10.1016/j.carbon.2019.04.118

Two publications based on work reported in chapter 5 remain in progress:

- J. C. Stallard, W. Tan, A. M. Boies, N. A. Fleck. "Effects of immersion and drawing in solvents and superacids on the mechanical and electrical properties of direct-spun carbon nanotube mats".

- J. C. Stallard, M. Glerum, A. M. Boies, M. F. L. De Volder, N. A. Fleck. "Immersion and drawing of direct-spun CNT mats in electrolytic fluids"

The work herein has been presented at a number of research talks, most notably:

- J.C Stallard, W. Tan, F.R. Smail, T.S. Gspann, A.M. Boies, N.A. Fleck. "The mechanical and electrical properties of direct-spun carbon nanotube mats", *Micro and Nanomechanics Systems, 10th European Solid Mechanics Conference*, Bologna, Italy, July 2018. (Keynote).

- J.C. Stallard, "Mechanical properties of carbon nanotube webs". *International Workshop on Graphene and Carbon Nanotubes in Experimental Mechanics*, Manchester, UK, May 2019. (Invited).

- J.C. Stallard. "The properties of direct-spun carbon nanotube mats". *Nano-Carbon Enhanced Materials (NCEM) Consortium*, Cambridge, July 2019. (Guest Speaker).

Chapter 2

Literature review

2.1 The manufacture and properties of macroscopic CNT materials

The density, Young's modulus, strength, and electrical and thermal conductivity of CNT materials and CNT-polymer composites span many orders of magnitude as a function of their manufacturing routes and resultant microstructures. Now, routes for CNT synthesis and methods for the manufacture of macroscopic CNT materials are discussed, and their properties are summarised with charts to explore their relationship with microstructure.

2.1.1 Production of CNTs

Early methods of CNT production such as the arc-discharge method developed by Iijima in 1991 [1] and the laser ablation method reported by the Nobel Laureate Richard Smalley in 1995 [33] required high energy inputs, for relatively low CNT yields. This motivated the development of vapour-phase catalytic production methods as used in the commercial manufacture of carbon fibres [75]. Whilst the earliest report of CNT growth from a vapour phase was reported in 1993 [32], the use of transition metal catalysts enabled CNT growth at lower temperatures. In 1996 researchers grew CNT forests from the surface of silicon substrates seeded with metal nanoparticles [51], and in 1998, Dresselhaus *et al.* reported the formation of CNTs from a *floating catalyst* within a furnace [76]. At first, CNTs did not develop in sufficient quantities to be spun directly from the reactor, and simply collected on the internal reactor walls [76]. The optimisation of reactor parameters by Li *et al.* — particularly the control of sulphur content — enabled the creation of CNTs at a sufficient rate to form an aerogel that could be spun directly from the furnace [31]. Today, floating catalyst

(or fluidised bed) chemical vapour deposition production methods, where catalyst particles are suspended as a homogeneous mix with source hydrocarbon gases, remain the dominant method for industrial CNT production [48, 49]. CVD methods are capable of producing large volumes of CNTs continuously, with a degree of control over their properties (number of walls, diameter, length and chirality). For example, carbon monoxide may be used as a carbon source with an iron pentacarbonyl catalyst to produce SWNTs in a pressurised furnace — the so-called HiPco process [77]. A catalyst of cobalt, molybdenum and silicon dioxide is also used to preferentially produce SWNTs [78]. For direct-spun CNT mat and fibres, the relative proportions of SWNTs, DWNTs and MWNTs, and the process yield, are both sensitive to the choice of carbon precursor (for instance, methane, acetylene or ethylene), and to the ratio of iron and sulphur catalysts; the influence of process parameters upon materials manufactured with the Cambridge direct-spinning process are reviewed elsewhere [53].

2.1.2 Classification and manufacture of macroscopic CNT materials

Consider macroscopic materials which are predominantly comprised of CNTs. Their methods of manufacture may be divided into three families, together resulting in eight different types of CNT material. The three families, the methods which comprise them, and sketches of their resultant morphologies, are illustrated in Figure 2.1.

- The first family of macroscopic CNT materials are manufactured from vertically aligned CNT arrays grown from substrates by chemical vapour deposition. These so-called CNT "forests" may be (i) densified into pillars [79], (ii) spun into 1-dimensional fibres [80], or (iii) drawn into 2-dimensional mats [80].

- The second family utilises liquids to create suspensions of short, mass-produced CNTs. These CNT-solvents suspensions can be filtered to create (iv) random planar "buckypaper" mats [81]. Alternatively, the pultrusion (v) of high weight-fraction CNT suspensions into a bath of coagulating fluid creates an aligned fibre [82], akin to the spinning process used to manufacture polymer fibres of ultra-high molecular weight [83]. Additionally, porous CNT foams (vi) are often produced from aqueous gel precursors by critical point drying, or freeze drying [84].

- The final family uses direct-spun carbon nanotube aerogels, produced via the aforementioned Cambridge direct-spinning process [31]. Direct-spun fibres (vii) are produced via on-line solvent-condensation of the aerogels [22]; alternatively the spinning of aerogel layers onto a rotating mandrel produces direct-spun mats [85], labelled (viii).

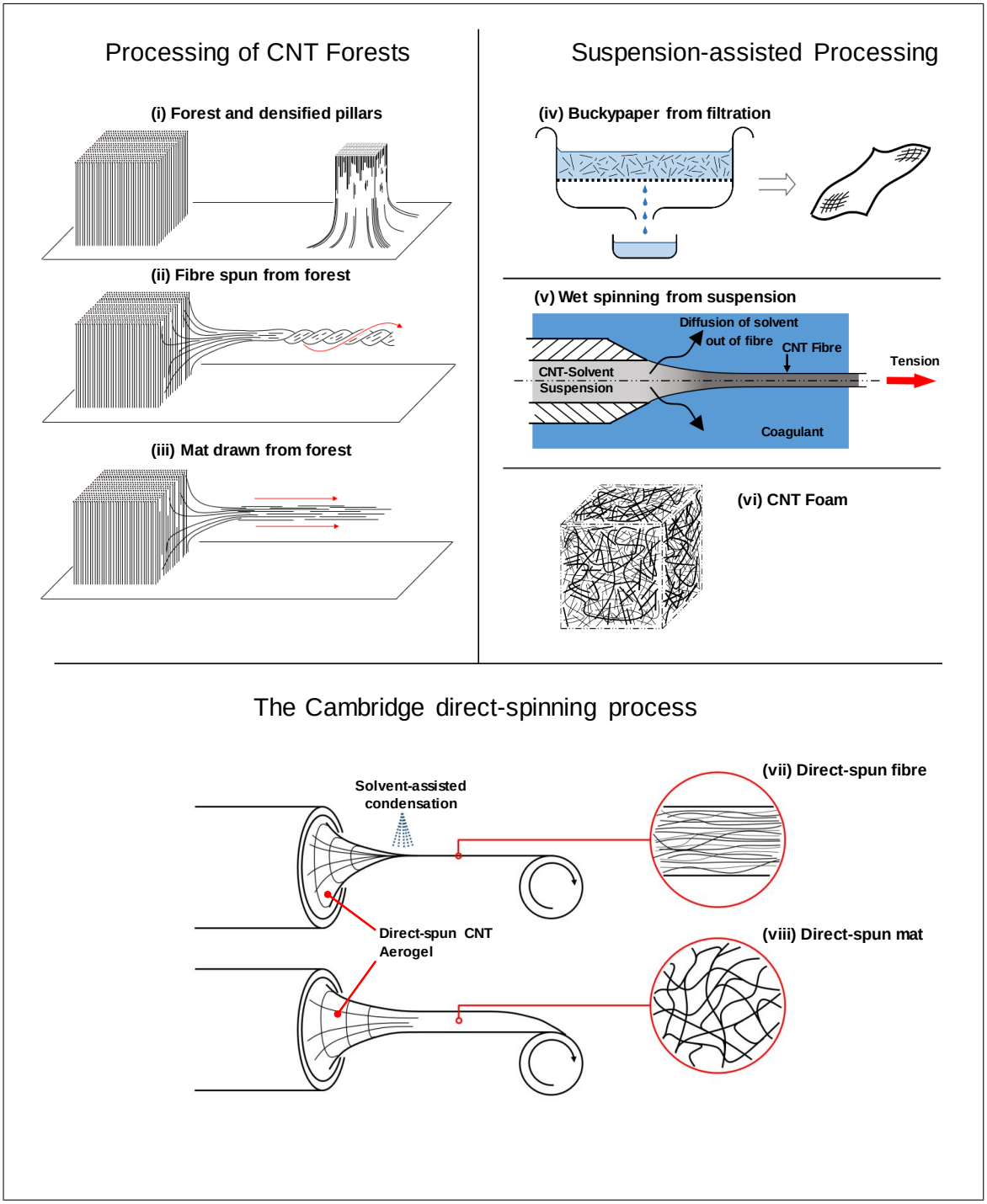

Fig. 2.1 Classes and manufacturing methods of different macroscopic materials predominantly consisting of carbon nanotubes.

2.1.3 The properties and microstructure of CNT material classes

Now consider the mechanical properties and behaviour of different macroscopic CNT materials. The performance of materials in a given application can be compared with a *merit index* [12], the definition of which is specific to the intended use. For the sake of comparison, the Young's modulus and strength of materials are often normalised by their density — referred to as specific properties. In this instance, the specific modulus and strength are a measure of the mechanical efficiency of the different CNT materials under uniaxial stress — tensile in the case of CNT fibres and mats, and compressive for CNT foams, forests and densified pillars. The specific Young's modulus and strength of macroscopic carbon nanotube materials as reported in literature are plotted in Figure 2.2, alongside the properties of carbon nanotube walls [7–11], for which a density of 2,300 kg/m^3 is assumed [86], and common engineering materials [12, 13]. The charts include the data of CNT yarns spun from forests [27, 87–102], mats drawn from CNT arrays [87, 88, 103–108], buckypapers [105, 109–120], fibres spun from suspensions [121–128], direct-spun CNT mats [85, 129–146], fibres and aerogels [54, 135, 141, 147–170], CNT foams [84, 171–181] and CNT forests and densified pillars [79, 170, 182–208]. Many reviews of macroscopic CNT material classes are available in literature [19, 209–223].

The combination of specific modulus and strength measured for isolated carbon nanotube walls in uniaxial tension is unmatched by all other engineering materials plotted in Figure 2.2, and the specific mechanical properties of aligned carbon nanotube mats and fibres can exceed those of metal alloys and composites. Substantial variation in specific strength and modulus occurs both within and between the different CNT material classes. By comparison, the variation in the specific tensile strength and modulus of the constituent CNT walls is relatively minor: it follows that the wide range in specific Young's modulus and strength observed across all CNT material classes is due to their varied microstructures and resultant micromechanical deformation.

Charts that summarise the elastic Young's moduli E, strength σ, electrical and thermal conductivity, and density ρ of macroscopic CNT material classes are presented in Figures 2.3, 2.4, 2.5 and 2.6 respectively. Note that the bulk density of CNT materials ranges from a few kg/m^3 for CNT foams to over 1,000 kg/m^3 for CNT fibres, and their moduli range from tens of kPa to hundreds of GPa, see Figure 2.3. Large differences in strength and conductivity are also observed. Wide variation in all properties occurs between the CNT material classes, and also within the individual classes themselves.

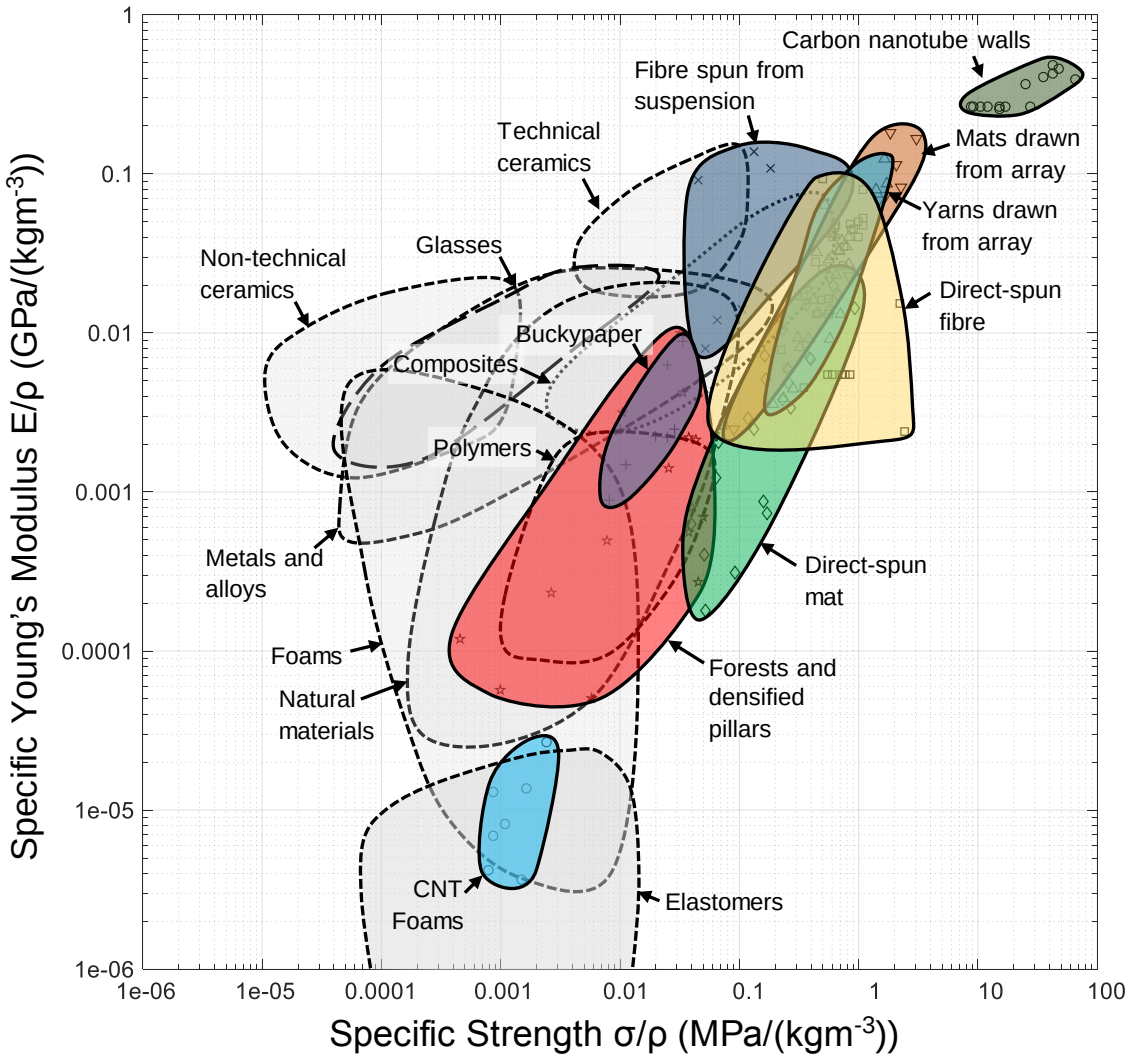

Fig. 2.2 The specific strength and modulus of macroscopic CNT material classes compared to those of engineering materials [12].

A Voigt bound is plotted in Figure 2.3, based upon the in-plane Young's modulus of a CNT wall (i.e. graphene) of 1 TPa [224]. The Young's modulus of macroscopic CNT materials is much below this Voigt bound. A similar observation can be made for strength as follows: If the ultimate tensile strength of CNT walls is assumed to be 100 GPa, all CNT morphologies lie more than an order of magnitude below the Voigt bound for ultimate tensile strength, as drawn in Figure 2.4. In broad terms, the Young's modulus E and compressive yield strength σ of CNT foams and CNT forest-based materials appear to scale with density ρ according to $E \sim \rho^3$ and $\sigma \sim \rho^2$ respectively. This scaling law is representative of cellular solids such as 2-dimensional hexagonal honeycombs [225].

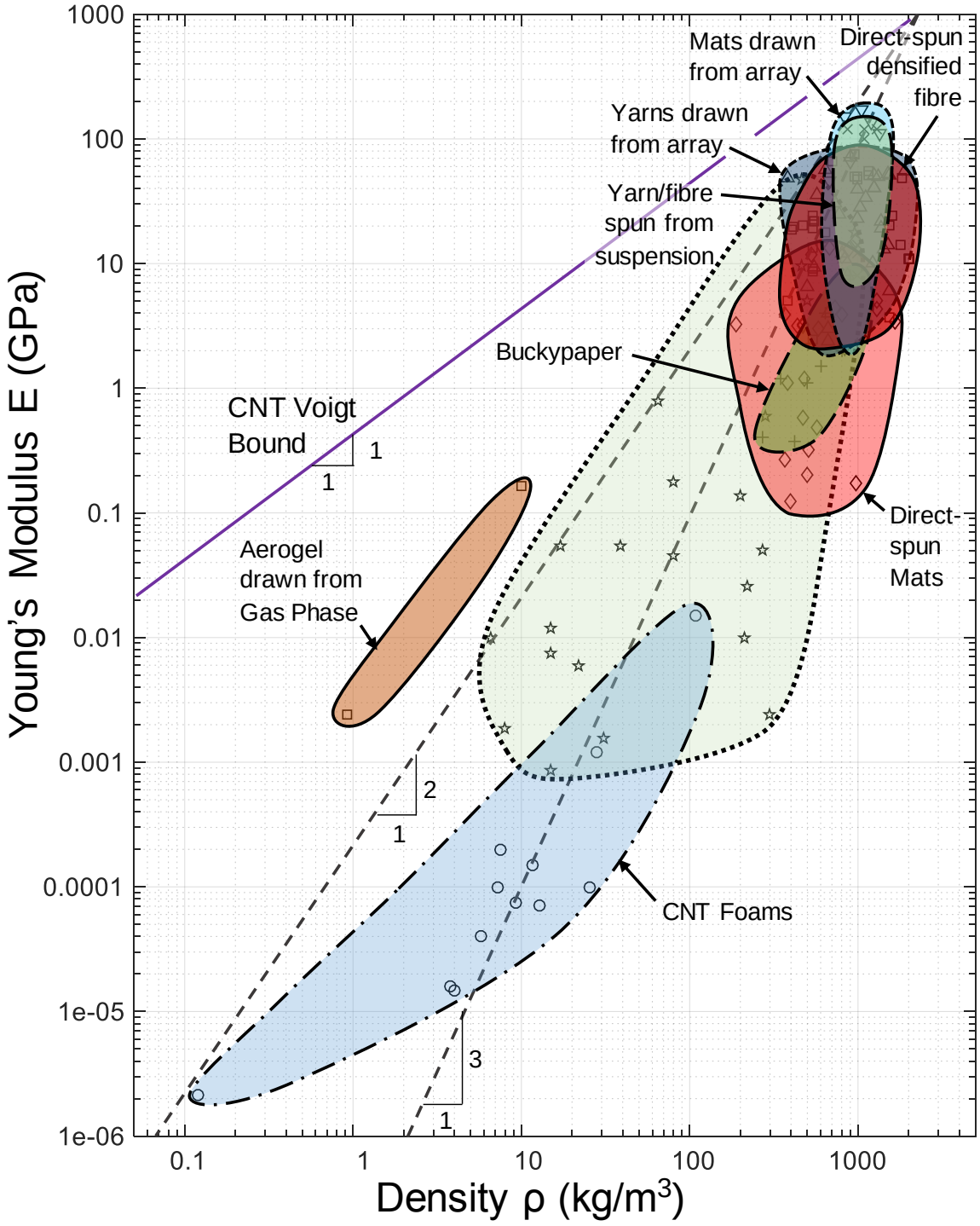

Fig. 2.3 Young's modulus versus density of CNT material classes.

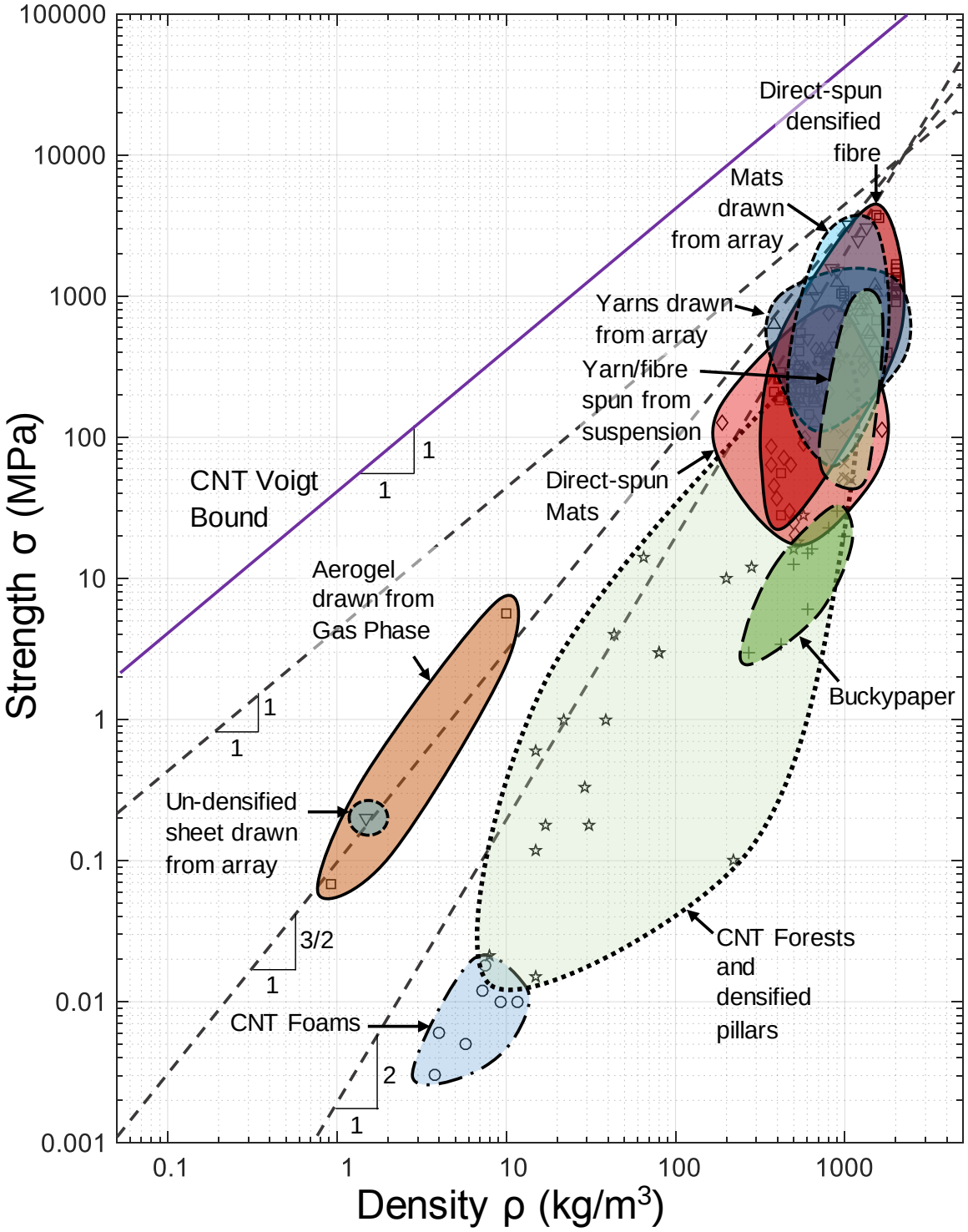

Fig. 2.4 Strength versus density of CNT material classes.

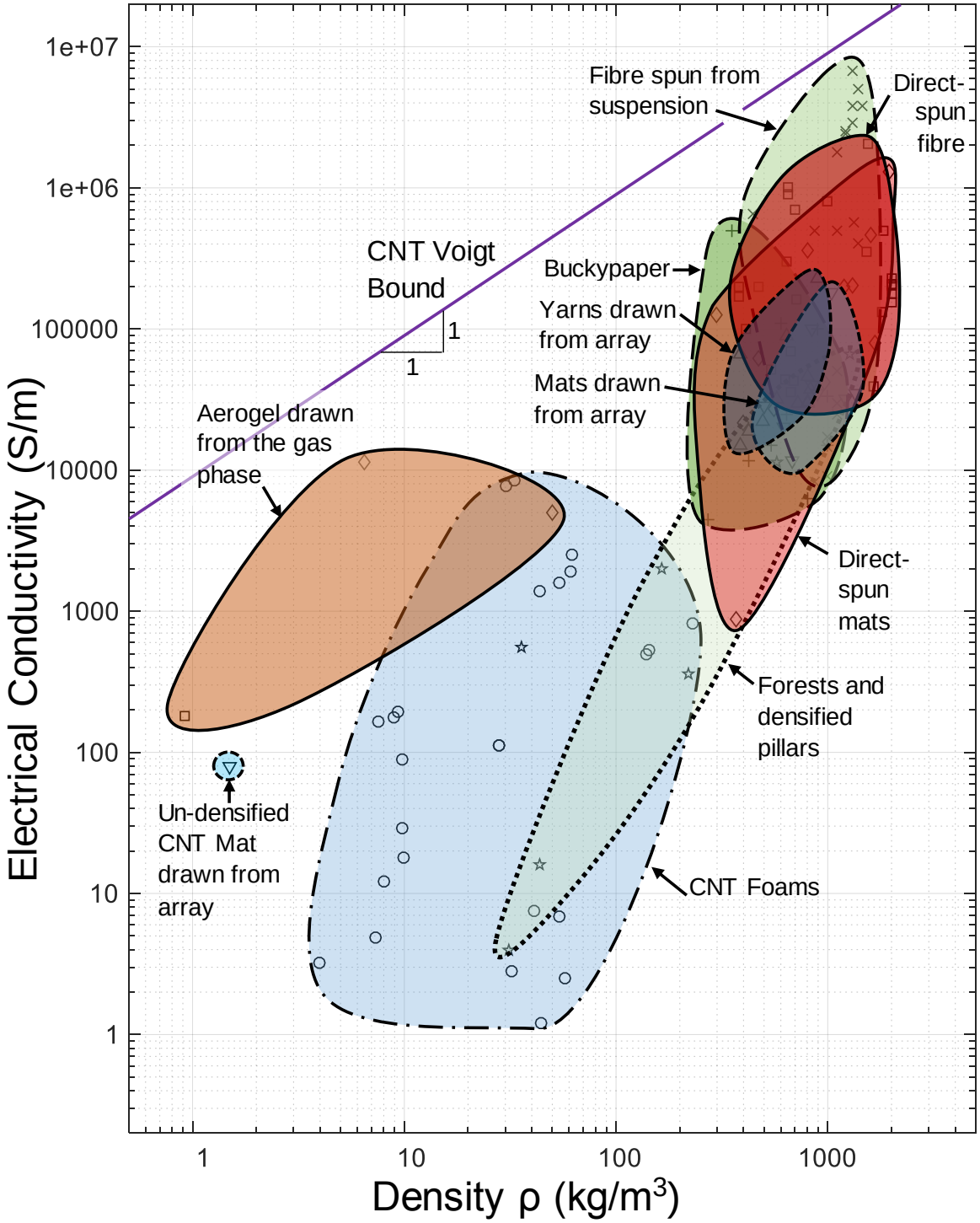

Fig. 2.5 Electrical conductivity versus density for CNT material classes.

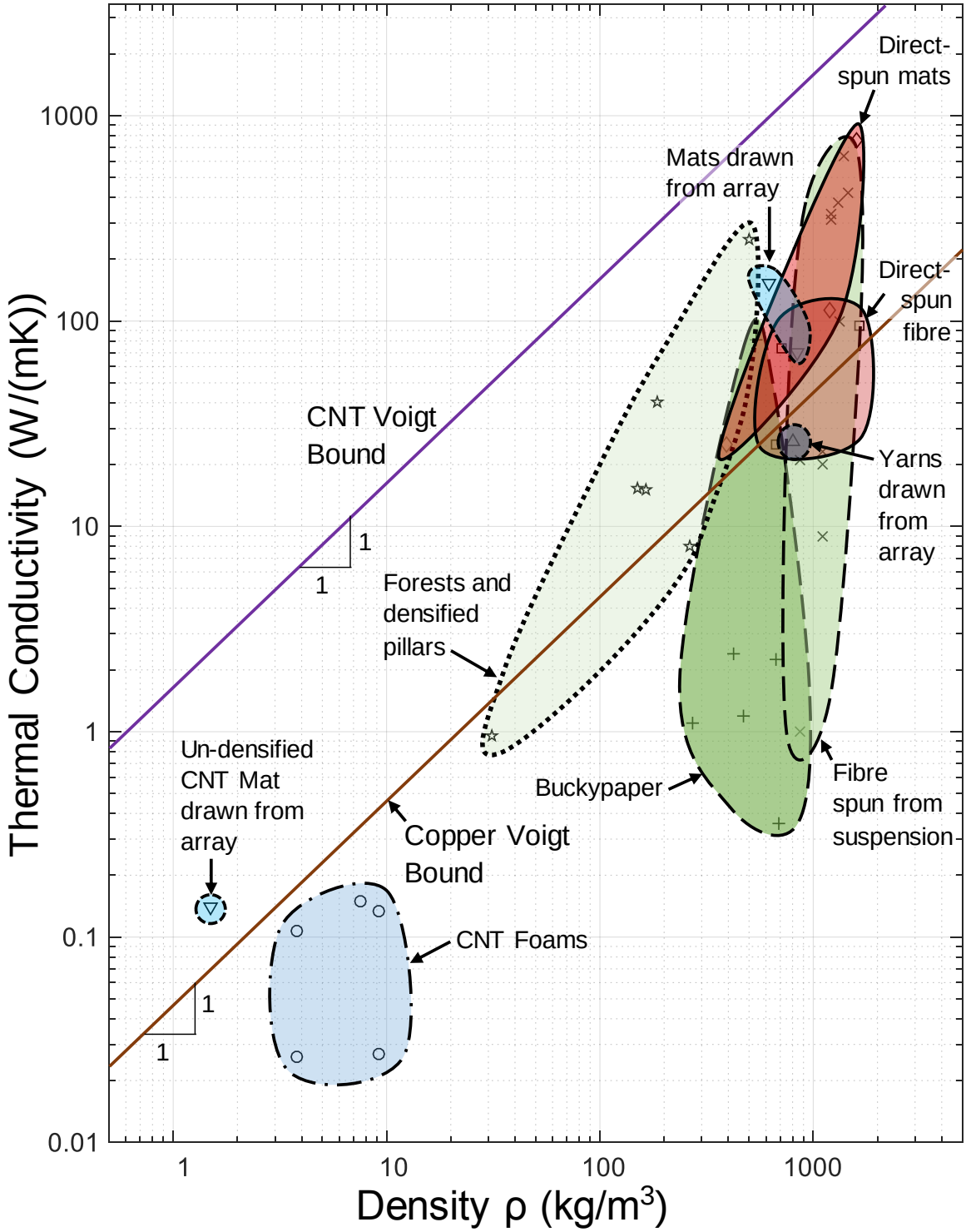

Fig. 2.6 Thermal conductivity versus density for CNT material classes.

Consider the properties of aligned CNT materials, such as fibres spun from suspensions, and mats drawn from CNT arrays. Their Young's modulus and strength vary by up to two orders of magnitude for a given density. Electrical conductivity varies considerably within individual material classes and between them. A Voigt bound is drawn in Figure 2.5, based upon the highest measured electrical conductivity of an individual CNT in literature [24]. Fibres spun from suspensions may possess high values electrical conductivity close to that of individual CNTs. Such values of high electrical conductivity are due to doping from acids used in manufacture, or are obtained via treatment with iodine [121].

Now consider the chart of thermal conductivity versus density, Figure 2.6. A Voigt bound based upon the thermal conductance of CNT walls [14] is also included, which all macroscopic CNT materials lie below. A line of specific thermal conductivity κ/ρ=0.0449 m^4/Ks^3, equal to that of pure copper [226], has been added to Figure 2.6. This line lies well below that of many CNT materials.

The Young's modulus E is plotted against the strength σ of the macroscopic CNT material classes in Figure 2.7, and the electrical conductivity of the CNT material classes is plotted against their thermal conductivity in Figure 2.8. The regions of material property space occupied by the CNT materials are annotated with micrographs of their microstructures from literature [72, 81, 93, 121, 170, 171]. Direct-spun CNT mats and fibres with little anisotropy present in their constituent microstructure of CNT bundles possess in-plane strengths and Young's moduli similar to those of amorphous polymers [12]; in contrast, mats and fibres with high degrees of microstructural alignment possess a tensile modulus and strength in the range of metal alloys [12]. The buckling of CNT forests under compressive strain results in moduli and strength much below that measured in tension [170]. Electrical and thermal conductivity also vary widely depending on microstructure. The greatest values occur for dense, aligned microstructures — in particular for CNT fibres spun from suspensions [121].

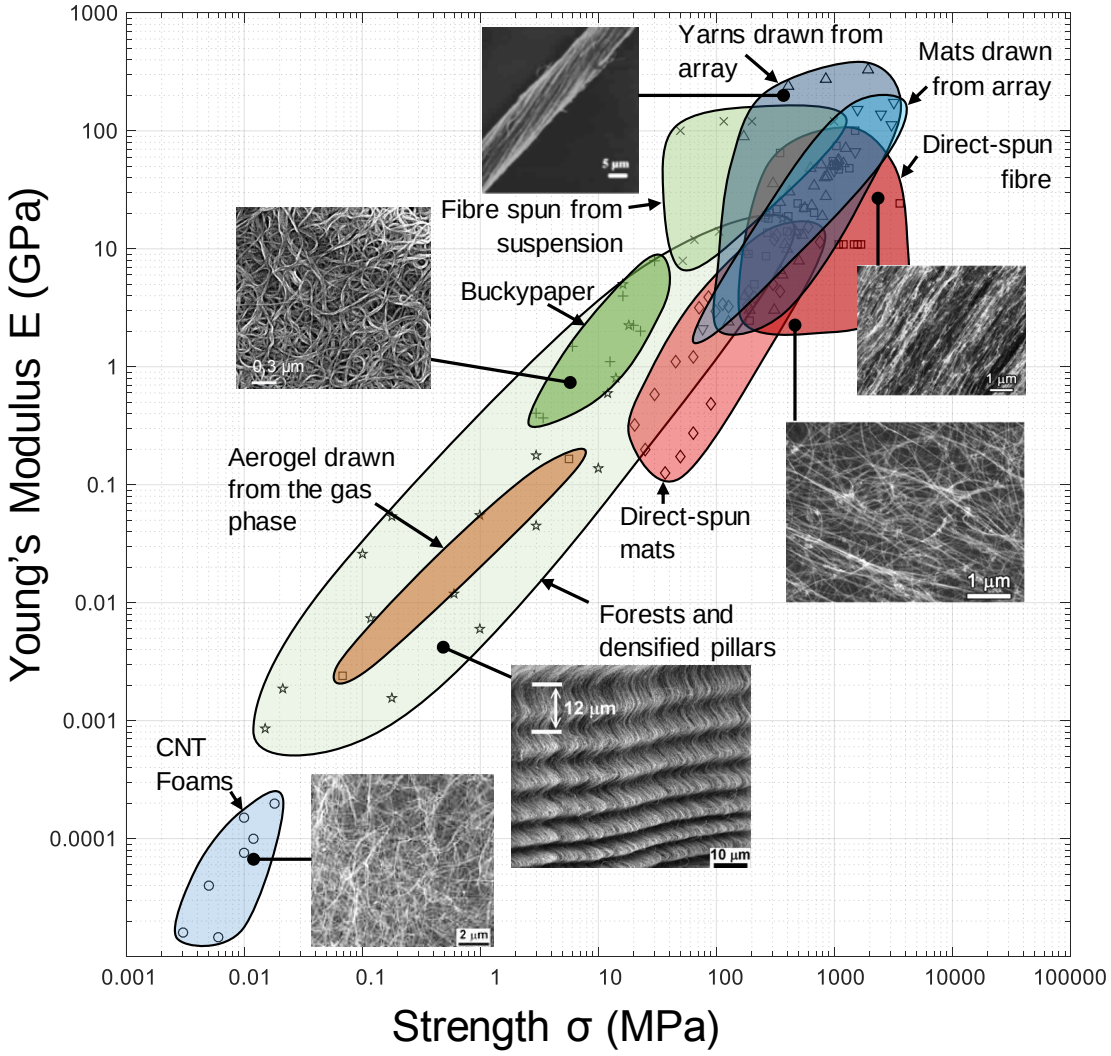

Fig. 2.7 The Young's modulus and strength of macroscopic carbon nanotube material classes annotated with images of microstructure reproduced from [72, 81, 93, 121, 170, 171].

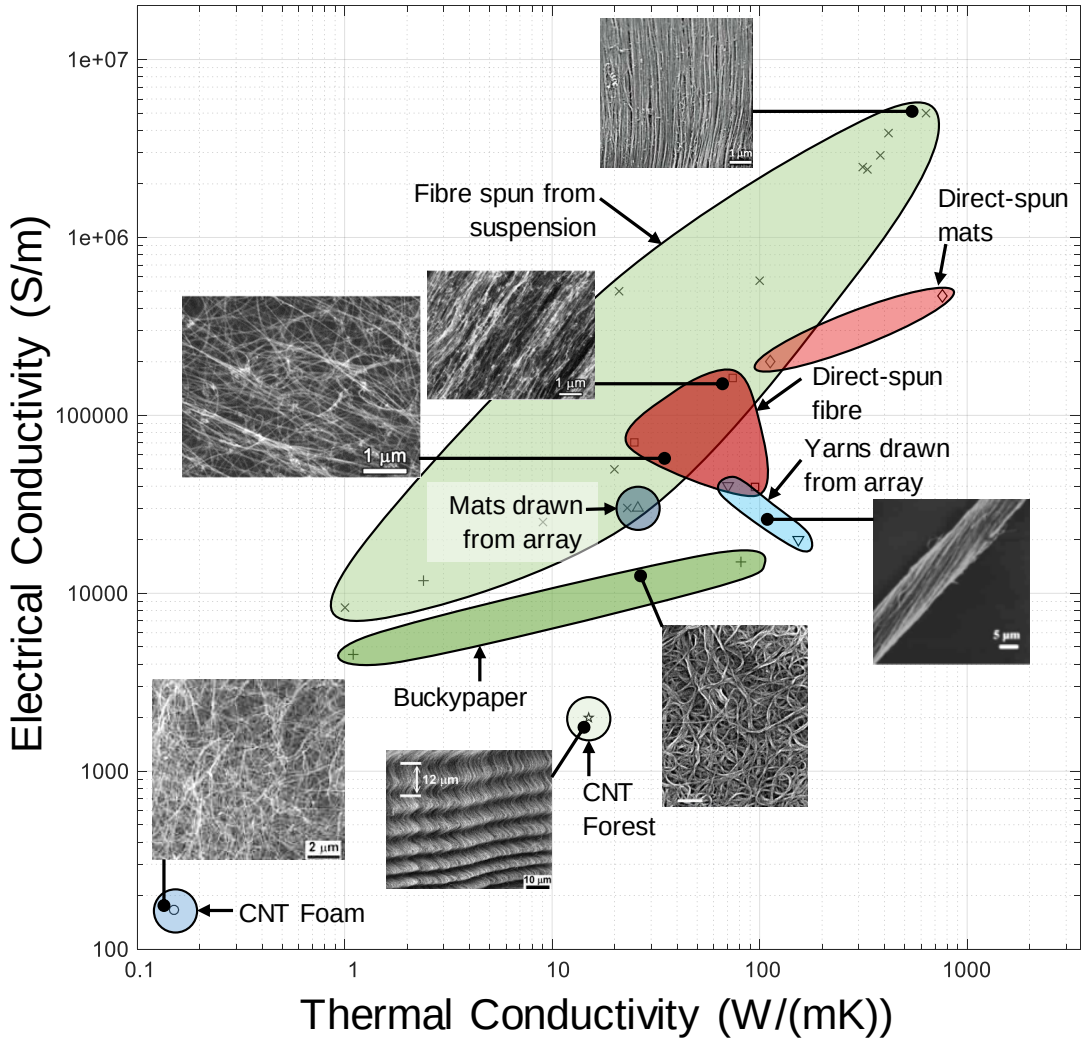

Fig. 2.8 The electrical conductivity and thermal conductivity of macroscopic carbon nanotube material classes annotated with images of microstructure reproduced from [72, 81, 93, 121, 170, 171].

2.2 Mechanics of the direct-spun CNT mat microstructure

Recall the three distinct hierarchies of the of direct-spun CNT mat microstructure described earlier in section 1.3: the carbon nanotube, nanotube bundle, and network of interconnected CNT bundles. The mechanical phenomena relevant to each microstructural scale are now discussed with reference to the literature.

2.2.1 Properties and behaviour of carbon nanotubes

Carbon nanotubes represented a challenge for early researchers, as their size rendered conventional experimental techniques for the establishment of material properties unsuitable. A range of bespoke experimental techniques were thus developed to determine their mechanical properties, and have since been supplemented with a range of micromechanical modelling methods [227].

Tensile modulus and strength of CNTs

Predictions for the axial Young's modulus and bending stiffness of carbon nanotubes were suggested by Ruoff and Lorentz in 1995 [233]. With calculations based upon the in-plane moduli of graphite, with a 0.34 nm spacing between adjacent CNT walls, they suggested that the walls possessed a modulus of $\sim$1 TPa.

The first measurements of the CNT wall modulus were obtained by Treacy, Ebbesen and Gibson in 1996 [234]. Transmission electron microscopy (TEM) was used to observe isolated CNTs, clamped at one end. The vibration amplitude at the free end was measured as a function of temperature, and the value of wall tensile modulus was inferred from consideration of thermal excitation and CNT dimensions — on average 1.8 TPa. Their method was improved by Poncharal *et al.* [235], who excited end-clamped CNTs at their natural vibration frequency with an electrically induced force. The Young's modulus of smaller diameter CNT walls was calculated to be 1 TPa, though the measured transverse stiffness was much below that predicted with Euler theory for CNTs with diameters of over 12 nm. This discrepancy was attributed to deformation switching from Euler bending to periodic buckling within the walls, as observed elsewhere [233].

Numerical atomistic calculations used to predict the strength of defect-free CNT walls under tensile load suggested failure stresses exceeding 100 GPa [236]. Tensile tests on isolated CNTs by Yu *et al.* [7] using a nanostressing stage contained within a scanning

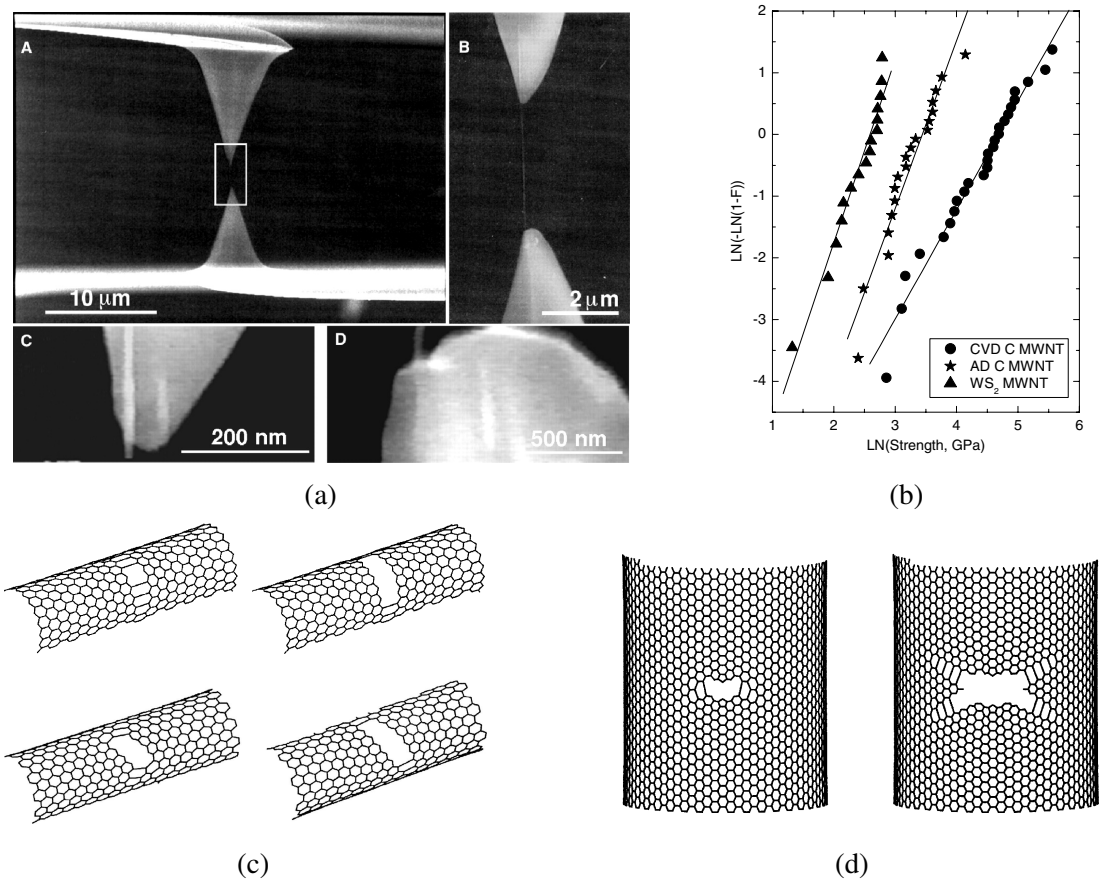

Fig. 2.9 The tensile strength of CNTs. (a) Tensile testing of CNTs with a *nanostressing stage*, reproduced from [7]. (b) A Weibull strength plot for different types of CNT, reproduced from [228]. Images of atomistic simulation reproduced from [229] of the effect of defects and chirality upon CNT tensile strength for (c) flaws in the *zig-zag* direction within CNTs of different chirality and (d) the growth of flaws in armchair CNTs.

electron microscope (SEM) allowed direct axial measurement of the CNT modulus and ultimate strength, see Figure 2.9a. MWNTs were attached to two opposing atomic force microscope tips by soldering with an electron beam. Upon assuming that only the outer layer of the MWNT bore stress and had thickness equal to the interlayer spacing between the shells of 0.34 nm, the modulus of the CNT wall was measured to lie between 270 GPa and 950 GPa, and the tensile strength between 11 GPa and 63 GPa. Tensile tests on isolated CNTs were subsequently conducted by Ding *et al.* [237], who recorded outer wall strengths between 10 GPa and 66 GPa, and Young's modulus between 620 GPa and 1200 GPa, with a mean Young's modulus of 940 GPa. Tensile tests of pristine CNTs by Peng *et al.* [10] confirmed the atomistic predictions for defect-free CNTs, recording wall strengths up to 110 GPa and Young's moduli in a narrow range between 990 GPa and 1105 GPa. The

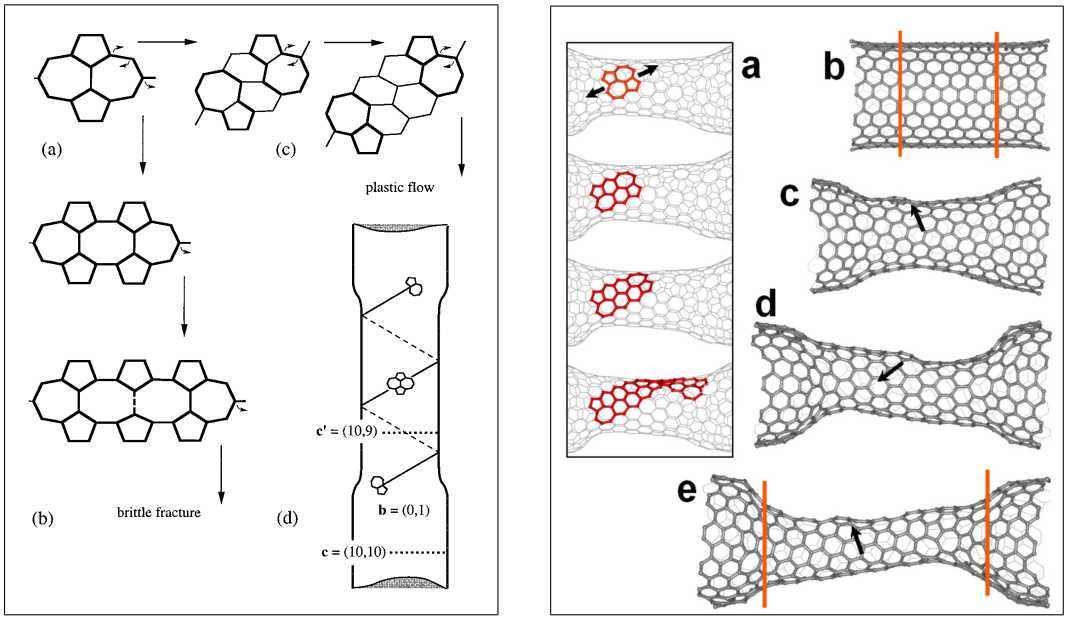

(a) (b)

Fig. 2.10 At higher temperatures, SWNTs of certain chirality may undergo plastic flow [230]. Plastic deformation occurs due to dislocation-like movement of the Stone-Wales defect as sketched in (a), reproduced from [231]. (b) Atomistic simulation of plastic flow in CNTs at high temperature, reproduced from [232].

measured stress-strain response of CNTs at room temperature is elastic brittle [7, 10, 237], and the distribution of tensile strength according to the literature is captured by Weibull theory [228, 238], see Figure 2.9b. Weibull theory is commonly used to predict the strength of elastic brittle materials, for example ceramics, which fail due to the fast fracture of pre-existing flaws [239]. The failure of multi-walled CNTs in tension is typically accompanied by sword-in-sheath like pull-out of the inner shells [7] due to weak van der Waals bonds between neighbouring walls. The discrepancy between the measured and ideal ultimate tensile strength of CNT walls has been understood with numerical simulation of defects within CNT walls under tension [240–242], for example in Figure 2.9c and 2.9d. These studies explain the role of flaws in reducing the tensile strength of the walls, and its dependence upon the wall chiral vector [243]. The prediction that CNTs of certain dimensions and chiral vectors could deform plastically at high temperature [244] due to dislocation-like movement of the Stone-Wales defect [231, 245] as illustrated in Figure 2.10a and Figure 2.10b was experimentally verified by Huang *et al.* [230], though the deformation mechanism does not occur at room temperature. The ductile and brittle regimes of behaviour are surmised by theoretical failure regime maps in literature [246, 247].

Bending and other behaviour under transverse loading

CNTs are capable of undergoing large recoverable deformations in bending, as reported by Iijima [248] and Falvo *et al.* [249], see Figure 2.11b-d. The nonlinear elastic deformation of CNTs (kinking, buckling and self-collapse) has been successfully captured with atomistic simulations, see Figure 2.12a and Figure 2.12b [248, 250–252], and continuum theory is also well suited to modelling the deformation of large, multiwalled CNTs, as demonstrated by Pantano, Parks and Boyce [253, 254], and illustrated in Figure 2.12c. Their method models CNT walls with finite element shells [254], which are assigned elastic constants based upon the flexural modulus of the CNT wall (deduced from atomistic simulation), the in-plane Poisson ratio of single-crystal graphite, and the tensile modulus of the CNT walls. The van der Waals interaction between the CNT walls is represented with the Lennard-Jones potential. Close agreement between atomistic simulations of CNT walls, predictions from shell theory, and experimental observation is obtained across a wide variety of different load cases, including interaction between CNTs and substrates, self-collapse, and determination of the buckling wavelength under flexure [254]. The transverse Young's modulus of individual carbon nanotubes measured by indentation with the tip of an atomic force microscope lies between 0.3 GPa and 40 GPa [255–257], rising with increasing strain [255, 256].

2.2.2 Properties and behaviour of carbon nanotube bundles

Due to van der Waals attraction between their walls, CNTs readily self-assemble into close-packed, crystalline bundles [258, 259]. In these bundles, the walls of adjacent CNTs flatten against one [260], creating an area of contact between adjacent CNTs through which shear stress can be transferred [261, 262]. The size of this contact area is dependent upon CNT diameter [261, 263] and number of walls [262]. The shear stiffness and strength of the van der Waals bond between the walls of an individual CNT, and between CNTs within bundles, is much below the in-plane modulus and tensile strength of the walls. The weak van der Waals bonds endow bundles with a low shear modulus, and their shear deformation may dominate their total deflection under transverse loads. The transverse stiffness of CNT bundles was measured by Salvetat *et al.*, using the tip of an atomic force microscope to apply load [264], see Figure 2.13a. For CNT bundles of the smallest diameter, calculation of the CNT wall modulus from the measured transverse stiffness using Euler theory infers a value of 1 TPa, close to that measured in tensile tests of CNT walls elsewhere [10]. The wall modulus calculated in this manner decreases with increasing bundle diameter, see Figure 2.13b. Upon assuming the value of axial bundle modulus was invariant, the longitudinal bundle shear modulus was deduced to lie between 0.7 GPa and 6.5 GPa $\pm 50\%$ [264].

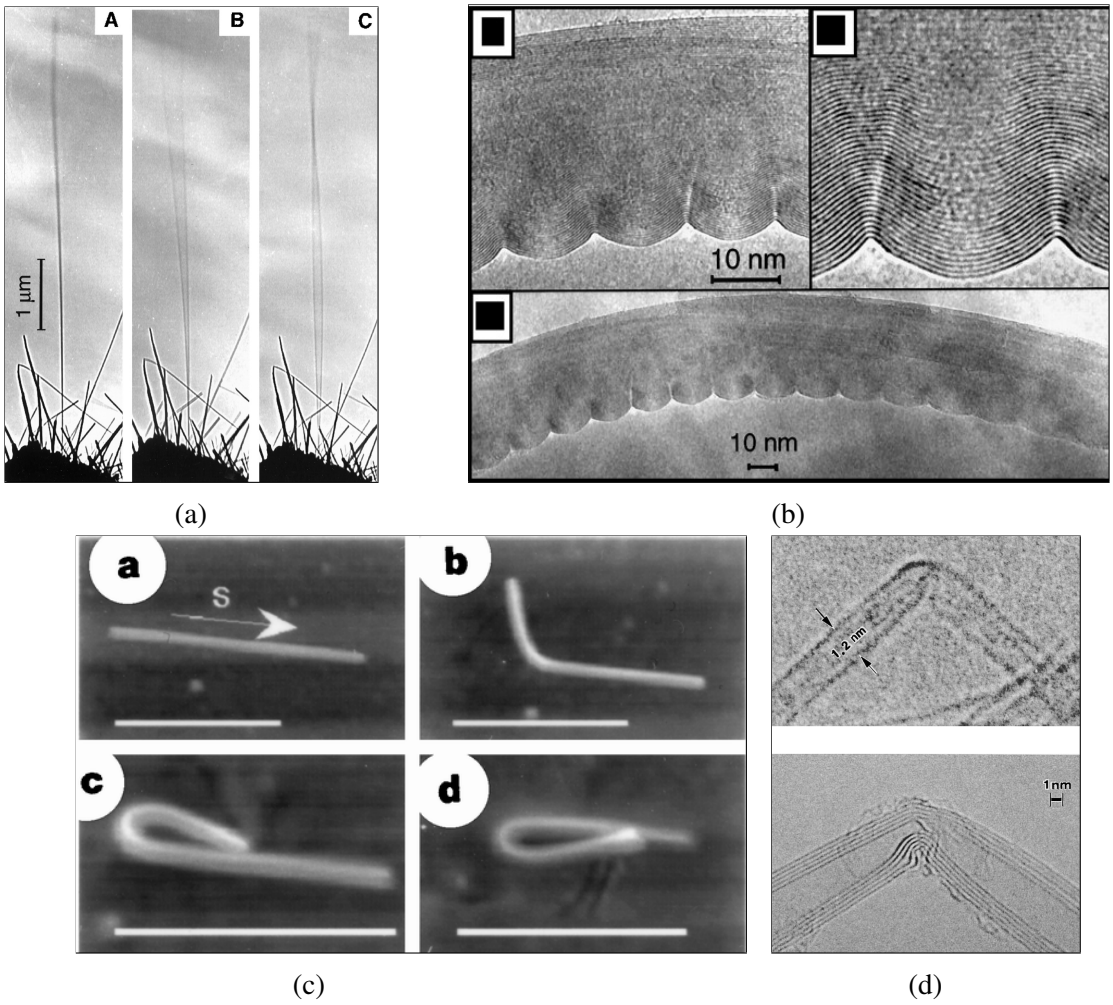

Fig. 2.11 (a) Electromechanical resonance measurement of the CNT wall modulus, (b) the wave-like buckling pattern observed on the inner wall of large diameter MWNTs in bending, both reproduced from [235]. (c) The reversible deformation of CNTs in bending at large deflections, reproduced from [249]. (d) TEM images of CNT wall kinking, reproduced from [248]; note that the walls remain intact.

Recorded failure loads during tensile tests of carbon nanotube bundles [265–267] suggest that only the outermost CNTs in bundles fracture, and a sword-in-sheath failure mechanism is observed in experiment [266, 267] where inner CNTs within the bundle pull out of the outermost fractured CNTs. Little stress is transferred into the inner CNTs due to the low stiffness and strength of the van der Waals bonds between adjacent CNTs, as is also the case for the walls within individual tubes [10]. The irradiation of CNT bundles forms covalent cross-links between CNTs, which results in fracture across the entire cross-section at much greater tensile load [266].

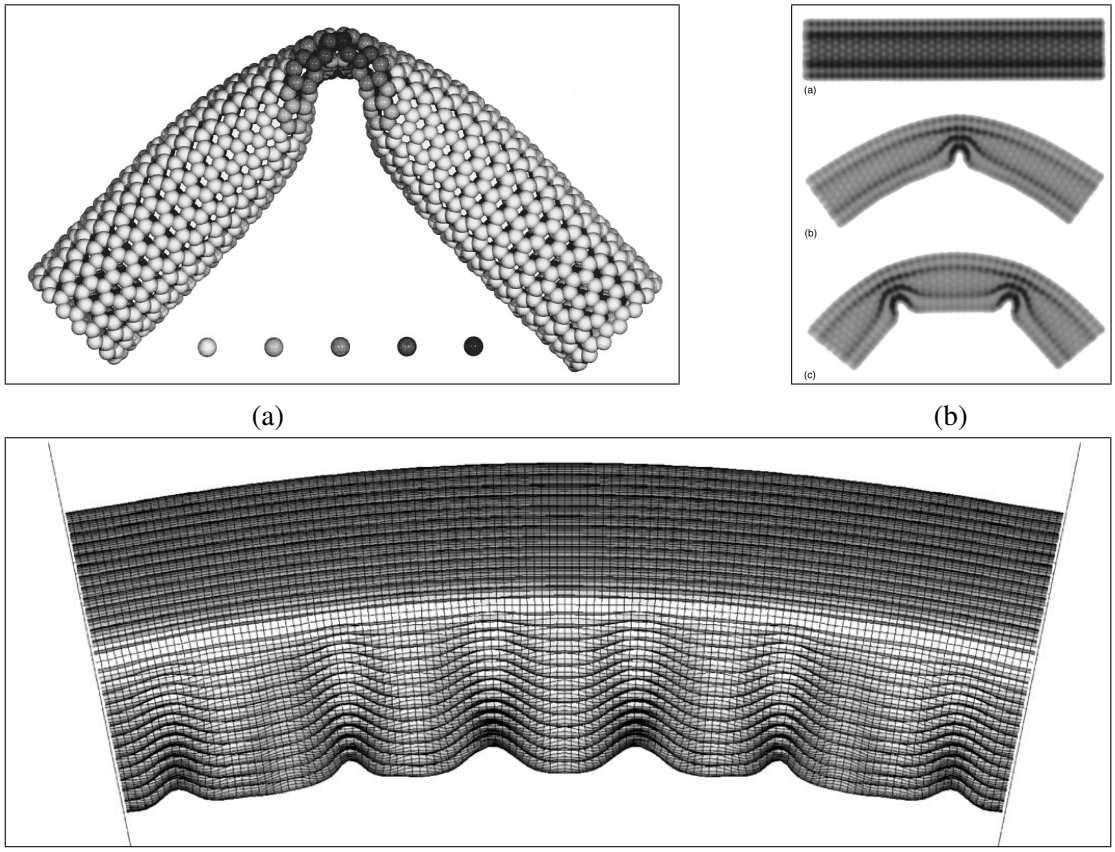

Fig. 2.12 Modeling approaches for the bending deformation of CNTs. (a) Kinking of a SWNT and (b) kinking of a DWNT, both images of atomistic simulation are reproduced from [248]. (c) Modeling of a multiwalled CNT of large diameter in bending using shell theory and finite element simulation reproduced from [253]. Note the appearance of multiple kinks spaced apart in multi-walled CNTs.

Finally consider the stiffness and strength of CNT bundles upon the application of hydrostatic stress, and loading in the radial direction. In-situ X-ray diffraction studies of SWNT bundles under hydrostatic pressure suggest that the bulk modulus of CNT bundles lies between 34 GPa [268] and 42 GPa [269]. Although measurements differ depending on CNT geometry, radial collapse (bifurcation) or elastic nonlinearity is typically reported for hydrostatic pressures between 1 GPa and 1.5 GPa [269–271], and the onset of permanent, irreversible deformation is reported for pressures between 2.9 GPa and 5.2 GPa [269–271]. Predictions for the transverse Young's modulus of SWNT bundles range from 17 GPa to 63 GPa [272–274].

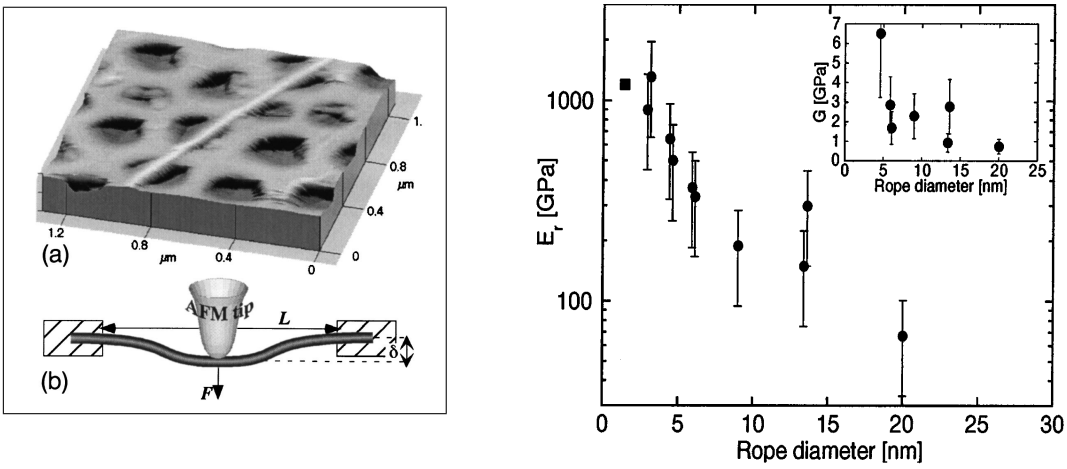

(a) (b)

Fig. 2.13 (a) Transverse deflection of CNT bundles using an atomic force microscope (AFM) tip; bundles are laid across a porous substrate. (b) An *effective modulus* E_r as calculated from the bundle stiffness in transverse deflection and dimensions with Euler bending theory decreases with increasing bundle diameter due to the low bundle shear modulus. Both images are reproduced from [264].

Properties of the van der Waals bond between CNT walls and graphitic layers

Measurements of shear yield strength reported in the literature for a variety of graphitic systems, including between the walls of an individual CNT, between adjacent CNTs within bundles, and between graphite layers, are summarised in Table 2.1. The introduction of covalent bonding between CNTs by irradiation may increase the flexural rigidity of CNT bundles under transverse deflection by up to a factor of 30 [275]. Whilst the bond between pristine CNT surfaces may yield at a stress of only 0.05 MPa [276], the introduction of defects in the walls may increase the shear yield stress to 70 MPa [277], and lap shear tests of the bond between CNT bundles coated with polymers during the chemical vapour deposition process reveal shear strengths of up to 400 MPa [267, 278]. The bond between adjacent pristine CNT surfaces with long overlap lengths is expected to lie between 30 MPa and 60 MPa [279]. Theory suggests that the shear strength measured between pristine CNTs arises due to pinning by defects [280] as opposed to the weak van der Waals bonding alone.

Now consider the van der Waals attraction between CNT walls. The van der Waals forces between CNT walls are dominated by the contribution of dispersion forces, which are electromagnetic in origin [291, 292]. Forces of this nature are characterised by a Hamaker constant A, as derived from Lifshitz theory. This relates to their surface energy γ via the relationship $\gamma = A/\left(24\pi D_0^2\right)$, with the intermolecular spacing $D_0 = 0.165$ nm [293, 294].

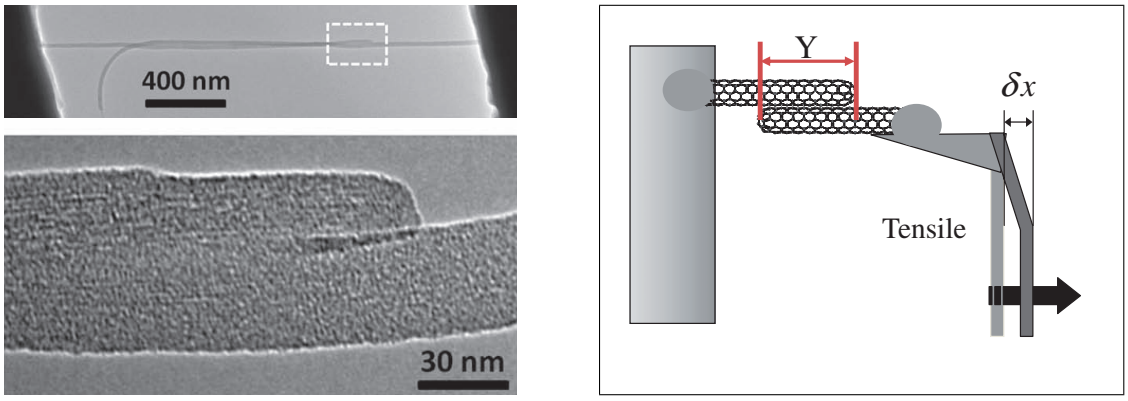

(a) (b)

Fig. 2.14 Measurement of the shear strength between CNT walls. (a) Lap shear tests on carbon nanotube bundles; image reproduced from [278]. (b) Lap shear tests between individual CNTs, reproduced from [277].

Accurate measurements of surface energy may be obtained through use of a *surface force apparatus* as illustrated in Figure 2.15a [292, 295], using the *jump method* as pioneered by Tabor and Winterton [296]; recent measurements performed on few-layer graphene [295] have reported surface energies of $\gamma = 0.119$ J/m^2 and 0.115 J/m^2 for few-layer and single-layer graphene respectively. The surface energy between CNTs and between graphite layers has been also been measured with a variety of other experimental techniques, including peeling of CNTs from substrates as illustrated in Figure 2.15b [294] and heat of wetting experiments on graphite crystals [297, 298]. Data reported in literature is summarised in Table 2.2.

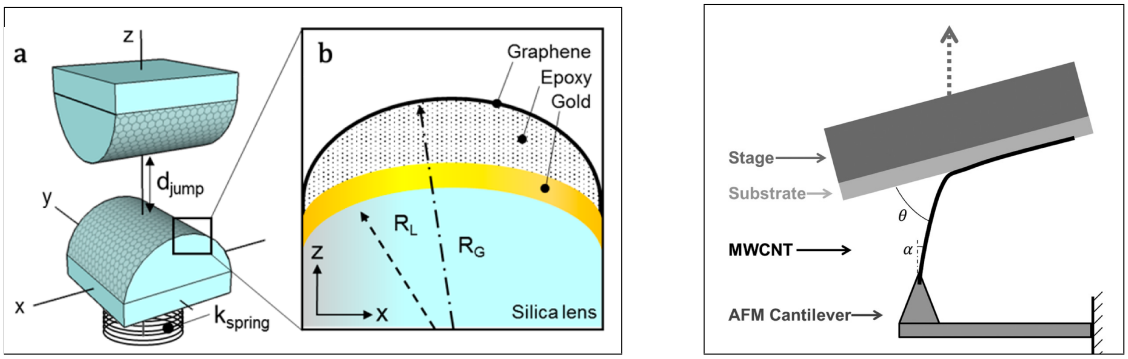

(a) (b)

Fig. 2.15 Measurement of the van der Waals attraction between graphitic layers. (a) Measurement with surface force apparatus, image reproduced from [295]. (b) Peeling of a CNT from a graphite substrate to quantify surface energy, image reproduced from [294].

Table 2.1 Experimental measurements of the interlayer shear strength in graphitic systems.

Method	Measured shear strength	Reference
AFM tip used to slide a MWNT against a SWNT	4 ± 1 MPa	[281]
AFM tip used to slide a MWNT against a SWNT: measurement of static friction	up to 1.4 GPa	[282]
Telescopic sliding of shells within a MWNT	Static: 0.66 MPa Dynamic: 0.43 MPa	[283]
Controlled sliding and pull-out of shells from within an MWNT	Static: 0.3 MPa Dynamic: 0.08 MPa	[284]
Interlayer shear strength of graphite	0.48 MPa	[285]
Shearing of graphite layers	< 3.3 MPa	[286]
Controlled pull-out of shells from a DWNT	2.6 Pa	[287]
Shear strength in crystal graphite	0.25 MPa to 0.75 MPa Average 4.8 MPa	[288]
Sliding of carbon nanotubes on graphite surfaces	2 MPa	[289]
Telescopic sliding of MWNTs	Static shear strength < 0.04 MPa	[276]
Sliding of MWNTs grown by CVD with lap shear test	≈ 74 MPa	[277]
Sliding of MWNTs grown by CVD with lap shear test	30 MPa to 60 MPa	[279]
Sliding of a smaller inner bundle of DWNTs out of a larger bundle	7.8 MPa	[290]
Lap shear tests of CNT bundles grown by CVD	330 ± 80 MPa	[278]

Table 2.2 Measurement and prediction of the surface energy between CNT walls, graphene and graphite.

Method	Measured surface energy (J/m^2)	Reference
Experiments		
Peeling of MWNT from a graphene sheet	0.2 ± 0.09 0.36 ± 0.16 Depending on assumed contact area	[294]
Heat of wetting for graphite crystals	0.260/2	[297, 298]
Observation of collapsed MWNTs, and interpretation with elastic analytical model	Range: 0.06/2 to 0.43/2.† Average 0.21/2. †	[299]
Thermal desorption spectroscopy and calculation assuming pairwise additivity.	0.34/2 to 0.40/2 †	[300]
Interlayer pull-out of graphite sheets (Mode II)	0.18/2 to 0.20/2	[301]
Peeling of a graphite crystal (Mode I)	0.27/2 to 0.36/2	[302]
Self-retraction of graphite upon pull-out (Mode II)	0.330/2	[303]
Interfacial sliding of graphite (Mode II)	0.222/2 to 0.232/2	[304]
Adhesion force with atomic force microscopy	0.307/2	[305]
Single-layer graphene in dry nitrogen, crossed cylinders with surface force balance	0.111 to 0.119	[295]
Few-layer graphite in dry nitrogen, crossed cylinders with surface force balance	0.116 to 0.122	[295]
Inferred from elastic strain energy of a curved graphene sheet over a blister	0.210/2 to 0.232/2	[306]
Intrinsic friction analysis, microscopic determination of the Hamaker constant, and solution from universal distance.	0.14	[307]
Scanning force microscopy measurement of deflections and friction.	0.14	[307]
Theory		
Summation of the Lennard-Jones potential	0.330/2	[298]

† Converted assuming the areal density of carbon atoms within CNT walls (i.e. graphene) is 3.82×10^{19} m^{-2} [308]

2.2.3 Microstructure and behaviour of direct-spun carbon nanotube mats and fibres

Consider the interconnected network of carbon nanotube bundles that comprises the microstructure of direct-spun carbon nanotube mats and fibres. The shape of the measured stress-strain response varies with microstructural alignment of the CNT bundle network [72]. The ductility of aligned CNT fibres may be as little as 3% with relatively little yield prior to failure [54], whereas more isotropic direct-spun materials can exhibit an elasto-plastic stress-strain response, with hysteresis during unloading, and ductility of up to 0.4 [309]. Examples of the stress-strain response are given in Figures 2.16a and 2.16b; note the considerable hardening in the stress-strain response of Figure 2.16a. Interrupted tensile tests reveal microstructural alignment in the direction of stretch, to which the hardening in the stress-strain response may be attributed, as shown in Figure 2.17 [310]. Tensile drawing and pressing may be used to enhance the tensile strength and modulus of the mats [311], as in Figure 2.16b. Direct spun mats and fibres have a fibrous fracture surface [262], and the ultimate tensile strength of the fibres is insensitive to the presence of knots [312]. They develop kinks under bending [312] similar to those observed in polymer fibres of high molecular weight [313].

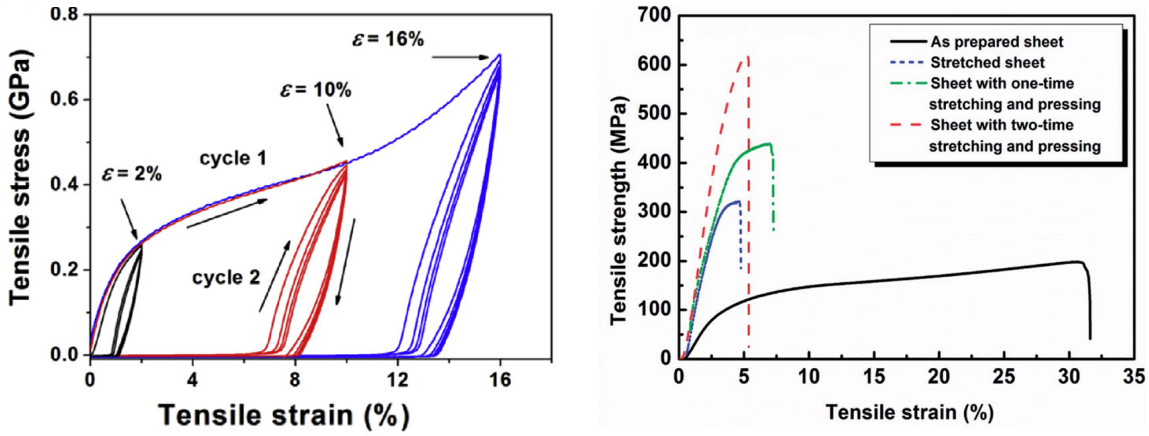

(a) (b)

Fig. 2.16 (a) Strain-induced hardening of carbon nanotube fibre and elasto-plastic response with hysteresis during cyclic loading, reproduced from [311]. (b) The increase in Young's modulus and strength due to stretching and pressing, reproduced from [144].

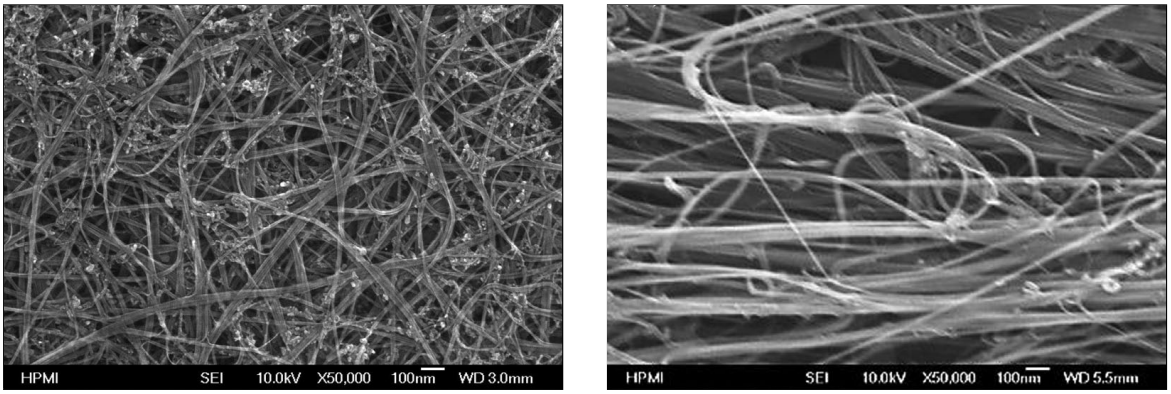

(a) (b)

Fig. 2.17 Microstructure of carbon nanotube mat (a) at 0% strain, and (b) after application of 40% tensile strain. Both images reproduced from [310].

The strength of aligned CNT fibres

Experimental measurements of CNT fibre tensile strength reported in the literature have been reviewed by Behabtu *et al.* [209] as a function of CNT length and aspect ratio (the CNT length divided by the diameter). The tensile strength of CNT fibres was found to increase with increasing aspect ratio up until a plateau strength. This plateau strength lies much below the tensile strength of individual CNT walls. Recall that the bond between the walls of adjacent CNTs is several orders of magnitude below the tensile strength of the walls, see Table 2.1, and it is through this bond that stress is transferred between CNTS within the fibre. It has been suggested that stress within CNT bundles builds up over their length due to shear lag — when the bundle length exceeds the critical shear lag length [279], the CNT fibre strength is limited by CNT bundle tensile strength [280]. The failure strength of CNT fibres with aligned bundle microstructures has been predicted with Weibull statistics and shear lag theory [314], using bundle tensile strength distributions obtained from tensile tests on CNT bundles and individual CNTs [7, 266], and measurements of inter-bundle shear strength from experiment [278, 279]. Two types of CNT fibre were studied: a direct-spun fibre from a CVD reactor consisting of CNTs with a typical length of 60 µm, and a fibre spun from a CNT suspension with shorter CNTs of 5 µm length. The model predicted a switch in failure mechanism from progressive tensile failure of individual CNT bundles in the direct-spun fibre to failure governed by interfacial slip in fibres comprised of shorter CNTs. In broad terms, predicted failure strengths are close to those measured in experiment.

The stress-strain response of isotropic CNT mats

Bundles in direct-spun mats form an interconnected network. In this network, joins are formed between CNT bundles — either due to the branching of CNTs from one bundle to another, or where bundles cross each other, see Figure 1.7 in section 1.3. The term *nodal connectivity* is defined as the number of network struts (in this case, CNT bundles) which meet at each joint, or *node*, within a network of joined struts [225]. Joints formed by branching are between 3 CNT bundle struts, whilst a joint formed at a location where two bundles cross one another has a connectivity of 4. Overall, these two types of joint give rise to an overall nodal connectivity for the carbon nanotube bundle network of between 3 and 4.

Other 2-dimensional random network microstructures which possess a nodal connectivity in this range deform predominantly due to bending and shearing of the struts that comprise them, as opposed to axial stretch [315]. The in-plane Young's modulus of such network microstructures may be influenced by the following characteristics [316]:

1. Joint properties: The torsional and translational stiffness of the joints between CNT bundle struts. Do joints between CNT bundles transfer bending moments and axial forces, or are bundles free to rotate or slip relative to one another upon the application of macroscopic strain?

2. The average distance between nodes in the network which are connected by a CNT bundle strut.

3. The mechanical properties of CNT bundles: what is the effect of the low bundle shear modulus reported in literature?

4. The geometry of CNT bundle struts: how does waviness of CNT bundle struts between two connected junctions alter the Young's modulus of the bundle network?

The influence of joint torsional stiffness upon the modulus of a carbon nanotube network was investigated by Berhan *et al.* [317]. The differing nature of joints was noted: crossed CNT bundles, where the presence of contaminants may or may not act as adhesive, joints formed by CNT exchange from bundle to bundle, or by CNTs themselves branching due to splitting of their source catalyst nanoparticles during growth. Using Euler beams, the modulus of a CNT network was simulated as a function of the joint torsional stiffness. The influence of bond torsional stiffness upon the network modulus was found to be minor.

Consider the effect of the average distance between two joints in the network which are linked by a CNT bundle strut. For 2-dimensional networks of low relative density that consist of enthalpic filaments which deform by Euler bending, this effect has been widely studied [318]. For such networks, the macroscopic in-plane modulus E scales with the mean distance between connected nodes within the network l_c (where rigid joints are formed) according to $E \sim 1/\left(l_c^3\right)$ [318, 316]. This scaling is dimensionally identical to that predicted for honeycomb lattices which also deform due to the bending of the connected struts [225].

Now consider the influence of the weak van der Waals bonds between adjacent CNTs within bundles upon the network modulus. Experiments have shown that these weak bonds endow the bundles with a low shear modulus, and thus reduce their transverse stiffness [264]. Simulations in literature of cytoskeletal bundles [319] with similarly low shear stiffness between fibres indicate that Timoshenko beam theory provides a useful estimation for their transverse stiffness. It remains to verify the influence of their low shear modulus upon the macroscopic network modulus.

The influence of bundle waviness in CNT mats was explored by Berhan *et al.* [320] with simulation of a cross-linked network of wavy elastic fibres. Whilst the tensile stiffness of fibre struts may be highly sensitive to waviness [321, 322], its influence upon the predicted modulus of a CNT mat network was predicted to be relatively minor for waviness amplitudes comparable in magnitude to the diameter of the constituent CNT bundles [320], see Figure 2.18.

Now consider the uniaxial yield strength in tension of a broadly isotropic CNT bundle network. The ductile stress-strain response observed during tensile testing occurs at a flow strength far below the measured tensile strength of CNTs in uniaxial tension. Coarse-grained numerical simulations of a bundled network of short CNTs reported in literature [323] suggest that yield occurs due to the relative slip between adjacent CNTs, see Figure 2.19b. Nonetheless, direct experimental observation of the micromechanical deformation mechanisms remain absent from the literature.

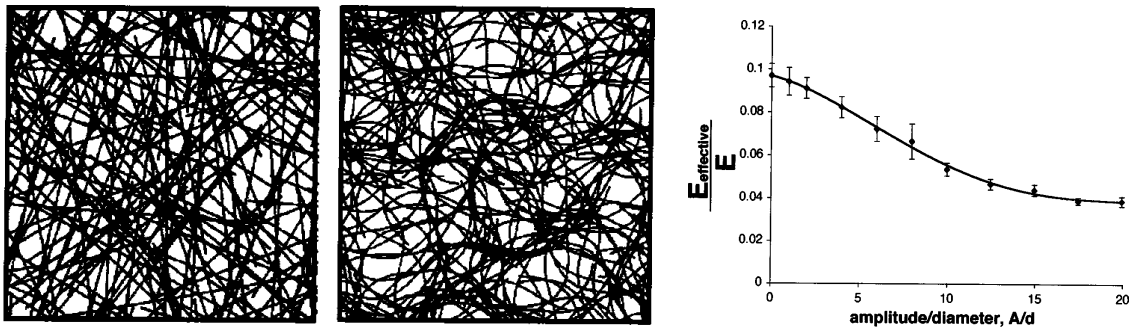

(a) (b) (c)

Fig. 2.18 Cross-linked network of (a) straight and (b) wavy enthalpic filaments. (c) The predicted effect of waviness upon the modulus of a crosslinked network of CNTs. All images are reproduced from [320].

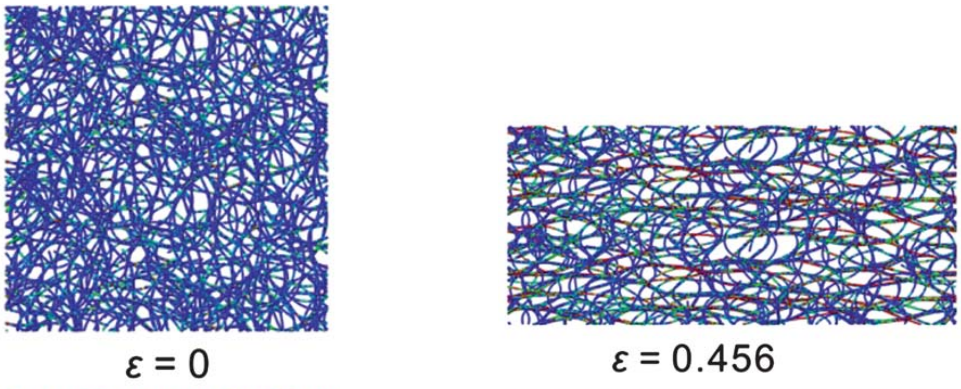

(a) (b)

Fig. 2.19 Coarse-grained simulation of a carbon nanotube network at strain of (a) 0% and (b) 45.6%. Slip and pull-out occurs between the relatively short CNTs (100 nm length). Image reproduced from [323].

2.3 CNT-polymer composites

2.3.1 Classes of CNT-polymer composites and their manufacture

CNT-polymer composite classes, their microstructures, and their methods of manufacture are illustrated in Figure 2.20 and Figure 2.21. They are summarised as follows:

- **Suspension Casting:** Short CNTs in powder form can be dispersed in molten polymers or polymer-solvent solutions, often with the aid of surfactants [324] and shear-mixing [325], see Figure 2.20a. These CNT-polymer suspensions are cast into a mould to form CNT-polymer composites [326–328]. The content of CNTs in such composites is typically less than 4% by weight, with isotropic orientation.

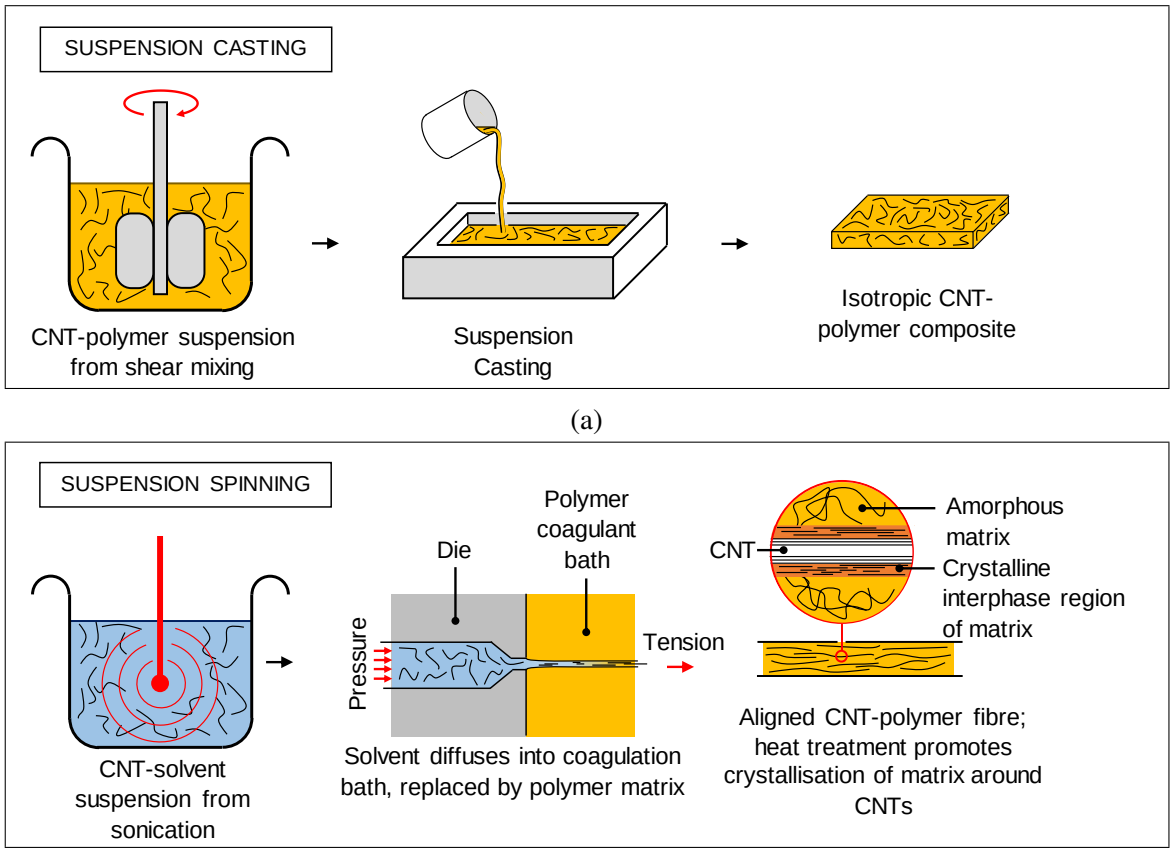

Fig. 2.20 Manufacture of CNT-epoxy composites via CNT suspension processing: (a) suspension casting of CNT-polymer suspensions, (b) wet-spinning of CNT-solvent suspensions into a polymer coagulation bath.

- **Suspension Spinning:** CNT-solvent suspensions are formed through sonication, often with the aid of chemical functionalisation of CNT outer walls, or surfactants. Unidirectional CNT-polymer composite fibres may be spun from these CNT-solvent suspensions by injection of the suspension into a polymer coagulating solution under tension [35, 329, 330], see Figure 2.20b. Heat treatment of the resultant fibre promotes crystallisation of the polymer matrix around the CNTs. This enhances the unidirectional tensile strength, modulus and energy to failure of the composite fibres [330].

- **Infiltration & Cure:** Buckypaper mats manufactured by the filtration of CNT-solvent suspensions [331–334], direct-spun CNT mats and fibres [74, 137, 152, 309, 335, 336], vertically-aligned CNT forests [337] and forest-derived mats and fibres [105, 338–344] may all be infiltrated with polymer solutions. The subsequent cure of the solution – either by cooling below the polymer glass transition temperature, solvent evaporation, or polymer crosslinking, forms CNT-polymer composites, see Figure 2.21.

The reported Young's moduli and strength of these classes of CNT-based composites [35, 73, 74, 89, 137, 152, 309, 326–336, 338–345] are assembled in Figure 2.22, alongside the strength and Young's modulus of CNT walls [10, 7]. The Young's moduli and strength of the CNT composites are much below those of CNT walls [346–349], and are dependent on the orientation of the CNT reinforcement [350] and CNT volume fraction [337]. The chart of electrical and thermal conductivity, Figure 2.23, is assembled from data reported in the literature [14, 334, 345, 351–360]. It reveals that the electrical and thermal conductivity of CNT composites may be several orders of magnitude below that of individual CNT walls; electrical and thermal conductivity vary not only within individual CNT-polymer composite classes, but also between the classes.

Consider the in-plane Young's modulus of CNT and carbon fibre-polymer composites as a function of their reinforcement Young's modulus and volume fraction. The in-plane Young's modulus of carbon nanotube composites E as reported in the literature [35, 73, 74, 89, 137, 152, 309, 326–336, 338–345] and in this thesis are compared with those reported for long fibre carbon fibre composites [361–366] in Figure 2.24. For the sake of comparison, the Young's modulus of the composites E is normalised by the Young's modulus of their reinforcement E_R, and plotted against the reinforcement volume fraction f_R. For CNT-polymer composites, the reinforcement volume fraction is set to equal that of the CNT bundles: $f_R = f_B$. Most quasi-isotropic CNT-epoxy composites have a CNT bundle volume fraction $f_B \leq 0.40$ [74, 137, 359, 367], whereas for aligned CNT-epoxy composites, f_B

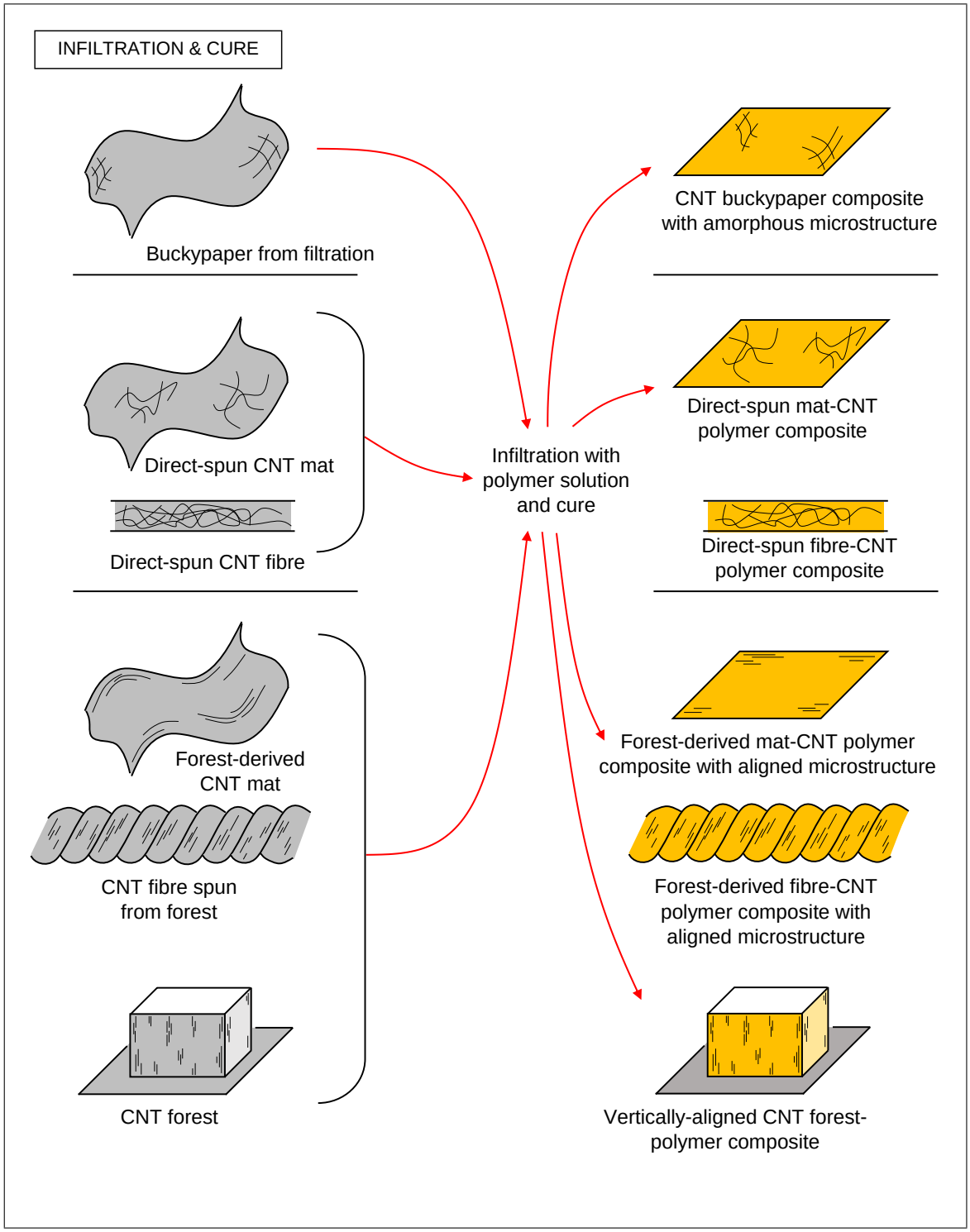

Fig. 2.21 Manufacture of CNT-epoxy composites: Infiltration of CNT buckypapers, direct-spun mats, CNT-forests, and forest-derived mats and fibres.

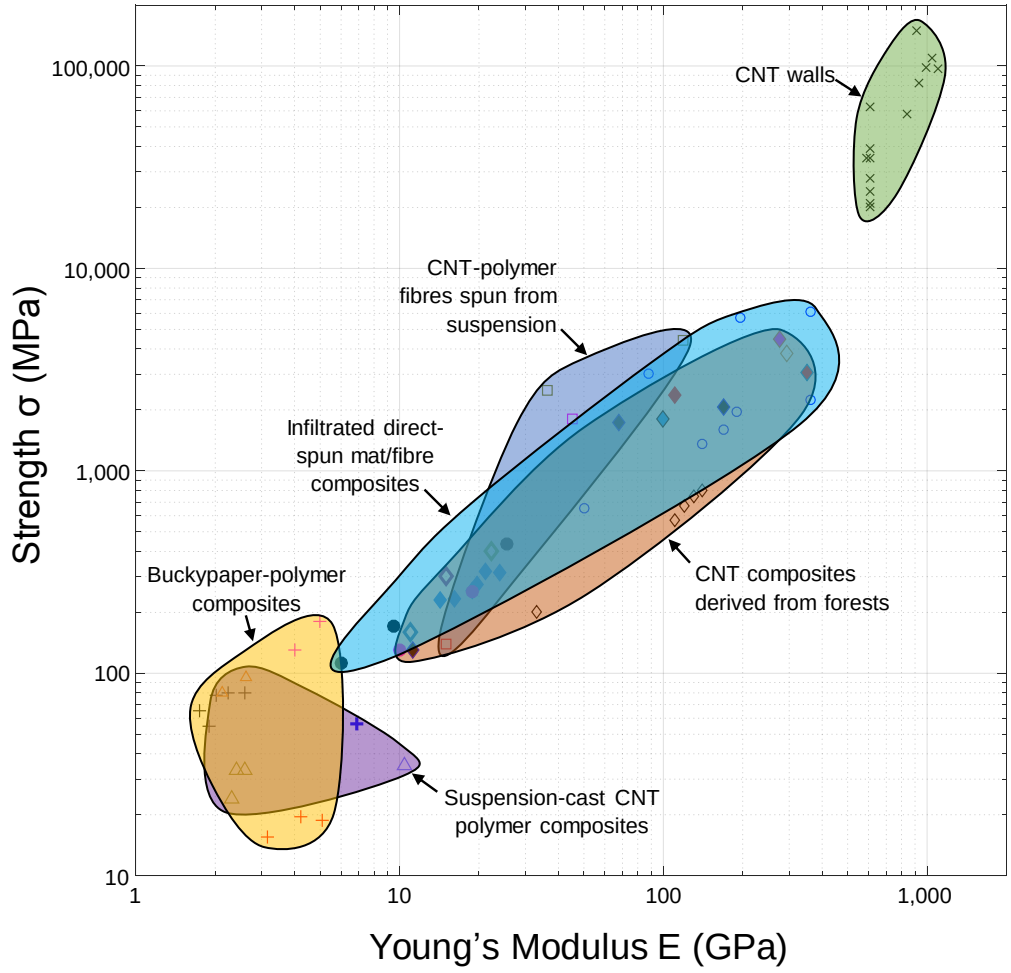

Fig. 2.22 The Young's modulus and strength of carbon nanotube-polymer composites.

is typically in the range $0.60 \leq f_B \leq 0.70$ [309, 335, 368]. The reinforcement Young's modulus E_R for CNT-based composites and carbon fibre composites is chosen as follows. For the CNT-based composites, the Young's modulus E is normalised by that of an individual CNT bundle, for which the reinforcement Young's modulus E_R is taken to be 680 GPa as determined in this thesis (see section 3.4). The axial Young's modulus of a unidirectional (UD) carbon fibre-epoxy lamina can be two orders of magnitude greater than the transverse Young's modulus due to the extreme anisotropy of the fibres. Here, the term *"composite Young's modulus"*, E, is defined as the largest principal value of the modulus tensor. It is this Young's modulus, normalised by the Young's modulus of the carbon fibres as used in each separate study [361–366] that is plotted in Figure 2.24 as a function of reinforcement volume fraction f_R; data are included in Appendix A.

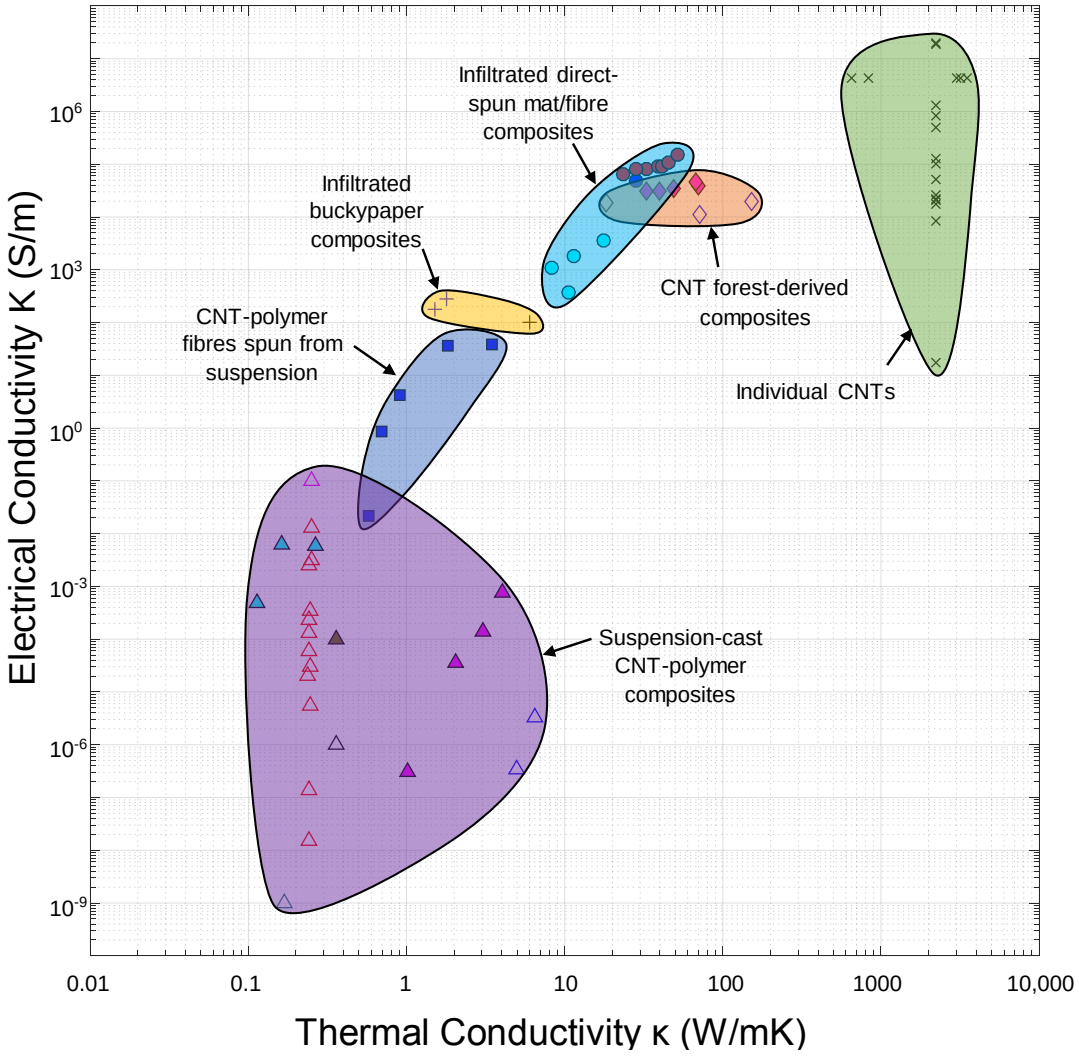

Fig. 2.23 The electrical and thermal conductivity of carbon nanotube-polymer composites.

Voigt and Reuss bounds are included in Figure 2.24, based upon a reinforcement Young's modulus of 680 GPa, and a matrix Young's modulus of 3 GPa. The knockdown in macroscopic Young's modulus from the Voigt bound is sensitive to composite microstructure. The Young's modulus of unidirectional (UD) carbon-fibre reinforced polymer (CFRP) composite is close to the Voigt bound, whilst the Young's modulus of a quasi-isotropic planar CFRP laminate lies below it by a factor of about 3 due to the presence of reinforcement fibres oriented away from the principal direction. Note that the modulus of the unidirectional forest-drawn CNT-polymer composites are below the Voigt bound by more than a factor of 2, whilst those measured from composites of direct-spun CNT mats lie on average more than a factor of 3 below those drawn from forests.

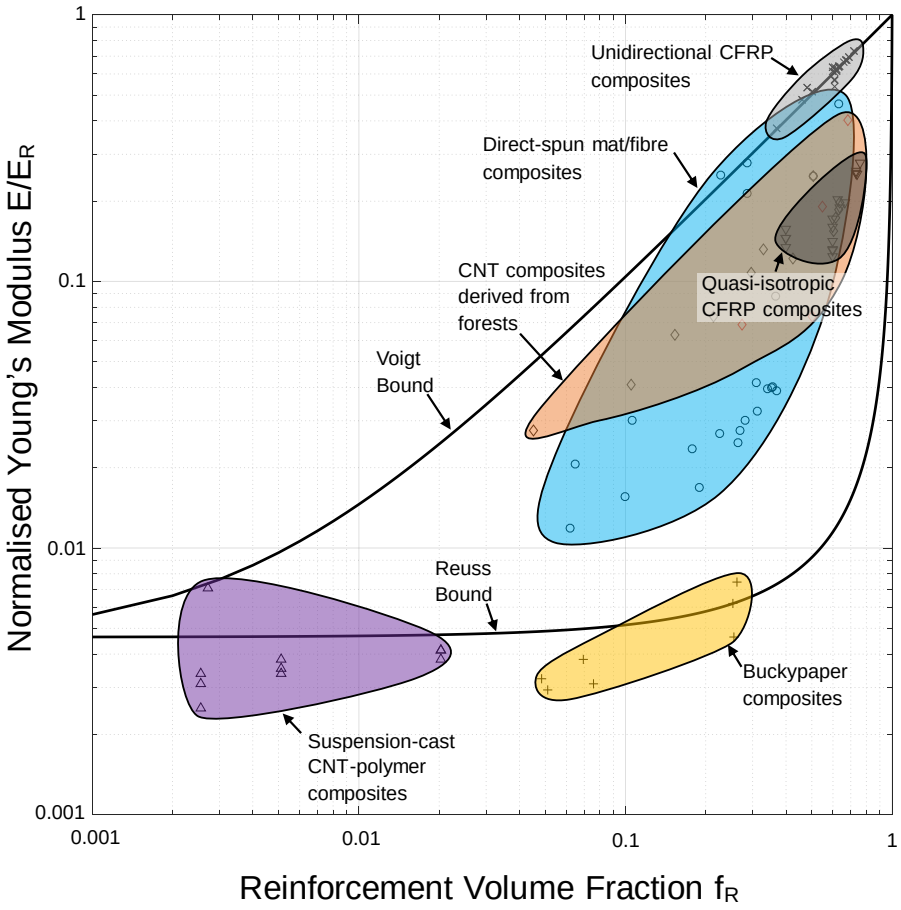

Fig. 2.24 The Young's modulus of carbon nanotube-polymer composites and carbon fibre-polymer composites normalised by the reinforcement Young's modulus, and plotted against the reinforcement volume fraction.

2.3.2 Interaction between CNTs and polymer matrix

The results of pull-out tests upon CNTs or CNT bundles embedded in polymer matrices are recorded in Table 2.3. The interfacial shear strength is calculated based upon the CNT diameter, embedded length, and measured load. Note that the strength of the bond can be several hundred MPa, and varies widely, even for relatively similar polymer matrices. The influence of interfacial shear strength upon the mechanical properties of fibre composites is well documented in the literature. Fibre composites may undergo a transition from ductile to brittle failure as matrix shear strength is increased [369], and the high toughness of many natural fibre or tablet-based composites (for instance nacre or keratin) arises due to evolved control of the inter-particle shear strength and reinforcement particle dimensions [279, 370].

Table 2.3 Pull-out experiments on CNTs embedded in polymer matrices

Matrix & CNT Type	Diameter (nm)	Interfacial Shear Strength (MPa)	Fracture Energy (J/m^2)	Embedded Length (μm)	Reference
DWNT Epoxy Epon 828	2.0 3.2 4.2	202-628 130-270 96-151	1.07 - 1.50 0.29 - 0.40 0.29 - 0.40	0.06 - 1.2	[371]
MWNT Epoxy Epon 828	64.0 94.4 95.7 93.7 77.3 70.3 71.8 95.5 70.0 53.5 83.5 64.1 61.3 69.3 67.5	1.84 11.17 2.41 4.77 12.45 5.56 3.69 9.98 2.86 6.80 9.39 10.91 4.49 2.64 4.66	0.05 - 0.25	1.25 - 8.22	[372]
MWNT Epoxy Araldite LY 564 SWNT bundle	8.2 11.0 24.0 13.4 13.4 24.0 11.6	376 318 35 38 77 91 366	26.4 36.9 8.2 0.9 5.35 5.54 25.5		[373] [373]
MWNT Epoxy Poxipol	80±30	30.0		0.3 - 3.2	[374]
MWNT Polyethylene Butene	5 - 10 15 - 20 20 - 25 30 - 35	45 - 130 0 - 60 20 - 60 10 - 18	22 - 68 7 - 22 5 - 14 2 - 7	0.001 - 0.060	[375]
MWNT Polyethylene Butene	32-136	47		0.040 - 0.070	[376]
MWNT PEEK PEEK heated 573K 1 hr, at 1MPa	140 130 120 82 87 150 130 97 91 74 61 140	6.9 5.2 4.1 5.6 5.1 3.5 5.6 7.1 6.1 8.3 14.0 10.0		4.8 4.7 6.5 5.3 3.3 2.9 5.3 4.0 4.9 2.6 4.3 3.9	[377]
DWNT PMMA	2.0 3.1 4.2	Av. 68, Max. 372 Av. 44, Max. 155 Av. 32, Max. 85	0.5 - 0.8 0.135 - 0.215 0.054 - 0.087	0.210 - 1.45	[378]

Studies of the molecular arrangement of polymer molecules surrounding carbon nanotubes have revealed that polymer chains may form a crystalline layer upon the exterior of CNT bundles — either as a periodic, lamellar structure [5], or as a uniform crystalline layer with the molecular orientation parallel to the CNT longitudinal axis [330] or perpendicular [379] to it as a transcrystalline layer. Upon composite fracture, CNTs or CNT bundles pulled from the bulk matrix often remain coated with a polymer layer [330, 380]; this phenomenon has also been observed in composites of direct-spun CNT fibres and epoxy [74].

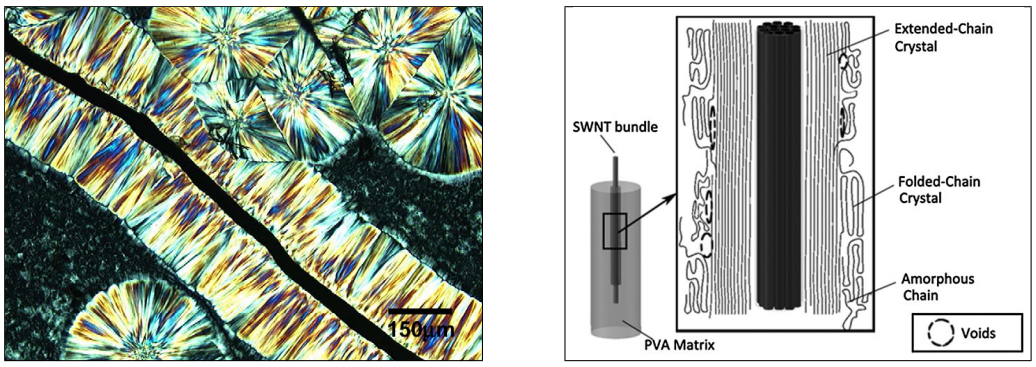

(a) (b)

Fig. 2.25 Detail of the interphase region surrounding CNTs in polymer composites: (a) Image of a transcrystalline polymer interphase layer, reproduced from [379], (b) suggested lamellar structure of the interphase layer in PVA-SWNT fibres, reproduced from [330].

2.3.3 The relationship between epoxy infiltration and mechanical properties of direct-spun mat-epoxy composites

Upon infiltration and cure of an epoxy matrix, the tensile strength and Young's modulus of highly aligned direct spun CNT fibre-epoxy composites is close to that predicted by a Voigt bound based upon the Young's modulus of the fibre used as reinforcement, the matrix Young's modulus, and the respective volume fractions of the reinforcement fibre and matrix [74]. In contrast, the tensile strength of composites manufactured via infiltration of broadly isotropic direct-spun CNT mats may increase by up to a factor of 2 [381], which is well beyond the prediction arising from a Voigt bound similarly based on the properties of the direct-spun CNT mat reinforcement and polymer matrix. The micromechanical origin of this synergistic increase upon polymer infiltration and cure remains unclear — as is the role of any polymer layer upon the bundles of enhanced strength and modulus.

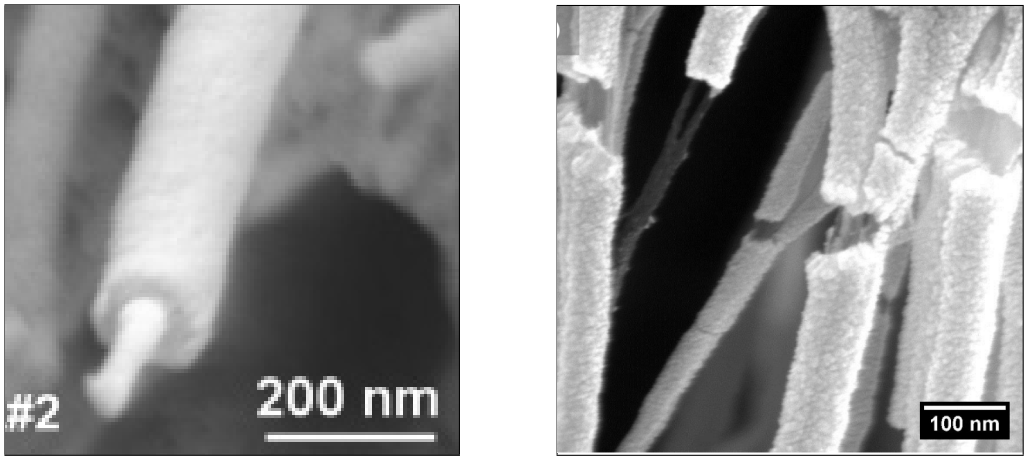

(a) (b)

Fig. 2.26 CNT-sheathing in polymer composites: (a) Pull-out of a single CNT coated with an interphase layer in a polystyrene matrix, reproduced from [380]; (b) polymer sheathing of CNT bundles in composites of direct-spun CNT mats and epoxy, image reproduced from [74].

Micromechanical models of the CNT-polymer composite microstructure often assign CNTs elastic properties which are based upon their properties in uniaxial tension. Micromechanical simulations of CNTs embedded in an epoxy matrix have illustrated the influence of CNT waviness upon the elastic Young's modulus of CNT-polymer composites [350], and the use of short-fibre theory provides a useful prediction for the modulus of CNT-polymer composites containing separated carbon nanotubes of length between 0.5 μm and 2 μm [367]. Nonetheless the CNTs within direct-spun mat-epoxy composites appear to remain within a bundled network before and after the infiltration and cure of an epoxy matrix [74, 381], and the effects of this microstructure upon the macroscopic properties of the CNT-polymer composites remain unexplored.

2.4 Fluid processing of CNTs

2.4.1 The interaction between CNTs and fluids

Early researchers anticipated that CNTs would be *"super straws"*, with their nano-sized dimensions enabling fast transport of fluids due to capillary effect [382–384]. Molten metals may be introduced into the interior of CNTs by annealing [385], electrowetting [386], or due to surface tension alone [387]. Experiments and contact-angle calculations indicate that liquids flow into the centre of CNTs without other stimuli (for instance electrically-induced forces or external hydrostatic pressure) when the surface tension of the liquid is below approximately 0.18 Jm^{-2} [388]. In-situ microscopy has shown that water condensates, evaporates and may be transported within CNTs [389], see Figure 2.27a; the pressure-driven flow rate of water and solvents such as ethanol, iso-propanol, hexane and decane through CNT membranes in line with the CNT longitudinal direction far exceeds predictions of the Hagen-Poiseuille equation, and does not decrease with increasing solvent viscosity [390, 391]. CNT networks are permeable through the gaps between CNTs and in some cases also through their interiors [383]. The wettability of CNT walls is sensitive to the degree of graphitisation; CVD-grown CNTs may be wetted by water, depending on the crystallinity of the graphitic lattice comprising their outer wall [392].

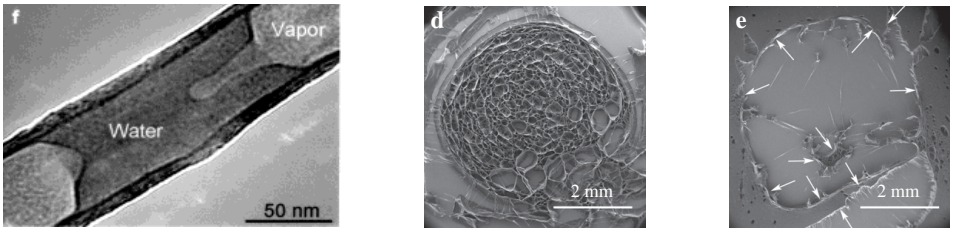

(a) (b) (c)

Fig. 2.27 (a) Water inside a nanotube, reproduced from [389], CNT fibres after infiltration and evaporation of (b) NMP and (c) ethylene glycol, reproduced from [73].

2.4.2 The effect of solvent infiltration upon direct-spun mat properties

Solvent infiltration of direct-spun fibres with organic solvents, for example acetone or ethanol, results in mechanical softening and alters their electrical resistance [393]. In-situ crystallography of direct-spun CNT mats has shown that bundled CNTs within them remain in contact with one another when immersed in organic solvents such as acetone, ethanol or toluene [393]. The infiltration of solvents and subsequent evaporation may be used to

densify the fibres through capillary force, which increases their tensile strength and modulus, predominantly by virtue of their higher density, see Figures 2.27b and 2.27c [73].

2.4.3 CNT-fluid suspensions

The interfacial surface energy due to van der Waals interactions between adhered particles such as CNTs can be reduced by the presence of a third, fluid medium around them [291]. When combined with fluids, CNTs may disperse to form a stable suspension.

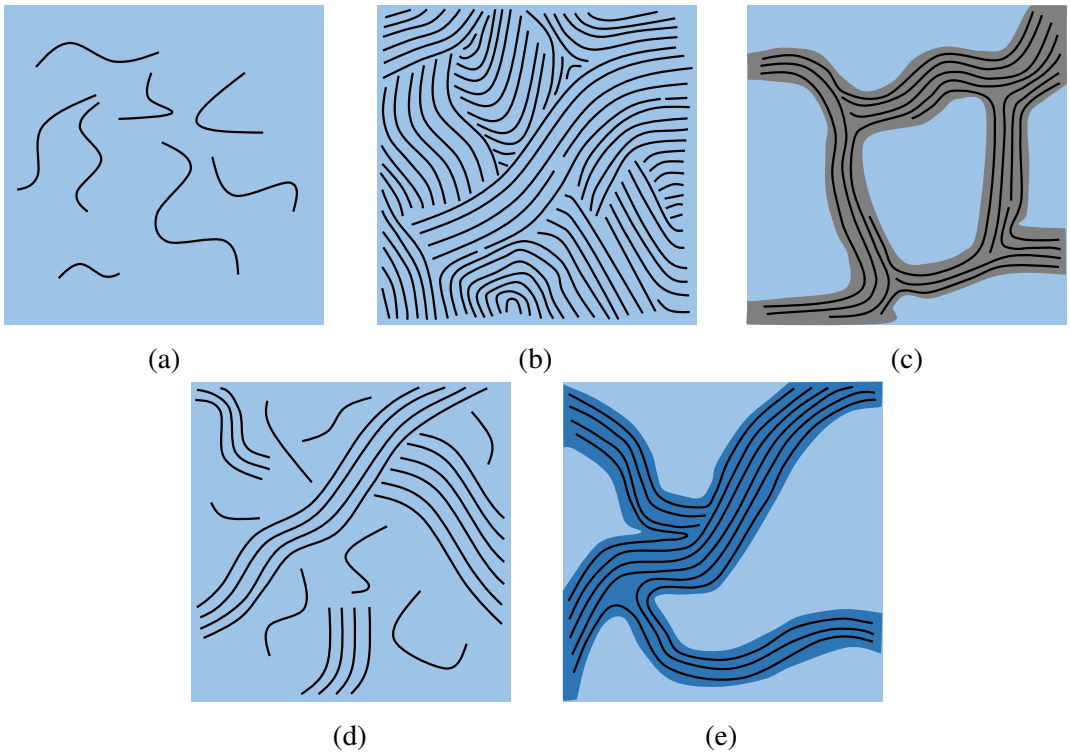

Fig. 2.28 Phase behaviour of CNTs dispersed in fluids. The isotropic (a) and nematic (b) phases; (c) Infiltrated CNT agglomerate without fluid penetration of the CNT bundles. A combination of the isotropic and nematic phases, the bi-phasic arrangement (d) and the crystal solvate phase (e) of infiltrated bundles, which does not result in CNT separation.

The phases which CNTs may form in fluid suspensions are illustrated in Figure 2.28. The arrangement of CNTs dispersed in fluids is lyotropic — influenced by the volume fraction of CNTs. At low volume fractions, individual CNTs or small CNT bundles can form an isotropic phase with no dominant orientation, as sketched in Figure 2.28a. If the forces opposing van der Waals attraction are sufficiently strong and short range, CNTs are able to form a nematic phase [394]. In this phase the nanotubes lie parallel to one another in

large crystals, see Figure 2.28b. An individual CNT may have translational freedom to move axially within its crystal, but cannot easily rotate out of alignment with neighbouring CNTs. If the infiltrated fluid is incapable of penetrating the CNT bundle structure, it may simply infiltrate the pores between the bundles, see Figure 2.28c. At volume fractions between the isotropic and nematic equilibrium concentrations, a mixture of isotropic and nematic phases is formed: the so-called bi-phasic regime as sketched in Figure 2.28d. The crystal solvate bundle microstructure occurs when a fluid is able to penetrate the CNT bundle microstructure, but does not actually separate the CNTs into a nematic phase [395], see Figure 2.28e.

Agglomerated CNTs do not spontaneously disperse when immersed in most organic solvents, and their dispersion in organic solvents of low viscosity relies on sonication in the first instance, although MWNTS may be dispersed in viscous polymer melts by shear mixing [325]. Sonication induces high local shear stresses due to cavitation of the solvent, which are of sufficient magnitude to separate CNTs from their bundles. Tensile stresses build up along the CNT length through shear lag, causing scission. The length of separated CNTs after sonication is thus limited by their tensile strength and dimensions, typically to below 10 μm [396].

CNT suspensions are formed via a number of different methods, which are the subject of many reviews in literature [394, 397–399]. All fall into one of the four categories illustrated in Figure 2.29, and are described as follows:

- **Suspension in common solvents:** CNTs may be dispersed in a range of common solvents by dilution to sufficiently low volume fractions, see Figure 2.29a [400]. In certain solvents, the enthalpy of mixing at low volume fractions is slightly negative [401], which results in an equilibrium isotropic suspension of CNTs and small bundles.
- **Surfactant-assisted dispersion:** CNT walls may be treated by attaching surfactant molecules with non-covalent bonds, see Figure 2.29b. These may include dispersants such as Triton X-100 [324] (as found in many household liquid detergents), or other long molecules such as DNA [402, 403].
- **Functionalisation-assisted dispersion:** Chemical reactions in acids or other liquids can covalently link functional groups or molecules to the outer CNT walls [404], as sketched in Figure 2.29c.
- **Spontaneous dispersion in superacids:** Strong acids such as fuming sulphuric acid (oleum) and chlorosulfonic acid are able to separate bundled CNTs from one another upon their immersion [405]. Reaction with the acid molecules leads to the development

of a net positive charge upon the CNT walls, and the formation of an electrical double layer [406], as sketched in Figure 2.29d. The resultant electrostatic repulsion maintains the separation between the CNTs [395].

CNT suspensions formed by the above methods vary in CNT volume fraction and resultant CNT-fluid phase behaviour. The measured CNT volume fractions and observed phase morphologies which result from the above methods as reported in literature are plotted in Figure 2.30. Note that the volume fraction of CNTs in suspension achieved by the different methods spans several orders of magnitude as a function of the chosen solution chemistry and CNT geometry.

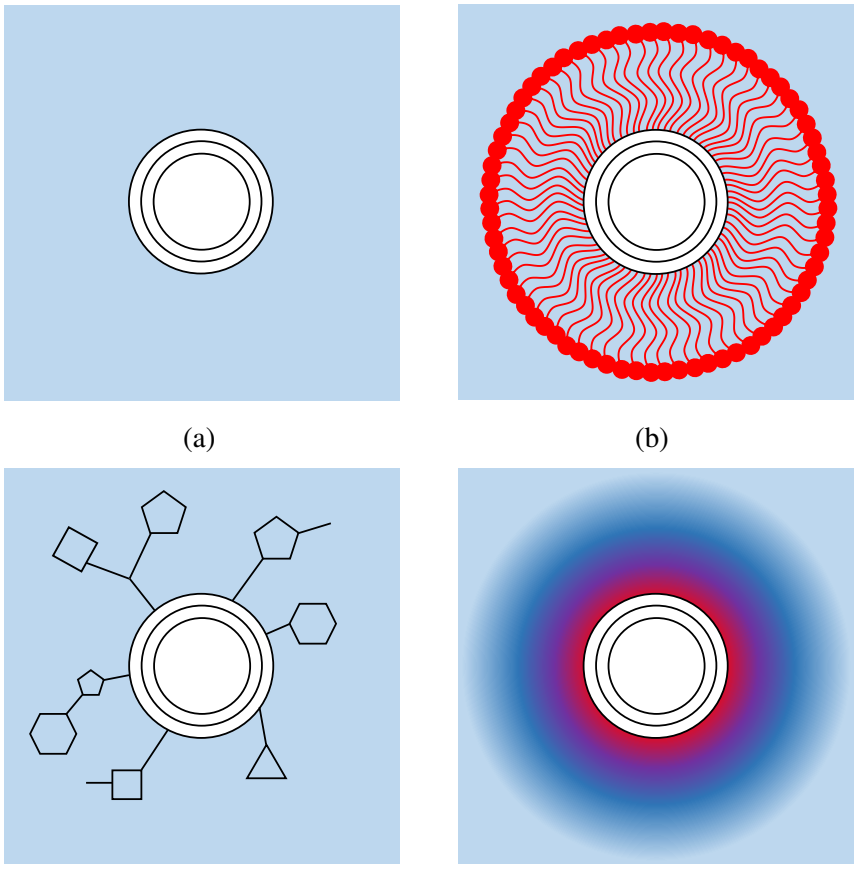

Fig. 2.29 Methods for dispersing CNTs in fluids: The suspension of CNTs (a) in common solvents by dilution, (b) assisted by surfactant molecules, (c) assisted by functionalisation of CNT walls, and (d) due to double-layer electrostatic repulsion in superacids.

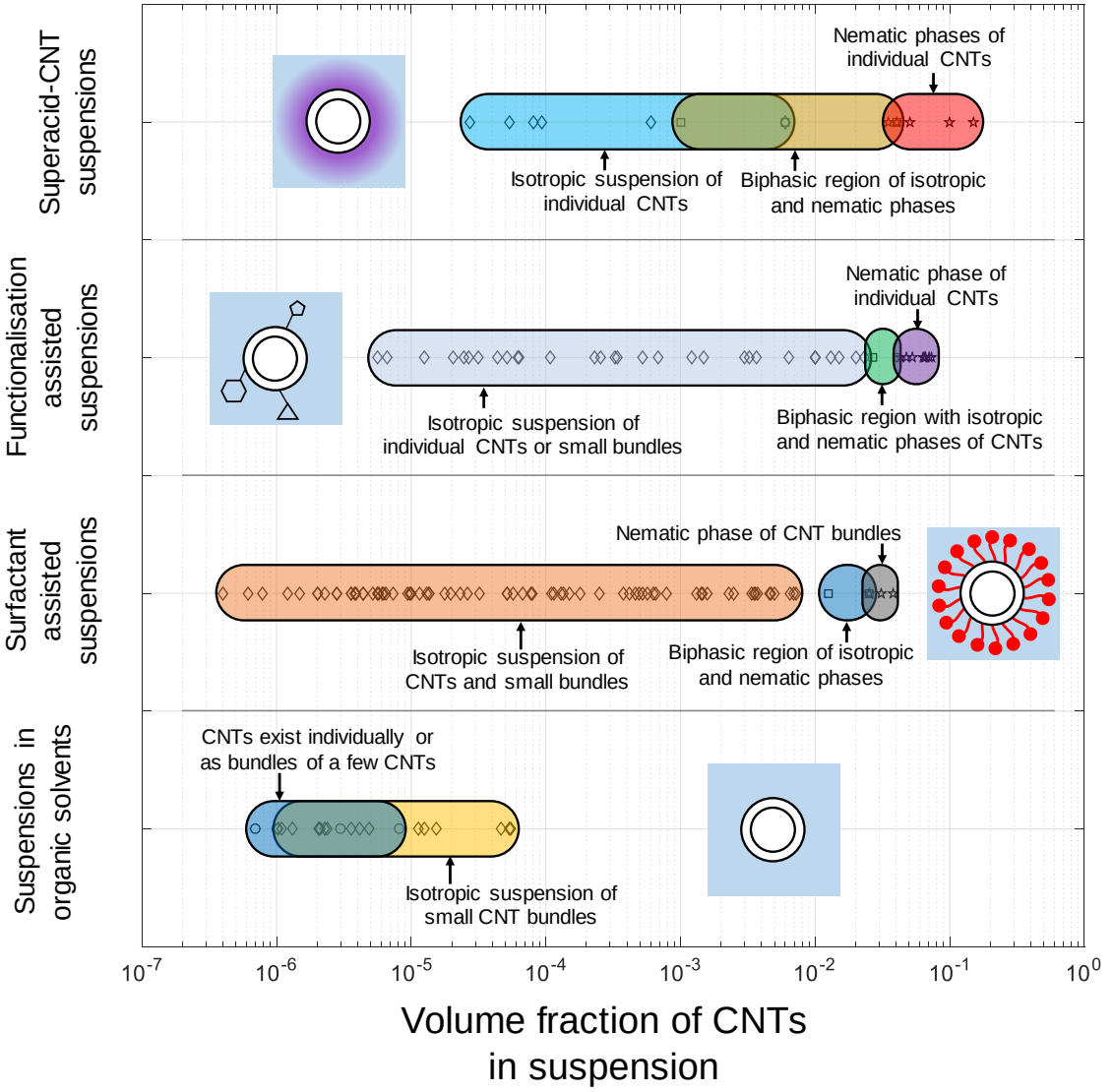

Fig. 2.30 The CNT volume fraction in suspensions as reported in literature for organic solvents alone [400, 401, 404, 407–410], surfactant-assisted suspensions, [402–404, 411–428], functionalisation-assisted suspensions [429–438] and in superacids [395, 439].

Suspensions of CNTs and small CNT bundles in organic solvents are restricted to low volume fractions of below about 5×10^{-5}. Although relationships have been proposed between the achievable volume fraction of individual CNTs which can be suspended in organic solvents and solubility parameters, they do not capture the observed behaviour of CNT suspensions for all organic solvents [400]. At higher volume fractions, organic solvents may infiltrate CNT bundles to form a crystal solvate, but are incapable of separating CNTs from a bundled state [395].

Consider the suspensions of CNTs in organic solvents or in water upon treatment of their outer walls with surfactants. In surfactant-assisted suspensions individual CNTs may exist in an isotropic phase up to volume fractions of about 0.007. Upwards of this volume fraction, CNTs may form bi-phasic or nematic dispersions of small bundles, such as in the case of DNA-coated CNTs [402, 403]. These phases exist up to a volume fraction of about 0.04.

Upon functionalisation of their outer walls, CNTs form an isotropic phase in suspensions, which may exist up to CNT volume fractions exceeding 0.02. Covalent functionalisation methods are also able to form the bi-phasic and nematic phases, the latter at volume fractions up to 0.07 [437, 438].

Now consider CNT suspensions in superacids. Superacids can disperse individual CNTs in a nematic phase at a volume fraction of up to 0.15 [395]. For CNT fibre spinning, the use of superacids offers a number of other advantages in comparison to the other dispersion methods, as follows:

- Superacids do not rely on sonication for initial separation, and so can produce fibres of long length CNTs, which is advantageous for structural applications [209].
- Covalently bonded functional groups can affect the nature of the electrical or thermal interaction between CNTs, which can be to the detriment of macroscopic electrical and thermal conductivity [349]. Defects in the graphitic lattice of CNT walls due to covalent functionalisation may affect the electrical and mechanical properties of individual CNTs [9, 25].
- The removal of surfactant molecules after fibre spinning may require additional processing steps. Like functional groups, residual molecules may also influence the electrical or thermal conductivity of spun fibres, or the strength of the bond between CNTs.
- Superacid processing results in residual doping, which increases the electrical conductivity of superacid-spun fibres by a factor of 6 compared to an un-doped fibre [121].

2.5 Summary

2.5.1 CNT material properties, microstructure and processing

Behaviour of CNTs and their macroscopic materials

- The walls of individual CNTs possess an axial modulus of 1 TPa, and tensile strength of several GPa. In contrast the van der Waals bonds between them are of much lower shear yield strength and stiffness. The shear strength of the bond between CNT walls varies by several orders of magnitude, whereas the values of measured surface energy recorded in literature lie within a comparatively narrow range. The low shear strength and shear modulus of the bond between CNT walls endows CNT bundles with anisotropic mechanical stiffness and strength.
- The properties (modulus, strength, and electrical and thermal conductivity) of macroscopic materials comprised of CNTs vary by several orders of magnitude as a function of their macroscopic density and microstructure, which depend upon their method of manufacture.
- The modulus and strength of CNT mats and fibres are sensitive to the degree of microstructural alignment and CNT length: aligned fibres are of low ductility and possess a tensile modulus and strength much above that of more isotropic direct-spun mats. The stress-strain response of direct-spun mats may be ductile and exhibit strain hardening.

CNT-polymer composites

- The modulus, strength and electrical and thermal conductivity of CNT-polymer composites are also sensitive to the degree of microstructural alignment, and CNT volume fraction.
- The measured shear strength of the bond between CNT walls and a polymer matrix varies widely across the literature.
- In a number of CNT-polymer composites, a layer of polymer is formed upon the CNT walls of enhanced strength and stiffness, which results in sheathing of CNTs or CNT bundles upon pull-out. Such a layer exists in composites of direct-spun CNT fibres and epoxy.

CNT suspensions and fluid processing

- CNT suspensions exist in a variety of different phases — isotropic phases form at low volume fraction, and nematic phases at higher volume fraction.
- Organic solvents are only capable of creating CNT suspensions with low CNT volume fractions, with the aid of extensive sonication.
- Of all methods used to disperse CNTs at high volume fractions, superacids are used to create suspensions of the highest CNT volume fraction and length.

2.5.2 Open questions in literature regarding direct-spun CNT mats

- Theoreticians have illustrated the importance of joint morphology, CNT bundle waviness, and bundle length between joints upon the modulus of broadly isotropic CNT mats; it is hypothesised that the low bundle shear modulus may also influence their behaviour. Whilst in-situ tests have shed light on the evolution of microstructure under strain, there is little experimental evidence for which mechanisms of deformation dominate. Such observation is required to conform the role of microstructure upon properties. For other porous materials such as foams [225], the experimental observation of deformation taking place at a single microstructural point has been instrumental in developing concise, useful models and understanding of the micromechanical phenomena dictating their macroscopic behaviour.
- The origin of the synergistic increase in the modulus and strength of direct-spun mats upon the infiltration and cure of an epoxy matrix remains unclear. The effect of the epoxy coating upon the CNT bundle surface observed upon pull-out is undetermined — how does this layer and the bulk matrix cause strengthening and stiffening compared to the unreinforced mat?
- Superacids promote the separation of CNTs into a nematic phase of high volume fraction. Already exploited for the manufacture of CNT fibres of high modulus and electrical conductivity, it remains to establish if superacid infiltration and drawing can enhance the mechanical stiffness and strength of the direct-spun CNT mat in a similar manner.

Chapter 3

Mechanical and electrical properties of a direct-spun carbon nanotube mat

3.1 Summary

Microscopy studies of direct-spun CNT mat microstructure during interrupted tensile tests [136, 267, 310, 311] have shed light on the microstructural changes during tensile strain, but do not inform about the deformation mechanisms. To do so, direct observation of the CNT mat microstructure during tensile testing is required. In this chapter, the mechanical and electrical properties and piezoresistive response of a direct-spun carbon nanotube mat are measured. A small degree of in-plane anisotropy is observed, and the macroscopic in-plane tensile response is elasto-plastic in nature, with significant orientation hardening. In-situ microscopy reveals that the nanotube bundles do not slide past each other at their junctions under macroscopic strain. A micromechanical model is developed to relate the macroscopic modulus and flow strength to the longitudinal shear response of the individual nanotube bundles.

3.2 Materials and methods

A direct-spun CNT mat was provided by Tortech Nano Fibers Ltd[1]. Before characterisation, the mat was immersed in acetone for 5 min, dried in air for 20 min, and heated at 70 °C for 1 hour, to ensure that any areas of delamination between sock aerogel layers within the mat were removed. The mat has a nominal thickness of 60 µm, as confirmed by X-ray tomography scans and micrometre measurements. The mat areal density is 0.0234 kg/m^2, and the volumetric mat density is 390 kg/m^3.

Chemical and physical composition

The chemical composition of the mat was determined by thermogravimetric analysis, conducted using a PerkinElmer TGA 4000. The temperature was held at 100 °C to remove adsorbed moisture, then increased at a scan rate of 5 °C/min. The Raman spectrum of the CNT mat was obtained with an EZRAMAN-N instrument, using a laser power of 50 mW, a laser wavelength of 532 nm, and 3 scans at 30 s integration time.

Bundle density was determined with helium pycnometry (performed by Quantachrome UK Ltd[2]). This involves placing a CNT mat sample in a chamber of known volume, which is then purged of air and pressurised with helium gas. After the pressure of this chamber is measured, a valve is opened to link it with another chamber of known volume, initially at vacuum. After the pressure has stabilised, it is recorded; the perfect gas law is then used to calculate the sample volume from the measured gas pressures and known chamber volumes.

Uniaxial tensile response

Uniaxial tensile tests were performed using a screw-driven test machine, with the loading direction inclined at 0°, 45° and 90° to the draw direction of the CNT mat onto the mandrel during manufacture. The test set-up is shown in Figure 3.1a. The in-plane strain state was measured in the central portion of the sample by tracking the movement of dots of white paint applied prior to testing, using a digital camera and image processing software. Roller-grips enabled high tensile strains to be reached, with failure occurring at a strain level of 20% to 30%. In-situ tensile tests were conducted with a micro-test stage equipped with a 2 N load cell, inside a scanning electron microscope (SEM).

[1]Tortech Nano Fibers Ltd, Hanassi Herzog St., Koren Industrial park, Ma'alot Tarshiha, 24952 Israel.
[2]Quantachrome Ltd., Units 6 and 7 Pale Lane Farm, Pale Lane, Hook, RG27 8DH, UK.

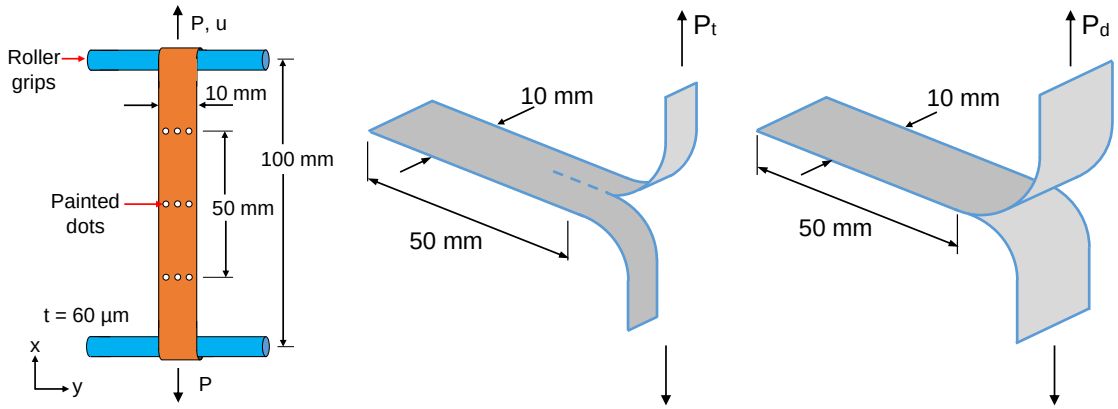

(a) (b) (c)

Fig. 3.1 Mechanical testing techniques: (a) schematic of tensile test setup with sample dimensions and strain measurement techniques. (b) In-plane fracture 'trouser tear' test, (c) delamination peel test.

Toughness

The in-plane toughness G_c was measured by a trouser-tear test [440], illustrated in Figure 3.1b. This toughness is determined from the steady state load for tearing, P_t , and the sample thickness, t, according to $G_c = 2P_t/t_s$ [441]. Trouser-tear tests were attempted in two directions, with the tear direction aligned with the draw direction, and in the transverse in-plane direction. Additionally, the out-of-plane delamination toughness, G_d, was quantified by a peel test [442], as illustrated in Figure 3.1c. The toughness G_d is related to the peel force P_d and the sample width w_s according to $G_d = 2P_d/w_s$.

Electrical Properties

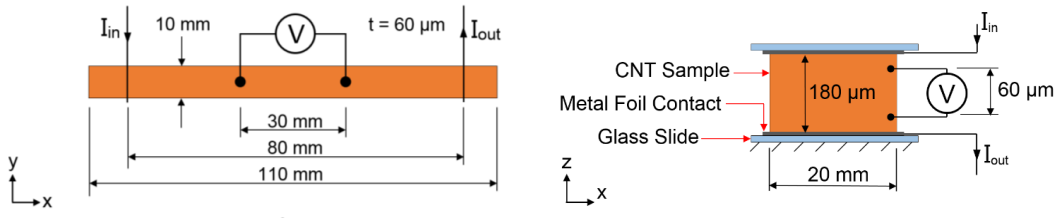

(a) (b)

Fig. 3.2 Four point probe measurement for (a) in-plane and (b) out-of-plane electrical conductivity.

Now consider the measurement of electrical properties. The in-plane and through-thickness electrical conductivity were measured using a 4-point probe method, as illustrated in Figure 3.2. A 4-point probe was also used to measure the in-plane electrical resistance during tensile testing, at a strain rate of $\dot{\varepsilon} = 10^{-4}$ s^{-1}. The instrumentation circuit developed to record the value of sample resistance during testing is described in Appendix B. The tensile strain and in-plane resistance were measured with full, partial and cyclic unloading of stress, and a limited number of creep tests at constant stress were also performed.

Stress-strain and piezoresistive response under out-of-plane uniaxial compression

The out-of-plane compressive and piezoresistive behaviour of the direct-spun mat was also measured: the experimental methods and results are presented in Appendix C.

3.3 Results

3.3.1 Chemical and physical composition

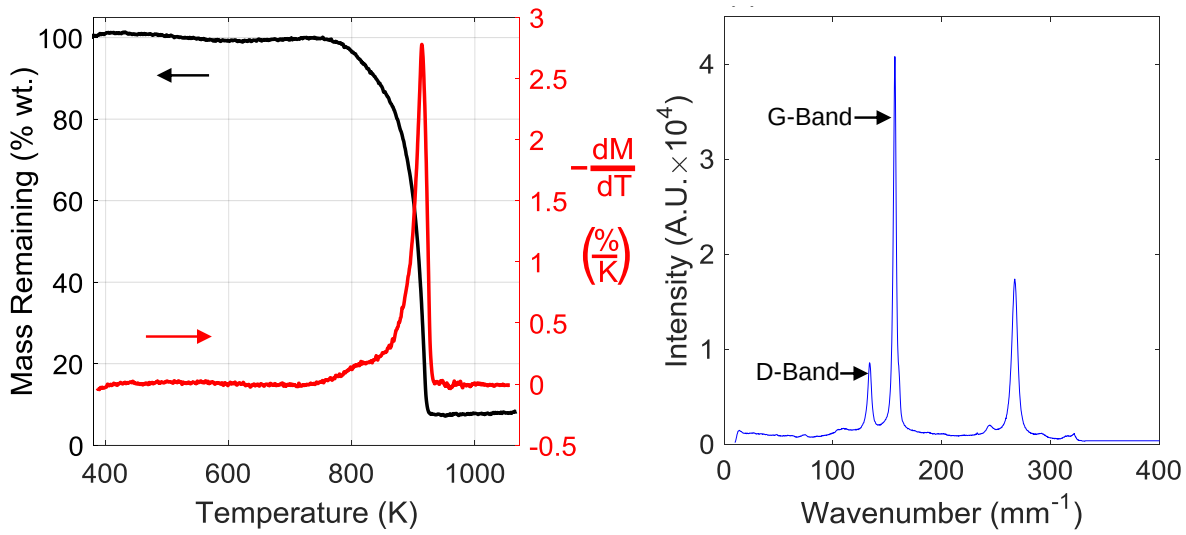

(a) (b)

Fig. 3.3 (a) Thermogravimetric analysis of CNT mat in air, (b) Raman spectra of CNT mat.

The percentage of sample mass remaining and the rate of mass change with respect to temperature during thermogravimetric analysis are plotted in Figure 3.3a. The results revealed an iron content of 6 wt.%, remainder CNT.

A Raman spectrum of the CNT mat is illustrated in Figure 3.3b. The high intensity G-band at 158 mm^{-1} corresponds to vibration of bonds within the plane of the CNT wall. Dividing the G-band intensity by that of the D-band at 134 mm^{-1} gives a G/D ratio of 4.5. The D-band results from the breathing mode of a six-fold aromatic ring, and cannot occur unless disorder is present, either in the crystalline structure of the CNT walls, or in the form of additional amorphous carbon materials [443, 444]. The relatively high G/D ratio observed here indicates that neither of those defects are particularly prevalent. The absence of radial breathing modes at low frequency (< 50 mm^{-1}) indicates that small diameter single- or double-walled CNTs are not present within the mat [443]. A bundle density $\rho_B = 1560$ kg/m^3 was revealed from helium pycnometry.

3.3.2 Uniaxial tensile response

The nominal stress–strain response, as illustrated in Figure 3.4a, exhibited an initial linear behaviour, followed by a strain-hardening plastic response at approximately 4% strain. Above 15% strain, the hardening rate increases. The response has a moderate degree of anisotropy. The in-plane transverse strain is plotted as a function of tensile strain in Figure 3.4b. The apparent Poisson's ratio, ν_{12}, initially equals 0.6, but increases to between 2.7 and 3.5 at higher strains. An explanation for these high values of ν_{12} is evident from images taken during in-situ tensile testing, see Figure 3.4c, which illustrate the appearance of out-of-plane wrinkles at the micron level. This wrinkling appears to contribute to the compressive transverse strain. No noticeable rate dependency was observed for strain rates between 10^{-4} s^{-1} and 10^{-2} s^{-1}, as illustrated in Figure 3.4d for samples aligned with the draw direction.

3.3.3 Toughness

Trouser-tear tests along the draw direction were performed from starter cracks cut parallel to the draw direction. The average value of tear energy from these trouser tests was $G_c =$ 22 kJ/m^2. Trouser-tests were unable to grow starter cracks cut transverse to the draw direction; instead, kinking of the starter crack occurred and no useful data were obtained. The delamination toughness from a peel test was found to be $G_d = 5.4$ J/m^2. This is about four orders of magnitude below the in-plane toughness.

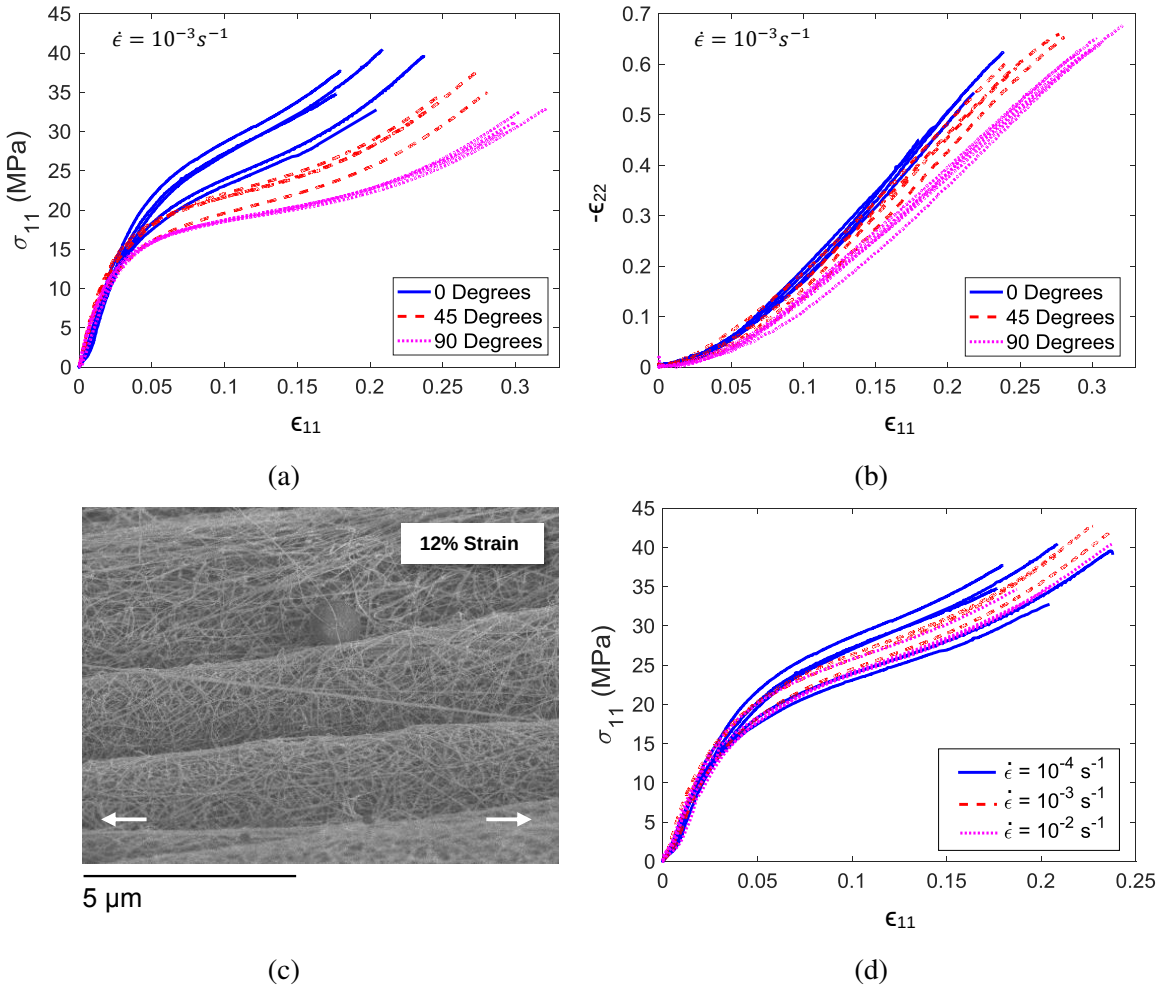

Fig. 3.4 Uniaxial tensile response: (a) in-plane stress–strain response for different material orientations, (b) relationship between tensile and transverse strains. (c) The appearance of transverse wrinkles during in-situ tensile testing; the arrows indicate the direction of tensile straining. (d) The effect of strain rate upon the uniaxial tensile response for samples aligned with the draw-direction.

3.3.4 Electrical properties

The in-plane conductivity exhibited a small degree of anisotropy, with values of 40.4 kS/m parallel to the manufacturing draw direction, 35.8 kS/m at 45°, and 32.5 kS/m at 90°. In the through-thickness direction, electrical conductivity was about 6 orders of magnitude lower, at 6.39×10^{-2} S/m.

3.3.5 Unloading and creep tests

A 4-point probe, as illustrated in Figure 3.5a, was used to measure the in-plane electrical resistance during tensile testing, at a strain rate of $\dot{\varepsilon} = 10^{-4}$ s^{-1}. The tensile strain and in-plane resistance were measured with full, partial and cyclic unloading of stress, and also at constant stress. Typical responses are presented, with sample resistance normalised by the initial resistance R_0.

The stress–strain and resistance-strain response with periodic partial unloading of samples at 0°, 45° and 90° to the draw direction are illustrated in Figure 3.5b. Despite the presence of structural anisotropy, the piezoresistive response, R/R_0 versus ε_{11} is qualitatively similar for all directions. Little mechanical or electrical hysteresis is present upon partial unloading. The unloading stiffness E_U during the unloading cycle is defined as $E_U = \Delta\sigma_{11}/\Delta\varepsilon_{11}$, where $\Delta\sigma_{11}$ is the change in nominal stress during unloading and $\Delta\varepsilon_{11}$ is the corresponding change in true strain. The gauge factor, GF, is defined as $GF = \Delta(R/R_0)/\varepsilon_{11}$, where $\Delta(R/R_0)$ is the change in normalised sample resistance during the unloading cycle. The unloading stiffness and gauge factor are plotted against nominal strain in Figure 3.5c. E_U increases with strain for all sample orientations, with the initial rate of increase highest for the 0° samples. The gauge factor during unloading also increases with strain. Figure 3.5d illustrates the effect of full unloading for a sample oriented at 0° to the draw direction. Both the resistance-strain and stress–strain responses exhibit hysteresis, and both a permanent strain and permanent change in sample resistance are evident upon unloading.

A stable response to cyclic stress is of importance in many sensing and structural applications. An initial exploration into the response under cyclic uniaxial loading was conducted by applying four loading packets of ten unloading cycles, with results as illustrated in Figure 3.5e. The loading packets labelled 1, 2, and 3 all resulted in permanent drift in the piezoresistive and stress–strain responses. The last set of loading cycles involved cyclic excursions well below the current yield strength, as denoted by the symbol $\Delta\sigma$ in Figure 3.5e. This loading packet gave rise to an elastic response.

The creep behaviour of the CNT mat was investigated by holding a sample at a constant tensile stress of 8.3 MPa, 17 MPa, and then at 25 MPa, each time for 1500 s, before unloading the sample to 17 MPa for a further 1500 s. The strain, ε_{11}, recorded at each of these constant stresses is plotted against time in Figure 3.5f. No noticeable creep was observed in the final phase of holding at 17 MPa. Also, no noticeable change in electrical resistance occurred whilst the sample was held at constant stress.

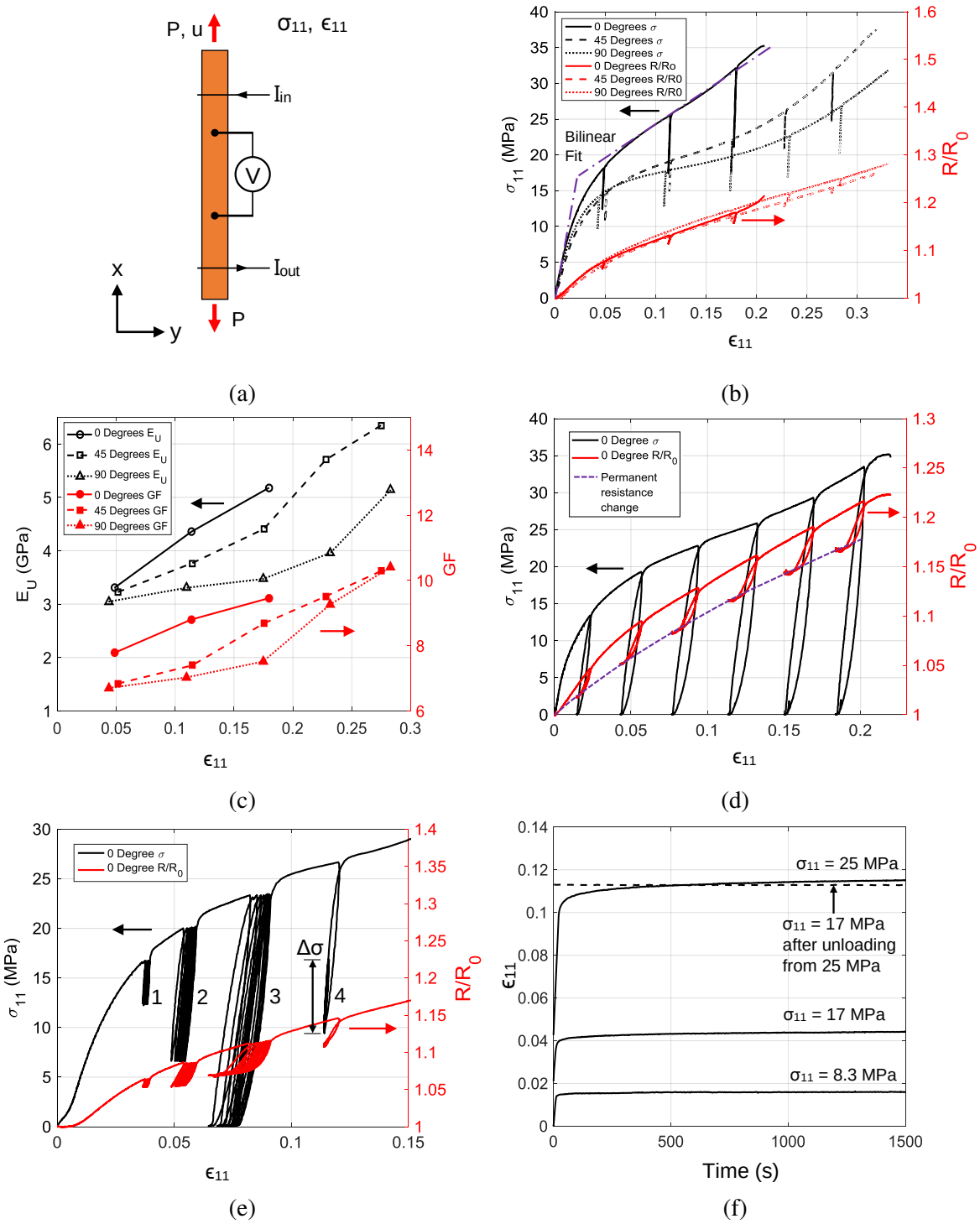

Fig. 3.5 Nonlinear and piezoresistive behaviour of carbon nanotube mat: (a) schematic of tensile test setup with four point probe, (b) anisotropic response with partial unloading, (c) unload modulus and gauge factor as a function of applied strain for different sample orientations to the draw-direction, (d) full unloading cycles revealing plastic strains and resistance change, (e) drift and hysteresis under cyclic loading, and (f) creep curves showing the effects of constant stress on the tensile strain. Unless otherwise stated, stresses and strains are nominal, calculated from initial sample dimensions.

3.3.6 In-situ observations of deformation mechanisms

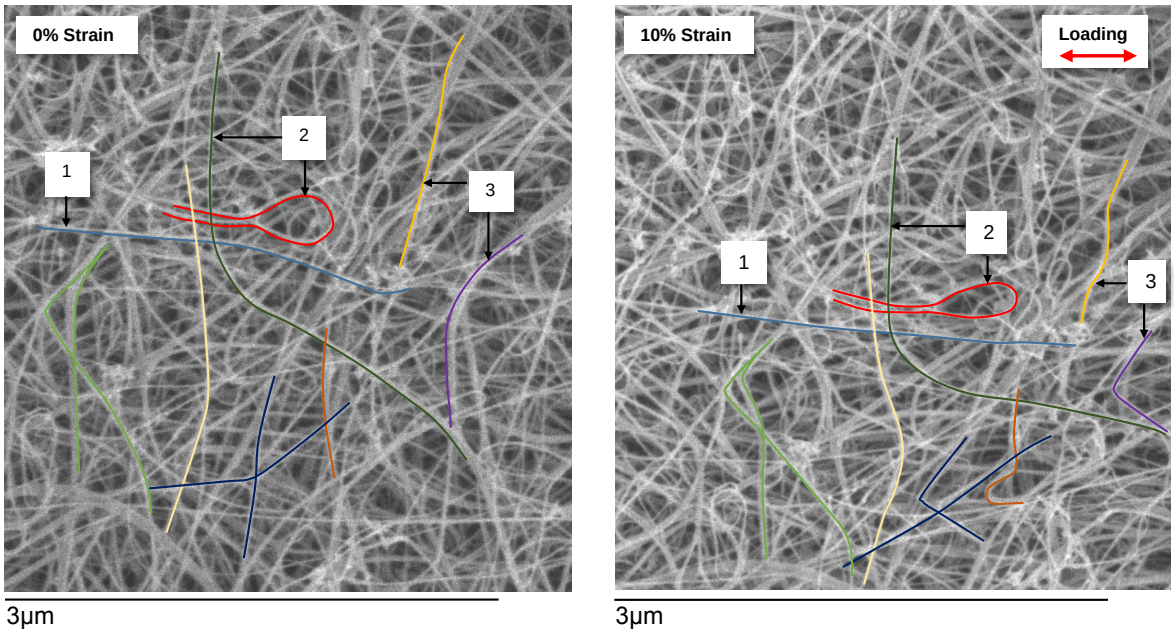

(a) (b)

Fig. 3.6 Microstructural changes during yield: (a) SEM image of CNT mat microstructure prior to loading, and (b) the same area of mat microstructure at 10% macroscopic strain, with bundles highlighted for discussion.

An understanding of the origin of mechanical properties in direct-spun mats is aided by observation of the deformation mechanisms at the microstructural scale. Unlike other in-situ studies of CNT mats that have been reported in the literature [310, 136], in the present study the same microstructural area is observed before and after deformation. This enables identification of the main deformation mechanisms. For example, images of microstructure are presented in Figures 3.6a and 3.6b, for strains of 0%, and 10% respectively, with specific bundles and locations of interest annotated. The bundles labelled 1 and 2 straighten and orient along the loading direction, whereas the transverse bundle labelled 3 undergoes buckling. In these case, joints formed between the CNT bundles where CNTs branch from one bundle to another and where CNT bundles cross, remain intact. The bundles do not slip past one another at the joints between them, nor do they rotate relative to one another at the joints themselves.

3.4 A model for in-plane mechanical properties

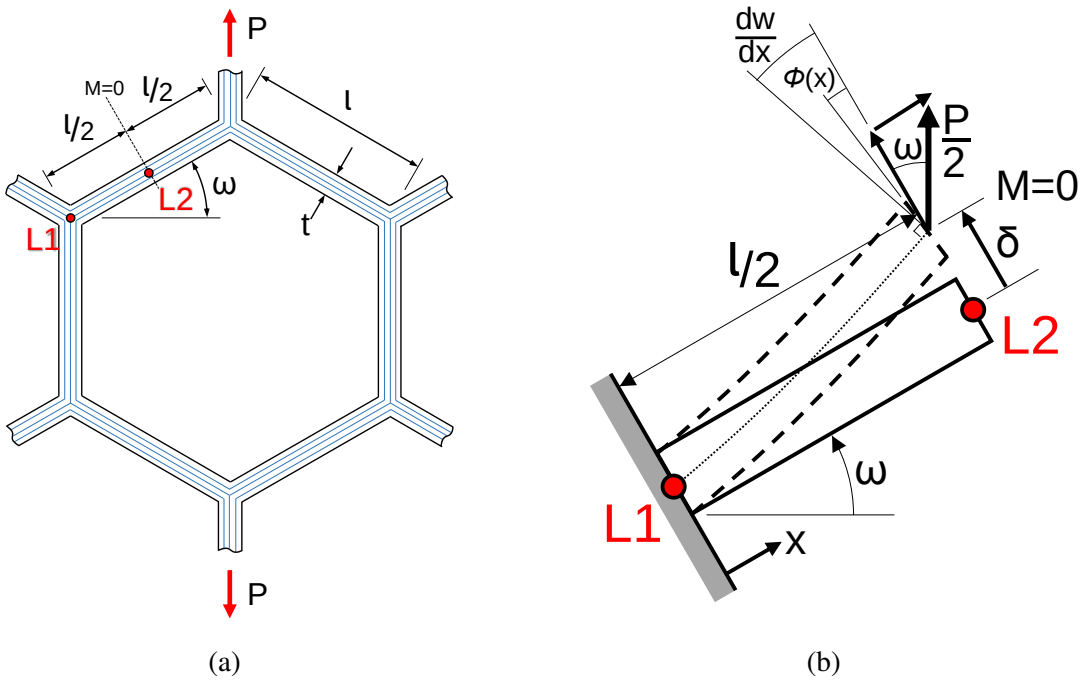

(a) (b)

Fig. 3.7 (a) Geometry of a honeycomb unit cell of CNT bundle network microstructure (depth b into page); (b) loading and deformation of an inclined strut modelled with Timoshenko beam theory.

There is a major deficit in stiffness and strength when one compares individual CNTs with bulk CNT materials. In the case of direct-spun mats, why does a random, interconnected network of CNT bundles possess inferior tensile properties to those of individual CNTs? This question is addressed via the model below.

At the microstructural level, the junctions between CNT bundles are of low nodal connectivity, of between 3 and 4. Consequently, the mechanical properties are governed by the bending and shear response of CNT bundles, rather than by their axial stretch [315]. Furthermore, where joints between bundles exist, experimental observations of the mat microstructure during tensile testing suggests that they transfer rotational and translational forces between one another without relative slip or rotation between bundles occurring at the joints themselves. For an approximate prediction of stiffness and strength, this justifies the use of a periodic 2D honeycomb unit cell, as illustrated in Figure 3.7a, with struts of thickness t and length l that deform by bending and shearing [225, 315]. CNT bundles form the struts of this unit cell, and are connected to one another at nodes by the exchange of

nanotubes from one bundle to the next. The relative density of the network $\bar{\rho} = \rho_{Mat}/\rho_B$ is written as follows [225]:

$$\bar{\rho} = \frac{3}{2\cos(\omega)(1+\sin(\omega))}\left(\frac{t}{l}\right) \tag{3.1}$$

where ω is the angle of the inclined strut to the horizontal, see Figure 3.7b. For a regular, quasi-isotropic honeycomb, ω equals $\pi/6$ [225]. Relatively little in-plane anisotropy was observed during tensile testing, thus this value is adopted in this study for development of the micromechanical model. Upon neglecting axial stretch of the struts, and upon taking P as the load on each vertical strut, one half of a beam inclined to the loading direction is analysed using Timoshenko beam theory with symmetry boundary conditions, as illustrated in Figure 3.7b. The beam of length $l/2$ is built-in at its left-hand end, labelled $L1$. It is subjected to an end load $P/2$ at its point of inflection ($M = 0$), at location $L2$. The co-ordinate along the beam mid-surface is x. The bending moment along the beam $M(x)$ and shear force $Q(x)$ are given by:

$$M(x) = \frac{P}{2}\left(\frac{l}{2} - x\right)\cos(\omega) \tag{3.2}$$

and

$$Q(x) = \frac{P}{2}\cos(\omega) \tag{3.3}$$

respectively. Now, write ϕ as the angle of rotation of the normal to the mid-surface and w as the transverse displacement of the mid-surface. Then, Timoshenko beam theory [445] for a bundle of axial modulus E_B and shear modulus G_B states that:

$$M(x) = E_B I\frac{\partial \phi}{\partial x} \tag{3.4}$$

and

$$Q(x) = sAG_B\left(-\phi + \frac{\partial w}{\partial x}\right) \tag{3.5}$$

where I is the second moment of area, A the cross-sectional area, and the shear coefficient equals $s = 8/9$ [445]. Equation 3.4 is substituted into Equation 3.2 and integrated to obtain

$$\phi = \frac{x(l-x)P\cos(\omega)}{4E_B I} \tag{3.6}$$

Substitution of Equations 3.6 and 3.3 into 3.5, followed by rearrangement and integration, yields

$$w = \frac{Px\cos(\omega)}{2sAG_B} + \frac{\left(\frac{x^2 l}{2} - \frac{x^3}{3}\right) P\cos(\omega)}{4E_B I} \tag{3.7}$$

Since $\delta = w\left(x - \frac{l}{2}\right)$, if follows that

$$\delta = \left(\frac{l}{4sAG_B} + \frac{l^3}{48E_B I}\right) P\cos(\omega) \tag{3.8}$$

and the macroscopic strain ε^∞ in the direction of loading follows immediately as

$$\varepsilon^\infty = \frac{2\delta\cos(\omega)}{(1+\sin(\omega))l} \tag{3.9}$$

Now, the macroscopic stress σ^∞ is given by $\sigma^\infty = P/(2lb\cos(\omega))$, and upon making the substitution for the bundle area $A = tb$, and the second moment of area $I = bt^3/12$, the macroscopic modulus $E_{Mat} = \sigma^\infty/\varepsilon^\infty$ reads

$$E_{Mat} = \frac{1+\sin(\omega)}{\cos^3(\omega)} \left[\frac{1}{sG_B}\left(\frac{l}{t}\right) + \frac{1}{E_B}\left(\frac{l}{t}\right)^3\right]^{-1} \tag{3.10}$$

It remains to estimate the shear modulus G_B and axial Young's modulus E_B for a bundle. Whilst the axial bundle modulus derives from covalent bonding within the CNT wall, the shear modulus is dictated by the much more compliant van der Waals bonding between adjacent CNTs. The approach of [261] is followed in estimating the axial bundle modulus as $E_B = (\rho_B/\rho_w)E_w$ where $\rho_w = 2200$ kg/m^3 (i.e. that of graphene at an interlayer spacing of 0.34 nm). For $E_w = 1$ TPa, it follows that $E_B = 680$ GPa. Values for G_B in literature have been deduced from in-situ 3-point bending tests [264, 275] and from thermal vibration [446], varying from 0.7 to 6.5 GPa $\pm$ 50%. The measured mat modulus of 3.3 GPa from unloading tests and assumed value for E_B implies $G_B = 9.5$ GPa via 3.10, which is within the range of experimental measurements [264]. Inspection of Equation 3.10 reveals the relative contribution of the shear and bending deformation to the macroscopic modulus. Since $sG_B \ll E_B(t/l)^2$, it is clear that the shear modulus of the bundle dominates the deformation, as opposed to the stiffer covalent bonding along the CNT walls. The validity of Timoshenko beam theory as derived above in estimating the honeycomb modulus is confirmed by comparing predictions of Timoshenko beam theory to the results of finite element simulation, see Appendix D.

Now consider the tensile yield strength of the hexagonal lattice. The tensile stress on the outermost fibre of the inclined strut, due to the bending moment $M(x)$ and axial tension, is given by $\sigma_B = Mt/2I + (P/2tb)\sin(\omega)$, whereas the average shear stress on the cross section due to the shear force $Q(x)$ is given by $\tau_B = Q(x)/A$. As the bending moment is greatest at the location labelled $L1$ on the inclined strut illustrated in Figure 3.7b, σ_B and τ_B have the following maximum values:

$$\sigma_B = \left(\frac{27}{4(1+\sin(\omega))^2 \bar{\rho}^2} + \frac{3\sin(\omega)}{2(1+\sin(\omega))\bar{\rho}} \right) \sigma^{\infty} \tag{3.11}$$

and

$$\tau_B = \left(\frac{3\cos(\omega)}{2(1+\sin(\omega))\bar{\rho}} \right) \sigma^{\infty} \tag{3.12}$$

The ratio between bundle tensile stress and average shear stress is given by

$$\frac{\sigma_B}{\tau_B} = \frac{9}{2\cos(\omega)(1+\sin(\omega))\bar{\rho}} + \frac{\sin(\omega)}{\cos(\omega)} \tag{3.13}$$

Now, for a relative density $\bar{\rho} = 0.25$ and $\omega = \pi/6$, it follows that $\sigma_B/\tau_B = 14.4$. If the ratio of bundle tensile strength σ_{Bf} to bundle shear strength τ_{Bf} is greater than σ_B/τ_B, macroscopic yield will be limited by the bundle shear strength, rather than by the fracture of CNT walls. The following argument supports this premise, on the basis that the ratio σ_{Bf}/τ_{Bf} is more than four times greater than σ_B/τ_B, as is justified below.

Tensile tests conducted on individual CNT bundles grown by the chemical vapour deposition process suggest that the wall fracture strength of individual CNTs σ_{wf} lies between 5.5 GPa and 25 GPa [267]. Assume that the bundle strength scales with the CNT wall strength σ_{wf} according to $\sigma_{Bf} = (\rho_B/\rho_w)\,\sigma_{wf}$, and take $\sigma_{wf} = 5.5$ GPa. Then, the bundle fracture strength equals $\sigma_{Bf} = 3.7$ GPa.

Now consider the CNT bundle shear strength τ_{Bf}. Values for the bond shear strength between CVD-grown tubes, as measured in the literature, vary from 0.04 MPa to 70 MPa [276, 277], with values sensitive to the concentration of graphitic defects [277, 280]. For adjacent pristine CNT surfaces with long overlap lengths, the bond shear strength lies between 30 MPa and 60 MPa [279]. Here, we shall assume the value $\tau_{Bf} = 60$ MPa, as this implies a macroscopic yield stress of 17 MPa from Equation 3.12, close to the experimental measurements, and lies within the range of values reported in literature. Consequently, $\sigma_{Bf}/\tau_{Bf} = 62$, and so the macroscopic yield strength is limited by the bundle shear strength.

The conclusion that the shear strength of CNT bundles limits the macroscopic yield strength of direct-spun mats, as opposed to the bundle axial strength, is consistent with the observations of bundle deformation during in-situ testing, and explains why the random arrangement of CNT bundles within the mat results in a severe knockdown in mechanical properties when compared to those of individual CNTs in longitudinal tension.

3.5 Conclusions

Characterisation of a commercially produced direct-spun mat revealed in-plane electrical conductivities of between 32.5 kS/m and 40.4 kS/m, elastic moduli of 3.0 GPa to 3.4 GPa, and an ultimate tensile strength between 30 MPa and 40 MPa. The through-thickness electrical conductivity and the toughness of the bond between adjacent layers within the CNT mat were found to be much below the values of electrical conductivity and toughness measured in-plane. Macroscopic deformation of CNT mat is accompanied by reorientation of the bundle network along the loading direction. Measurements of sample resistance measured in line with the direction of tensile stress during tensile testing increase by between 20% and 30% before final failure. A portion of this additional resistance is recovered upon unloading during tensile testing. Where joints between bundles exist, observation of the mat microstructure during tensile loading reveal that they transfer translational forces and moments between one another without relative slip or rotation between CNT bundles at the joints themselves. A micromechanical model was developed to relate the direct-spun mat properties to those of the CNT bundle network, based upon 2D honeycomb microstructure of CNT bundle struts which are connected to one another at nodes. It illustrates that the longitudinal shear deformation of CNT bundles dominates, and accounts for the knockdowns in CNT mat mechanical properties compared to those of individual CNTs in uniaxial tension.

Chapter 4

Mechanical and electrical properties of direct-spun mat-epoxy composites

4.1 Summary

This study aims to determine the effect of epoxy infiltration and cure upon the tensile stress-strain response and electrical conductivity of direct-spun CNT mat-epoxy composites over a broad compositional range, and to understand the relationship between microstructure and properties through experiment and micromechanical modelling. The volume fraction of epoxy is varied widely by suitable dilution of the epoxy resin with acetone before infiltration. Subsequent evaporation of the acetone, followed by a cure cycle, leads to composites of varying volume fraction of CNT, epoxy and air. The modulus, strength, electrical conductivity and piezoresistivity of the composites are measured. The CNT mats and their composites exhibit an elastic-plastic stress-strain response under uniaxial tensile loading, and the degree of anisotropy is assessed by testing specimens in 0°, 45° and 90° directions with respect to the draw direction of mat manufacture. The electrical conductivity scales linearly with CNT volume fraction, irrespective of epoxy volume fraction. In contrast, the modulus and strength depend upon both CNT and epoxy volume fractions in a non-linear manner. The macroscopic Young's modulus of the CNT mat-epoxy composites are far below the Voigt bound based upon the modulus of CNT walls and epoxy. A micromechanical model is proposed to relate the macroscopic modulus and yield strength of a CNT mat-epoxy composite to the microstructure.

4.2 Manufacture and composition of materials

4.2.1 Direct-spun CNT mat

Direct-spun CNT mat was provided by Tortech Nano Fibers Ltd[1]. The mat is of width 0.9 m and thickness 70 μm, and is comprised of flattened CNT aerogel socks. Each flattened sock is of width 80 mm and thickness about 170 nm, and is comprised of a network of branched CNT bundles, forming an interconnected network. Each bundle consists of between 10 and 40 closely packed CNTs. As discussed in section 2.2.3, direct-spun CNT materials can possess in-plane anisotropy in their mechanical and electrical properties, and the degree of anisotropy is sensitive to the ratio of the velocity of the drawn aerogel to that of the gas flow within the reactor [72]. As before, the principal material orientation is parallel to the draw direction of the CNT sock in the reactor during manufacture.

4.2.2 Manufacture of CNT-epoxy composites

The production method for fabricating the CNT-epoxy composites is sketched in Figure 4.1. Direct-spun CNT mat samples of width 10 mm, length 80 mm, and nominal thickness 70 μm were cut from a single ply. They were then infiltrated by a solution of epoxy in acetone, followed by evaporation of the acetone under vacuum, before curing in a hot press. The epoxy resin was bisphenol-A IN2 infusion resin and a hexane hardener[2]. The epoxy resin and hardener were mixed in the proportion 10:3 by mass, and were then diluted with acetone. The mass concentration of resin and hardener in this solution, denoted φ, varied from 0.001 to 1.0. By infiltrating the CNT mat with epoxy-acetone solutions of selected values of φ, the volume fraction of epoxy in the cured composite could be suitably controlled. After immersion of the CNT mat samples in the epoxy-acetone solution for 60 s, manufacture proceeded along one of two routes, see Figure 4.1. In the first route, the infiltrated CNT mat samples were placed between an inner layer of PTFE release film and an outer breather layer, and a vacuum bagging system[3] was used to apply a consolidation pressure of $P = 0.1$ MPa (1 atm), at a temperature of 40 °C for 1 hour. Excess resin was absorbed by the breather layer material on each side of the CNT-epoxy composites during consolidation. Samples were then cured in a hot-press at 120 °C for 3 hours, with a constant pressure of 0.6 MPa applied in the through-thickness direction. An alternative production route was used to

[1]Tortech Nano Fibers Ltd, Hanassi Herzog St., Koren Industrial park, Ma'alot Tarshiha, 24952 Israel.

[2]IN2 epoxy infusion resin was obtained from Easy Composites Ltd., Park Hall Business Village, Longton, Stoke on Trent, Staffordshire, ST3 5XA, UK.

[3]A vacuum bagging system was obtained from Easy Composites Ltd., Park Hall Business Village, Longton, Stoke on Trent, Staffordshire, ST3 5XA, UK.

manufacture CNT composites of higher CNT volume fraction: infiltrated CNT mat samples were placed between PTFE films, and were subjected to a through-thickness pressure of $P = 10$ MPa between the loading platens of a screw-driven test machine. Since the samples were compressed between the PTFE films, squeeze-out of excess epoxy was prevented. After the consolidation pressure had been applied for 3 hours, allowing the epoxy to cure partially within the densified CNT mat, the samples were placed within the same vacuum bagging system as that described above (pressure of $P = 0.1$ MPa and a temperature of 40 °C for 1 hour) to remove residual acetone and volatile compounds. The samples were then cured in a hot press at 120 °C for 3 hours, under the same conditions as for the first route.

Dogbone specimens of pure, void free epoxy were also prepared for uniaxial tensile testing. Epoxy solutions were cast into a mould, and degassed in a vacuum chamber for 1 hour, before curing at 120 °C for 3 hours. To determine the effect of acetone dilution upon the mechanical properties of the epoxy, additional dogbone samples were cast from a solution of acetone and epoxy, with $\varphi = 0.5$. The acetone was then removed by degassing under vacuum in the same manner, and the sample was cured as described above.

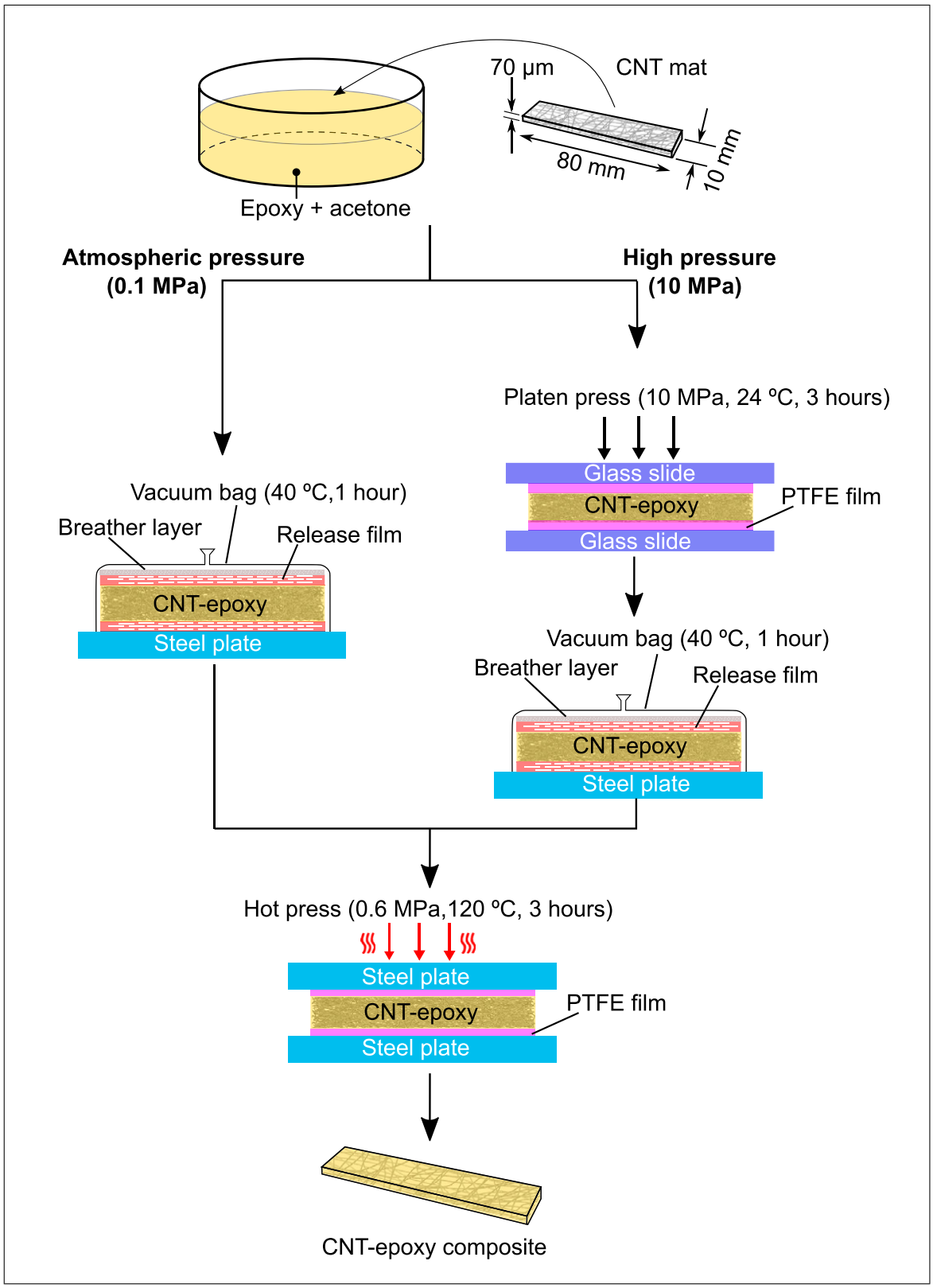

Fig. 4.1 Methodology of CNT-epoxy composite manufacture.

4.2.3 Composition and physical properties of CNT mat and composites

The volume fraction of CNT bundles f_B and volume fraction of epoxy f_e are related to the corresponding weight fractions of CNT bundles and epoxy w_B and w_e respectively, as follows. Write ρ_B as the CNT bundle density and ρ_e as the measured epoxy density. Then upon writing ρ as the measured composite density, it follows that

$$f_B = w_B \frac{\rho}{\rho_B}, \quad f_e = w_e \frac{\rho}{\rho_e}. \tag{4.1}$$

The weight fraction of CNT bundles in the composite w_B is the ratio of the mass of CNT bundles to the mass of the composite, and the weight fraction of epoxy follows directly as $w_e = 1 - w_B$. Both the mass of the CNT mat before infiltration and the mass of the cured CNT-epoxy composite were measured with a mass balance. The width and length of samples was measured with a Vernier scale. The sample thickness was measured with a micrometer, and averaged from ten readings along the sample length. For samples of direct-spun CNT mat, the thickness was confirmed by X-ray tomography, as this method avoids compression of the sample during measurement. The density of the composite ρ was determined via its mass and volume. The density of the CNT bundles was measured as described in section 3.2, $\rho_B = 1560$ kg/m^3. The density of epoxy, as calculated from the measured epoxy dogbone sample dimensions and mass, was $\rho_e = 1120$ kg/m^3. Finally, the porosity of the composites, referred to here as the volume fraction of air f_a, was determined by subtracting the calculated volume fractions of CNT bundles and epoxy from unity.

The densities of the mat and of the CNT-epoxy composites, and the volume fractions of CNT bundles, epoxy and air are recorded in Table 4.1 as functions of the weight fraction of epoxy in the infiltration solution φ and of the through-thickness pressure P applied after infiltration. The as-received CNT mat specimens (absent infiltration) are labelled (1). CNT mat-epoxy composites manufactured at $P = 0.1$ MPa are labelled (2) to (9) in order of increasing φ, such that (9) corresponds to a composite made from undiluted epoxy ($\varphi = 1.0$) and CNT mat. Cured epoxy dogbone samples with initial concentration of epoxy in acetone $\varphi = 0.5$ and $\varphi = 1.0$ are labelled (10) and (11), respectively. Two composites (5h) and (6h) were manufactured with the high pressure route (for which $P = 10$ MPa), from an epoxy-acetone mix equal to that of samples (5) and (6), respectively. Additionally, a sample of direct-spun mat (1h) was infiltrated with acetone and subjected to the same through-thickness pressure of $P = 10$ MPa for 3 hours.

Table 4.1 Composition of direct-spun CNT mat and CNT-epoxy composites as a function of the manufacturing process parameters.

Sample label	Epoxy mass concentration	Consolidation pressure	Average density	Average volume fraction		
	φ	P (MPa)	ρ (kg/m^3)	f_B	f_e	f_a
(1)	0	0.1	234	0.15	0	0.85
(1h)	0	10	296	0.19	0	0.81
(2)	0.001	0.1	276	0.17	0.01	0.82
(3)	0.01	0.1	330	0.19	0.03	0.78
(4)	0.10	0.1	469	0.20	0.14	0.66
(5)	0.12	0.1	605	0.23	0.22	0.55
(5h)	0.12	10	811	0.29	0.32	0.39
(6)	0.17	0.1	771	0.25	0.34	0.41
(6h)	0.17	10	983	0.35	0.39	0.26
(7)	0.30	0.1	906	0.20	0.53	0.27
(8)	0.75	0.1	986	0.18	0.63	0.19
(9)	1	0.1	1060	0.11	0.79	0.10
(10)	1	0.1	1120	0	1	0
(11)	0.50	0.1	1120	0	1	0

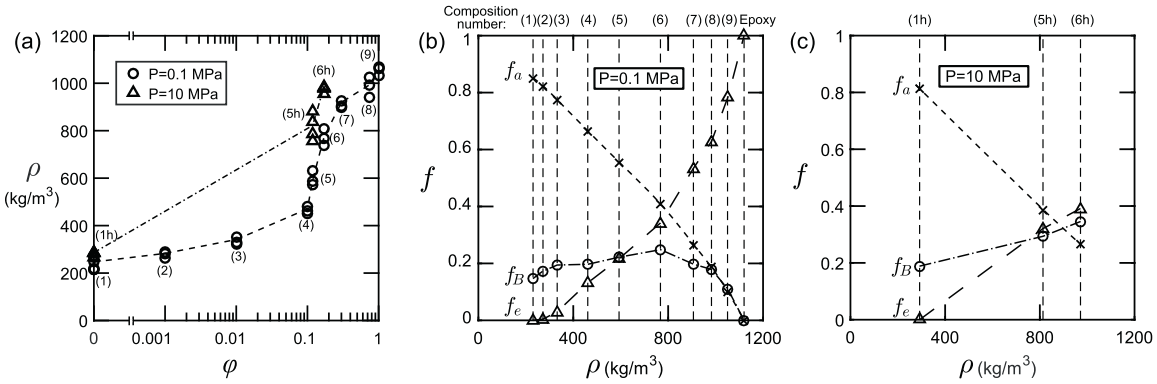

Fig. 4.2 (a) Density ρ of dry mat and cured composites, plotted against the concentration of epoxy by weight φ for the infiltration solution used in manufacture. The volume fractions f of CNT bundles, epoxy and air in the cured composite are plotted against bulk density in (b) for samples manufactured with a consolidation pressure $P = 0.1$ MPa, and in (c) for samples subjected to a 10 MPa pressure prior to vacuum.

The dependence of cured composite density ρ upon the initial epoxy concentration φ of the epoxy-acetone solution is plotted in Figure 4.2a for $P = 0.1$ MPa and $P = 10$ MPa. The density ρ relates to the densities and volume fractions of CNT bundles and epoxy according to $\rho = f_B\rho_B + f_e\rho_e$. Note that ρ increases monotonically with increasing φ, for each selected value of P. Thus, it is convenient to report the composition and properties of each composite against ρ rather than the process variable φ. It is also clear from Figure 4.2a that ρ increases with increasing P at any fixed value of φ. The volume fractions of CNT bundles, epoxy and air are plotted against the macroscopic composite density in Figure 4.2b for composites fabricated at $P = 0.1$ MPa, that is by consolidation under vacuum before curing, and in Figure 4.2c for samples that were subjected to a through-thickness pressure $P = 10$ MPa after infiltration. Samples fabricated at $P = 0.1$ MPa possess a maximum CNT volume fraction of $f_B = 0.25$ at $\rho = 771$ kg/m^3, see sample (6) in Figure 4.2b. In contrast, f_B rises monotonically with increasing ρ for the choice $P = 10$ MPa for the range of composite compositions studied herein, see Figure 4.2c. The non-linear dependence of f_B upon (ρ, P) arises from the transient consolidation response of the bundles in the presence of an evaporating solvent, acetone, and a curing epoxy matrix.

4.3 Measured properties of CNT mat and CNT-epoxy composites

4.3.1 Morphology of CNT mats and CNT-epoxy composites

The CNT mat and CNT composite microstructures were imaged by scanning electron microscope (SEM), using a voltage of 5 kV and a spot size of 3 µm. A field emission transmission electron microscope (FEGTEM), fitted with energy-dispersive X-ray spectroscopy (EDX) was used to characterise the bundle microstructure of the CNT mat and CNT-epoxy composites. Samples of the as-received CNT mat were prepared for TEM analysis by depositing a small quantity of aerogel layers from the delaminated mat onto a copper mesh, with the aid of acetone solvent. Composites were also prepared for TEM analysis by using a modified epoxy resin containing uniformly distributed silicon side-groups[4], so that the distribution of epoxy in the composite could be identified by elemental EDX mapping of the silicon group distribution. A focused ion beam (FIB)[5] was used to mill samples of direct-spun CNT mat and CNT-epoxy composites in their through-thickness direction in order to reveal the bundle microstructure in the cross-sectional view. A beam current of 2.8 nA was used for refined milling prior to imaging. For TEM analysis, samples were also prepared by FIB cutting, using a lift-out process as described elsewhere [447]. This method produced samples of suitable thickness between 100 nm and 150 nm.

Plan views of CNT mat microstructure and CNT composite microstructure with selected values of epoxy content are presented in Figures 4.3a-c, and images of their cross-section in the through-thickness direction are shown in Figures 4.3d-f. The CNT mat microstructure, as displayed in Figures 4.3a and 4.3d, consists of a random network of CNT bundles, with branching of CNTs from bundle to bundle. The bundle cross sections are typically circular. In composites of low epoxy content, the epoxy coats the CNT bundle network uniformly, see Figures 4.3b and 4.3e. The cross-sections of some of the CNT bundles appear flattened compared to the dry state. As the epoxy content increases, it progressively fills the air space between CNT bundles until close to fully dense, see Figures 4.3c and 4.3f. SEM and TEM images of the CNT-epoxy composite cross-section reveal an almost uniform volume fraction f_e of epoxy in the through-thickness direction.

[4]SILIKOFTAL® ED, Evonik, Tego House, Chippenham Dr, Kingston, Milton Keynes, MK10 0AF, UK.

[5]SEM/FIB Workstation, Helios Nanolab DualBeam 600. Thermo Fisher Scientific, 168 Third Avenue, Waltham, MA, USA 02451.

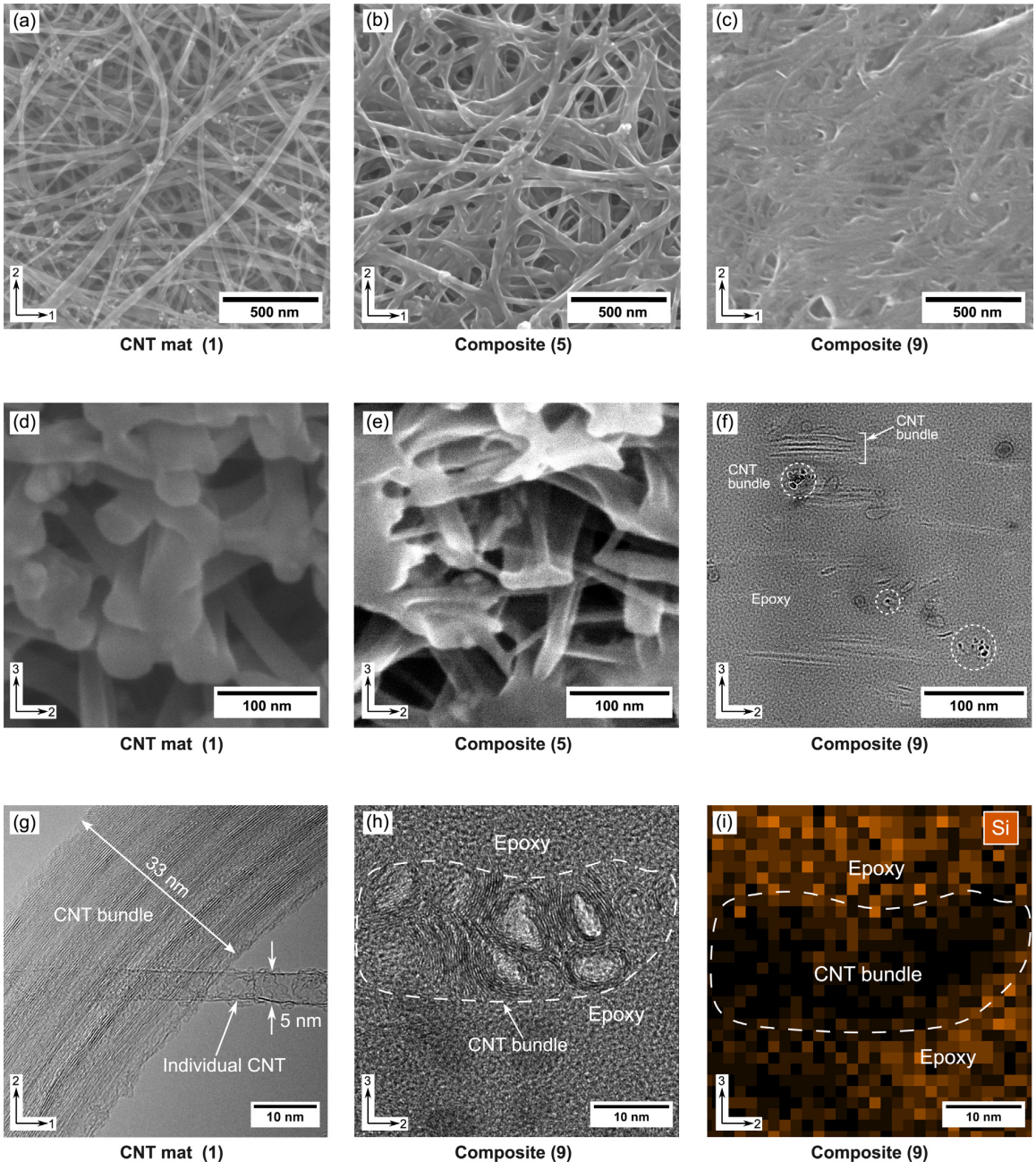

Fig. 4.3 (a) Plan-view of (a) CNT mat, (b) composite (5) and (c) composite (9). FIB-milled cross-sections for (d) dry mat, (e) composite (5) and (f) composite (9). (g) Plan view of a CNT bundle in dry mat; (h) FIB-milled cross-section of composite (9), with (i) distribution of silicon-tagged epoxy. Images (a)–(e) taken in SEM, (f)–(i) in TEM.

A plan view image of a CNT bundle in the as-received direct-spun mat from TEM is shown in Figure 4.3g, revealing the crystalline, close-packed CNT bundle microstructure. A complementary, transverse image of a CNT bundle cross section in the direct-spun mat/silicone epoxy resin composite, produced from a cross-sectional cut of the composite in the through-thickness direction, is given in Figure 4.3h. The CNTs are predominantly multi-walled, and the individual CNTs within a bundle remain close-packed after epoxy infiltration. Elemental mapping of this bundle cross-sectional view is shown in Figure 4.3i, revealing the distribution of silicon-tagged epoxy within the microstructure. The elemental mapping shows that the epoxy resin surrounds the bundle, and wets the bundle surface, but does not penetrate the voids between neighbouring CNTs within each bundle.

4.3.2 Uniaxial tensile tests

Uniaxial tensile tests were performed on the CNT mat, CNT-epoxy composites, and the epoxy matrix, using a screw-driven test machine[6] at a strain rate of $\dot{\varepsilon} = 10^{-4}$ s^{-1}. The ends of the specimens were placed in wedge grips and were cushioned by paper end tabs, see Figure 4.4a. The axial nominal strain in the gauge section was measured by tracking the axial displacement of two dot stickers. The dots were of diameter 0.5 mm and of spacing 30 mm, and were adhered to the sample prior to testing. The relative displacement of the dots was recorded at a frequency of 1 Hz with a suitable camera system[7]. For the as-received direct-spun CNT mat, the yield stress is inferred from the stress-strain response via a bilinear fit, whilst for the CNT-epoxy composites, it is determined by finding the intersection of the stress-strain curve with a line drawn parallel to the initial, linear portion of the stress-strain response but offset by 0.2% in strain. The dimensions of the cast epoxy samples for uniaxial tensile testing are given in Figure 4.4b; the tensile strain was also measured with the optical extensometer as described above.

The tensile uniaxial stress-strain response of CNT mat, CNT-epoxy composites and epoxy are plotted in Figure 4.5a-c. In order to determine the degree of in-plane anisotropy, tensile tests were conducted on samples of dry mat (1) and composite (9), oriented at 0°, 45° and 90° to the principal material orientation, see Figure 4.5a. Both materials exhibit moderate in-plane anisotropy. The ductility of the composite is inferior to that of the as-received mat, but the strength and stiffness are both enhanced. The uniaxial tensile responses of CNT mat-epoxy composite samples oriented at 0° to the principal material direction, and consolidated under

[6]Instron Ltd, Coronation Road, High Wycombe, Buckinghamshire, HP12 3SY, UK. A load cell of maximum capacity 500 N was used for all tests.

[7]GOM UK Ltd, 14 Siskin Parkway East, The Cobalt Centre, Coventry CV3 4PE, UK

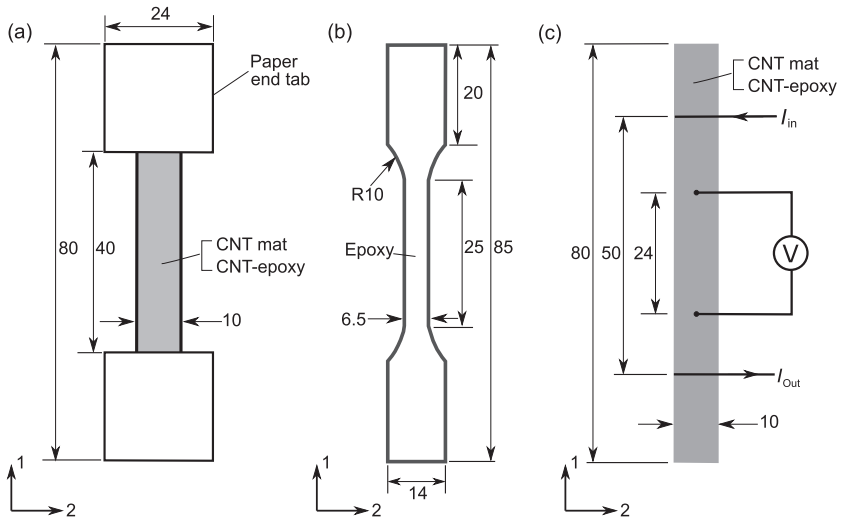

Fig. 4.4 Specimen geometries, (a) for uniaxial tensile tests on CNT mat or CNT-epoxy composites, (b) epoxy dog-bone sample, with thickness 6 mm. (c) Four-point probe method used to measure the electrical conductivity. All dimensions are in mm.

atmospheric vacuum, are compared with those of the as-received CNT mat and cured epoxy dogbone samples in Figure 4.5b. Note that the stress-strain responses of the composites are much above than those of the epoxy and direct-spun mat. The mechanical behaviour of the epoxy dogbone samples is almost insensitive to the initial concentration of epoxy in acetone, prior to evaporation of the acetone, see samples (10) and (11) in Figure 4.5b. The stress-strain response of samples oriented in-line with the principal material direction and subjected to a 10 MPa pressure prior to cure are compared with those of samples consolidated under vacuum in Figure 4.5c. Consolidation with a 10 MPa through-thickness pressure results in a stress-strain response much above that measured for other direct-spun mat and composite samples; these composites exhibit the highest strength of 410 MPa and Young's modulus of almost 30 GPa measured in the present study.

The modulus, yield strength and ultimate strength of CNT mat-epoxy composites, direct-spun mat, and epoxy are plotted against the measured sample density in Figure 4.5d, 4.5e and 4.5f, respectively. The modulus and strength are dependent on the volume fraction of both CNTs and epoxy in a non-linear manner. The greatest measured Young's modulus and yield strengths of CNT-epoxy composites lie approximately an order of magnitude above the corresponding values for the unreinforced, as-received CNT mat, or the epoxy measured in bulk form. Also, the high pressure cure cycle leads to an increase in modulus and strength by a factor of about 2 for the same density.

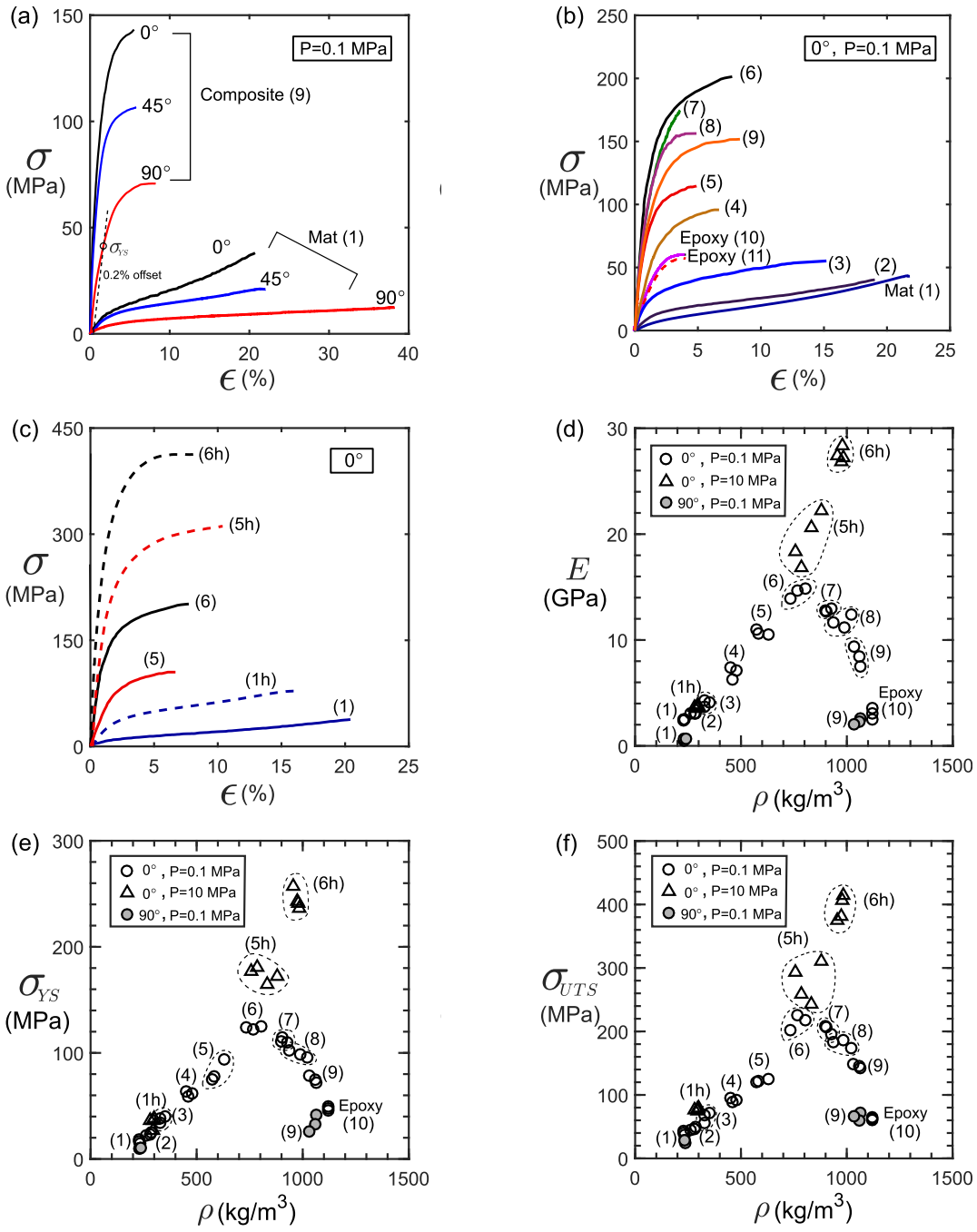

Fig. 4.5 Stress versus strain response of composites and mat (a) in 3 orientations, (b) manufactured at $P = 0.1$ MPa. Materials manufactured with $P = 1$ MPa and $P = 10$ MPa are compared in (c). Dependence of modulus E upon density ρ in (d), yield strength σ_{YS} in (e) and ultimate tensile strength σ_{UTS} in (f) for the composites, direct-spun mat, and epoxy.

4.3.3 In-plane electrical properties, unloading and piezoresistive behaviour

The in-plane electrical conductivity of the CNT mat and CNT-epoxy composites was measured with a four-point probe method prior to mechanical tensile testing; the sample dimensions and experimental setup are described in Figure 4.4c. Contacts of adequately low resistance for 4-point testing were made by laying the samples on copper contacts. The presence of breather layer material on each side of the composites during cure meant that excess resin was removed by the applied vacuum and reliable electrical contacts were achieved. The only instance where the electrical contact did require improvement was for composite (9); in this case, mild sanding of the surface was sufficient to ensure a satisfactory electrical contact. To verify that the electrical current density was constant over the sample cross-section, measurements of the potential drop along the gauge length were taken on the side of the sample on which the current probes were placed, and also on the opposite side. These measurements indicated a uniform current flow throughout the sample thickness.

The in-plane electrical conductivity measured from samples of direct-spun CNT mat and of CNT-epoxy composite (9) oriented at 0°, 45° and 90° to the principal material orientation are given in the bar chart of Figure 4.6a; the electrical conductivity of both the direct-spun mat and composite exhibit similar levels of anisotropy. The electrical conductivity of direct-spun CNT mats and composites measured along the principal material orientation is plotted against the CNT volume fraction f_B in Figure 4.6b: note that the electrical conductivity K scales linearly with CNT volume fraction f_B.

To compare the in-plane piezoresistive behaviour and post-yield mechanical response of the CNT mat (1) and CNT-epoxy composite (9), A limited number of tensile tests were also conducted with simultaneous measurement of the electrical resistance within the central portion of the sample gauge length; the results are given in Figure 4.6c. Current and voltage probes were attached to the sample with electrically conductive silver paint, and the resistance was measured at a frequency of 1 Hz. A constant current of 25 mA was supplied to the sample throughout the test, and partial unloading was conducted at regular intervals. The measured sample resistance R is normalised in Figure 4.6c by its value R_0 at the start of the test. The unloading modulus E_U as defined by the gradient of the stress-strain response at the onset of unloading. Both are plotted in Figure 4.6d as a function of tensile strain. The unloading modulus of the CNT mat increases with increasing strain, and this is due to the progressive alignment of CNT bundles with the loading direction as observed in section 3.3.6. In contrast, the unloading modulus of the composite decreases with increasing strain. This

is suggestive of microstructural damage, presumably in the form of cracking of the epoxy matrix [221].

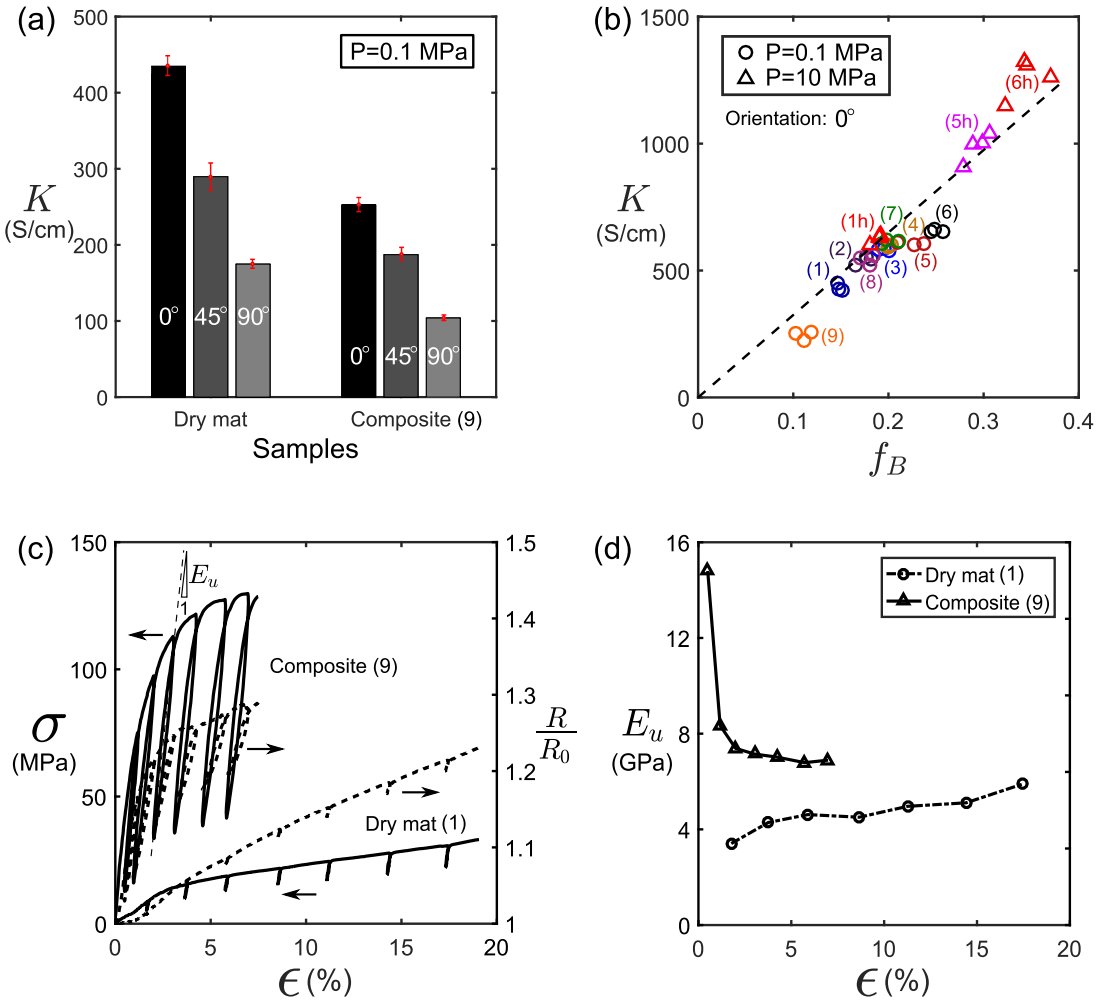

Fig. 4.6 (a) The electrical conductivity of the CNT mat (1) and CNT-epoxy composite (9) in different directions. (b) Electrical conductivity in the principal material direction plotted against CNT volume fraction. (c) Piezoresistive and unloading response, showing evolution of sample resistance with strain for dry mat and composite. The Young's moduli measured upon unloading are plotted against the applied tensile strain in (d).

4.4 A micromechanical model for modulus and yield strength

A micromechanical model is now developed, based on the characterisation of the underlying material microstructure, to understand the origin of the stiffening and strengthening due to the epoxy matrix within the CNT mat.

4.4.1 An idealisation of CNT mat-epoxy composite microstructure

The unreinforced CNT mat microstructure consists of an interlinked network of nanotube bundles. The bundles are connected by the branching of CNTs from one bundle to the next. This random, interconnected, dry bundle network has a nodal connectivity of between 3 and 4, and the in-situ experiments described in section 3.3.6 reveal that it deforms in a foam-like manner, predominantly due to bending and shearing of the CNT bundles, rather than by their axial stretch. For an estimation of strength and stiffness, this microstructure motivates the use of a periodic, planar hexagonal honeycomb network, represented by a repeating honeycomb unit cell of interlinked CNT bundle struts and epoxy, as illustrated in Figure 4.7a. Used in section 3.4 as an idealisation for the CNT dry mat, this type of unit cell provided a useful estimate of the dry CNT mat modulus and yield strength. Microscopy of the composites reveals that the outer surfaces of the CNT bundles are coated with epoxy, and that the epoxy does not infiltrate the bundles, see Figure 4.3h and 4.3i. An increase in epoxy volume fraction leads to progressive filling of the pores between the bundles. Here, the volume fractions of CNT bundles, epoxy and air in the planar unit cell are varied according to their values recorded in experiment, and the epoxy extends from the CNT bundle struts into the centre of the pores, with thickness equivalent to that of the bundles in the out-of-plane direction, see Figure 4.7b.

Finite element calculations were conducted to model the stress-strain response of the honeycomb unit cell in plane stress, using the commercially available finite element package ABAQUS[8]. The simulation set up and boundary conditions are illustrated in Figure 4.7c; the roller boundary conditions were defined such that there are vanishing components of stress in the x_2 direction, and to achieve symmetry and deformation consistent with that of the periodic honeycomb network. A perfect bond between the CNT bundles and epoxy is assumed. The degree of anisotropy of response of the unit cell is controlled by suitable choice of the initial value of the angle ω, which is a measure of the alignment of the CNT bundle microstructure with the principal material direction.

[8] ABAQUS (V. 6.14). Dassault Systèmes, 334-335 Cambridge Science Park Rd., Cambridge, CB4 0WN.

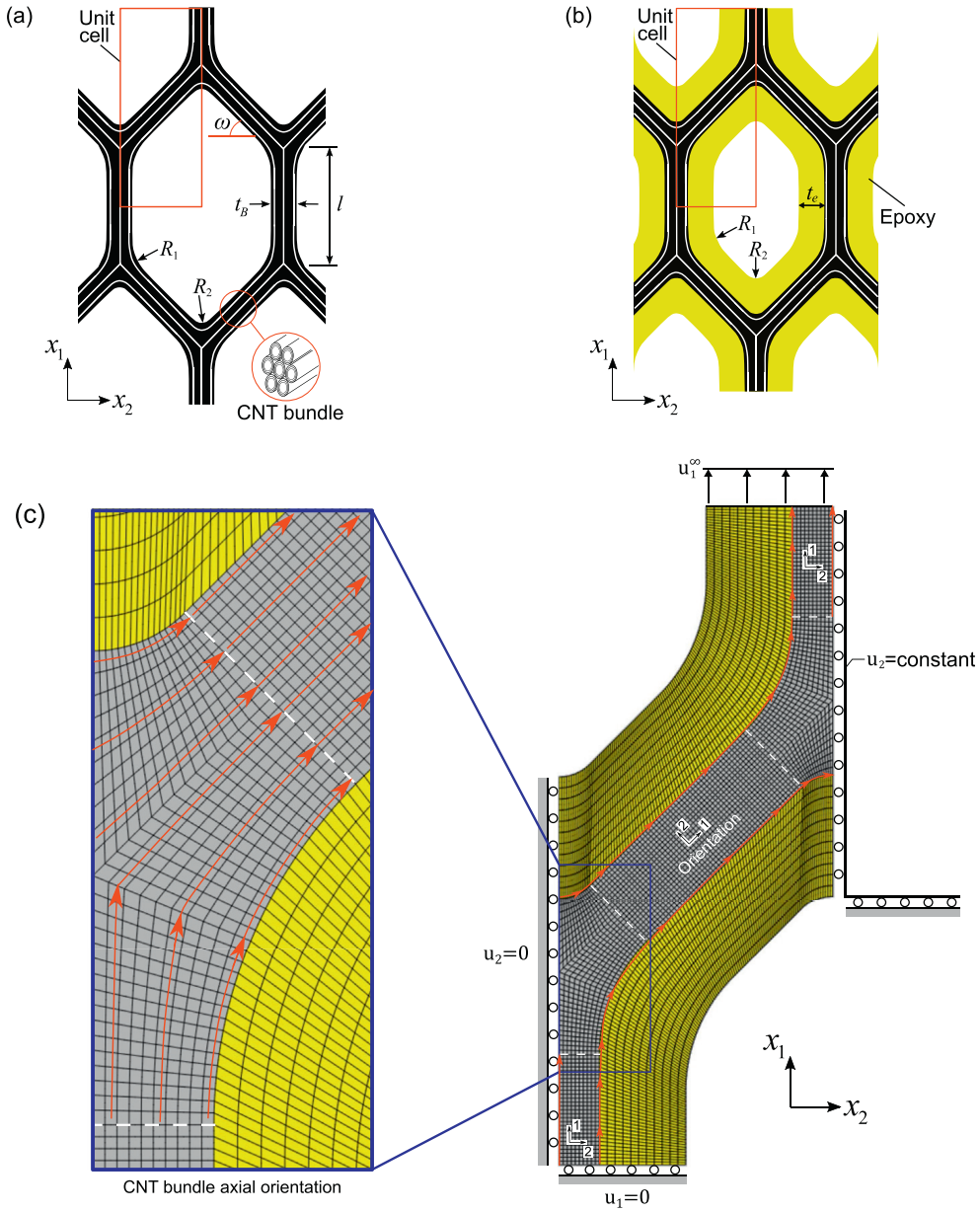

Fig. 4.7 The planar honeycomb unit cell idealisation of (a) CNT mat and (b) CNT-epoxy composite microstructure with $\omega = 45°$. Details of the simulation setup and boundary conditions for the repeating unit cell analysed are shown in (c); note the variation of material orientation around the node.

Images of the unit cells of CNT bundles, epoxy and air used in simulation are given in Figure 4.8, along with the notation used for unit cell dimensions. The ratio of the CNT bundle thickness to the length of unit cell struts t_B/l and the ratio of the epoxy layer thickness to unit cell strut length t_e/l are recorded in Table 4.2 for each of the simulated unit cells. The ratios

of the fillet radii to bundle thickness, R_1/t_B and R_2/t_B, are 2.0 and 0.54 respectively, with the exception of composite 6(h), where an elliptical pore was used instead, see Figure 4.8.

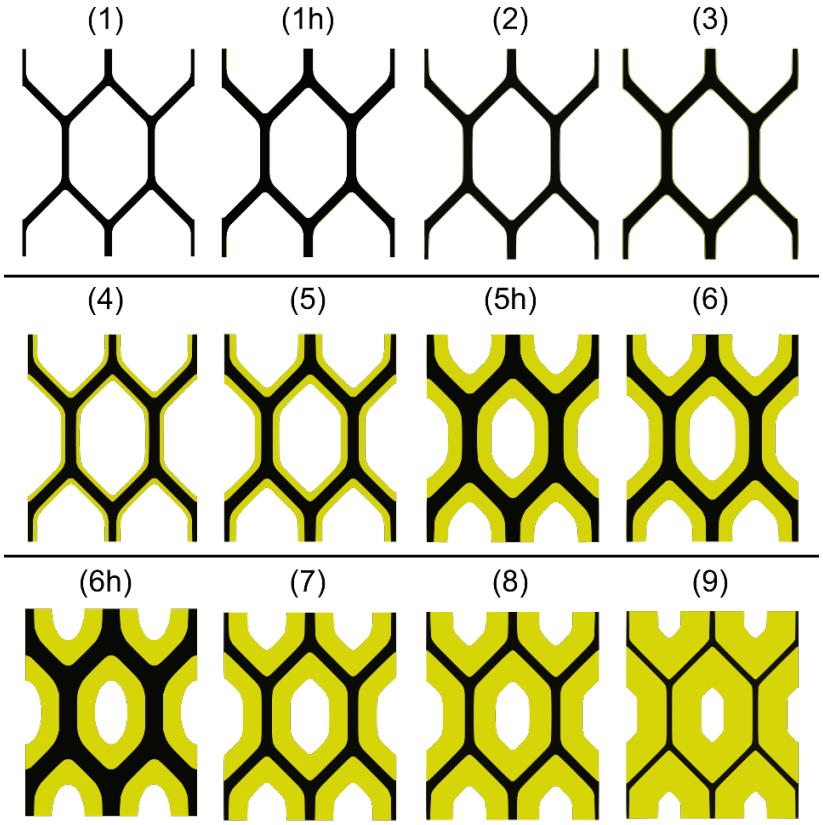

Fig. 4.8 Finite element models of dry CNT mat and CNT-epoxy composites.

Table 4.2 Normalised values of CNT bundle thickness, epoxy layer thickness and fillet radii of junctions between CNT bundle struts for FE simulation

Material	t_B/l	t_e/l
(1)	0.12	0
(1h)	0.16	0
(2)	0.15	0.019
(3)	0.17	0.013
(4)	0.17	0.069
(5)	0.18	0.11
(5h)	0.25	0.23
(6)	0.21	0.23
(6h)	0.29	0.29
(7)	0.17	0.31
(8)	0.15	0.36
(9)	0.09	0.48

4.4.2 Constitutive model for CNT bundles and matrix

Covalent bonding within the CNT walls endows them with high axial strength and stiffness. In contrast, the bonds between adjacent CNT tubes are comparatively weak, and hence the longitudinal shear modulus and shear strength of CNT bundles is much below their axial modulus and strength in tension, as described in section 2.2.2 [10, 264, 275]. Upon recognising that CNT bundles are transversely isotropic with respect to their longitudinal axis, labelled as the 11-direction, the CNT bundles are idealised as an anisotropic, homogeneous continuum. Their constitutive relationships are defined as follows.

First, consider the elastic response of CNT bundles. The elastic strain ε^e_{ij} is related to the stress σ_{ij} by:

$$\begin{Bmatrix} \varepsilon^e_{11} \\ \varepsilon^e_{22} \\ \varepsilon^e_{33} \\ \gamma^e_{23} \\ \gamma^e_{13} \\ \gamma^e_{12} \end{Bmatrix} = \begin{bmatrix} \frac{1}{E^B_{11}} & -\frac{\nu_{21}}{E^B_{22}} & -\frac{\nu_{31}}{E^B_{33}} & 0 & 0 & 0 \\ -\frac{\nu_{12}}{E^B_{11}} & \frac{1}{E^B_{22}} & -\frac{\nu_{32}}{E^B_{33}} & 0 & 0 & 0 \\ -\frac{\nu_{13}}{E^B_{11}} & -\frac{\nu_{23}}{E^B_{22}} & \frac{1}{E^B_{33}} & 0 & 0 & 0 \\ 0 & 0 & 0 & \frac{1}{G^B_{23}} & 0 & 0 \\ 0 & 0 & 0 & 0 & \frac{1}{G^B_{13}} & 0 \\ 0 & 0 & 0 & 0 & 0 & \frac{1}{G^B_{12}} \end{bmatrix} \begin{Bmatrix} \sigma^e_{11} \\ \sigma^e_{22} \\ \sigma^e_{33} \\ \tau^e_{23} \\ \tau^e_{13} \\ \tau^e_{12} \end{Bmatrix} \tag{4.2}$$

The modulus of CNT walls measured in axial tension, and based upon an assumed interlayer spacing of 0.34 nm, is taken to be 1 TPa [10, 237, 448]. The axial bundle modulus E^B_{11} is estimated by assuming all CNT walls within the bundle cross-section are subjected to a uniform tensile strain: The longitudinal CNT bundle modulus E^B_{11} is related to the wall modulus E_w and wall density ρ_w by $E^B_{11} = E_w(\rho_B/\rho_w)$ [261]. Substitution of the measured values of measured bundle density ρ_B and wall density $\rho_w = 2300$ kg/m^3 implies that $E^B_{11} = 680$ GPa. Suggested values within the literature for the transverse Young's modulus $E^B_{22} = E^B_{33}$ of single-walled CNT bundles range from 17 GPa to 63 GPa [272–274]. Here, it is assumed that $E^B_{22} = E^B_{33} = 50$ GPa, and the Poisson ratio is $\nu_{12} = \nu_{13} = 0.3$. The low values of bundle shear moduli G^B_{12}, G^B_{13} and G^B_{23} all result from the weak interfacial bonding between CNTs; for the purposes of analysis, they are all taken to be equal. By calibration of the predicted macroscopic stiffness of the CNT honeycomb with the measured modulus of the dry unreinforced CNT mat upon unloading, it was deduced in section 3.4 that $G^B_{12} = 9.5$ GPa, and this value is used again herein.

Now consider the anisotropic strength and post-yield behaviour of a CNT bundle. Hill's anisotropic yield criterion [449] is used here to represent the post-yield behaviour of the CNT bundles. The total strain rate $\dot{\varepsilon}_{ij}$ is the sum of the elastic strain rate $\dot{\varepsilon}^e_{ij}$ and plastic strain rate $\dot{\varepsilon}^p_{ij}$,

$$\dot{\varepsilon}_{ij} = \dot{\varepsilon}^e_{ij} + \dot{\varepsilon}^p_{ij}. \tag{4.3}$$

The plastic strain rate is defined by the associated flow rule,

$$\dot{\varepsilon}^p_{ij} = \dot{\lambda}\frac{\partial \Phi}{\partial \sigma_{ij}}, \tag{4.4}$$

in terms of a plastic multiplier $\dot{\lambda}$ and the Hill potential Φ, as defined by:

$$2\Phi = F(\sigma_{22}-\sigma_{33})^2 + G(\sigma_{33}-\sigma_{11})^2 + H(\sigma_{11}-\sigma_{22})^2 + 2L\tau_{23}^2 + 2M\tau_{31}^2 + 2N\tau_{12}^2. \tag{4.5}$$

The constants F, G and H are directly related to the tensile yield strength of the CNT bundle in uniaxial tension, σ^B_{11}, σ^B_{22} and σ^B_{33}, such that

$$G+H = \frac{1}{\left(\sigma^B_{11}\right)^2};\ F+H = \frac{1}{\left(\sigma^B_{22}\right)^2};\ G+F = \frac{1}{\left(\sigma^B_{33}\right)^2}. \tag{4.6}$$

The constants L, M and N follows from the shear yield strengths, where

$$L = \frac{1}{2\left(\tau^B_{23}\right)^2};\ M = \frac{1}{2\left(\tau^B_{31}\right)^2};\ N = \frac{1}{2\left(\tau^B_{12}\right)^2}. \tag{4.7}$$

Experiments on individual CNT bundles from direct-spun fibres reveal that the tensile wall fracture strength σ_w lies between 5.5 GPa and 25 GPa [267]. Here, the bundle axial strength is estimated by assuming that it, like the axial bundle modulus, scales with the CNT wall strength and bundle density, according to $\sigma^B_{11} = \sigma_w(\rho_B/\rho_w)$. Upon taking $\sigma_w = 5.5$ GPa [267], the axial bundle fracture strength is estimated to be 3.7 GPa. The longitudinal and transverse shear yield strengths τ^B_{12}, τ^B_{13} and τ^B_{23}, and the remaining transverse normal yield strengths σ^B_{22} and σ^B_{33}, are set to equal τ^B_y, which is calibrated to the macroscopic CNT mat yield strength measured in tensile testing. A hardening modulus of value $10^{-4}E^B_{11}$ for all stress components was employed post-yield to ensure converged results. The epoxy matrix is treated as an isotropic elastic, perfectly plastic solid that satisfies J_2 flow theory. A summary of all material properties used in the finite element simulations is provided in Table 4.3.

Table 4.3 Material constants used in the finite element analysis.

Material	Material Constants
CNT Bundle	$E_{11}^B = 680$ GPa, $E_{22}^B = E_{33}^B = 50$ GPa
	$G_{12}^B = G_{23}^B = {}_{13}^B = 9.5$ GPa
	$\nu_{12} = \nu_{13} = 0.3$
	$\sigma_{11}^B = 3700$ MPa
	$\sigma_{22} = \sigma_{33} = \tau_y^B = 80$ MPa (CNT bundle absent epoxy)
	$\sigma_{22} = \sigma_{33} = \tau_y^B = 250$ MPa (epoxy-coated CNT bundle)
	$\tau_{12}^B = \tau_{23}^B = \tau_{13}^B = \tau_y^B$
Epoxy	$E^E = 3.0$ GPa
	$\nu_E = 0.3$
	$\sigma_y^E = 60$ MPa

4.4.3 Calibration of the unit cell model

The honeycomb model was calibrated via the following steps.

Step (I): The elastic response of the dry honeycomb (absent epoxy) was determined for uniaxial loading in the x_1 and x_2 directions, in order to obtain E_{11}/E_{22} for $30^\circ \leq \omega \leq 50^\circ$. The sensitivity of E_{11}/E_{22} to the initial value of ω is shown in Figure 4.9a, and the measured ratio $E_{11}/E_{22} = 6.4$ implies that $\omega = 45^\circ$.

Step (II): The uniaxial yield strength of the honeycomb unit cell was predicted for compositions (1) and (9), again for loading in the x_1 and x_2 directions. The initial inclination of the unit cell wall ω was set to be 45° for all simulations, but the bundle shear strength τ_y^B was varied. By matching the predicted macroscopic yield strength σ_{11}^y to the measured value of the CNT dry mat (1), the value of CNT bundle shear strength was deduced to equal $\tau_y^B = 80$ MPa. Likewise, by matching the predicted value of σ_{11}^y to the measured value for the CNT-epoxy composite (9) a value of CNT bundle shear yield strength $\tau_y^B = 250$ MPa was determined.

4.4.4 Prediction of the calibrated model

It remains to compare the predictions of the honeycomb model with the measured uniaxial response of the CNT-epoxy composites. The measured and predicted stress-strain responses

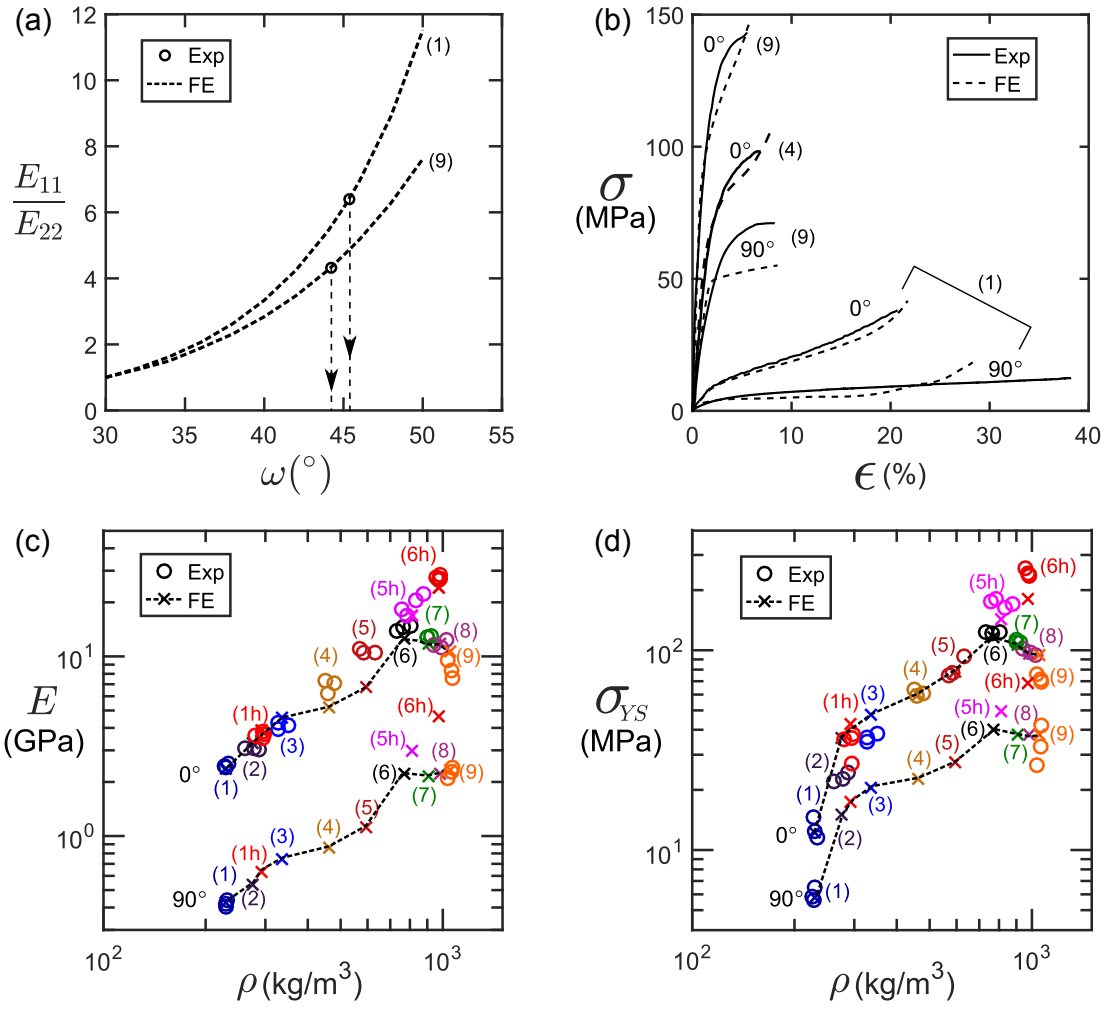

Fig. 4.9 (a) The ratios of the predicted in-plane Young's moduli in principal and transverse directions are plotted as a function of ω in (a), alongside the experimentally measured values. Measured and predicted uniaxial stress-strain responses are plotted in (b), and the Young's modulus and yield strength of manufactured CNT mat and composites in the principal material direction are compared with the unit cell predictions in (c) and (d) respectively.

for tensile loading in the x_1 and x_2 directions are shown in Figure 4.9b for dry CNT mat (1) with $f_e = 0$, CNT-epoxy composite (4) with $f_e = 0.14$, and CNT-epoxy composite (9) with $f_e = 0.79$. Adequate agreement is evident including the degree of anisotropy in yield behaviour. It is emphasised that the approach is an approximation for the detailed geometry of the network and so precise quantitative agreement is not to be expected.

Now the finite element predictions for the modulus and yield strength in the principal material direction are compared against experiment over the range of manufactured mat and

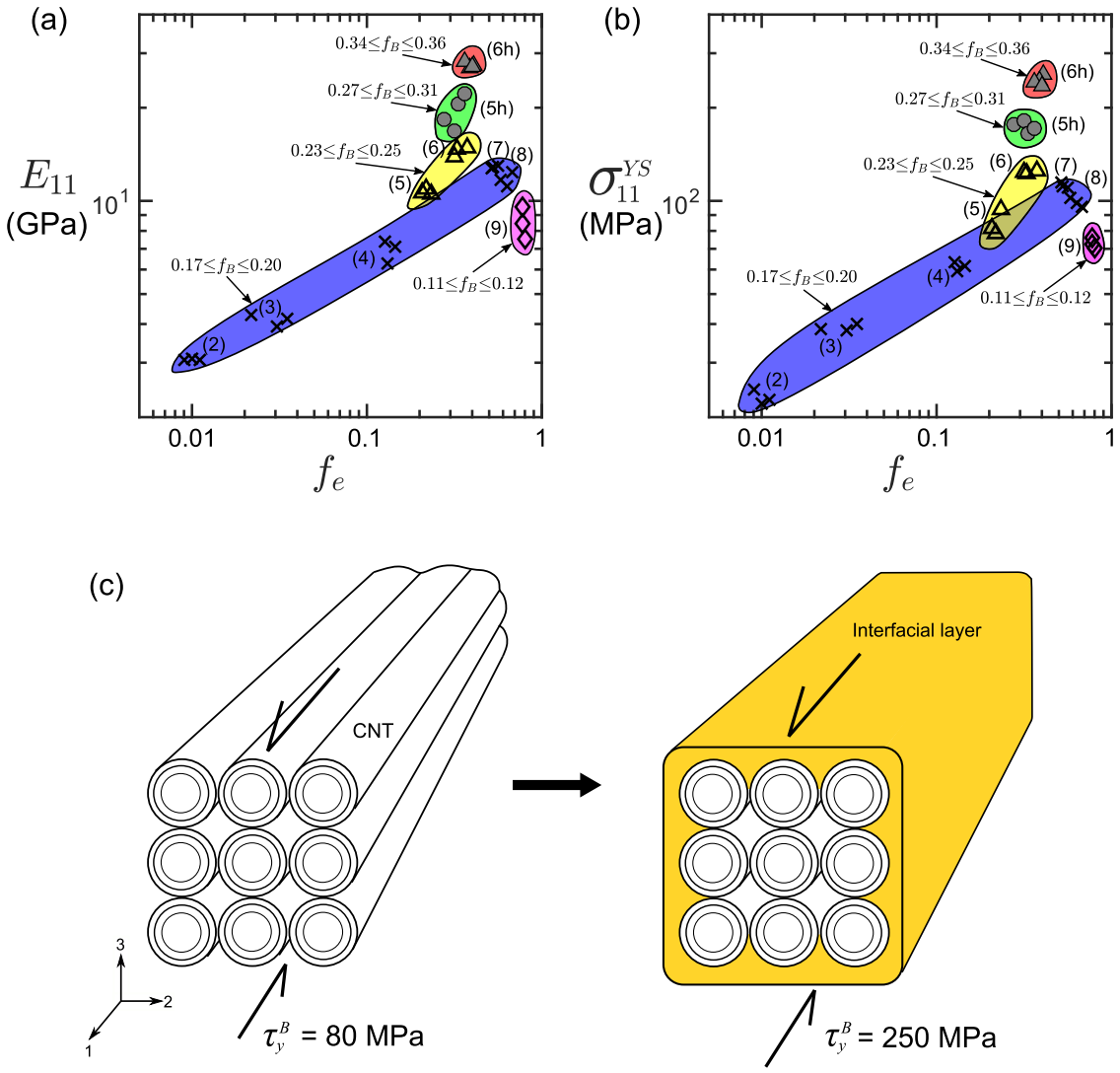

Fig. 4.10 The measured Young's modulus (a) and yield strength (b) for CNT-epoxy composites, as a function of epoxy and carbon nanotube bundle volume fractions. (c) CNT bundles are coated with an interfacial layer of epoxy with enhanced yield strength after epoxy infiltration and cure.

composite compositions. The predictions and experimental measurements of Young's modulus and yield strength are plotted against bulk density in Figure 4.9c and 4.9d respectively. In broad terms, the predictions of macroscopic modulus and yield strength from the unit cell model capture the trend in the experiments over the compositional range, although some scatter is present in the experimental data.

The measured Young's modulus E_{11} and yield strength σ_{11}^{YS} of the CNT-epoxy composites are plotted against epoxy volume fraction f_e in Figure 4.10a and 4.10b respectively. For composites with $0.17 \leq f_B \leq 0.2$, both E_{11} and σ_{11}^{YS} increase by a factor of about 5 with increasing epoxy content. The presence of epoxy within the pores of the CNT bundle network restricts the foam-like deformation observed for CNT mats absent epoxy, and so enhances their Young's modulus and strength. For the range of epoxy content $0.3 \leq f_e \leq 0.4$, it is also clear that an increase in CNT bundle volume fraction from 0.25 to 0.35 increases E_{11} and σ_{11}^{YS}.

The unit cell model suggests a significant increase in the longitudinal shear strength of the CNT bundles τ_y^B from 80 MPa to 250 MPa upon the coating of CNT bundles with epoxy, and the source of this increase in bundle shear strength is now discussed. As surmised in section 2.3.2, the epoxy bonds strongly to the surfaces of the CNT bundles [348, 450], and forms a layer of enhanced strength, as sketched in Figure 4.10c. It is known from fractography [74] that this layer of epoxy has a yield strength much above that of the epoxy matrix which fills the voids within the bundle network: Images of the fracture surface of direct-spun CNT mat-epoxy composites reveal that CNT bundles protruding from the fracture surface are coated with this epoxy sheath. Pull-out tests upon individual CNTs embedded in epoxy reveal that the strength of the epoxy layer which coats the CNTs can be over 350 MPa [378, 373], even reaching 630 MPa [371]. The epoxy adheres adjacent CNTs within the outer layer of the bundle, and thereby increases the bundle longitudinal shear strength. Note that this effect is represented in the 2D unit cell idealisation by increasing the shear strength of the CNT bundles τ_y^B.

4.5 Concluding discussion

Composites were manufactured by infiltration of direct-spun CNT mats with solutions of epoxy and acetone. Following curing, the composition of the manufactured composites varied widely; the volume fraction of CNT bundles varied between 0.11 and 0.35, the volume fraction of epoxy from 0.01 to 0.79, and the porosity ranged from 0.10 to 0.82. The epoxy content in the cured composite increased with the concentration of epoxy in the infiltration solution; the application of a pressure $P = 10$ MPa in the through-thickness direction after infiltration was used to attain higher CNT volume fractions. The epoxy matrix does not penetrate the CNT bundles, but progressively fills the pores between the CNT bundles as the epoxy volume fraction increases.

The Young's modulus, yield strength and ultimate strength of the CNT mat-epoxy composites are significantly above those of the dry CNT mat or cured epoxy. By suitable choice of composition, composites exhibit an ultimate strength of 410 MPa and modulus of almost 30 GPa. Both values represent an increase in over an order of magnitude compared to the properties of the as-received CNT mat. The measured electrical conductivity of the mats and composites scales linearly with CNT volume fraction and is insensitive to the epoxy content.

The CNT-epoxy composite is idealised as a periodic honeycomb network in finite element simulations. The model is able to describe the degree of elastic and plastic anisotropy of the composite and the dependence of modulus and yield strength upon composition. By suitable correlation of the predicted and measured yield strengths of the composite, the inferred shear strength of a bundle is found to rise from 80 MPa in the absence of epoxy to 250 MPa when epoxy is present. These values are consistent with effects and values reported in the literature. It is deduced from comparison of measured composite properties against composition, and via simulation, that the properties of the composite are sensitive to the coating of CNT bundles with an interfacial layer of high strength epoxy, the epoxy volume fraction within the pores, and the CNT bundle volume fraction.

Chapter 5

Effects of immersion and drawing in solvents and superacids upon the mechanical and electrical properties of direct-spun carbon nanotube mats

5.1 Summary

The mechanical and electrical behaviour of a direct-spun carbon nanotube mat is investigated upon fluid immersion. Infiltration of the mat by acetone, ethanol, toluene, N-methyl-2-pyrrolidone or chloroform reduces the yield and failure strength from that measured in dry air by up to 70%, but the ductility and qualitative shape of the stress-strain response remain unchanged. In contrast, immersion in chlorosulfonic acid reduces tensile strength by almost 2 orders of magnitude, decreases the initial modulus by 3 orders of magnitude, and increases ductility by up to a factor of 7. A drawing process is then devised where direct-spun mats are immersed in chlorosulfonic acid and then drawn in chloroform or a weak solution of chloroform and chlorosulfonic acid to a chosen nominal stress. The infiltrated fluids are then removed, and the sample dried. The properties of the drawn mats are investigated as a function of the content of chlorosulfonic acid in the drawing solution, and the tensile stress applied during drawing. By drawing in this manner, the modulus of the direct-spun CNT mat can be increased by almost 2 orders of magnitude, and the tensile strength by over a factor of 7. The tensile strength, modulus and electrical conductivity of these drawn direct-spun mats are much above with those of samples drawn in air or whilst immersed in chloroform.

Elastic calculations are performed to predict the contact area between adjacent CNTs within bundles upon the infiltration of organic solvents. The predicted contact area scales linearly with the measured macroscopic yield strength of the CNT mat, suggesting that the predicted reduction in contact area between neighbouring CNTs is sufficient to explain the observed softening in the uniaxial stress-strain response. In contrast, the significant increase in ductility upon the infiltration of chlorosulfonic acid is attributed to the separation of CNTs within their bundles due to double layer repulsion. This effect is investigated with experimental measurements, predictions from the Gouy-Chapman theory, and other findings reported in the literature.

5.2 Properties and microstructure of direct-spun CNT mat

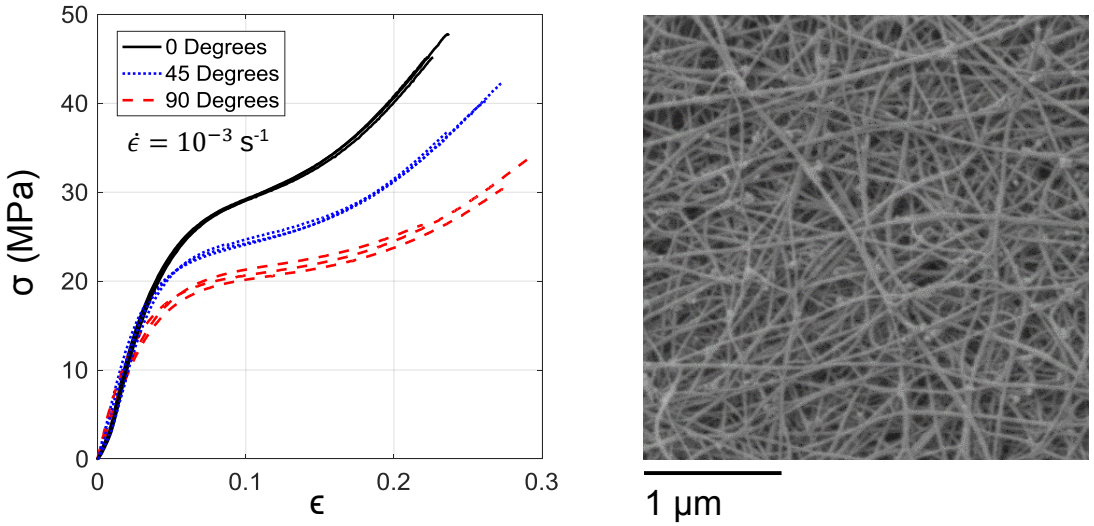

(a) (b)

Fig. 5.1 (a) The in-plane uniaxial stress-strain response measured at 0°, 90° and 45° from the principal material direction, and (b) SEM image of the direct-spun CNT mat microstructure.

Direct-spun CNT mats obtained from Tortech Nanofibers Ltd.[1] were of nominal thickness 55 μm as confirmed by micrometre measurements and X-ray computed tomography scanning. Before characterising physical, mechanical or electrical properties, samples cut from the mat were soaked in acetone for 1 minute, dried in air at room temperature for 15 minutes, and then heated in an oven at 70 °C for 1 hour to remove any residual solvent residue. The measured density of the direct-spun CNT mat was 240 kg/m^3.

[1]Tortech Nano Fibers Ltd, Hanassi Herzog St., Koren Industrial Park, Ma'alot Tarshiha, 24952, Israel.

The in-plane stress-strain response of the dry CNT mat in air was measured by conducting uniaxial tensile tests with a screw-driven tensile test machine at strain rate $\dot{\varepsilon} = 10^{-3}$ s^{-1}, for samples cut at 0°, 45° and 90° to the principal material direction. The test setup is as described earlier in Figure 3.1a . The strain state was measured in the central portion of the sample gauge length by recording the position of dots of white paint applied to the sample with a digital camera and image processing software. The electrical resistance of the direct-spun mat was measured using a four-point probe method as illustrated earlier in Figure 3.2a, and the mat microstructure was imaged with a scanning electron microscope[2].

The uniaxial in-plane stress-strain response of the as-received direct-spun CNT mat in air is plotted in Figure 5.1a for samples oriented at 0°, 45° and 90° to the direction of drawing from the CVD reactor. The nominal stress σ and nominal strain ε are based upon the original sample area and length respectively. The initial linear response is followed by a yielding-type behaviour at approximately 5% nominal strain. The rate of hardening increases with increasing strain until failure occurs at a nominal strain between 0.2 and 0.3. The Young's modulus as determined from the initial linear portion of the stress-strain curve is approximately equal to 0.5 GPa for all orientations.

The in-plane electrical conductivity was 46 kS/m, 43 kS/m and 40 kS/m for samples oriented at 0°, 45° and 90° to the principal material direction respectively. An image of the mat microstructure is shown in Figure 5.1b, revealing the interconnected network of CNT bundles. The bundles form junctions with one another at crossing points, and where CNTs transfer from one bundle into another.

[2]Zeiss Evo LS15 Scanning Electron Microscope, ZEISS House Building 1030, Cambourne Business Park, Cambourne, Cambridge CB23 6DW.

5.3 Mechanical and electrical properties of CNT mats in fluids

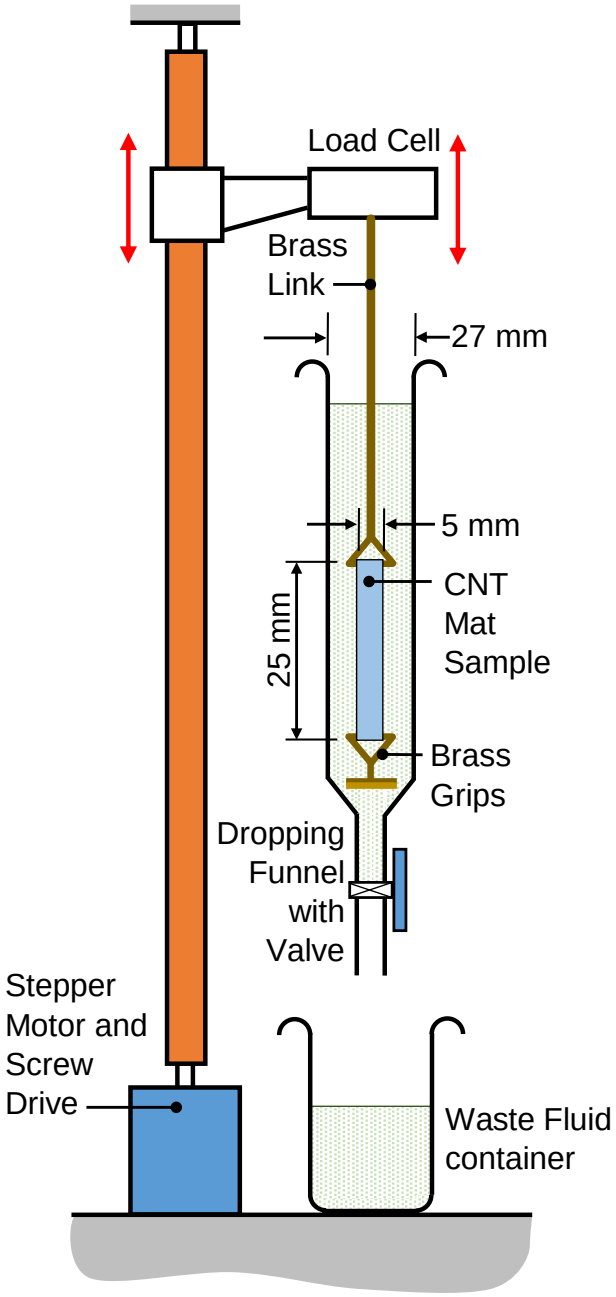

Fig. 5.2 Custom-built screw-driven tensile test machine used for measuring the mechanical properties of direct-spun CNT mats upon fluid immersion.

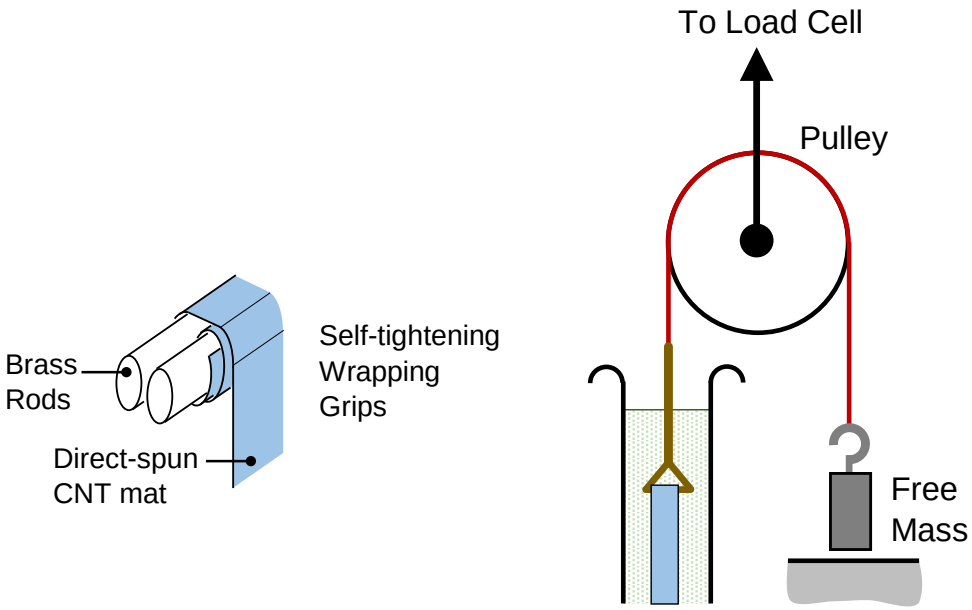

(a) (b)

Fig. 5.3 (a) Detail of the self-tightening wrapping grips used for tensile testing of immersed CNT mat samples, (b) application of dead-loads to investigate the creep response.

Consider the effect of fluid immersion upon the mechanical properties of direct-spun CNT mats. Tensile tests on samples of direct-spun mat immersed in fluids were performed with a custom-built screw-driven tensile test machine, as illustrated in Figure 5.2. Self-tightening wrapping grips were used to apply load to the sample whilst it was immersed in an open-ended dropping funnel filled with fluid, see Figure 5.3a. The grips and apparatus were manufactured from brass as it limits attack by chlorosulfonic acid. As described previously, the strain state in the centre portion of the sample gauge length was measured by recording the position of dots of white paint applied to the sample before immersion, with a digital camera and image processing software.

Samples were immersed in ethanol, toluene, NMP and chloroform for 3 hours with no stress applied, before their tensile stress-strain response was measured whilst immersed at a strain rate of $\dot{\varepsilon} = 10^{-3}$ s^{-1}. Similarly, samples were immersed in acetone for 3 hours and in chlorosulfonic acid for 5 minutes before their stress-strain response was measured for strain rates $\dot{\varepsilon} = 10^{-4}$ s^{-1} to $\dot{\varepsilon} = 10^{-1}$ s^{-1}. Additionally, direct-spun CNT mat samples were immersed in chlorosulfonic acid for 5 minutes, before the chlorosulfonic acid was drained from the dropping funnel and replaced with chloroform. The chloroform was then drained

after 1 minute and replaced with a solution a solution of chloroform and chlorosulfonic acid, of acid volume fraction f_{CSA}, and a uniaxial tensile test was conducted with the sample immersed in this solution, at a strain rate of $\dot{\epsilon} = 10^{-3}$ s^{-1}. The volume fraction f_{CSA} of chlorosulfonic acid was varied to establish its effect upon the stress-strain response.

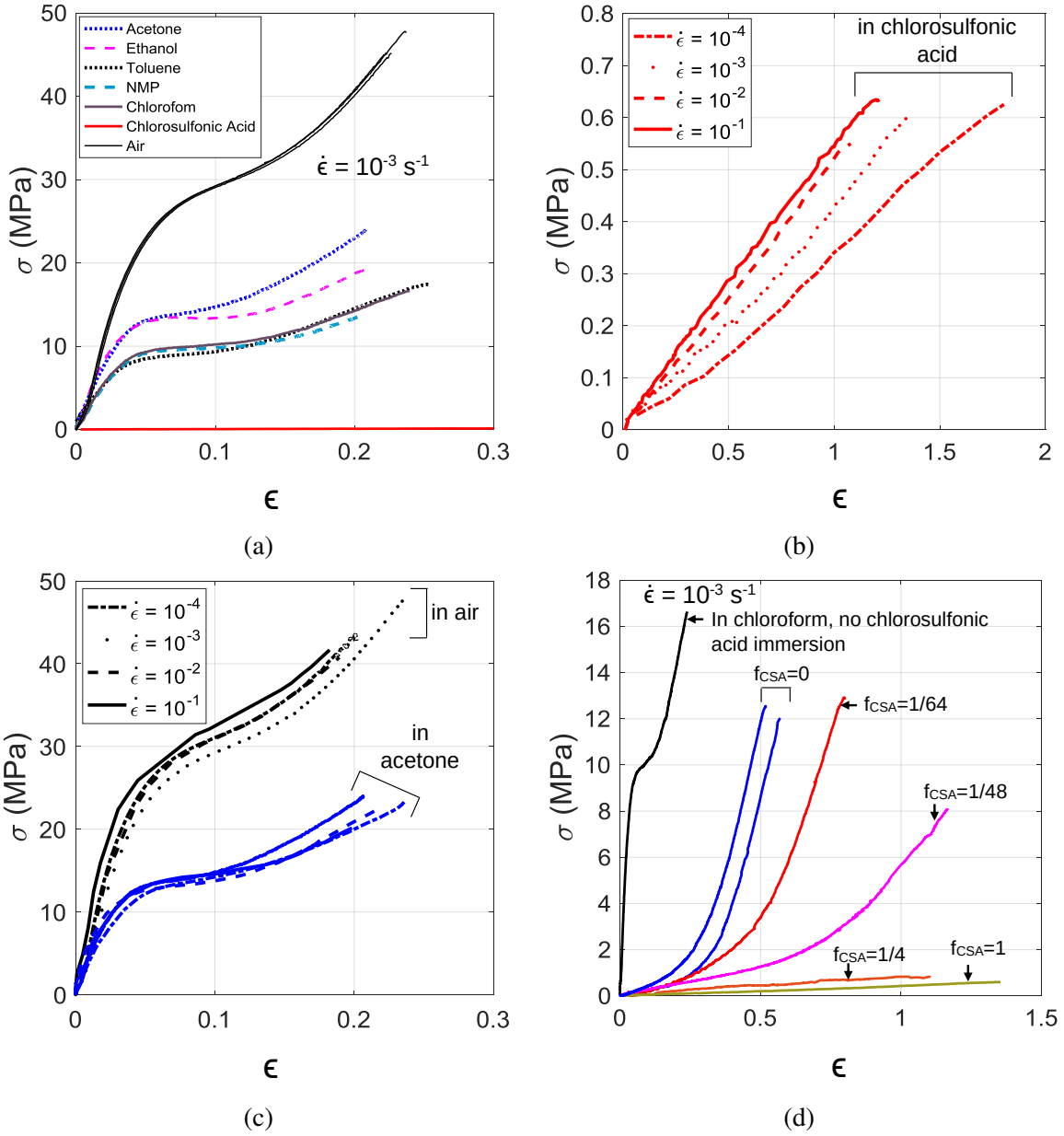

Fig. 5.4 (a) Stress-strain response of direct-spun mat whilst immersed in solvents at a strain rate $\dot{\epsilon} = 10^{-3}$ s^{-1}. Stress-strain response at strain rates from $\dot{\epsilon} = 10^{-4}$ s^{-1} to $\dot{\epsilon} = 10^{-1}$ s^{-1} (b) in chlorosulfonic acid and (c) in air and acetone. (d) Stress-strain response in solutions of chlorosulfonic acid and chloroform of varying composition after immersion in chlorosulfonic acid.

The tensile stress-strain response measured in the fully immersed state in a selection of solvents and chlorosulfonic acid is compared with that measured in dry air in Figure 5.4a, for samples aligned with the principal material direction, at strain rate $\dot{\varepsilon} = 10^{-3}$ s^{-1}. Immersion in the solvents acetone, ethanol, toluene, NMP and chloroform softens the mat: The tensile strength is reduced by up to 70% compared with that in dry air, but the shape of the stress-strain response remains qualitatively similar, as does the sample ductility. Additional softening is evident upon immersion in NMP, chloroform and toluene compared to that in acetone and ethanol. For acetone, a decrease in the immersion time before tensile testing from 3 hours to 5 seconds had no noticeable effect upon the stress versus strain response.

The measured stress-strain response upon immersion in chlorosulfonic acid is shown in Figure 5.4b. Immersion in chlorosulfonic acid leads to an increase in ductility (to 1.3 for $\dot{\varepsilon} = 10^{-3}$ s^{-1}), and the ultimate tensile strength is reduced by almost two orders of magnitude, to about 0.6 MPa. The nominal stress-strain response measured whilst immersed in chlorosulfonic acid is relatively linear up to the point of failure. For samples immersed in chlorosufonic acid, the ductility increases with decreasing strain rate, reaching a value of 1.8 for $\dot{\varepsilon} = 10^{-4}$ s^{-1}.

The tensile stress-strain response of direct-spun mat samples measured in dry air and whilst immersed in acetone is plotted in Figure 5.4c for strain rates in the range $\dot{\varepsilon} = 10^{-4}$ s^{-1} to $\dot{\varepsilon} = 0.1$ s^{-1}. Within this range of strain rates, the stress versus strain response in dry air and in acetone are largely unaltered.

Now consider the uniaxial stress-strain response of samples immersed in chlorosulfonic acid for 5 minutes, then chloroform for 1 minute, before immersion and tensile testing in a solution of chloroform and chlorosulfonic acid. The stress-strain response of these samples is recorded in Figure 5.4d, and compared with the stress-strain response of a sample immersed in chloroform alone. The stress-strain response of the sample drawn in chloroform ($f_{CSA} = 0$) after immersion in chlorosulfonic acid differs considerably from that the sample immersed in chloroform: initially of low modulus of approximately 4 MPa, the stress-strain response hardens considerably at strains above 0.4. As the chlorosulfonic acid content f_{CSA} is increased, the sample ductility initially rises, before the tensile strength drops dramatically, and the stress-strain behaviour approaches that of the direct-spun CNT mat tested whilst immersed in chlorosulfonic acid ($f_{CSA} = 1$).

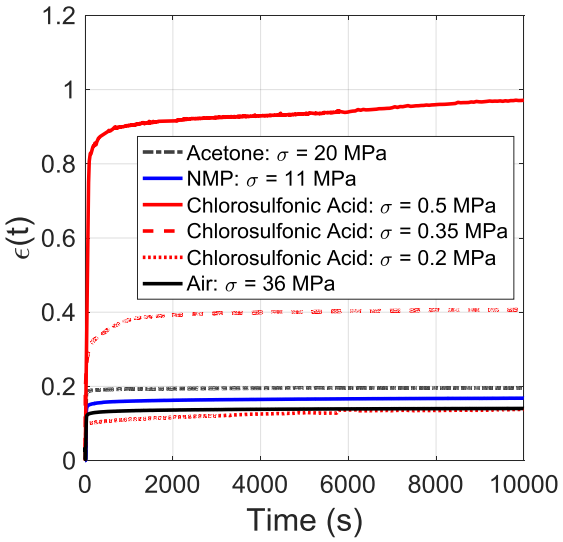

Fig. 5.5 Creep response of direct-spun CNT mats whilst immersed in different fluids.

The creep response was also investigated by applying dead loads to immersed samples of direct-spun mat via a mass and pulley system, see Figure 5.3b. Samples of direct-spun mat were immersed in acetone and NMP for 3 hours, and in chlorosulfonic acid for 5 minutes before the creep response $\varepsilon(t)$ was measured upon application of the dead load; the creep response in air was also recorded for comparison. The creep strain $\varepsilon(t)$ is plotted in Figure 5.5. Negligible creep occurs in dry air, or whilst immersed in acetone or chloroform. In contrast, immersion in chlorosulfonic acid leads to a creep response with comparatively lower dead loads.

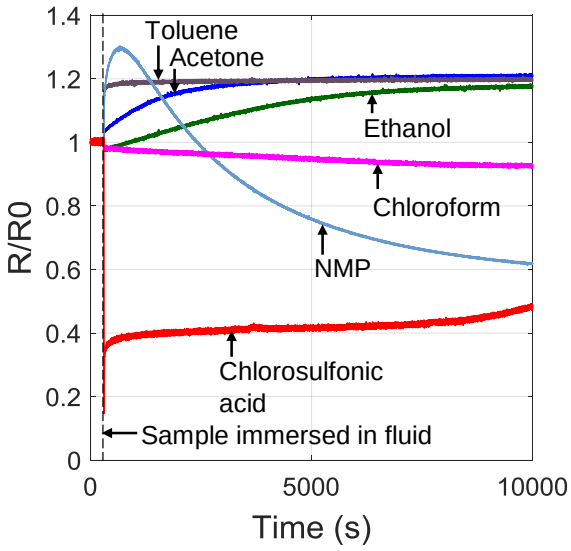

Fig. 5.6 Change in direct-spun mat electrical resistance upon fluid immersion.

Now consider the effect of fluid immersion upon the electrical resistance of the direct-spun mat. Samples cut in line with the principal material direction were affixed to a glass slide, whilst their resistance was recorded continuously at a frequency of 10 Hz with the 4-point probe method of Figure 3.2a using a test current of 10 mA. The sample was then immersed in acetone, ethanol, toluene, chloroform, NMP or chlorosulfonic acid, and the electrical resistance recorded. The sample resistance is plotted against time in Figure 5.6, with the resistance R normalised by the value recorded in dry air prior to fluid immersion, $R0$. The resistance of samples immersed in acetone, ethanol and toluene all rise upon immersion, approaching $R/R0 \approx 1.2$. In contrast, the resistance upon immersion in NMP rises then falls, and upon immersion in chloroform, the resistance falls with increasing time. In chlorofulsonic acid, the sample resistance drops to approximately 40% of its value in dry air upon immersion, before rising towards the end of the test; the almost immediate resistance change upon immersion is indicative of a fast reaction, which achieves equilibrium swiftly.

5.4 Effect of tensile drawing of direct-spun mats upon properties

Consider the effect of tensile drawing upon subsequent mechanical and electrical properties. The aim of the following experiments is to investigate if drawing in fluids can improve the properties of direct-spun mats, and how the properties of mats drawn whilst immersed in solutions of chlorosulfonic acid and chloroform compare to those drawn in air or organic solvents.

5.4.1 Drawing processes

Drawing was conducted using the experimental apparatus illustrated in Figure 5.2, with samples of direct-spun mat of width 5 mm, gauge length 25 mm, and thickness 55 µm. The samples were cut and drawn in line with the principal material direction. The following drawing processes were investigated:

Drawing in air

Samples of direct-spun mat were drawn in air at a strain rate of $\dot{\varepsilon} = 10^{-3}$ s^{-1} to 80% of their measured tensile strength in air. The load was then removed, and the samples were removed from the grips. They were immersed in acetone for 1 minute, dried in air at room temperature for 15 minutes, and then in an oven at 70°C for 1 hour to remove any residual acetone.

Dawing in chloroform

Samples of direct-spun mat were immersed in chloroform for 3 hours, then drawn whilst immersed at a strain rate $\dot{\varepsilon} = 10^{-3}$ s^{-1} to 80% of their measured tensile strength in chloroform. The samples were then dried in air at room temperature for 15 minutes, whilst the maximum tension used in drawing was maintained by application of a dead load, and then in an oven at 70°C for 1 hour. The load was then removed, and the samples were removed from the grips. They were immersed in acetone for 1 minute, dried in air at room temperature for 15 minutes, and then in an oven at 70°C for 1 hour to remove any residual acetone.

Immersion in chlorosulfonic acid and drawing in chlorosulfonic acid and chloroform

One of three routes was used to draw samples using solutions of chlorosulfonic acid and chloroform, referred to as routes (A), (B) or (C). In all routes, samples of direct-spun mat were first immersed in chlorosulfonic acid for 5 minutes. The chlorosulfonic acid was then drained from the dropping funnel and replaced with chloroform for one minute, which was then drained from the funnel. The samples were then immersed in a fluid, and drawn at a strain rate of $\dot{\varepsilon} = 10^{-3}$ s^{-1}, as follows:

Route A: the sample was immersed in chloroform, and drawn until a nominal stress of 10 MPa was reached.

Route B: The sample was immersed in a solution of chloroform and chlorosulfonic acid, of chlorosulfonic acid content $f_{CSA} = 1/64$ by volume, and drawn until a nominal stress of 10 MPa was reached.

Route C: The sample was immersed in a solution of chloroform and chlorosulfonic acid, of chlorosulfonic acid content $f_{CSA} = 1/64$ by volume, and drawn until a nominal stress of 5 MPa was reached.

When the nominal stress or either 5 MPa or 10 MPa was reached, it was held constant by application of a dead load whilst the fluid used in drawing was drained from the dropping funnel, and the samples immersed in chloroform for 20 minutes, acetone for 20 minutes, and distilled water for 1 hour, drained and replaced every 20 minutes. After confirming that the pH of the water had returned to neutral after one hour, the dead load was maintained whilst the samples were dried in an oven at 70°C for 1 hour, then at 115°C for a further hour. The dead load was then removed, and the samples were removed from the grips. They were

immersed in acetone for 1 minute, dried in air at room temperature for 15 minutes, and then in an oven at 70°C for 1 hour to remove any residual acetone.

To investigate the effect of immersion in the fluids used the above drawing processes, and subsequent fluid removal and heating upon the properties of the mat, an additional route was defined, named route (D), in which samples were immersed in the same fluids used in route (B) for the same durations, absent applied load or strain. The samples were then dried in the oven at identical temperature to routes (A), (B) or (C) but absent any load. They were then immersed in acetone for 1 minute, dried in air at room temperature for 15 minutes, and then in an oven at 70°C for 1 hour to remove any residual acetone.

5.4.2 Properties of drawn direct-spun mats

Now the effects of the above drawing processes on the mechanical and electrical properties of the direct-spun mat are reported. Tensile tests were used to establish the stress-strain response of the drawn mat samples. The cross sectional area of the drawn samples varied depending on the processing route, and was measured by X-ray computed tomography scanning before tensile testing. The central gauge section of the sample was weighed separately after testing so that its density could be determined. As described earlier, the electrical conductivity of the drawn direct-spun mats was established by 4-point probe testing; the length of the central gauge section was reduced to 12 mm for the measurement of shorter samples.

The nominal and specific tensile stress-strain responses of drawn direct-spun CNT mat samples are compared with those of the as-received mats in Figures 5.7a and 5.7b respectively. First consider the tensile stress-strain response of direct-spun mat samples immersed in chlorosulfonic acid, and drawn according to routes (A), (B) and (C). The greatest values of nominal and specific Young's modulus and strength were measured for samples drawn by route (B); their Young's modulus of approximately 55 GPa exceeds that measured for the original direct-spun mat by two orders of magnitude. The measured stress-strain response of the drawn mats is qualitatively different to that of the as-received direct-spun mat—they are elastic brittle, with failure at strains of less than 1%, and their specific Young's modulus is approximately 70% of that measured for commercially available carbon fibres [451]. Samples drawn in either air or chloroform possess values of nominal and specific strength and Young's modulus much above that of the original dry mat, however their stress-strain responses remain much below those of samples drawn after immersion in chlorosulfonic acid by routes (A), (B) and (C).

Now consider the stress-strain response of samples labelled (D), which were immersed in identical fluids to those used in route (B), for the same duration. These samples underwent slight in-plane shrinkage from their dimensions measured before immersion, and their mass increased by approximately 10%. The slack stress-strain response upon initial loading in Figures 5.7a and 5.7b is attributed to the wrinkling observed in the samples, accompanied by increased thickness; otherwise their yield strength and ultimate strength are both close to that of the original direct-spun CNT mat. It is therefore concluded that the tensile drawing whilst immersed in routes (A)-(C) is responsible for the enhancement in tensile strength and modulus, rather than the effects of fluid immersion and removal.

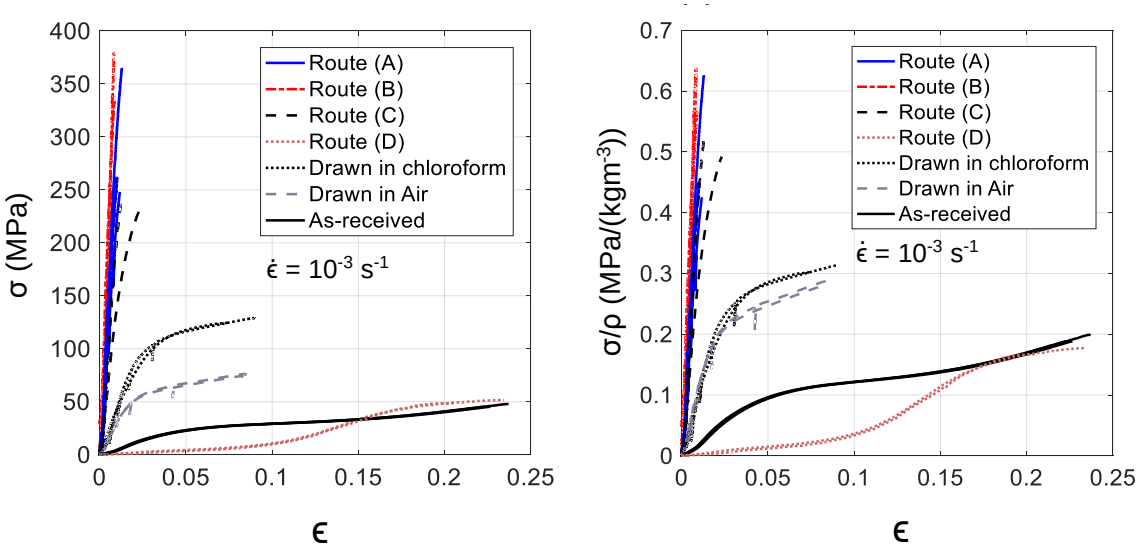

(a) (b)

Fig. 5.7 Nominal (a) and specific (b) stress-strain response of as-received and drawn direct-spun CNT mat samples.

Measurements of nominal and specific electrical conductivity are given in the bar charts of Figures 5.8a and 5.8b respectively. The nominal and specific electrical conductivity of direct spun mat samples were increased by drawing, with the highest values occurring for samples drawn after chlorosulfonic acid immersion according to route (B). Whilst samples processed via route (D) absent stretching possess greater electrical conductivity than that of the dry CNT mat due to doping of the mat by chlorosulfonic acid [121], their nominal and specific electrical conductivity remains far below that of the mat samples drawn according to routes (A), (B) and (C).

Images of the microstructure of the direct-spun CNT mat drawn in chloroform and according to route (B) are presented in Figure 5.9a and 5.9b respectively. The microstructure

of the as received direct-spun mat shown earlier in Figure 5.1b has no dominant bundle orientation, but the microstructures of both drawn samples reveal alignment in the direction of stretch. The mat drawn according to route (B) has a much denser, aligned microstructure of carbon nanotube bundles compared with the sample drawn in chloroform.

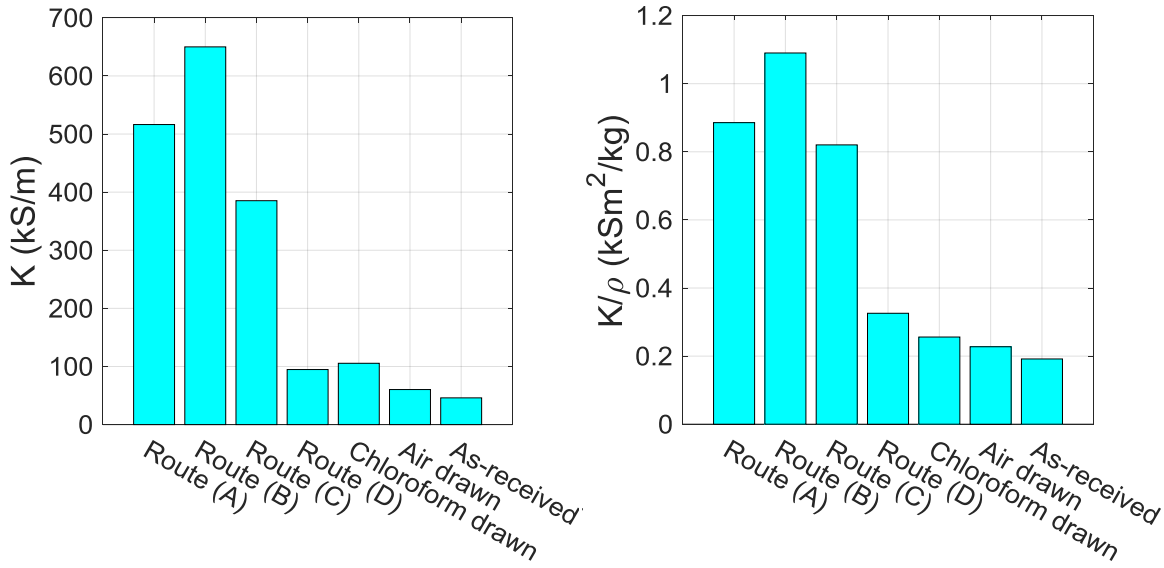

(a) (b)

Fig. 5.8 Nominal (a) and specific (b) electrical conductivity of as-received and drawn direct-spun CNT mat samples.

Now consider the Young's modulus and electrical conductivity of the drawn direct-spun mats as a function of their respective drawing processes. The Young's modulus and specific electrical conductivity of drawn direct-spun mat samples are plotted against the applied strain during drawing, denoted ε_P, in Figures 5.10a and 5.10b respectively. The effect of drawing is to increase the modulus by over two orders of magnitude in the case of mats drawn according to route (B), and in broad terms the Young's modulus increases monotonically with increasing draw strain. Consider the chart of specific electrical conductivity against draw strain, 5.10b. Whilst the immersion and subsequent removal of fluids for samples processed according to route (D) increases the specific electrical conductivity, the effect is minor when compared to the influence of the draw strain for samples drawn according to routes (A), (B) and (C).

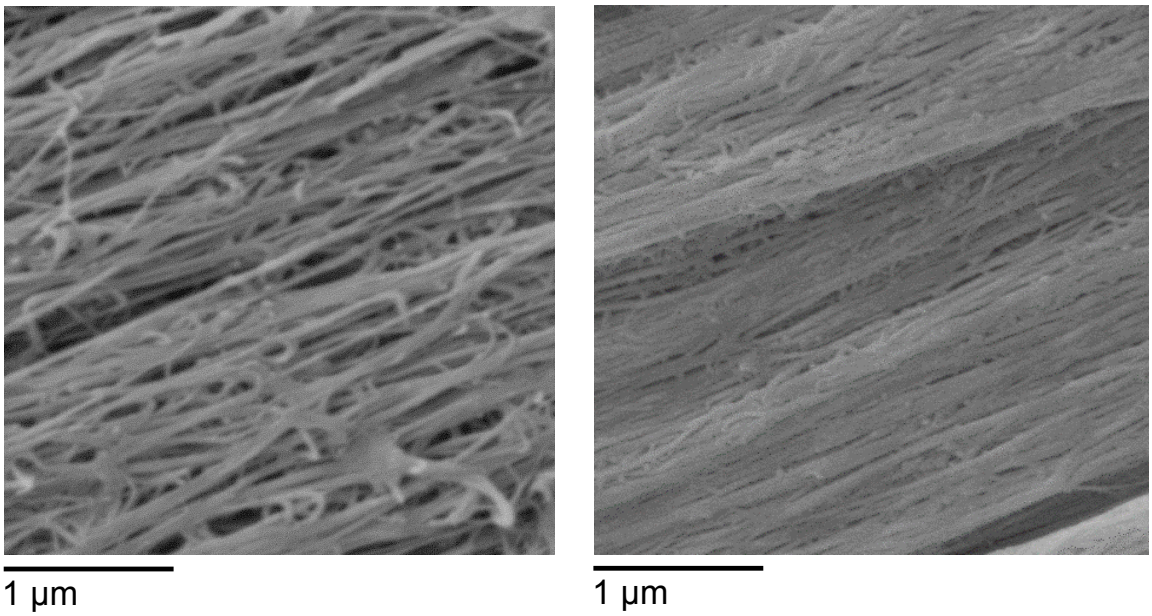

(a) (b)

Fig. 5.9 Microstructure of direct-spun mat samples drawn (a) in chloroform and (b) according to route (B).

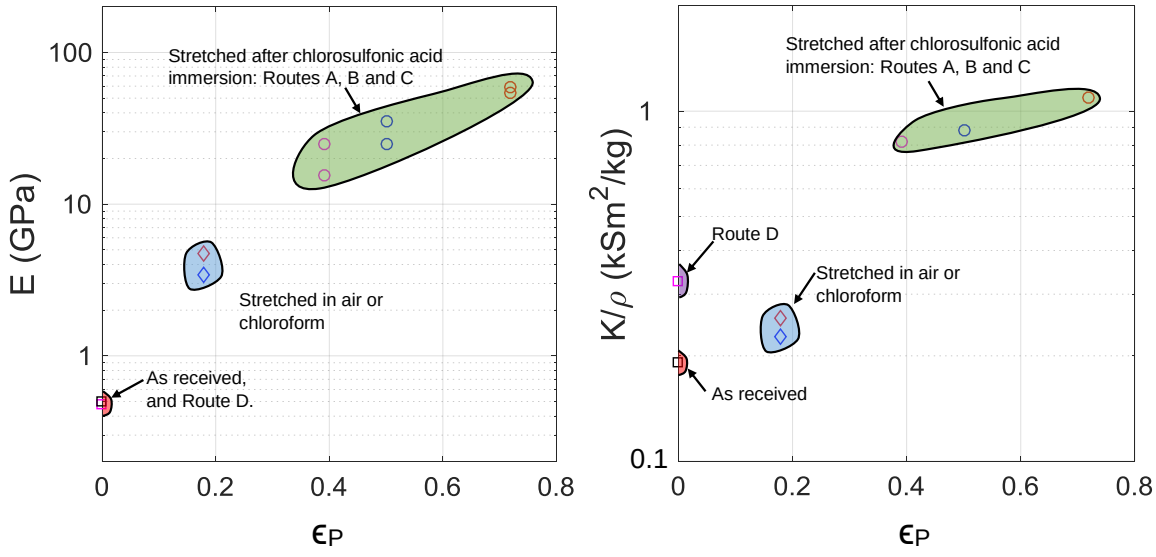

(a) (b)

Fig. 5.10 Effects of processing strain ε_P and drawing fluid upon (a) Young's modulus and (b) specific electrical conductivity for as-received and drawn direct-spun CNT mat samples

5.5 Discussion

The yield strength and Young's modulus of direct-spun mats are both reduced by the infiltration of different fluids: immersion in acetone, ethanol, toluene, NMP and chloroform all give rise to a softened stress-strain response compared to that recorded in air albeit of similar shape, whereas the infiltration of chlorosulfonic acid leads to greatly reduced tensile strength and stiffness, with ductility much above that recorded in air or whilst immersed in the other solvents investigated herein. It remains to discuss the microstructural origin of the change in properties upon immersion in these liquids with regards to the CNT mat microstructure of interconnected CNT bundles.

In-situ microscopy studies of CNTs and CNT bundles have shown that organic solvents of surface energy up to approximately 0.18 J/m^2 [387, 389] readily flow into the pores between CNT in bundles and into the CNTs themselves. It is expected that the presence of fluids within the pores between adjacent CNTs adhered to one another by dispersion forces reduces the energy of adhesion between their walls [291]. When in contact within bundles, the walls of CNTs deform locally, allowing them to form areas of contact [263]. It is through these contacts that forces are transferred between them [279]. Numerous studies (for instance [254, 262, 263]) have elucidated that this area of contact is sensitive to the CNT diameter, number of walls, and surface energy between them; predictions of the contact area from atomistic and continuum theory agree well with experimental measurements [254, 262, 452]. It remains to determine how this contact area will be affected by the infiltration of fluids for the mat studied herein.

Previously in section 3.4, a model was proposed for the modulus and flow strength of direct-spun mats, based upon a honeycomb unit cell of CNT bundle struts. This model captures the observed foam-like deformation in experiment, due to the bending and shearing of the CNT bundles, and also provided a useful prediction for the properties of direct-spun mats upon the infiltration and cure of an epoxy matrix, see section 4.4. This model and other models for the strength of direct-spun fibres [262, 279] argue that the yield strength of direct-spun materials is sensitive to the shear strength of the bond between adjacent CNTs; in the case of isotropic direct-spun CNT mats the model of section 3.4 suggests that the macroscopic flow strength of the CNT mats σ_y scales with the longitudinal shear yield strength of the CNT bundle τ_B according to $\sigma_y \sim \tau_B$. Lap shear tests of the bond formed between overlapping CNTs grown by chemical vapour deposition reveal that the shear strength of the bond between overlapping CNTs scales linearly with both the contact length and width, for bond lengths of less than approximately 300 nm [279, 453, 277, 454]. This implies

that the area of contact between two CVD-grown CNTs possesses a uniform shear yield strength, which is estimated to lie between approximately 30 MPa and 70 MPa [279]. Now, micromechanical models of the CNT bundle microstructure are used to estimate how the geometry and nature of the contact area between adjacent CNTs within bundles is altered upon the infiltration of organic solvents and chorosulfonic acid within the mat microstructure.

5.5.1 The effect of organic solvent infiltration upon CNT bundle microstructure

The area of contact where small particles adhere is dictated by the relative contribution of surface energy and elastic deformation [291]. The well-established JKR theory [455] treats the edge of the adhesive contact between two particles as an elastic singularity. By equating the energy release rate at this location to the adhesion energy, predictions of the contact area may be obtained from elastic calculation.

Images of a cross-sectional view of the CNT bundle microstructure within the mats studied herein were presented earlier in Figure 4.3 of section 4.3. The images show that CNTs within the direct-spun mat are typically of 6 nm outer diameter with between 4 and 7 walls, and flatten against one another to form areas of contact. The CNT bundle microstructure is simplified here for the purposes of analysis to a hexagonally packed, periodic bundle microstructure, as illustrated in Figure 5.11a. This simplification facilitates the use of periodic boundary conditions upon a repeating unit cell of bundle microstructure, see Figure 5.11b.

Consider the mechanical properties and deformation of the CNT walls. The accuracy of continuum shell theory is well-established for modelling the deformation of individual CNTs [254, 253]. The in-plane modulus of CNT walls with the typical interlayer spacing of 0.34 nm [1] is often quoted as approximately 1 TPa, yet a shell of this modulus with thickness equal to the interlayer spacing possesses a flexural bending stiffness far above that of a graphene layer [254]. Studies in literature have demonstrated that experimental observations such as the rippling of the walls of multi-walled CNTs in bending [235], the kinking of single-walled CNTs [248], and the self-collapse of larger diameter CNTs [456, 262] may be captured by assuming a shell thickness of approximately 0.075 nm, and isotropic elastic behaviour, with Young's modulus $E_G = 4.84$ TPa, and Poisson ratio $\nu_G = 0.19$ [254]. Here, CNT walls of this thickness are modelled in plane strain with 8-noded continuum finite elements using quadratic shape functions, see Figure 5.11b. The interlayer region between adjacent walls is meshed with the same elements; its elastic properties are chosen as follows.

Consider the nature of the van der Waals bond between adjacent CNT walls. In crystal graphite, the Young's modulus measured perpendicular to the basal plane is far below the in-plane modulus [457, 458], and the shear strength of the bond between adjacent CNT walls within a CNT is sufficiently small [457, 458] that frictionless slip may be assumed without consequence [254]. Here, local material orientations 1 and 2 are defined as parallel to the radial and hoop direction respectively, see Figure 5.11b. The interlayer region is assigned the following anisotropic elastic constitutive relationship, which relates the elastic stress σ_{ij} to the strain state ε_{ij} in plane strain:

$$\begin{Bmatrix} \sigma_{11} \\ \sigma_{22} \\ \sigma_{12} \end{Bmatrix} = \begin{bmatrix} E_{11}^{vdw} & 0 & 0 \\ 0 & E_{22}^{vdw} & 0 \\ 0 & 0 & G_{12}^{vdw} \end{bmatrix} \begin{Bmatrix} \varepsilon_{11} \\ \varepsilon_{22} \\ \frac{1}{2}\varepsilon_{12} \end{Bmatrix} \tag{5.1}$$

The modulus assigned to the interlayer region in the radial direction is $E_{11}^{vdw} = 28.5$ GPa, as this value corresponds to an overall wall modulus in the radial direction of 36.5 GPa — the out-of-plane modulus of a graphite crystal [457]. A value for the shear modulus G_{12}^{vdw} deduced from measured shear modulus of a graphite crystal [457] in a similar manner gives rise to stresses far above the measured interlayer shear yield strength [283, 279]. Consequently G_{12}^{vdw} is set to be artificially low (0.01 GPa), and simulation results are insensitive to variation of its value by an order of magnitude either way. For simplicity the modulus in the hoop direction E_{22}^{vdw} is set to equal E_{11}^{vdw}; as the stiffness of the walls in the hoop direction is dominated by the in-plane stiffness of the graphene layers, variation of E_{22}^{vdw} has a negligible effect upon the simulation results.

The relationship between adhesion energy and area of contact was estimated as follows. The fraction of the CNT wall in contact with its neighbour, denoted Ω, was varied between 0 and 0.8. For a chosen value of Ω a finite element mesh was constructed, with the mesh locally refined around the edge of the chosen contact area, see Figure 5.11b. Elements at the tip of the contact area were partially collapsed — the nodes on their sides radiating from the edge of the contact area were shifted to form so-called quarter point elements [459], to resolve the singular stress field around the edge. All nodes in the contact area were displaced to a line parallel with the x-direction, and the location of this line in the y-direction was obtained iteratively such that the sum of all nodal reaction forces resolved into the y-direction along its length was equal to zero (the case of no net hydrostatic stress acting upon the bundle). Suitable refinement of the mesh around the edge of the contact area and calculation with a J-integral [460] yielded the value of energy release rate, equal to the energy of adhesion.

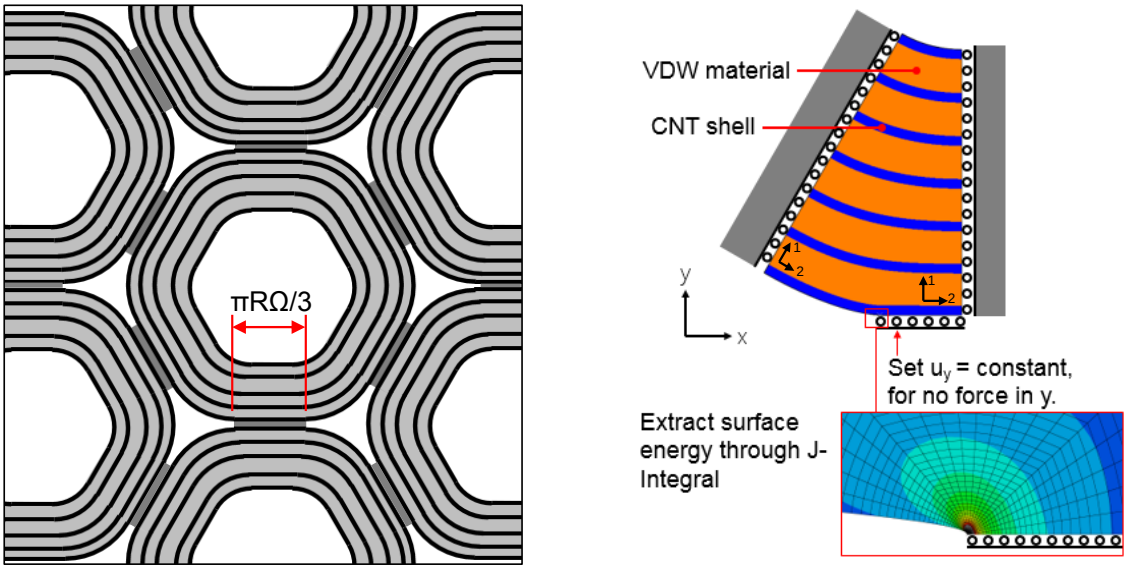

(a) (b)

Fig. 5.11 (a) Periodic CNT bundle microstructure and (b) finite element analysis of a repeating unit cell of CNT bundle microstructure.

The value Ω is plotted against the corresponding value of surface energy determined from finite element simulation in Figure 5.12a, for CNTs of 6 nm outer diameter, with between 1 and 7 walls. For single-walled CNTs, the predictions are close to those obtained with analytical solutions elsewhere in literature [262]. Note that for a given value of surface energy, the fraction of the outer wall in contact with neighbouring CNTs decreases with increasing numbers of walls.

Now consider the surface energy of the bond between the walls of neighbouring CNTs with and without the presence of organic solvents in the pores between them. Accurate measurements of surface energy may be obtained with a surface force apparatus [291]. For dry graphene layers, researchers using this technique have reported a value of $\gamma_{ss} = 0.119$ J/m^2 for few layer graphene and 0.115 J/m^2 for single-layer graphene [295]; these values are close to the measurement obtained through heat of wetting experiments for graphite crystals, 0.130 J/m^2 [297, 298]. Here, the surface energy between the dry CNT walls is taken to be 0.119 J/m^2.

The surface energy between CNT walls separated in the presence of a fluid, denoted γ_{sls}, is written in terms of the surface energy of the walls γ_{ss}, liquid γ_{ll}, and liquid-CNT wall interface γ_{sl} [291] as follows,

$$\gamma_{sls} = \gamma_{ss} + \gamma_{ll} - 2\gamma_{sl} \tag{5.2}$$

The surface energy between the liquid and CNT walls γ_{sl} is estimated with the following combining relationship [291]:

$$\gamma_{sl} = \sqrt{\gamma_{ss}\gamma_{sl}} \tag{5.3}$$

Values of γ_{ll} are listed in Table 5.1, with values of γ_{sls} calculated from equations 5.2 and 5.3. Note that upon the infiltration of solvents studied herein, the predicted surface energy between the walls reduces to between 17% and 33% of its value in air.

Table 5.1 Values of solvent surface energy [86] and predicted surface energy for CNT walls separated in the presence of solvents.

Solvent	γ_{ll} (J m^{-2})	γ_{sls} (J m^{-2})
Acetone	0.02271	0.0377
Ethanol	0.02191	0.0388
Toluene	0.02791	0.0316
Chloroform	0.02665	0.0330
NMP	0.04021	0.0209

Now, consider the relationship of the area of contact between neighbouring CNTs and the macroscopic yield strength of direct-spun mats measured whilst immersed in organic solvents. Predictions for Ω upon the infiltration of each solvent into the CNT bundle microstructure are obtained from the charts of Figure 5.12a by setting the surface energy equal to γ_{sls} as recorded in Table 5.1. The yield strength of the direct spun mats measured whilst immersed in fluids, denoted σ_y, is defined as the measured nominal stress during tensile testing recorded at a nominal strain of 0.05. The yield stress measured upon immersion in each solvent and in the dry state is plotted against the predicted value of Ω for CNTs of 6 nm outer dimeter with between 4 and 7 walls in Figure 5.12b. In broad terms, the yield strength σ_y scales almost linearly with the predicted value of Ω. This linear scaling suggests that whilst the area of contact between the CNTs is reduced by the presence of solvents within the bundle pores, the shear yield stress of the bond itself is little changed in comparison to the dry state. Hence, it is the reduction in contact area between adjacent CNTs which leads to softening of the direct-spun mat yield strength upon organic solvent infiltration. This observation is consistent with experimental and numerical studies reported elsewhere, which suggest that the bond between CNTs grown by chemical vapour deposition possesses an intrinsic shear yield stress, independent of the width of the contact between them [279, 454].

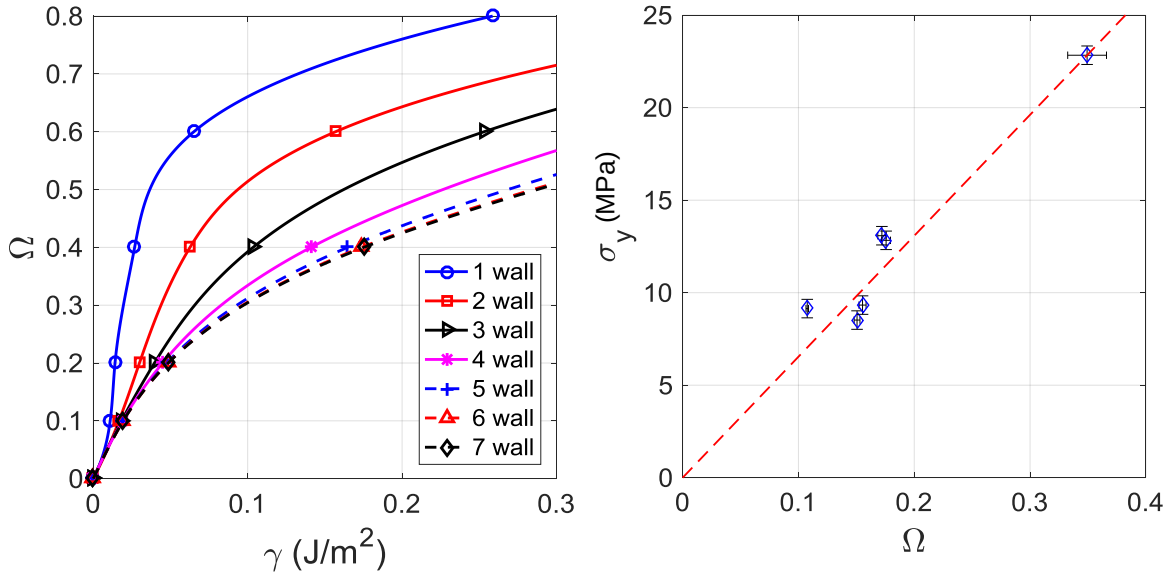

(a) (b)

Fig. 5.12 (a) The predicted fraction of external CNT wall in contact with adjacent CNTs as a function of surface energy and number of walls for CNTs of 6 nm outer diameter. (b) The measured yield strength of direct-spun CNT mat samples plotted against the predicted fraction of external CNT wall in contact for air and upon infiltration of each respective solvent.

5.5.2 The effect of chlorosulfonic acid infiltration upon CNT bundle microstructure

The separation of bundled CNTs upon immersion in chlorosulfonic acid is well documented in literature [395, 405]. Reports of small-angle neutron scattering measurements of single-walled CNTs dispersed in chlorosulfonic acid inform that they are separated from one another in a nematic phase with a spacing of between 10 nm and 30 nm between their outer walls [461]. This measured spacing is consistent with the volume fraction of CNTs in solution, which may be as high as 15% [395]. Here, it is expected that the infiltration of chlorosulfonic acid within the bundles separates adjacent CNTs bonded in the dry state by van der Waals attraction, and this separation results in the major reduction in macroscopic strength and stiffness observed upon uniaxial tensile testing whilst immersed in chlorosulfonic acid.

The measured ductility and rate-dependent stress-strain behaviour of the direct-spun mat whilst immersed in chlorosulfonic acid is similar to the behaviour of amorphous polymers at temperatures above their glass transition, in the so-called rubbery plateau [462]. In these polymers, the constrained movement of the long-chain polymer molecules relative to one

another, referred to as reptation, is restricted by a combination of stokes friction and the dislocation-like slip of van der Waals bonds between adjacent molecules [462]. For the mat measured here, tensile failure in air follows considerable hardening in the stress-strain response at a nominal strain of between 0.2 and 0.3. A plausible explanation for much greater ductility upon immersion in chlorosulfonic acid is that reptation takes place, made possible by the separation of adjacent CNTs within their bundles.

The immersion of carbon nanotubes in chlorosulfonic acid results in a reversible chemical reaction [406], which endows their outer walls with a net-positive charge. Chlorosulfonic acid obeys Brønsted-Lowry theory upon reactions with bases, as below.

$$\mathrm{HA} + \mathrm{B} \leftrightarrows \mathrm{A}^- + \mathrm{BH}^+, \tag{5.4}$$

where HA is an acid, B a base, HA^- the conjugate based of the acid, and BH^+ the conjugate acid that results from protonation of the base. At equilibrium, this reversible reaction occurs in both forward and backward directions at equal rate. In the case of carbon nanotubes and chlorosulfonic acid, the reaction of equation 5.4 is written as follows [406]:

$$[\mathrm{HSO_3Cl}]_m + \mathrm{C}_x \leftrightarrows [\mathrm{C}_x\mathrm{H}_m^+] + [\mathrm{ClSO_3^-}]_m \tag{5.5}$$

The carbon nanotube is represented by the molecule C_x. Upon reaction with chlorosulfonic acid $\mathrm{HSO_3Cl}$, the CNT's conjugate acid $\mathrm{C}_x\mathrm{H}_m^+$, accompanied by chlorosulfate $\mathrm{ClSO_3^-}$ in solution as the conjugate base. This reaction results in a fractional positive charge $\zeta^+ = m/x$ associated with each carbon atom within the outer CNT wall [406]. Literature informs that the frequency of the G-band with approximate wavenumber of 158 mm^{-1} is sensitive to the presence of positive charge [395, 308, 463]. The shift of wavenumber upon charging is denoted ΔG, and the study of charging in double-walled CNTs suggests that ΔG is related to ζ^+ according to $\Delta G = 35.0\zeta^+ + 10.1\sqrt{\zeta^+}$ mm^{-1} [463]. Here, a sample of direct-spun mat was placed between two glass coverslips, and the Raman spectra of the sample was measured before and after infiltration with chlorosulfonic acid. The spectra are plotted in Figure 5.13. The measured shift of $\Delta G = 2.894$ mm^{-1} implies that $\zeta^+ = 0.031$. Multiplication by the areal density of carbon atoms in the outer wall, $P_S = 3.82 \times 10^{19}$ m^{-2} [308], and fundamental charge e suggests a surface charge density q_s upon the outer wall of 0.19 Cm^{-2}.

It is expected that the presence of surface charge should be accompanied by a potential difference ψ_S between the CNT outer wall and surrounding chlorosulfonic acid. Here, ψ_S was measured using the electrochemical cell illustrated in Figure 5.14. A sample of direct-

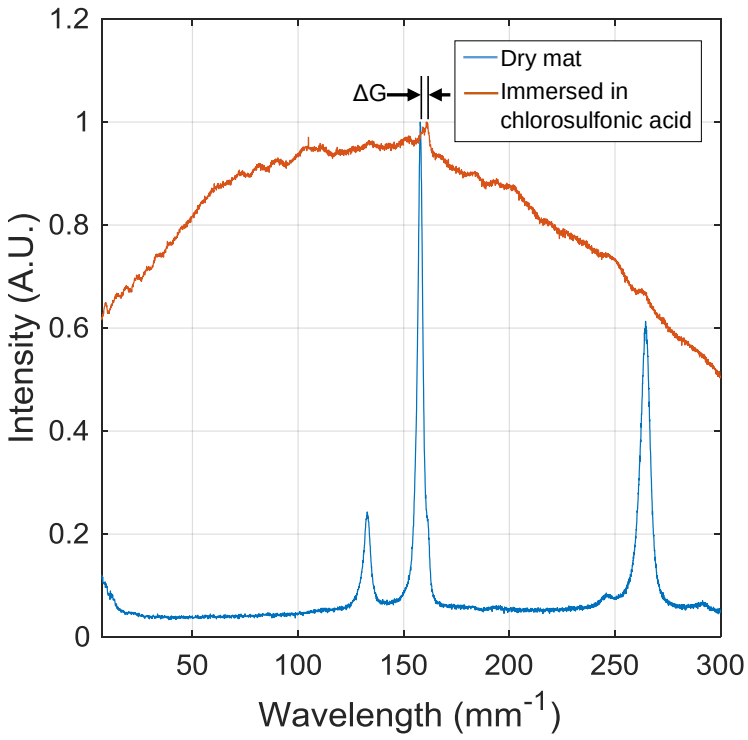

Fig. 5.13 The Raman spectra of dry CNT mat and CNT mat immersed in chlorosulfonic acid. Note the shift ΔG of the G-band frequency.

spun mat held with a brass grip was partially immersed in a glass beaker of chlorosulfonic acid. The beaker was electrically connected via a salt bridge containing a weak solution of chlorosulfonic acid in concentrated sulphuric acid to another beaker of concentrated sulphuric acid, in which a reference electrode (saturated calomel) was placed. The potential difference between the reference electrode and brass contact holding the CNT mat was measured with a potentiostat. Subtraction of the characteristic potential difference of the reference electrode from the measured voltage yielded a surface potential $\psi_S = 0.54$ V.

It remains to explain how the immersion of direct-spun CNT mats in chlorosulfonic acid separates bundled CNTs. According to equation 5.5, each proton upon the outer CNT wall is balanced by a negatively charged chlorosulfate ion in solution. It is anticipated that these ions will be attracted to the positively charged CNT walls by electrostatic force, and that a resultant region of elevated chlorosulfate ion density forms around the CNT walls, in the form of an electrical double layer [464]. The double layer around two CNTs in solution is sketched in Figure 5.15. CNTs in solution are attracted to one another by van der Waals forces. If two CNTs come into close proximity, it is expected that the interaction of their double layers

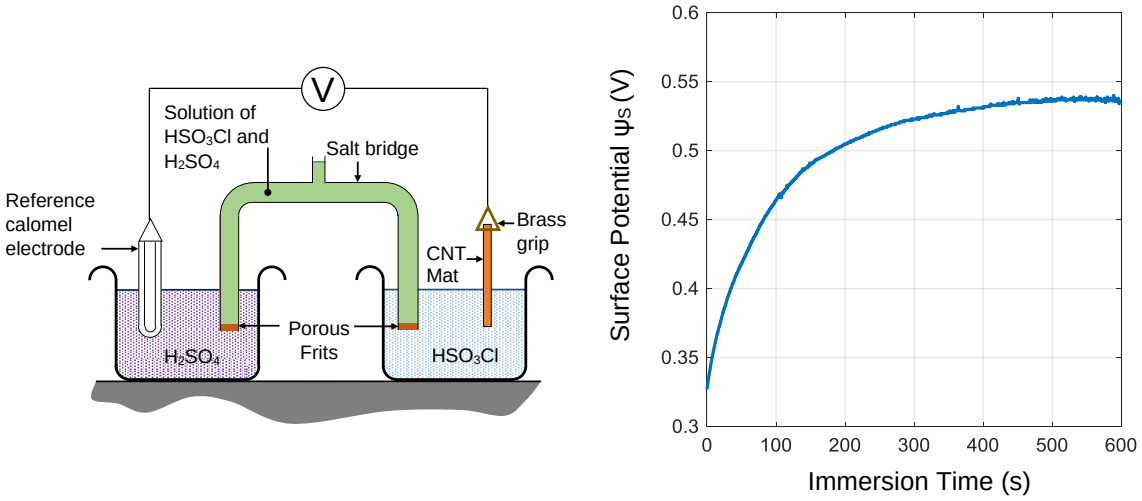

(a) (b)

Fig. 5.14 (a) Experimental apparatus for measurement of surface potential ψ_S, (b) the measured surface potential plotted against time upon immersion in chlorosulfonic acid.

gives rise to an electrostatic repulsive force between them, which is sufficient to prevent their aggregation. The variation of electrical potential and ion distribution within the electrical double layer and resultant forces which develop between charged particles dispersed in electrolytes has been widely studied with the theories of Derjaguin, Landau, Verwey and Overbeek, collectively termed DLVO theory [465, 466]. Now, approximate predictions for the competing van der Waals and electrostatic interaction potentials are obtained by invoking the Gouy-Chapman model [464].

An electrical double layer consists of two regions, see Figure 5.15. An inner region, the so-called Stern layer of thickness δ lies close to the CNT wall; ions may adsorb to the wall inside this region. Outside, a diffuse region exists where the ion distribution is dictated by competition between electrostatic and thermal forces. In total, the sum of charge contained within the outer diffuse layer q_D, the inner Stern layer q_δ, and upon the surface of the CNT wall q_S, balance as below.

$$q_D + q_S + q_\delta = 0 \tag{5.6}$$

The DLVO theory is a valid mean-field theory for sufficiently dilute electrolytes, where the average separation between ions within an electrolytic fluid is far above the Bjerrum length l_B, defined as follows,

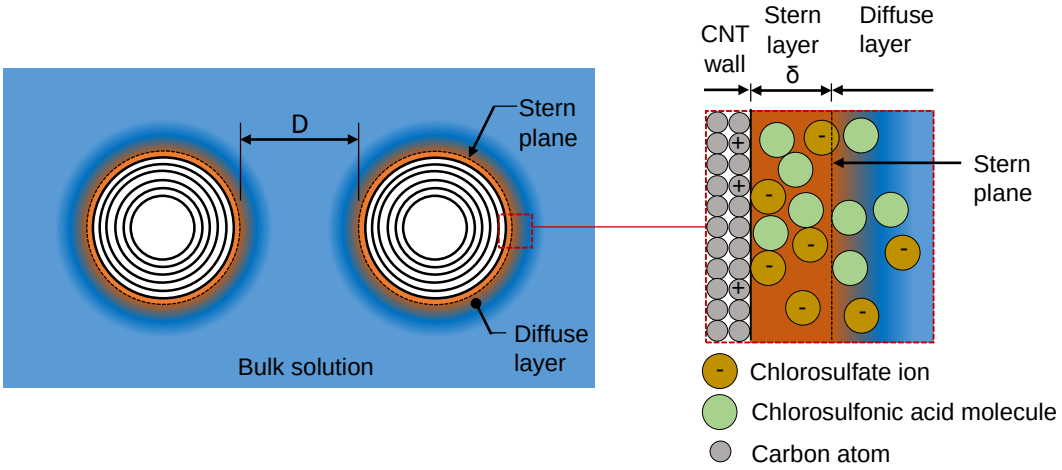

Fig. 5.15 Sketch of the suggested of the double layer structure surrounding CNTs immersed in chlorosulfonic acid, and detail of the diffuse and compact Stern layer adjacent to the CNT wall.

$$l_B = \frac{e^2}{4\pi\varepsilon_0\varepsilon_r kT} \tag{5.7}$$

where $\varepsilon_0\varepsilon_r$ is the electrolyte permittivity, k the Boltzmann constant and $T = 300$ K the temperature. Upon taking the relative permittivity of chlorosulfonic acid from literature as $\varepsilon_r = 60$ [467], the Bjerrum length $l_B \approx 1$ nm. Chlorosulfate ions arranged in a hexagonally packed lattice with spacing equal to the Bjerrum length would have a number density of approximately 1.4×10^{27} m^{-3}. Here, the number concentration of ions in chlorosulfonic acid was estimated by conductivity measurements taken with a 4-point cell. The measured specific conductance of 0.135 s/m suggests a bulk ion number concentration of $n_0 = 1.25 \times 10^{25}$ m^{-3}, which is much below the limiting density estimated above. Further details of the conductivity measurement technique and this calculation are found in Appendix E.

Consider the decay of electrical potential within the diffuse layer. The value of electrical potential ψ is defined as 0 within the bulk solution, and rises over the diffuse layer to a value ψ_D at the boundary between the diffuse and Stern layers — the Stern plane. Within the Stern layer the potential continues to rise with decreasing distance from the wall, reaching the value of the surface potential ψ_S. The well-established Gouy-Chapman theory predicts the potential ψ to vary within the diffuse layer as a function of distance x from the Stern plane, as follows,

$$\psi = \frac{2kT}{e} \log \left[\frac{1 + \Gamma \exp\left(-x/\lambda_D\right)}{1 - \Gamma \exp\left(-x/\lambda_D\right)} \right], \tag{5.8}$$

The parameter $\Gamma = \tanh\left(e\psi_D/4kT\right)$. The decay constant λ_D is the Debye length, defined for a symmetrical electrolyte as follows:

$$\lambda_D = \sqrt{\frac{\varepsilon_r \varepsilon_0 kT}{2e^2 n_0}} \tag{5.9}$$

Here, the calculated λ_D based upon the estimated ion density and assumed relative permittivity is 1.9 nm. The Debye length typically matches the observed decay in experiments for $\lambda_D > d$ [468, 469], where d is the ion diameter. Based upon its molecular volume [291, 467], a chlorosulfonic acid molecule has diameter $d = 0.54$ nm, which is much below the estimated λ_D. Integration of the ion density as predicted by the Poisson-Boltzmann equation yields the following expression for the total charge within the diffuse layer q_D per unit area of CNT wall [464],

$$q_D = \sqrt{8 n_0 \varepsilon_r \varepsilon_0 kT} \sinh\left(\frac{e\psi_D}{2kT}\right). \tag{5.10}$$

Consider the charge within Stern layer. The extent of chlorosulfate ion adsorption to the surface of the CNT wall may be written as a function of the electrical potential at the Stern plane ψ_D, the areal charge density corresponding to a monolayer of adsorbed, hexagonally packed chlorosulfate ions $q_L = -2e/\left(\sqrt{3}d^2\right)$, and the van der Waals bonding energy between a chlorosulfate ion and the CNT wall ϕ, as follows [464],

$$q_\delta = q_L \frac{M_{CSA} n_0}{\rho_{CSA} N_A} \exp\left(-\frac{-e\psi_D + \phi}{kT}\right). \tag{5.11}$$

N_A is Avogadro's constant, and M_{CSA} and ρ_{CSA} are the molar mass and volumetric density of chlorosulfonic acid respectively, with values of 0.117 kg mol^{-1} and 1753 kg m^{-3} [467]. Estimation based upon Liftshitz theory [291] informs that $|\phi| \ll kT$; hence its value was omitted without effect.

Now consider the forces that develop between two CNTs of radius R at close proximity due to the van der Waals attraction and the interaction of their double layers. Upon neglecting the thickness of the Stern layer, the attractive van der Waals and repulsive double layer potentials per unit length, denoted U_{VDW} and U_{DL} respectively, are estimated according to the linear superposition approximation [464] and the Derjaguin approximation [291], and

are written in terms of the separation distance D between their CNT outer walls, the Hamaker constant A, and other parameters. Further details of derivation are given in Appendix F.

$$U_{VDW} = -\frac{A}{24} R^{\frac{1}{2}} D^{-\frac{3}{2}} \tag{5.12}$$

$$U_{DL} = \left(64\sqrt{\pi} n_o kT R^{\frac{1}{2}} \lambda_D^{\frac{3}{2}} \Gamma^2 \right) \exp\left(-D/\lambda_D\right) \tag{5.13}$$

The Hamaker constant A between the CNTs approaching across a fluid medium is estimated using Lifshitz theory [291] as a function of the refractive index μ_{CNT}, and dielectric constant ε_{CNT} of the CNT walls and those of the fluid medium μ_f and ε_f as follows:

$$A \approx \frac{3}{4} kT \left(\frac{\varepsilon_{CNT} - \varepsilon_f}{\varepsilon_{CNT} + \varepsilon_f} \right)^2 + \frac{3h\nu_e}{16\sqrt{2}} \frac{\left(\mu_{CNT}^2 - \mu_f^2\right)^2}{\left(\mu_{CNT}^2 + \mu_f^2\right)^{\frac{3}{2}}} \tag{5.14}$$

The dispersion frequency is taken to be that of graphite $\nu_e = 3.4 \times 10^{15}$ rad s^{-1} [293]. For CNT walls interacting across air, (for which $\varepsilon_f = \mu_f = 0$), the Hamaker constant is related to their surface energy according to $A = 24\pi D_0^2 \gamma_{ss}$ [48,83], where the intermolecular cut-off distance $D_0 = 0.165$ nm [291]. Upon recognising that the relative permittivity of CNT walls relates to their refractive index according to $\varepsilon_{CNT} = \mu_{CNT}^2$, rearrangement of equation 5.14 followed by substitution of the Hamaker constant derived from the reported surface energy in literature $\gamma_{ss} = 0.119$ J/m^2 [295] suggests that $\mu_{CNT} \approx 2.01$. Now, for the CNTs attracting across chlorosulfonic acid, for which $\mu_f = 1.437$ and $\varepsilon_f = 60$ [80], it is estimated that $A = 1.04 \times 10^{-19}$ J.

The potential of the interaction between the CNTs, U_{DLVO}, is simply the sum of the van der Waals and double-layer interaction [464],

$$U_{DLVO} = U_{VDW}(D) + U_{DL}(D). \tag{5.15}$$

The predicted potential U_{DLVO} is plotted in Figure 5.16 for values of ψ_D ranging from 0 V to 0.125 V; the value of potential ψ_D and corresponding surface charge q_S is annotated, calculated from the sum of double layer charge q_D given by equation 5.10, Stern layer charge q_δ of equation 5.11, and overall charge balance of equation 5.6. The potential $\psi_D = 0.125$ V corresponds to a surface charge of 0.19 Cm^{-2}, equal to that inferred earlier from Raman measurement.

It is expected that upon immersion in chlorosulfonic acid, neighbouring CNTs will be repelled from one another by short-range electrostatic forces from their position at the primary minimum [470]. In CNT-chlorosulfonic acid suspensions described in literature, CNTs may exist in a nematic phase state where they are separated but remain at a short distance from one another along their lengths, or form an isotropic phase [395]. Note that the magnitude of both predicted potentials depend identically upon the CNT radius R, hence the shape of the predicted DLVO interaction potential plotted in Figure 5.16 is invariant to the CNT geometry. Measurements of the distance between CNTs in a nematic phase obtained from small-angle neutron scattering suggest that the distance between their walls lies between 9 nm and 34 nm [461]. At these separation distances, forces calculated with the Derjaguin approximation may not be considered highly accurate [288], but are nonetheless a small fraction of those which occur at close separation distances. For the potentials calculated herein, a secondary minimum is predicted at a position of about 10 nm separation between the CNTs — such a secondary minimum usually arises in predicted DLVO potentials due to the different decay rates of van der Waals and electrostatic forces [464]. If sufficiently deep, this secondary minimum may promote a weaker form of aggregation, where particles are separated at short distances from one another in the suspension [464]. Other numerical models in the literature aimed at predicting the phase behaviour of carbon nanotubes in superacid suspensions [470] suggest that the relative volume fractions of nematic and isotropic phases in suspensions are sensitive to the depth of an approximated potential well.

5.5.3 The drawing of direct-spun mats whilst immersed in fluids

In summary, the state of bundle microstructure inferred from the experiments and predictions is sketched in Figure 5.17. The effect of organic solvent infiltration is to reduce the contact area between adjacent CNTs, but not to separate them or alter the shear yield stress of the bond between them from that in the dry state. In contrast, the infiltration of chlorosulfonic acid promotes CNT separation; upon replacement of the chlorosulfonic acid with chloroform, the measured tensile stress versus strain response lies between that measured upon immersion in chloroform alone and that measured whilst immersed in chlorosulfonic acid. It appears that the bonds between adjacent CNTs remain sufficiently weak due to the presence of residual chlorosulfonic acid which remains after draining and replacement with chloroform. Chlorosulfonic acid decomposes upon contact with water [467]; its neutralisation by rinsing after drawing, followed by oven drying, appears to return the strength of the bonds between adjacent CNTs to a similar value to that before immersion.

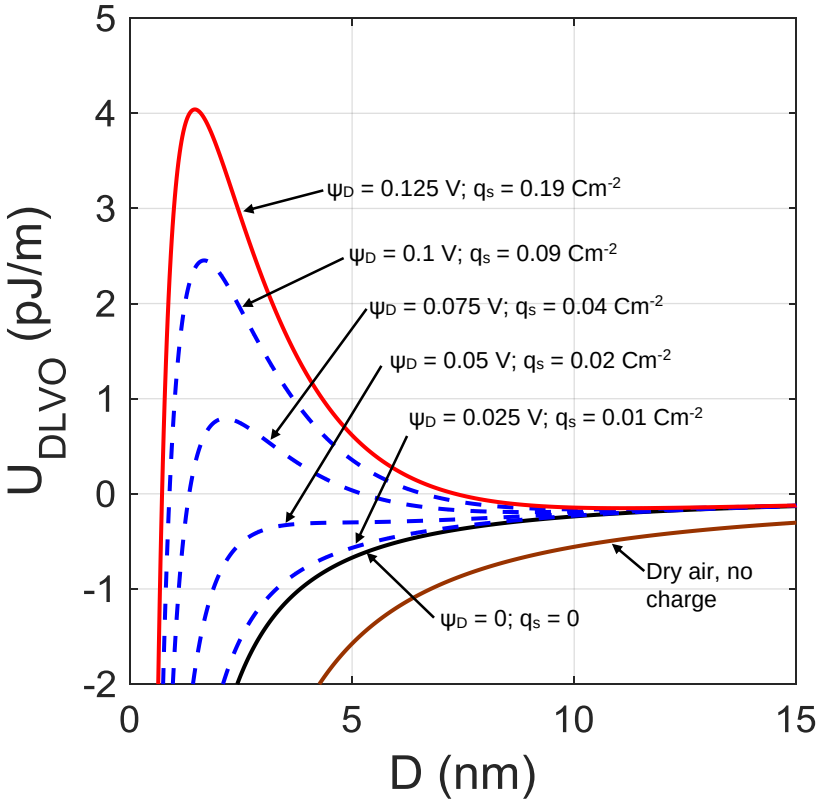

Fig. 5.16 The predicted DLVO interaction potential as a function of separation distance between two parallel CNTs of 6 nm diameter immersed chlorosulfonic acid, for varying values of electrical potential ψ_D and corresponding surface charge q_S. The van der Waals attraction predicted for dry air, in the absence of surface charge, is also included for comparison.

5.6 Conclusions

The reported specific modulus and strength of different macroscopic materials with carbon nanotubes as their primary constituents vary over several orders of magnitude as a function of their manufacture and resultant morphology. In the case of direct-spun CNT mats, their specific modulus in their principal direction as reported in literature varies by almost three orders of magnitude. Isotropic direct-spun mats deform due to the bending and shearing of the interconnected bundle network which comprises their microstructure. This foam-like deformation arises from their random microstructure of CNT bundles which form an interconnected network of low nodal connectivity.

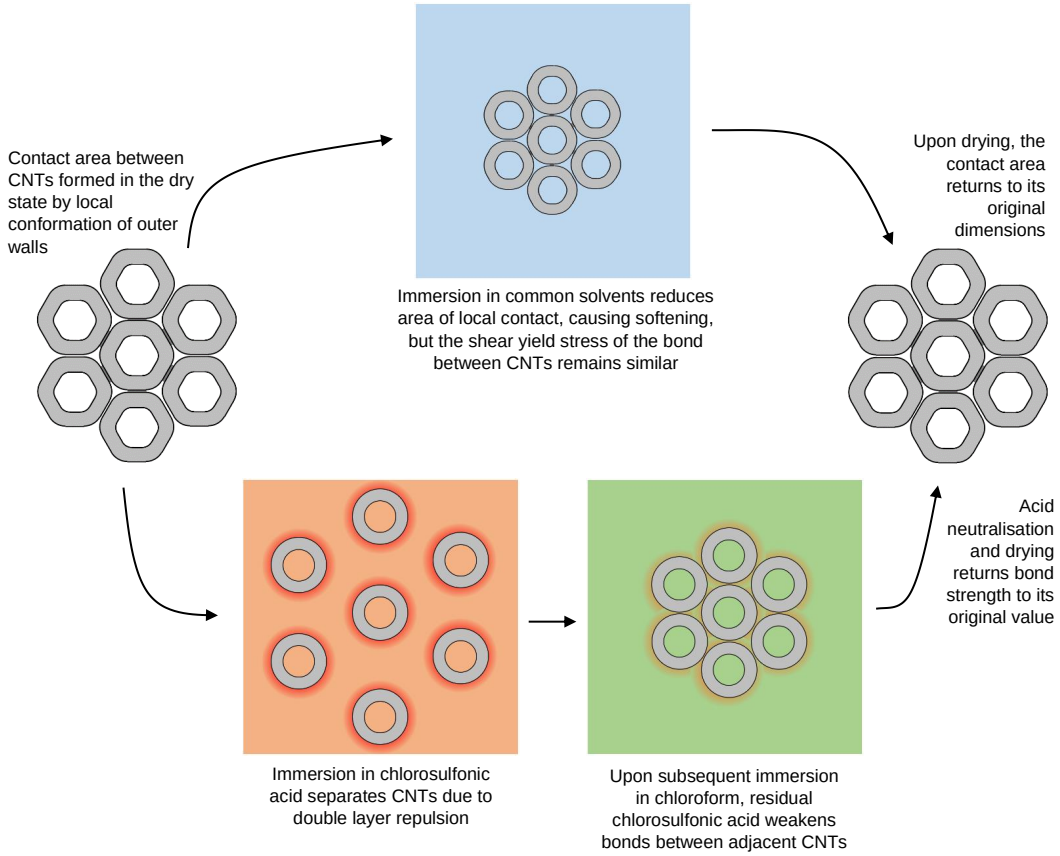

Fig. 5.17 The alteration of bundle microstructure during drawing processes.

With the aim of enhancing microstructural alignment through tensile drawing, the stress-strain response of a direct-spun mat was measured in air and whilst immersed in a range of organic solvents and chlorosulfonic acid. Immersion in the organic solvents results in softening, but the shape of the stress versus strain response and ductility remain similar. The softening observed upon immersion in the common solvents acetone, ethanol, toluene, chloroform and NMP was attributed to a reduction in the area of contact between adjacent CNTs: The macroscopic yield strength of the immersed mats was found to scale linearly with predictions of the contact area between neighbouring CNTs within bundles. In contrast, the reduction in tensile strength upon chlorosulfonic acid infiltration by approximately two orders of magnitude is attributed to the separation of the CNTs within their bundles due to double layer repulsion. Approximate predictions for the forces between two parallel CNTs immersed in chlorosulfonic acid were obtained with DLVO theory, and suggest that the effect of double-layer repulsion is sufficient to separate the CNTs into the nematic phase which is reported in literature [395, 461].

The immersion of direct-spun mats in chlorosulfonic acid, followed by tensile drawing in a solution of chlorosulfonic acid and chloroform, acid neutralisation and drying, was shown to increase the tensile modulus of the mat by two orders of magnitude, and the ultimate tensile strength by over a factor of 7. The changes in mechanical properties were attributed to the aligned microstructure of the drawn mats, as opposed to any residual influence of the infiltrated fluids used in drawing, whilst the specific electrical conductivity was sensitive to both the applied drawing strain and choice of drawing fluid. The study confirms the influence of microstructure upon the properties of direct-spun CNT mats, illustrating how their modulus, strength and electrical conductivity may be enhanced through fluid-assisted drawing.

Chapter 6

Conclusions and further work

6.1 Conclusions

The walls of individual carbon nanotubes possess exceptional properties: a tensile modulus of about 1 TPa, tensile strengths from 10 GPa to 100 GPa, and a thermal conductivity of up to 3500 W/mK. These measured values exceed those of all conventional engineering materials. The measured specific electrical conductivity of carbon nanotube walls varies widely, and can match that of metal alloys. The measured density, modulus, strength and electrical and thermal conductivity of macroscopic CNT materials — CNT forests, pillars, foams, mats and fibres — all span multiple orders of magnitude. Aligned CNT mats and fibres possess a tensile modulus and strength in the range of metal alloys and other high-performance fibres, whilst the modulus and strength of isotropic CNT mats of equivalent density is typically much below that of the aligned CNT morphologies.

To confirm the micromechanical basis of direct-spun CNT mat mechanical properties, a direct-spun mat was studied. The microstructure of direct-spun carbon nanotube mats consists of an interconnected network of CNT bundles. The bundles are joined at locations where they cross one another, and where individual CNTs cross from one bundle to another. For relatively isotropic direct-spun mats, the observation of this microstructure during uniaxial tensile testing reveals that the bundles do not slip or rotate relative to one another at points where joints form between them. Instead the bundles remain connected as a network, bending and shearing as tensile strain is applied. During the tensile stress-strain response, CNT bundle struts which are initially inclined relative to the direction of tensile strain reorient in line with the load, and may straighten or kink. Initial yielding is dictated by the longitudinal shear strength of the CNT bundles, and subsequently the stress-strain response exhibits considerable hardening as the bundle microstructure reorients in line with the loading di-

rection. The elastic modulus measured during unloading increases with increasing tensile strain, and final failure in tension is preceded by a 'lock up' in the stress-strain response. The electrical resistance of direct-spun samples increases by between 20% and 30% of their initial resistance during tensile testing, confirming that a conductive network of CNT bundles remains intact up until final failure.

The features of the measured stress-strain response of direct-spun CNT mats described above are captured with a micromechanical model based up a honeycomb unit cell of CNT bundle microstructure. In the unit cell model, the CNT bundle struts deform by bending and shearing upon the application of tensile load. The model provides a useful estimate of the direct-spun mat modulus and yield strength. It elucidates the sensitivity of the macroscopic mat modulus and strength to the longitudinal shear modulus and shear strength of the carbon nanotube bundles, and to the network structure, which by virtue of its geometry leads to bending and shear deformation of the CNT bundle struts.

The longitudinal shear strength of CNT bundles is sensitive to the area of contact between adjacent CNTs. This contact area depends upon the diameter of CNTs and number of walls, and upon the surface energy of the bond between their walls. The infiltration of solvents reduces the surface energy between CNTs. This decreases the area of contact between the bundled CNTs, and with it the longitudinal bundle shear strength. This in turn reduces the macroscopic yield strength of the mat. Upon immersion into chlorosulfonic acid, the CNTs separate from one another within their bundles. In this separated state they transfer little stress between one another. This effect reduces the tensile strength of the mat by almost two orders of magnitude, and increases the ductility more than five-fold over that measured with tensile tests in air.

The dependence of direct-spun mat properties upon the CNT bundle network geometry and CNT bundle properties gave rise to the investigation of two different approaches aimed at enhancing the mechanical and electrical properties of direct-spun mats. In the first approach the mats were infiltrated with an epoxy-acetone solution, followed by evaporation of the acetone and cure of the epoxy under the influence of mechanical pressure. In the second approach the mats were drawn under tension in air, a variety of organic solvents, and in solutions of chlorosulfonic acid and chloroform, with the aim of aligning the CNT bundle microstructure and thus restricting its foam-like deformation upon uniaxial tension.

Consider the effects of the infiltration and cure of an epoxy matrix. Epoxy does not infiltrate the CNT bundles themselves. At low matrix volume fractions, the epoxy coats the bundles, forming a thin layer of enhanced yield strength. Thereafter, the epoxy progressively fills the voids between the bundles as its volume fraction increases, forming plate-like structures which extend into the pores until the composites are close to fully dense. The micromechanical model for the yield strength and modulus of direct-spun CNT mats was also used to predict properties of the CNT-epoxy composites over their compositional range, and captures the variation in yield strength and Young's modulus over the range of manufactured composite compositions. Calibration of the experimental results with the value of carbon nanotube bundle longitudinal shear yield strength used in finite element simulation of the CNT-polymer composite microstructure revealed that the bundle longitudinal shear strength after infiltration and cure of an epoxy matrix is much above its value in the dry state. This effect is responsible for much of the increase in the measured mat yield strength upon the infiltration and cure of an epoxy matrix. In addition, the experiments and model also reveal that the filling of the pores within the CNT bundle network with an epoxy matrix also increases the CNT mat yield strength — and results in a Young's modulus much above that of the CNT mat in the dry state. The electrical conductivity of the composites scales linearly with the CNT volume fraction, and is insensitive to the epoxy content.

Now consider the effect of fluid-assisted tensile drawing in solutions of chlorosulfonic acid and chloroform upon the mechanical properties and microstructure of the direct-spun CNT mats. The effect of this process is an increase in the direct-spun mat modulus by over two orders of magnitude, and the tensile strength by a factor of seven. The enhancement in mechanical properties is attributed to the effect of drawing in the presence of the chosen fluids, as opposed to any permanent chemical effects resulting from immersion. Microscopy of the drawn mat samples reveals substantial alignment of the CNT bundle microstructure in the direction of stretch. This aligned microstructure endows the mats with elastic, brittle behaviour compared to their ductile, compliant response in the dry state. The electrical conductivity measured after drawing is increased, due in part to the chemical effects of fluid immersion, and in part due to drawing. The increase in the Young's modulus and strength of the mats upon drawing in solutions of chlorosulfonic acid and chloroform is much above that obtained from drawing in organic solvents alone.

Direct-spun materials like those studied in this thesis may possess in-plane moduli and strengths in the range of amorphous polymers. Their Young's moduli and strength are much below those of individual CNT walls as a consequence of the weak van der Waals bonds

between neighbouring CNTs upon which the transfer of stress also relies, and due to their microstructure which can give rise to compliant deformation of their constituent CNT bundle network at the microscale. The macroscopic properties of the direct-spun mats are thus highly sensitive to the arrangement of the CNT bundle networks that comprise them, and to the strength and stiffness of the bonds between the CNTs within their bundles. In this thesis, it is the manipulation of the arrangement and properties of the mat's constituent CNT bundle network via processing which gives rise to striking enhancement in modulus and strength.

6.2 Further work

6.2.1 The understanding of direct-spun CNT mat properties

The toughness of direct-spun CNT mats

- The measured in-plane toughness of direct-spun CNT mats is relatively high: Exceeding that of natural composites such as wood fractured perpendicular to the grain direction, skin, or nacre [471], the toughness lies within the range of metal alloys yet at a much lower macroscopic density [12]. Initial experiments have indicated that the in-plane toughness decreases upon infiltration and cure of an epoxy matrix. Whilst the stress-strain behaviour of the mat was found to be broadly isotropic, the fracture behaviour was anisotropic – the crack kinking rather than propagating perpendicular to the principal material direction.

- The micromechanical origin of the in-plane toughness of direct-spun CNT mats remains to be determined. The relative contributions of CNT breakage and pull-out at the crack surface versus plasticity within the process zone around the crack tip are yet to be assessed.

- The high toughness could be investigated by in-situ testing, with observation of the CNT bundle microstructure surrounding the crack tip. Immersion of the direct-spun CNT mats in organic solvents would allow variation of the yield strength, and the shear lag length of CNTs is expected to increase with the decreasing bond area upon immersion. Such an experiment could inform of the relative importance of crack-tip plasticity versus CNT breakage and pull-out.

Variation in the modulus and strength of isotropic direct-spun CNT mats

- The specific tensile modulus and ultimate tensile strength of broadly isotropic direct-spun CNT mats differs by up to a factor of two in experiment, yet the origin of this variation remains unclear: it may be due to the properties of the bond between adjacent CNTs, or the geometrical arrangement of CNT bundles within the network microstructure.
- This variation could be investigated with finite element analysis of the CNT bundle microstructure, and through mechanical testing of CNT bundles using nano-manipulation techniques [472].

The electrical properties of direct-spun CNT materials

- A fundamental understanding of the electrical behaviour of direct-spun CNT mats remains elusive. The origin of the electrical conductivity in the dry state is of industrial interest, as is the effect of chemical doping.
- The conductivity of aligned CNT fibres is close to that of highly-oriented pyrolytic graphite crystals [121]. Literature informs that the electrical conductivity of aligned CNT fibres is broadly constant over a wide temperature range, but decreases sharply at low temperatures [121]; in contrast the in-plane electrical conductivity of highly oriented pyrolytic graphite crystals increases with decreasing temperature [473].
- It remains to measure the electrical conductivity of the direct-spun mats over as a function of temperature, anisotropy, current density, and frequency. The results from such experiments could be compared with tests upon samples of highly oriented pyrolytic graphite, and doped CNT mats. Findings could help to ascertain the electrical phenomena which limit direct-spun mat conductivity.

6.2.2 The properties and behaviour of direct-spun CNT mat-epoxy composites

The toughness of direct-spun CNT mat-epoxy composites

- The layered CNT mat microstructure endows direct-spun mats with a low delamination toughness. The effect of epoxy infiltration and cure upon the delamination toughness of direct-spun CNT mats is yet to be ascertained.

- The in-plane fracture toughness of composites is sensitive to the shear strength of the bond between fibre and matrix. By suitable variation of the matrix yield strength, it may be possible to tune the fracture toughness and strength of the composites. For instance, the application of a lubricant to CNT bundles or the epoxy coated-bundle network before further infiltration may increase the fracture toughness though internal slip and dissipation during crack advance. To date research has focussed on creating strong bonds between CNTs and polymer matrices, yet longer pull-out lengths and enhanced toughness may be possible by reducing the bond strength [369].

The modulus and strength of direct-spun CNT mat-epoxy composites

- The compressive yield strength of many fibrous composites is limited my microbuckling rather than axial fibre crush [474]. The compressive yield strength of direct-spun CNT mat-epoxy composites is yet to be measured — is it equivalent to that in tension, and what is the effect of anisotropy?

- Whilst the tensile strength and modulus of relatively isotropic CNT mats is greatly enhanced upon the infiltration and cure of an epoxy matrix, the effect of epoxy infiltration and cure upon drawn direct-spun CNT mat properties has not been investigated — the filling of pores within the bundle network may no longer influence the tensile modulus, similarly the ultimate strength of aligned CNT mats may be affected differently by the coating of CNT bundles with epoxy.

6.2.3 Fluid-assisted drawing of direct-spun CNT mats

- The DLVO model used herein to estimate the effects of double layer repulsion between CNTs upon chlorosulfonic acid immersion informs that the phenomenon of CNT separation is electrochemical in origin.

- It follows that the application of a voltage between the CNT walls and a surrounding electrolyte may promote similar effects in other electrolytic liquids.

- If possible, the use of other fluids will enable industrial application of fluid-assisted drawing processes like that developed in this thesis, and may facilitate convenient control of the CNT mat strength and modulus during drawing through suitable variation of the double layer potential.

- Early experiments have revealed that the control of mechanical properties in this manner during drawing is possible for direct-spun mats immersed in sulphuric acid —

a voltage of about 1.7 V promotes the ductile, compliant stress-strain behaviour that occurs upon chlorosulfonic acid immersion. It remains to determine if the effect is possible in other fluids, and to explore the potential for processing.

References

[1] Sumio Iijima. Helical microtubules of graphitic carbon. *Nature*, 354:56–58, 1991.

[2] Vladimir L. Kuznetsov Marc Monthioux. Who should be given the credit for the discovery of carbon nanotubes? *Carbon*, 44:1621–1623, 2006.

[3] H. P. Bohem. The first observation of carbon nanotubes. *Carbon*, 35:581–584, 1997.

[4] Lukyanovich VM Radushkevich LV. O strukture ugleroda, obrazujucegosja pri termiceskom razlozenii okisi ugleroda na zeleznom kontakte. *Zurn Fisic Chim*, 26:88–95, 1952.

[5] M. S. Dresselhaus, G. Dresselhaus, and A. Jorio. Unusual properties and structure of carbon nanotubes. *Annual Review of Materials Research*, 34:247–278, 2004.

[6] Lichao Feng, Ning Xie, and Jing Zhong. Carbon nanofibers and their composites: a review of synthesizing, properties and applications. *Materials*, 7:3919–3945, 2014.

[7] Min-Feng Yu, Oleg Lourie, Mark J. Dyer, Katerina Moloni, Thomas F. Kelly, and Rodney S. Ruoff. Strength and breaking mechanism of multiwalled carbon nanotubes under tensile load. *Science*, 287:637–640, 2000.

[8] N. M. Pugno and R. S. Ruoff. Nanoscale weibull statistics. *Journal of Applied Physics*, 99:024301, 2006.

[9] Min-Sheng Wang, Dmitri Golberg, and Yoshio Bando. Tensile tests on individual carbon nanotubes: linking nanotube strengths with its defects. *Advanced Materials*, 22:4701–4075, 2010.

[10] Bei Peng, Mark Locascio, Peter Zapol, Shuyou Li, Steven L. Mielke, George C. Schatz, and Horacio D. Espinosa. Measurements of near ultimate strength for multiwalled carbon nanotubes and irradiation-induced crosslinking improvements. *Nature Nanotechnology*, 3:626–631, 2008.

[11] B. G. Demczyk, Y. M. Wang, J. Cumings, M Hetman, W. Han, A. Zettl, and R. O. Ritchie. Direct mechanical measurement of the tensile strength and elastic modulus of multiwalled carbon nanotubes. *Materials Science and Engineering A*, 334:173–178, 2002.

[12] Michael F. Ashby and David R. H. Jones. *Engineering materials 1: an introduction to their properties and applications*. Butterworth-Heinemann, Oxford, UK, 2002.

[13] M. F. Ashby and Granta Design. *CES EduPack*. Ansys, Canonsburg, Pennsylvania, USA, 2019.

[14] Eric Pop, David Mann, Qian Wang, Kenneth Goodson, and Hongjie Dai. Thermal conductance of an individual single-wall carbon nanotube above room temperature. *Nano Letters*, 6:96–100, 2006.

[15] Choongho Yu, Li Shi, Zhen Yao, Deyu Li, and Arunava Majumdar. Thermal conductance and thermopower of an single-wall carbon nanotube. *Nano Letters*, 5:1842–1846, 2005.

[16] P. Kim, L. Shi, A. Majumdar, and P. L. McEuen. Thermal conductivity measurements of individual multiwalled nanotubes. *Physical Review Letters*, 21:215502, 2001.

[17] Tae Y. Choi, Dimos Poulikakos, Joy Tharian, and Urs Senohauser. Measurement of thermal conductivity of individual multiwalled carbon nanotubes by the 3-ω method. *Applied Physics Letters*, 87:013108, 2005.

[18] Michal T. Pettes and Li Sui. Thermal and structural characteristics of individual single-, double- and multi-walled carbon nanotubes. *Advanced Functional Materials*, 19:3918–3925, 2009.

[19] Agnieszka Lekawa-Raus, Jeff Patmore, Lukasz Kurzepa, John Bulmer, and Krzysztof Koziol. Electrical properties of carbon nanotube based fibres and their future use in electrical wiring. *Advanced Functional Materials*, 24:3661–3682, 2014.

[20] Meninder S. Purewal, Byung Hee Hong, Anirudhh Ravi, Bhupesh Chandra, James Hone, and Philip Kim. Scaling of resistance and mean free path of single-walled carbon nanotubes. *Physics Review Letters*, 98:186808, 2007.

[21] P. J. de Pablo, E. Graugnard, B. Walsh, R. P. Andres, S. Datta, and R. Reifenberger. A simple, reliable technique for making electrical contact to multiwalled carbon nanotubes. *Applied Physics Letters*, 74:323–325, 1998.

[22] Meng-Yen Tsai, Chung-Yi Yu, Chien-Hsin Yang, Nyan-Hwa Tai, Tsong-Pyng Perng, Chien-Ming Tu, Zishan Husain Khan, Yang-Chung Liao, and Cheng Chung Chi. Electrical transport properties of individual disordered multiwalled carbon nanotubes. *Applied Physics Letters*, 89:192115, 2006.

[23] Stefan Frank, Philippe Poncharal, Z. L. Wang, and Walt A. de Heer. Carbon nanotube quantum resistors. *Science*, 280:1744–1746, 1998.

[24] T. W. Ebbesen, H. J. Lezec, H. Hiura, J. W. Bennett, H. F. Ghaemi, and T. Thio. Electrical conductivity of individual carbon nanotubes. *Nature*, 382:54–56, 1996.

[25] Hongjie Dai, Eric W. Wong, and Charles M. Lieber. Probing electrical transport in nanomaterials: conductivity of individual carbon nanotubes. *Science*, 272:523–523, 1996.

[26] S. Agrawal, M. S. Raghuveer, H. Li, and G. Ramanath. Defect-induced electrical conductivity increase in individual multiwalled carbon nanotubes. *Applied Physics Letters*, 90:193104, 2007.

[27] Menghe Miao. Electrical conductivity of pure carbon nanotube yarns. *Carbon*, 49:3755–3761, 2011.

[28] Riichiro Saito, Mitsutaka Fujita, G. Dresselhaus, and M. S. Dresselhaus. Electronic structure of graphene tubules based on c_{60}. *Physica Review B*, 46:1804–1811, 1992.

[29] J. W. Mintmire, B. I Dunlap, and C. T. White. Are fullerene tubules metallic? *Physical Review Letters*, 68:631–634, 1992.

[30] Cheap tubes Ltd., Cambridgeport, and U.S.A. Carbon nanotube products, 2019. https://www.cheaptubes.com/, (Accessed: February 2019).

[31] Ya-Li Li, Ian A. Kinloch, and Alan H. Windle. Direct spinning of carbon nanotube fibres from chemical vapour deposition synthesis. *Science*, 304:276– 278, 2004.

[32] M. José Yacamán, M. Miki-Yoshida, L. Rendón, and J. G. Santiesteban. Catalytic growth of carbon microtubules with fullerene structure. *Applied Physics Letters*, 62:657–659, 1993.

[33] T. Guo, P. Nikolaev, A. Thess, D. T. Colbert, and R. E Smalley. Catalytic growth of single-walled nanotubes by laser vaporization. *Chemical Physics Letters*, 243:49–54, 1995.

[34] Jim Kong, Hyonsok T. Soh, Alan M. Cassell, Calvin F. Quate, and Hongjie Dia. Synthesis of individual single-walled carbon nanotubes on a patterned silicon wafer. *Nature*, 395:878–881, 1998.

[35] Brigitte Vigolo, Alain Pénicaud, Claude Coulon, Cédric Sauder, René Pailler, Catherine Journet, Patrick Bernier, and Philippe Poulin. Macroscopic fibers and ribbons of oriented carbon nanotubes. *Science*, 290:1331–1334, 2000.

[36] Nantero and USA. Nantero company overview, 2019. http://nantero.com/nantero-company-overview/management/, (Accessed: July 2019).

[37] Nanocomp, New Hampshire, and USA. About nanocomp. http://www.miralon.com/about-nanocomp, (Accessed: July 2019).

[38] Michael J. Bronikowski, Peter A. Willis, Daniel T. Colbert, K. A. Smith, and Richard E. Smalley. Gas-phase production of carbon single-walled nanotubes from carbon monoxide via the hipco process: A parametric study. *Journal of Vacuum Science & Technology A*, 19:1800, 2001.

[39] Tortech Nano Fibers. About tortech, 2019. https://www.tortechnano.com/cnt-fibers/, (Accessed: July 2019).

[40] Jenn Houston and Nanocomp Technologies. Juno spacecraft successfully enters jupiter's orbit with help of new hampshire company, 2016. http://www.miralon.com/newsblog/juno-spacecraft-successfully-enters-jupiters-orbit, (Accessed: July 2019).

[41] Linde Group. Linde electronics' carbon nanotube inks to drive innovation in next generation electronic devices, 2013. https://www.the-linde-group.com/en/news_and_media/press_releases/news_20130627.html, (Accessed: June 2019).

[42] Thomas Swan Ltd. Elicarb, 2019. https://thomas-swan.co.uk/chemical_products/elicarb/, (Accessed: June 2019).

[43] DexMat Ltd. About dexmat, 2019. https://dexmat.com/about/, (Accessed: June 2019).

[44] Kristyn Damadeo and Nasa Langley Research Centre. Nasa looking to tiny technology for big payoffs, 2018. https://www.nasa.gov/feature/langley/nasa-looking-to-tiny-technology-for-big-payoffs, (Accessed: July 2019).

[45] Ginger Gardiner and Composites World. Nanocomp technologies: About, 2016. https://www.compositesworld.com/articles/nanocomp-technologies-inc-merrimack-nh-us-, (Accessed: July 2019).

[46] Peter Clarke and EE Times. Fujitsu is licensee of nantero's carbon-nanotube ram, 2016. https://www.eetimes.com/document.asp?doc_id=1330387&#, (Accessed: July 2019).

[47] Sander J. Tans, Alwin R. M Verschueren, and Cees Dekker. Room-temperature transistor based on a single carbon nanotube. *Nature*, 292:45–52, 1998.

[48] Michael F. L. De Volder, Sameh H. Tawfick, Ray H. Baughman, and A. John Hart. Carbon nanotubes: present and future commercial applications. *Science*, 339:535–539, 2013.

[49] Morinobu Endo, Takuya Hayashi, and Yoong-Ahm Kim. Large-scale production of carbon nanotubes and their applications. *Pure Applied Chemistry*, 78:1703–1713, 2006.

[50] Yoshinori Ando Mukul Kumar. Chemical vapour deposition of carbon nanotubes: a review on growth mechanism and mass production. *Journal of Nanoscience and Nanotechnology*, 10:3739–3758, 2010.

[51] W. Z. Li, S. S. Xie, L. X. Qian, B. H. Chang, B. S. Zou, W. Y. Zhou, R. A. Zhao, and G. Wang. Large-scale synthesis of aligned carbon nanotubes. *Science*, 274:1701–1703, 1996.

[52] Chee Howe See and Andrew T. Harris. A review of carbon nanotube synthesis via fluidized-bed chemical vapour deposition. *Ind. Eng. Chem. Res*, 46:997–1012, 2007.

[53] Lee Weller, Fiona R. Smail, James A. Elliott, Alan H. Windle, Adam M. Boies, and Simone Hochgreb. Mapping the parameter space for direct-spun carbon nanotube aerogels. *Carbon*, 146:789–812, 2019.

[54] Krzysztof Koziol, Juan Vilatela, Anna Moisala, Marcelo Motta, Philip Cunniff, Michael Sennett, and Alan Windle. High-performance carbon nanotube fiber. *Science*, 318:1892–1895, 2007.

[55] Jessica P. Ryman-Rasmussen, Mark F. Cesta, Arnold R. Brody, Jeanette K. Shipley-Philips, Jeffrey I. Everitt, Earl W. Tewksbury, Owen R. Moss, Brian A. Wong, Darol E. Dodd, Melvin E. Andersen, and James C. Bonner. Inhaled carbon nanotubes reach the subpleural tissue in mice. *Nature Nanotechnology*, 4:747–751, 2009.

[56] Elsevier and Netherlands. Search on scopus for carbon nanotube related publications, 2019. https://www.scopus.com, (Accessed: February 2019).

[57] Google, Mountain View, California, and U.S.A. Search of google patent database for carbon nanotube related patents, 2019. https://patents.google.com/, (Accessed: February 2019).

[58] Germany Statista Inc, Hamburg. Market size of carbon nanotubes worldwide from 2012 to 2022, by application (in tons), 2019. https://www.statista.com/statistics/714708/carbon-nanotube-global-market-size-by-application/, (Accessed: February 2019).

[59] Ben Rogers, Jesse Adams, and Sumita Pennathur. *Nanotechnology: understanding small systems*. CRC Press, Taylor & Francis, Boca Raton, Florida, USA, 2015.

[60] Vivek Patel. Global carbon nanotube market – industry beckons, 2011. https://www.nanowerk.com/spotlight/spotid=23118.php, (Accessed: February 2019).

[61] Research and Markets Ltd. Carbon nanotubes (cnt) market by type, method, application – global forecast to 2023, 2018. https://www.marketsandmarkets.com/Market-Reports/carbon-nanotubes-139.html, Accessed: February 2019.

[62] Valentin N. Popov. Carbon nanotubes: properties and application. *Materials Science and Engineering R*, 43:61–102, 2004.

[63] Rasel Das, Md. Eaqub Ali, Sharifah Bee Abd Hamid, Seeram Ramakrishna, and Zaira Zaman Chowdhury. Carbon nanotube membranes for water purification: a bright future in water desalination. *Desalination*, 336:97–109, 2014.

[64] Jonathan N. Coleman, Umar Khan, Werner J. Blau, and Yurii K. Gun'ko. Small but strong: a review of the mechanical properties of carbon nanotube-polymer composites. *Carbon*, 44:1624–1652, 2006.

[65] M. J. Bieruck, M. C. Llaguno, M. Radosavljevic, J. K. Hyun, and A. T. Johnson. Carbon nanotube composites for thermal management. *Applied Physics Letters*, 80:2767–2769, 2002.

[66] Hua Huang, Changhong Liu, Yang Wu, and Shoushan Fan. Aligned carbon nanotube composite films for thermal management. *Advanced Materials*, 17:1652–1656, 2005.

[67] J. Hone, M. C. Llaguno, M. J. Biercuk, B. Batlogg A. T. Johnson, Z. Benes, and J. E. Fischer. Thermal properties of carbon nanotubes and nanotube-based materials. *Applied Physics A*, 74:339–343, 2002.

[68] Christine Jérôme Jean-Michel Thomassin, Thomas Pardoen, Christian Bailly, Isabelle Huyen, and Christophe Detrembluer. Polymer/carbon based composites as electromagnetic interference (emi) shielding materials. *Materials science and Engineering R*, 74:211–232, 2013.

[69] Luqi Liu, Wenjun Ma, and Zhong Zhang. Macroscopic carbon nanotube assemblies: preparation, properties, and potential applications. *Small*, 7:1504–1520, 2011.

[70] Christian Hoecker, Fiona Smail, Martin Pick, and Adam Boies. The influence of carbon source and catalyst nanoparticles on cvd synthesis of cnt aerogel. *Chemical Engineering Journal*, 314:388–395, 2017.

[71] T. S. Gspann, F. R. Smail, and A. H. Windle. Spinning of carbon nanotube fibres using the floating catalyst high temperature route: purity issues and the critical role of sulphur. *Faraday Discussions*, 173:47–65, 2014.

[72] Belén Alemán, Victor Reguero, Bartolomé Mas, and Juan J. Vilatela. Strong carbon nanotube fibers by drawing inspiration from polymer fiber spinning. *ACS Nano*, 9:7392–7398, 2015.

[73] Shan Li, Xiaohua Zhang, Jingna Zhao, Fancheng Meng, Geng Xu, Zhenzhong Yong, Jingjing Jia, Zuoguang Zhang, and Qingwen Li. Enhancement of carbon nanotube fibres using different solvents and polymers. *Composites Science and Technology*, 72:1402–1407, 2012.

[74] Anastasiia Mikhalchan, Thurid Gspann, and Alan Windle. Aligned carbon nanotube-epoxy composites: the effect of nanotube organization on strength, stiffness, and toughness. *Journal of Materials Science*, 51:10005–10025, 2016.

[75] Morinobu Endo. Grow carbon fibers in the vapor phase. *Chemtech*, 18:568–576, 1988.

[76] H. M. Cheng, F. Li, X. Sun, D. M. Brown, M. A. Pimenta, A. Marucci, G. Dresselhaus, and M. S. Dresselhaus. Bulk morphology and diameter distribution of single-walled carbon nanotubes synthesised by catalytic decomposition of hydrocarbons. *Chemical Physics Letters*, 289:602–610, 1998.

[77] Pavel Nikolaev, Michael J. Bronikowski, R. Kelly Bradley, Frank Rohmund, Daniel T. Colbert, K. A. Smith, and Richard E. Smalley. Gas-phase production of single-walled carbon nanotubes from carbon monoxide. *Chemical Physics Letters*, 313:91–97, 1999.

[78] B. Kitiyanan, W. E. Alvarez, J. H. Harwell, and D. E. Resasco. Controlled production of single-walled carbon nanotubes by catalytic decomposition of co on bimetallic co-mo catalysts. *Chemical Physics Letters*, 317:497–503, 2000.

[79] Michael De Volder, Sameh H. Tawfick, Sei Jin Park, Davor Copic, Zhouzhou Zhao, Wei Lu, and A. John Hart. Diverse 3d microarchitectures made by capillary forming of carbon nanotubes. *Advanced Materials*, 22:4384–4389, 2010.

[80] Mei Zhang, Ken R. Atkinson, and Ray H. Baughman. Multifunctional carbon nanotube yarns by downsizing an ancient technology. *Science*, 306:1358–1361, 2004.

[81] H. Muramatsu M. Endo, T. Hayashi, Y. A. Kim, M. Terrones, and M. S. Dresselhaus. Nanotechnology: 'buckypaper' from coaxial nanotubes. *Nature*, 433:476, 2005.

[82] W. Zhou, J. Vavro, C. Guthy, K. I. Winey, J. E. Fischer, L. M. Ericson, S. Ramesh, R. Saini, V. A. Davis, C. Kittrell, M. Pasquali, R. H. Hauge, and R. E. Smalley. Single wall carbon nanotube fibers extruded from super-acid suspensions: preferred orientation, electrical, and thermal transport. *Journal of Applied Physics*, 95:2004, 649-655.

[83] Paul Smith and Piet J. Lemstra. Ultra-high-strength polyethylene filaments by solution spinning/drawing. *Journal of Materials Science*, 15:505–514, 1980.

[84] Marcus A. Worsley, Joe H. Satcher, Jr., and Theodore F. Baumann. Synthesis and characterization of monolithic carbon aerogel nanocomposites containing double-walled carbon nanotubes. *Langmuir*, 24:9763–9766, 2008.

[85] Jinquan Wei, Hongwei Zhu, Yanhui Li, Bin Chen, Yi Jia, Kunlin Wang, Zhicheng Wang, Wenjin Liu, Jianbin Luo, Mingxin Zheng, Dehai Wu, Yanqiu Zhu, and Bingqing Wei. Ultrathin single-layered membranes from double-walled carbon nanotubes. *Advanced Materials*, 18:1695–1700, 2006.

[86] W. M. Haynes. *CRC Handbook of Chemistry and Physics*. CRC Press LLC, Boca Raton, Florida, USA, 2014.

[87] Ali E. Aliev, Csaba Guthy, Mei Zhang, Shaoli Fang, Anvar A. Zakhidov, John E. Fischer, and Ray H. Baughman. Thermal transport in mwnt sheets and yarns. *Carbon*, 45:2880–2888, 2007.

[88] Ken R. Atkinson, Stephen C. Hawkins, Chi Huynh, Chris Skourtis, Jane Dai, Mei Zhang, Shaoli Fang, Anvar A. Zakhidov, Sergey B. Lee, Ali E. Aliev, Christopher D. Williams, and Ray H. Baughman. Multifunctional carbon nanotube yarns and transparent sheets: Fabrication, properties and applications. *Physica B*, 394:339–343, 2007.

[89] Alexander E. Bogdanovich and Philip D. Bradford. Carbon nanotube yarn and 3d braid composites: part i: tensile testing and mechanical properties analysis. *Composites Part. A*, 41:230–237, 2010.

[90] Fei Deng, Weibang Lu, Haibo Zhao, Yuntian Zhu, Byung-Sun Kim, and Tsu-Wei Chou. The properties of dry-spun carbon nanotube fibers and their interfacial shear strength in an epoxy composite. *Carbon*, 49:1752–1757, 2011.

[91] Shaoli Fang, Mei Zhang, Anvar A. Zakhidov, and Ray H. Baughman. Structure and process-dependent properties of solid-state spun carbon nanotube yarns. *Journal of Physics and Condensed Matter*, 22:334221, 2010.

[92] Menghe Miao, Stephen C, Hawkins, Jackie Y. Cai, Thomas R. Gengenbach, Robert Knott, and Chi P. Huynh. Effect of gamma-irradiation on the mechanical properties of carbon nanotube yarns. *Carbon*, 49:4940–4947, 2011.

[93] Xiefei Zhang, Qingwen Li, Yi Tu, Yuan Li, James Y. Coulter, Lianxi Zheng, Yonghao Zhao, Qianxi Jia, Dean E. Peterson, and Yuntian Zhu. Strong carbon-nanotube fibers spun from long carbon-nanotube arrays. *Small*, 3:244–248, 2007.

[94] Xiefei Zhang, Qingwen Li, Terry G. Holesinger, Paul N. Arendt, Jianyu Huang, P. Douglas Kirven, Timothy G. Clapp, Raymond F. DePaula, Xiazhou Liao, Yonghao Zhao, Lianxi Zheng, Dean E. Peterson, and Yuntian Zhu. Ultrastrong, stiff and lightweight carbon nanotube fibres. *Advanced materials*, 19:4198–4201, 2007.

[95] Shanju Zhang, Lingbo Zhu, Marilyn L. Minus, Han Gi Chae, Sudhakar Jagannathan, Ching-Ping Wong, Janusz Kowalik, Luke B. Robertson, and Satish Kumar. Solid-state spun fibers and yarns from 1-mm long carbon nanotube forests synthesized by water-assisted chemical vapor deposition. *Journal of Materials Science*, 43:4356–4362, 2008.

[96] Kai Liu, Yinghui Sun, Ruifeng Zhou, Hanyu Zhu, Jiaping Wang, Liang Liu, Shoushan Fan, and Kaili Jiang. Carbon nanotube yarns with high tensile strength made by a twisting and shrinking method. *Nanotechnology*, 21:045708, 2010.

[97] Jiangtao Di, Shaoli Fang, Francisco A. Moura, Douglas S. Galvão, Julia Bykova, Ali Aliev, Mônica Jung de Andrade, Xavier Lepró, Na Li, Carter Haines, Raquel Ovalle-Robles, Dong Qian, and Ray H. Baughman. Strong, twist-stable carbon nanotube yarns and muscles by tension annealing at extreme temperatures. *Advanced Materials*, 28:6598–6605, 2016.

[98] Jandro L. Abot, Tareq Alosh, and Kalayu Belay. Strain dependence of electrical resistance in carbon nanotube yarn. *Carbon*, 70:95–102, 2014.

[99] Yoshinobu Shimamura, Kahori Oshima, Keiichiro Tohgo, Tomoyuki Fujii, Keiichi Shirasu, Go Yamamoto, Toshiyuki Hashida, Ken Goto, Toshio Ogasawara, Kimiyoshi Naito, Takayuki Nakano, and Yoku Inoue. Tensile mechanical properties of carbon nanotube/epoxy composite fabricated by pultrusion of carbon nanotube spun yarn preform. *Composites: Part A*, 62:32–38, 2014.

[100] Jackie Y. Cai, Jie Min, Jill McDonnell, Jeffrey S. Church, Christopher D. Easton, William Humphries, Stuart Lucas, and Andrea L. Woodhead. An improved method for functionalisation of carbon nanotube spun yarns with aryldiazonium compounds. *Carbon*, 50:4655–4662, 2012.

[101] Adrian Ghemes, Yoshitaka Minami, Junichi Muramatsu, Morihiro Okada, Hidenori Mimura, and Yoku Inoue. Fabrication and mechanical properties of carbon nanotube yarns spun from ultra-long multi-walled carbon nanotube arrays. *Carbon*, 50:4579–4587, 2012.

[102] Mei Zu, Qingwen Li, Yuntian Zhu, Yong Zhu, Guojian Wang, Joon-Hyung Byun, and Tsu-Wei Chou. Stress relaxation in carbon nanotube-based fibers for load-bearing applications. *Carbon*, 52:347–355, 2013.

[103] Mei Zhang, Shaoli Fang, Anvar A. Zakhidov, Sergey B. Lee, Christopher D. Williams Ali E. Aliev, Ken R. Atkinson, and Ray H. Baughman. Strong, transparent, multifunctional, carbon nanotube sheets. *Science*, 309:1215–1219, 2005.

[104] Liwen Zhang, Xin Wang, Weizong Xu, Yongyi Zhang, Qingwen Li, Philip D. Bradford, and Yuntian Zhu. Strong and conductive dry carbon nanotube films by microcombing. *Small*, 11:3830–3836, 2015.

[105] Ding Wang, Pengcheng Song, Canghong Liu, Wei Wu, and Shoushan Fan. Highly oriented carbon nanotube papers made of aligned carbon nanotubes. *Nanotechnology*, 19:075609, 2008.

[106] Yoku Inoue, Yusuke Suzuki, Yoshitaka Minami, Junichi Muramatsu, Yoshinobu Shimamura, Katsunori Suzuki, Adrian Ghemes, Morihiro Okada, Shingo Sabakibara, Hidenori Mimura, and Kimiyoshi Naito. Anisotropic carbon nanotube papers fabricated from multiwalled carbon nanotube webs. *Carbon*, 49:2437–2443, 2011.

[107] Jiangtao Di, Dongmei Hu, Hongyuan Chen, Zhenzhong Yong, Minghai Chen, Zhihai Feng, Yuntian Zhu, and Qingwen Li. Ultrastrong, foldable, and highly conductive carbon nanotube film. *ACS Nano*, 6:5457–5464, 2012.

[108] Yanjie Wang, Min Li, Yizhuo Gu, Xiaohua Zhang, Shaokai Wang, Qingwen Li, and Zuoguang Zhang. Tuning carbon nanotube assembly for flexible, strong and conductive films. *Nanoscale*, 7:3060–3066, 2015.

[109] Chunming Niu, Enid K. Sichel, Robert Hoch, David Moy, and Howard Tennent. High power electrochemical capacitors based on carbon nanotube electrodes. *Applied Physics Letters*, 70:1480–1482, 1997.

[110] Ray H. Baughman, Changxing Cui, Anvar A. Zakhidov, Zafar Iqbal, Joseph N. Barisci, Geoff M. Spinks, Gordon G. Wallace, Alberto Mazzoldi, Danilo De Rossi, Andrew G. Rinzler, Oliver Jaschinski, Siegmar Roth, and Miklos Kertesz. Carbon nanotube actuators. *Science*, 284:1340–1344, 1999.

[111] Shiren Wang, Zhiyong Liang, Ben Wang, and Chuck Zhang. High-strength and multifunctional macroscopic fabric of single-walled carbon nanotubes. *Advanced Materials*, 19:1257–1261, 2007.

[112] T. V. Sreekumar, Tao Liu, Satish Kumar, Lars M. Ericson, Robert H. Hauge, and Richard E. Smalley. Single-wall carbon nanotube films. *Chemistry of Materials*, 15:175–178, 2003.

[113] A. D. Bozhko, D. E. Sklovsky, V. A. Nalimova, A. G. Rinzler, R. E. Smalley, and J. E. Fischer. Resistance vs. pressure of single-wall carbon nanotubes. *Applied Physics A*, 67:75–77, 1998.

[114] Philip G. Whitten, Adrian A. Gestos, Geoffrey M. Spinks, Kerry J. Gilmore, and Gordon G. Wallace. Free standing carbon nanotube composite bio-electrodes. *J Biomed Mater Res B Appl Biomater*, 82:37–43, 2007.

[115] Sharali Malik, Harald Rösner, Frank Hennrich, Artur Böttcher, Manfred M. Kappes, Tilmann beck, and Markus Auhorn. Failure mechanism of free standing single-walled carbon nanotube thin films under tensile load. *Physical Chemistry Chemical Physics*, 6:3540–3544, 2004.

[116] I-Wen Peter Chen, Richard Liang, Haibo Zhao, Ben Wang, and Chuck Zhang. Highly conductive carbon nanotube buckypapers with improved doping stability via conjugational cross-linking. *Nanotechnology*, 22:485708, 2011.

[117] Wen-Tai Hong and Nyan-Hwa Tai. Investigations on the thermal conductivity of composites reinforced with carbon nanotubes. *Diamond and Related materials*, 17:1577–1581, 2008.

[118] Hongyuan Chen, Minghai Chen, Jiangtao Di, Geng Xu, Hongbo Li, and Qingwen Li. Architecting three-dimensional networks in carbon nanotube buckypapers for thermal interface materials. *Journal of Physical Chemistry C*, 116:3903–3909, 2012.

[119] J. E. Fischer, W. Zhou, J. Vavro, M. C. Llaguno, C. Guthy, R. Haggenmueller, M. J. Casavant, D. E. Walters, and R. E. Smalley. Magnetically aligned single wall carbon nanotube films: preferred orientation and anisotropic transport properties. *Journal of Applied Physics*, 93:2157–2163, 2003.

[120] Michael B. Jukubinek, Benham Ashrafi, Jingwen Guan, Michael B. Johnson, Mary Anne White, and Benoit Simard. 3d chemically cross-linked single-walled carbon nanotube buckypapers. *RSC Advances*, 4:57564–57573, 2014.

[121] Natnael Behabtu, Colin C. Young, Dmitri E. Tsentalovich, Olga Kleinerman, Xuan Wang, Anson W. K. Ma, Amram Bengio, Ron F. ter Waarbeek, Jorrit J. de Jong, Ron E. Hoogerwerf, Steven B. Fairchild, John B. Ferguson, Benji Maruyama, Junichiro Kono, Yeshayahu Talmon, Yachin Cohen, Marcin J. Otto, and Matteo Pasquali. Strong, light, multifunctional fibers of carbon nanotubes with ultrahigh conductivity. *Science*, 339:182–186, 2013.

[122] Lars M. Ericson, Hua Fan, Haiqing Peng, Virginia A. Davis, Wei Zhou, Joseph Sulpizio, Yuhuang Wang, Richard Brooker, Juraj Vavro, Csaba Guthy, A. Nicholas G. Parra-Vasquez, Myung Jong Kim, Sivarajan Ramesh, Rajesh K. Saini, Carter Kittrell, Gerry Lavin, Howard Schmidt, W. Wade Adams, W. E. Billups, Matteo Pasquali, Wen-Fang Hwang, Robert H. Hauge, John E. Fischer, and Richard E. Smalley. Macroscopic, neat, single-walled carbon nanotube fibers. *Science*, 305:1447–1450, 2004.

[123] Chengmin Jiang, Avishek Saha, Colin C. Young, Daniel Paul Hashim, Carolyn E. Ramirez, Pulickel M. Ajayan, Matteo Pasquali, and Angel A. Marti. Macroscopic nanotube fibers spun from single-walled carbon nanotube polyelectrolytes. *ACS Nano*, 8:9107–9112, 2014.

[124] L. Piraux, F. Abreu Araujo, and T. N. Biu. Two-dimensional quantum transport in highly conductive carbon nanotube fibers. *Physical Review B*, 92:085428, 2015.

[125] Francesca Mirri, Nathan D. Orloff, Aaron M. Forster, Rana Ashkar, Robert J. Headrick, E. Amram Bengio, Christian J. Long, April Choi, Yimin Luo, Angela R. Hight Walker, Paul Butler, Kalman B. Migler, and Matteo Pasquali. Lightweight, flexible, high-performance carbon nanotube cables made by scalable flow coating. *Applied Materials & Interfaces*, 8:4903–4910, 2016.

[126] Don Shiffler, Steve Fairchild, Wilkin Tang, Benji Maruyama, Ken Golby, Matthel LaCour, Matteo Pasquali, and Nathaniel Lockwood. Demonstration of an acid-spun single-walled nanotube fiber cathode. *IEEE Transactions on Plasma Science*, 40:1871–1877, 2012.

[127] S. B. Fairchild, J. Boeckl, T. C. Back, J. B. Ferguson, H. Koerner, P. T. Murray, B. Maruyama, M. A. Lange, M. M. Cahay, N. Behabtu, C. C. Young, M. Pasquali, N. P. Lockwood, K. L. Averett, G. Grun, and D. E. Tsentalovich. Morphology dependent field emission of acid-spun carbon nanotube fibers. *Nanotechnology*, 26:105706, 2015.

[128] Xuan Wang, Natnael Behabtu, Colin C. Young, Dmitri E. Tsentalovich, Matteo Pasquali, and Junichiro Kono. High-ampacity power cables of tightly-packed and aligned carbon nanotubes. *Advanced Functional Materials*, 24:3241–3249, 2014.

[129] Jian-Min Feng, Rui Wang, Ya-Li Li, Xiao-Hua Zhong, Lan Cui, Qian-Jin Guo, and Feng Hou. One-step fabrication of high quality double-walled carbon nanotube thin films by a chemical vapor deposition process. *Carbon*, 48:3817–3824, 2010.

[130] I. Stuart Fraser, Marcelo S. Motta, Ron K. Schmidt, and Alan H. Windle. Continuous production of flexible carbon nanotube-based transparent conductive films. *Science and Technology of Advanced Materials*, 11:045004, 2010.

[131] Dawid Janas and Krzysztof K. Koziol. Rapid electrothermal response of high-temperature carbon nanotube film heaters. *Carbon*, 59:457–463, 2013.

[132] Jae-Woo Kim, Emilie J. Siochi, Jennifer Carpena-Nunez, Kristopher E. Wise, John W. Connell, Yi Lin, and Russell A. Wincheski. Polyaniline/carbon nanotube sheet nanocomposites: fabrication and characterization. *ACS Applied Materials & Interfaces*, 5:8597–8606, 2013.

[133] Jae-Woo Kim, Godfrey Sauti, Emilie J. Siochi, Joseph G. Smith, Russell A. Wincheski, Roberto J. Cano, John W. Connell, and Kristopher E. Wise. Toward high performance thermoset/carbon nanotube sheet nanocomposites via resistive heating assisted infiltration and cure. *Applied Materials & Interfaces*, 6:18832–18843, 2014.

[134] Peng Liu, Thang Q. Tran, Zeng Fan, and Hai M. Duong. Formation mechanisms and morphological effects on multi-properties of carbon nanotube fibers and their polyimide aerogel-coated composites. *Composites Science and Technology*, 117:114–120, 2015.

[135] Fengmei Guo, Can Li, Jianquan Wei, Ruiqiao Xu, Zelin Zhang, Kunlin Wang, and Dehai Wu. Fabrication of highly conductive carbon nanotube fibers for electrical application. *Materials Research Express*, 2:095604, 2015.

[136] Fujun Xu, Baochun Wei, Wei Liu, Hongfei Zhu, Yongyi Zhang, and Yiping Qiu. In-plane mechanical properties of carbon nanotube films fabricated by floating catalyst chemical vapour decomposition. *Journal of Materials Science*, 50:8166–8174, 2015.

[137] Min Li, Zhenzhen Wang, Qianli Liu, Shaokai Wang, Yizhuo Gu, Yanxia Li, and Zuoguang Zhang. Carbon nanotube film/epoxy composites with high strength and toughness. *Polymer Composites*, 38:588–596, 2017.

[138] Joseph Severino, Jenn-Ming Yang, Larry Carlson, and Robert Hicks. Progression of alignment in stretched cnt sheets determined by wide angle x-ray scattering. *Carbon*, 100:309–317, 2016.

[139] Jiali Yu, Weibang Lu, Shaopeng Pei, Ke Gong, Liyun Wang, Linghui Meng, Yudong Huang, Joseph P. Smith, Karl S. Booksh, Qingwen Li, Joon-Hyung Byun, Youngseok Oh, Yushan Yan, and Tsu-Wei Chou. Omnidirectionally stretchable high-performance supercapacitor based on isotropic buckled carbon nanotube films. *ACS Nano*, 10:5204–5211, 2016.

[140] Heath E. Misak, James L. Rutledge, Eric D. Swenson, and Shankar Mall. Thermal transport properties of dry spun carbon nanotube sheets. *Journal of Nanomaterials*, 2016:9174085, 2016.

[141] Peng Liu, Zeng Fan, Anastasiia Mikhalchan, Thang Q. Tran, Daniel Jewell, Hai M. Duong, and Amy M. Marconnet. Continuous carbon nanotube-based fibers and films for applications requiring enhanced heat dissipation. *Applied Materials & Interfaces*, 8:17461–17471, 2016.

[142] Wenjun Ma, Li Song, Rong Yang, Taihua Zhang, Yuanchun Zhao, Lianfeng Sun, Yan Ren, Dongfang Liu, Lifeng Liu, Jun Shen, Zhengxing Zhang, Yanjuan Xiang, Weiya Zhou, and SiShen Xie. Directly synthesized strong, highly conducting, transparent single-walled carbon nanotube films. *Nano Letters*, 7:2307–2311, 2007.

[143] Jacob W. Singleton, Heath E. Misak, and Shankar Mall. Relationships between tensile behaviour, physical parameters and manufacturing parameters of carbon nanotube sheet. *Materials & Design*, 116:199–206, 2017.

[144] Qianli Liu, Min Li, Yizhuo Gu, Yongyi Zhang, Shaokai Wang, Qingwen Li, and Zuoguang Zhang. Highly aligned dense carbon nanotube sheets induced by multiple stretching and pressing. *Nanoscale*, 6:4338–4344, 2014.

[145] Wenjun Ma, Luqi Liu, Rong Yang, Taihua Zhang, Zhong Zhang, Li Song, Yan Ren, Jun Shen, Zhiqiang Niu, Weiya Zhou, and Sishen Xie. Monitoring a micromechanical process in macroscale carbon nanotube films and fibers. *Advanced Materials*, 21:603–608, 2009.

[146] Jack Alvarenga, Paul R. Jarosz, Chris M. Schauerman, Brian T. Moses, Brian J. Landi, Cory D. Cress, and Ryne P. Raffaelle. High conductivity carbon nanotube wires from radial densification and ionic doping. *Applied Physics Letters*, 97:182106, 2010.

[147] J. N. Wang, X. G. Luo, T. Wu, and Y. Chen. High-strength carbon nanotube fibre-like ribbon with high ductility and high electrical conductivity. *Nature Communications*, 5:3848, 2014.

[148] Marcelo Motta, Ya-Li Li, Ian Kinloch, and Alan Windle. Mechanical properties of continuously spun fibers of carbon nanotubes. *Nano Letters*, 5:1529–1533, 2005.

[149] Kelly L. Stano, Krzysztof Koziol, Martin Pick, Marcelo S. Motta, Anna Moisala, Juan J. Vilatela, Stuart Frasier, and Alan H. Windle. Direct spinning of carbon nanotube fibres from liquid feedstock. *International Journal of Material Forming*, 1:59–62, 2008.

[150] J. Chaffee, D. Lashmore, D. Lewis, J. Mann, M. Schauer, and B. White. Direct synthesis of cnt yarns and sheets. *NSTI-Nanotech*, 3:118–121, 2008.

[151] Richard J. Davies, Christian Riekel, Krzysztof K. Koziol, Juan J. Vilatela, and Alan H. Windle. Structural studies on carbon nanotube fibres by synchrotron radiation microdiffraction and microfluorescence. *Journal of Applied Crystallography*, 42:1122–1128, 2009.

[152] R. J. Mora, J. J. Vilatela, and A. H. Windle. Properties of composites of carbon nanotube fibres. *Composites Science and Technology*, 69:1558–1563, 2009.

[153] Xiao-Hua Zhong, Ya-Li Li, Ya-Kun Liu, Xiao-Hua Qiao, Yan Feng, Ji Liang, Jun Jin, Lu Zhu, Feng Hou, and Jin-You Li. Continuous multilayered carbon nanotube yarns. *Advanced Materials*, 22:692–696, 2010.

[154] Mark W. Schauer, David S. Lashmore, Diana J. Lewis, Benjamin M. Lewis, and Erik C. Towle. Strength and electrical conductivity of carbon nanotube yarns. *Material Research Society Syposium Proceedings*, 1258:263–268, 2010.

[155] Frances A. Hill. *Mechanical Energy Storage in Carbon Nanotube Springs*. Massachusetts Institute of Technology, USA, 2011.

[156] Qiu Li, Yi-Lan Kang, Wei Qiu, Ya-Li Li, Gan-Yun Huang, Jian-Gang Guo, Wei-Lin Deng, and Xiao-Hua Zhong. Deformation mechanisms of carbon nanotube fibres under tensile loading by in situ raman spectroscopy analysis. *Nanotechnology*, 22:225704, 2011.

[157] Amanda S. Wu, Xu Nie, Matthew C. Hudspeth, Weinong W. Chen, Tsu-Wei Chou, David S. Lashmore, Mark W. Schauer, Erick Tolle, and Jeff Rioux. Strain rate-dependent tensile properties and dynamic electromechanical response of carbon nanotube fibers. *Carbon*, 50:3876–3881, 2011.

[158] Amanda S. Wu, Tsu-Wei Chou, John W. Gillespie, Jr., David Lashmore, and Jeff Rioux. Electromechanical response and failure behaviour of aerogel-spun carbon nanotube fibres under tensile loading. *Journal of Materials Chemistry*, 22:6792–6798, 2012.

[159] Xiao-Hua Zhong, Ya-Li Li, Jian-Min Feng, Yan-Ru Kang, and Shuai-Shuai Han. Fabrication of a multifunctional carbon nanotube "cotton" yarn by the direct chemical vapour deposition spinning process. *Nanoscale*, 4:5614–5618, 2012.

[160] Juan J. Vilatela and Alan H. Windle. A multifunctional yarn made of carbon nanotubes. *Journal of Engineered Fibers and Fabrics*, 7:23–28, 2012.

[161] V. Sabelkin, H. E. Misak, S. Mall, R. Asmatulu, and P. E. Kladitis. Tensile loading behaviour of carbon nanotube wires. *Carbon*, 50:2530–2538, 2012.

[162] Yong-Mun Choi, Hungo Choo, Hyeonuk Yeo, Nam-Ho You, Dong Su Lee, Bon-Cheol Ku, Hwan Chul Kim, Pill-Hoon Bong, YoungJin Jeong, and Munju Goh. Chemical method for improving both the electrical conductivity and mechanical properties of carbon nanotube yarn via intramolecular cross-dehydrogenative coupling. *ACS Applied Materials & Interfaces*, 5:7726–7730, 2013.

[163] H. E. Misak, V. Sabelkin, S. Mall, and P. E. Kladitis. Thermal fatigue and hypothermal atomic oxygen exposure behaviour of carbon nanotube wires. *Carbon*, 57:42–49, 2013.

[164] Frances A. Hill, Timothy F. Havel, David Lashmore, Mark Schauer, and Carol Livermore. Storing energy and powering small systems with mechanical springs made of carbon nanotube yarn. *Energy*, 76:318–325, 2014.

[165] A. Abu Obaid, D. Heider, and J. W. Gillespie Jr. Investigation of electro-mechanical behaviour of carbon nanotube yarns during tensile loading. *Carbon*, 93:731–741, 2015.

[166] H. E. Misak and S. Mall. Electrical conductivity, strength and microstructure of carbon nanotube multi-yarns. *Materials and Design*, 75:76–84, 2015.

[167] H. E. Misak and S. Mall. Time-dependent electrical properties of carbon nanotube yarns. *New Carbon Materials*, 30:207–213, 2015.

[168] Thang Q. Tran, Zeng Fan, Anastasiia Mikhalchan, Peng Liu, and Hai M. Duong. Post-treatments for multifunctional property enhancement of carbon nanotube fibers from the floating catalyst method. *Applied Materials & Interfaces*, 8:7948–7956, 2016.

[169] Yanan Yue, Kang Liu, Man Li, and Xuejiao Hu. Thermal manipulation of carbon nanotube fiber by mechanical stretching. *Carbon*, 77:973–979, 2014.

[170] Anyuan Cao, Pamela L. Dickrell, W. Gregory Sawyer, Mehrdad N. Ghasemi-Nejhad, and Pulickel M. Ajayan. Super-compressible fomalike carbon nanotube films. *Science*, 310:1307–1310, 2005.

[171] Xuchan Gui, Jinquan Wei, Kunlin Wang, Anyuan Cao, Hongwei Zhu, Yi Jia, Qinke Shu, and Dehai Wu. Carbon nanotube sponges. *Advanced materials*, 22:617–621, 2010.

[172] Xuchun Gui, Anyuan Cao, Jinquan Wei, Hongbian Li, Yi Jia, Lili Fan, Kunlin Wang, Hongwei Zhu, and Dehai Wu. Soft, highly conductive nanotube sponges and composites with controlled compressibility. *ACS Nano*, 4:2320–2326, 2010.

[173] Ryan R. Kohlmeyer, Maika Lor, Jian Deng, Haiying Liu, and Jian Chen. Preparation of stable carbon nanotube aerogels with high electrical conductivity and porosity. *Carbon*, 49:2352–2361, 2011.

[174] Marcus A. Worsley, Sergei O. Kucheyev, Joshua D. Kuntz, Tammy Y. Olson, T. Yong-Jin Han, Alex V. Hamza, Joe H. Satcher, Jr., and Theodore F. Baumann. Carbon scaffolds for stiff and highly conductive monolithic oxide-carbon nanotube scaffolds. *Chemistry of Materials*, 23:3504–3061, 2011.

[175] Marcus A. Worsley, Sergei O. Kucheyev, Joe H. Satcher, Jr., Alex V. Hamza, and Theodore F. Baumann. Mechanically robust and electrically conductive carbon nanotube foams. *Applied Physics Letters*, 94:073115, 2009.

[176] Marcus A. Worsley, Peter J. Pauzauskie, Sergei O. Kucheyev, Joseph M. Zaug, Alex V. Hamza, Joe H. Satcher Jr., and Theodore F. Baumann. Properties of single-walled carbon nanotube-based aerogels as a function of nanotube loading. *Acta Materialia*, 57:5131–5136, 2009.

[177] Zhuyin Sui, Qinghan Meng, Xuetong Zhang, Rui Ma, and Bing Cao. Green synthesis of carbon nanotube-graphene hybrid aerogels and their use as versatile agents for water purification. *Journal of Materials Chemistry*, 22:8767–8771, 2012.

[178] Jianhua Zou, Jianhua Liu, Ajay Singh Karakoti, Amit Kumar, Daeha Joung, Qiang Li, Saiful I. Khondaker, Sudipta Seal, and Lei Zhai. Ultralight multiwalled carbon nanotube aerogel. *ACS Nano*, 4:7293–7302, 2010.

[179] Xuetong Zhang, Jiren Liu, Bin Xu, Yuefeng Su, and Yunjun Luo. Ultralight conducting polymer/carbon nanotube composite aerogels. *Carbon*, 49:1884–1893, 2011.

[180] Yufeng Luo, Shu Luo, Hengcai Wu, Mengya Li, Ke Wang, Lingjia Yan, Kaili Jiang, Qunqing Li, Shoushan Fan, and Jiaping Wang. Self-expansion construction of ultralight carbon nanotube aerogels with a 3d and hierarchical cellular structure. *Small*, 13:1700966, 2017.

[181] Shaghayegh Faraji, Kelly L. Stano, Ozkan Yildiz, Ang Li, Yuntian Zhu, and Philip D. Bradford. Ultralight anisotropic foams from layered aligned carbon nanotube sheets. *Nanoscale*, 7:17038, 2015.

[182] Qingjun Cai, Bing chung Chen, Yuan Zhao, Julia Mack, Yanbao Ma, Chung lung Chen, Hengzhi Wang, and Zhifeng Ren. Thermal property measurements of carbon nanotube forest synthesized by thermal cvd process. *Proceedings of the ASME Summer Heat Transfer Conference 2009*, 2:443–449, 2009.

[183] Christian P. Deck, Jason Flowers, Gregg S. B. McKee, and Kenneth Vecchio. Mechanical behaviour of ultralong multiwalled carbon nanotube mats. *Journal of Applied Physics*, 101:023512, 2007.

[184] Michael De Volder, Sameh Tawfick, Sei Jin Park, and A. John Hart. Corrugated carbon nanotube microstructures with geometrically tunable compliance. *ACS Nano*, 5:7310–7317, 2011.

[185] Michael De Volder, Sei Jin Park, Sameh H. Tawfick, Daniel O. Vidaud, and A. John Hart. Fabrication and electrical integration of robust carbon nanotube electrodes. *Journal of Micromechanics and Microengineering*, 21:045033, 2011.

[186] Don N. Futaba, Kenji Hata, Takeo Yamada, Tatsuki Hiraoka, Yuhei Hayamizu, Yozo Kakudate, Osamu Tanaike, Hiroaki Hatori, Motoo Yumura, and Sumio Iijima. Shape-engineerable and highly densely packed single-walled carbon nanotubes and their application as super-capacitor electrodes. *Nature Materials*, 5:987–994, 2006.

[187] Yuhei Hayamizu, Takeo Yamada, Kohei Mizuno, Robert C. Davis, Don N. Futaba, Motoo Yumura, and Kenji Hata. Integrated three-dimensional microelectromechanical devices from processable carbon nanotube wafers. *Nature*, 3:289–294, 2008.

[188] Yuhei Hayamizu, Robert C. Davis, Takeo Yamada, Don N. Futaba, Satoshi Yusada, Motoo Yumura, and Kenji Hata. Mechanical properties of beams from self-assembled closely packed and aligned single-walled carbon nanotubes. *Physical Review Letters*, 102:175505, 2008.

[189] Ilia Ivanov, Alexander Puretzky, Gyula Eres, Hsin Wang, Zhengwei Pan, Hongtao Cui, Rongying Jin, Jane Howe, and David B. Geohegan. Fast and highly anisotropic thermal transport through vertically aligned carbon nanotube arrays. *Applied physics Letters*, 89:223110, 2006.

[190] Ludovica Lattanzi, Jordan R. Raney, Luigi De Nardo, Abha Misra, and Chiara Daraio. Nonlinear viscoelasticity of freestanding and polymer-anchored vertically aligned carbon nanotube foams. *Journal of Applied Physics*, 111:074314, 2012.

[191] Cheng-Te Lin, Chi-Young Lee, Tsung-Shune Chin, Rong Xiang, Kei Ishikawa, Junichiro Shiomi, and Shigeo Maruyama. Anisotropic electrical conduction of vertically-aligned single-walled carbon nanotube films. *Carbon*, 49:1446–1452, 2011.

[192] Abha Misra, Julia R. Greer, and Chiara Daraio. Strain rate effects in the mechanical response of polymer-anchored carbon nanotube foams. *Advanced Materials*, 21:334–338, 2009.

[193] M. A. Panzer, G. Zhang, D. Mann, X. Hu, E. Pop, H. Dai, and K. E. Goodson. Thermal properties of metal-coated vertically aligned single-wall nanotube arrays. *Journal of Heat Transfer*, 130:052401, 2008.

[194] Siddhartha Pathak, Z. Goknur Cambaz, Surya R. Kalidindi, and J. Gregory Swadener andYury Gogotsi. Viscoelasticity and high buckling stress of dense carbon nanotube brushes. *Carbon*, 47:1969–1976, 2009.

[195] Siddhartha Pathak, Ee J. Lim, Parisa Pour Shahid Saeed Abadi, Samuel Graham, Baratunde A. Cola, and Julia R. Greer. Higher recovery and better energy dissapation at faster strain rates in carbon nanotube bundles: an in-situ study. *ACS Nano*, 6:2189–2197, 2012.

[196] Siddhartha Pathak, Nisha Mohan, Elizabeth Decolvenaere, Alan Needleman, Mostafa Bedewy, A. John Hart, and Julia R. Greer. Local relative density modulates failure and strength in vertically aligned carbon nanotubes. *ACS Nano*, 7:8593–8604, 2013.

[197] A. Qiu, D. F. Bahr, A. A. Zbib, A. Bellou, S. Dj. Mesarovic, D. McClain, W. Hudson, J. Jiao, D. Kiener, and M. J. Cordill. Local and non-local behaviour and coordinated buckling of cnt turfs. *Carbon*, 49:1430–1438, 2011.

[198] J. Suhr, P. Victor, L. Ci, S. Sreekala, X. Zhang, O. Nalamasu, and P. M. Ajayan. Fatigue resistance of aligned carbon nanotube arrays under cyclic compression. *Nature*, 2:417–421, 2007.

[199] S. Tawfick, K. O'Brien, and A. J. Hart. Flexible high-conductivity carbon-nanotube interconnects made by rolling and printing. *Small*, 5:2467–2473, 2009.

[200] Tao Tong, Yang Zhao, Lance Delzeit, Ali Kashani, M. Meyyappan, and A. Majumdar. Dense vertically aligned multiwalled carbon nanotube arrays as thermal interface materials. *IEEE transactions on components and packaging technologies*, 30:92–100, 2007.

[201] Geza Toth, Jani Maklin, Niina Halonen, Jaako Palosaari, Jari Juuti, Heli Jantunen, Krisztian Kordas, W. Gregory Sawyer, Robert Vajtai, and Pulickel M. Ajayan. Carbon-nanotube-based electrical brush contacts. *Advanced Materials*, 21:2054–2058, 2009.

[202] Yuan Xu, Yi Zhang, and Ephraim Suhir. Thermal properties of carbon nanotube array used for integrated circuit cooling. *Journal of Applied Physics*, 100:074302, 2006.

[203] Onnik Yaglioglu, Anyuan Cao, A. John Hart, Rod Martens, and A. H. Slocum. Wide range control of microstructure and mechanical properties of carbon nanotube forests: a comparison between fixed and floating catalyst cvd techniques. *Advanced Functional Materials*, 22:5028–5037, 2012.

[204] D. J. Yang, S. G. Wang, Q. Zhang, P. J. Sellin, and G. Chen. Thermal and electrical transport in multi-walled carbon nanotubes. *Physics Letters A*, 329:207–213, 2004.

[205] Xiaojun Liang, Jungho Shin, Daniel Magagnosc, Yijie Jiang, Sei Jin Park, A. John Hart, Kevin Turner, Daniel S. Gianola, and Prashant K. Purohit. Compression and recovery of carbon nanotube forests described as a phase transition. *International Journal of Solids and Structures*, 122-123:196–209, 2017.

[206] Assaf Ya'akobovitz, Mostafa Bedewy, Abhinav Rao, and A. John Hart. Strain relaxation and resonance of carbon nanotube forests under electrostatic loading. *Carbon*, 96:250–258, 2016.

[207] Anna Brieland-Shoultz, Sameh Tawfick, Sei Jin Park, Mostafa Bedewy, Matthew R. Maschmann, Jeffery W. Baur, and A. John Hart. Scaling the stiffness, strength and toughness of ceramic-coated nanotube foams into the structural regime. *Advanced Functional Materials*, 24:5728–5735, 2014.

[208] Matthew R. Maschmann, Gregory J. Ehlert, Sei Jin Park, David Mollenhauer, Benji Maruyama, A. John Hart, and Jeffery W. Bauer. Visualizing strain evolution and coordinated buckling within cnt arrays by in situ digital image correlation. *Advanced Functional Materials*, 22:4686–4695, 2012.

[209] Natnael Behabtu, Micah J. Green, and Matteo Pasquali. Carbon nanotube-based neat fibers. *Nano Today*, 3:24–34, 2008.

[210] Kaili Jiang, Jaiping Wang, Qunqing Li, Liang Liu, Changhong Liu, and Shoushan Fan. Superaligned carbon nanotube arrays, films, and yarns: a road to applications. *Advanced Materials*, 23:1154–1161, 2011.

[211] Stefania Nardecchia, Daniel Carriazo, M. Luisa Ferrer, María C. Gutiérrez, and Francisco del Monte. Three dimensional macroporous architectures and aerogels built of carbon nanotubes and/or graphene: synthesis and applications. *Chemical Society Reviews*, 42:794–830, 2013.

[212] Sherif Araby, Aidong Qiu, Ruoyu Wang, Zhiheng Zhao, Chun-Hui Wang, and Jun Ma. Aerogels based on carbon nanotube materials. *Journal of Materials Science*, 51:9157–9189, 2016.

[213] Eduard G. Rakov. Materials made of carbon nanotubes. the carbon nanotube forest. *Russian Chemical Reviews*, 82:538–566, 2013.

[214] Qing Cao and John A. Rogers. Ultrathin films of single-walled carbon nanotubes for electronics and sensors: a review of fundamental and applied aspects. *Advanced Materials*, 21:29–53, 2009.

[215] G. Gruner. Carbon nanotube films for transparent and plastic electronics. *Journal of Materials Chemistry*, 16:3533–3539, 2006.

[216] Hongwei Zhu and Bingqing Wei. Assembly and applications of carbon nanotube thin film. *Journal of Materials Science and Technology*, 24:447–456, 2008.

[217] Guanghui Xu, Qian Zhang, Weiping Zhou, Jiaqi Huang, and Fei Wei. The feasibiliy of producing mwcnt paper and strong mwcnt film from vacnt array. *Applied Physics A*, 92:531–539, 2008.

[218] Jiangtao Di, Xin Wang, Yajuan Xing, Yongyi Zhang, Xiaohua Zhang, Weibang Liu, Qingwen Li, and Yuntian T. Zhu. Dry-processable carbon nanotubes for functional devices and composites. *Small*, 10:4606–4625, 2014.

[219] Jiangtao Di, Xiaohua Zhang, Zhenzhong Yong, Yongyi Zhang, Da Li, Ru Li, and Qingwen Li. Carbon-nanotube fibers for wearable devices and smart textiles. *Advanced Materials*, 28:10529–10538, 2016.

[220] Menghe Miao. Yarn spun from carbon nanotube forests: Production, structure, properties and applications. *Particuology*, 11:378–393, 2013.

[221] Tsu-Wei Chou, Limin Gao, Erik T. Thostenson, Zuoguang Zhang, and Joon-Hyung Byun. An assessment of the science and technology of carbon nanotube-based fibers and composites. *Composites Science & Technology*, 70:1–19, 2010.

[222] Kaili Jiang, Qunqing Li, and Shoushan Fan. Nanotechnology: Spinning continuous carbon nanotube yarns. *Nature*, 419:801, 2002.

[223] Junbeom Park and Kun-Hong Lee. Carbon nanotube yarns. *Korean Journal of Chemical Engineering*, 29:277–287, 2012.

[224] Changgu Lee, Xiaoding Wei, Jeffrey W. Kysar, and James Hone. Measurement of the elastic properties and intrinsic strength of monolayer graphene. *Science*, 321:385–388, 2008.

[225] L. J. Gibson and M. F. Ashby. *Cellular solids: structure and properties*. Cambridge University Press, Cambridge, UK, 1997.

[226] C. Y. Ho, R. W. Powell, and P. E. Liley. Thermal conductivity of the elements: a comprehensive review. *Journal of Physical and Chemical Reference Data*, 3:Supplement No. 1, 1974.

[227] Dong Qian, Gregory J. Wagner, Wing Kam Liu, Min-Feng Yu, and Rodney S. Ruoff. Mechanics of carbon nanotubes. *Applied Mechanics Reviews*, 55:495–533, 2002.

[228] A. H. Barber, I. Kaplan-Ashir, S. R. Cohen, R. Tenne, and H. D. Wagner. Stochastic strength of nanotubes: an appraisal of available data. *Composites Science and Technology*, 65:2380–2384, 2005.

[229] T. Belytschko, and G. C. Schatz S. P. Xiao, and R. S. Ruoff. Atomistic simulations of nanotube fracture. *Physical Review B*, 65:235430, 2002.

[230] J. Y. Huang, S. Chen, Z. Q. Wang, K. Kempa, Y. M. Wang, S. H. Jo, G. Chen, M. S. Dresselhaus, and Z. F. Ren. Superplastic carbon nanotubes. *Nature*, 439:281, 2006.

[231] B. I. Yakobson. Mechanical relaxation and "intramolecular plasticity" in carbon nanotubes. *Applied Physics Letters*, 72:918–920, 1998.

[232] Feng Ding, Kun Jiao, Mingqi Wu, and Boris I. Yakobson. Pseudoclimb and dislocation dynamics in superplastic nanotubes. *Physical Review Letters*, 98:075503, 2007.

[233] R. S. Ruoff and D. C. Lorents. Mechanical and thermal properties of carbon nanotubes. *Carbon*, 33:925–930, 1995.

[234] M. M. J. Treacy, T. W. Ebbesen, and J. M. Gibson. Exceptionally high young's modulus observed for individual carbon nanotubes. *Nature*, 381:678–680, 1996.

[235] Philippe Poncharal, Z. L. Wang, Daniel Ugarte, and Walt A. de Heer. Electrostatic deflections and electromechanical resonances of carbon nanotubes. *Science*, 283:1513–1516, 1999.

[236] Shigenobu Ogata and Yoji Shibutani. Ideal tensile strength and band gap of single-walled carbon nanotubes. *Physical Review B*, 68:165409, 2003.

[237] W. Ding, L. Calabri, K. M. Kohlaas, X. Chen, D. A. Dikin, and R. S. Ruoff. Moduli, fracture strength and brittle vs plastic response of the outer shell of arc-grown multiwalled carbon nanotubes. *Experimental Mechanics*, 47:25–36, 2007.

[238] Asa H. Barber, Rodney Andrews, Linda S. Schadler, and H. Daniel Wagner. On the tensile strength distribution of multiwalled carbon nanotubes. *Applied Physics Letters*, 87:203106, 2005.

[239] Michael F. Ashby and David R. H. Jones. *Engineering Materials 2: an introduction to microstructures and processing*. Butterworth-Heinemann, Elsevier, Oxford, UK, 2013.

[240] Sulin Zhang, Steven L. Mielke, Roopam Khare, Diego Troya, Rodney S. Ruoff, George C. Schatz, and Ted Belytschko. Mechanics of defects in carbon nanotubes: atomistic and multiscale simulations. *Physical Review B*, 71:115403, 2005.

[241] Roopam Khare, Steven L. Mielke, Jeffrey T. Paci, Sulin Zhang, Roberto Ballarini, George C. Schatz, and Ted Belytschko. Coupled quantum mechanical/molecular mechanical modeling of the fracture of defective carbon nanotubes and graphene sheets. *Physical Review B*, 75:075412, 2007.

[242] Steven L. Mielke, Diego Troya, Sulin Zhang, Je-Luen Li, Shaoping Xiao, Roberto Car, Rodney S. Ruoff, George C. Schatz, and Ted Belytschko. The role of vacancy defects and holes in the fracture of carbon nanotubes. *Chemical Physics Letters*, 390:413–420, 2004.

[243] Akira Takakura, Ko Beppu, Taishi Nishihara, Akihito Fukui, Takahiro Kozeki, Takahiro Namazu, Yuehi Miyauchi, and Kenichiro Itami. Strength of carbon nanotubes depends on their chemical structures. *Nature Communications*, 10:3040, 2019.

[244] Marco Buongiorno Nardelli, B. I. Yakobson, and J. Bernholc. Brittle and ductile behaviour in carbon nanotubes. *Physical Review Letters*, 81:4656–4659, 1998.

[245] A.J. Stone and D.J. Wales. Theoretical studies of icosahedral c60 and some related species. *Chemical Physics Letters*, 128:501–503, 1986.

[246] Traian Drumatică, Ted Belytschko, and Boris I. Yakobson. Bond-breaking bifurcation states in carbon nanotube fracture. *Journal of Chemical Physics*, 118:9485–9488, 2003.

[247] Boris I. Yakobson Traian Drumatică, Ming Hua. Symmery-, time-, and temperature-dependent strength of carbon nanotubes. *PNAS*, 103:6105–6109, 2006.

[248] Simio Iijima, Charles Brabec, Amitest Maiti, and Jerzy Bernholc. Structural flexibility of carbon nanotubes. *Journal of Chemical Physics*, 104:2089–2092, 1996.

[249] M. R. Falvo, G. J. Clary, R. M. Taylor II, V. Chi, F. P. Brooks Jr, S. Washburn, and R. Superfine. Bending and buckling of carbon nanotubes under large strain. *Nature*, 389:582–584, 1997.

[250] B. I. Yakobson, C. J. Brabec, and J. Bernholc. Nanomechanics of carbon tubes: instabilities beyond linear response. *Physical Review Letters*, 76:2511–2514, 1996.

[251] M. Arroyo and T. Belytschko. Nonlinear mechanical response and rippling of thick multiwalled carbon nanotubes. *Physical Review Letters*, 92:215505, 2003.

[252] James A. Elliott, Jan K. W. Sandler, Alan H. Windle, Robert J. Young, and Milo S. P. Shaffer. Collapse of single-wall carbon nanotubes is diameter dependent. *Physical Review Letters*, 92:095501, 2004.

[253] Antonio Pantano, Mary C. Boyce, and David M. Parks. Nonlinear structural mechanics based modeling of carbon nanotube deformation. *Physical Review Letters*, 91:145504, 2003.

[254] Antonio Pantano, David M. Parks, and Mary C. Boyce. Mechanics of deformation of single- and multi-wall carbon nanotubes. *Journal of the Mechanics and Physics of Solids*, 52:789–821, 2004.

[255] Lianxi Shen and Jackie Li. Transversely isotropic elastic properties of single-walled carbon nanotubes. *Physical Review B*, 69:045414, 2004.

[256] Min-Feng Yu, Tomasz Kowalewski, and Rodney S. Ruoff. Investigation of the radial deformability of individual carbon nanotubes under controlled indentation force. *Physical Review Letters*, 85:1456–1459, 2000.

[257] I. Palaci, S. Fedrigo, H. Brune, C. Klinke, M. Chen, and E. Riedo. Radial elasticity of multiwalled carbon nanotubes. *Physical Review Letters*, 94:175502, 2005.

[258] R. R. Schlittler, J. W. Seo, J. K. Gimzewski, C. Durkan, M. S. Saifullah, and M. E. Welland. Single crystals of single-walled carbon nanotubes formed by self-assembly. *Science*, 292:1136–1139, 2001.

[259] Andreas Thess, Roland Lee, Pavel Nikolaev, Hongjie Dai, Pierre Petit, Jerome Robert, Chunhi Xu, Young Hee Lee, Seong Gon Kim, Andrew G. Rinzler, Daniel T. Colbert, Gustavo E. Scuseria, David Tománek, John E. Fischer, and Richard E. Smalley. Crystalline ropes of metallic carbon nanotubes. *Science*, 273:483–487, 1996.

[260] Rodney S. Ruoff, J. Tersoff, Donald C. Lorentz, Shekhar Subramoney, and Bryan Chan. Radial deformation of carbon nanotubes by van der waals forces. *Nature*, 364:514–516, 1993.

[261] J. Z. Liu, Q.-S. Zheng, L.-F. Wang, and Q. Jiang. Mechanical properties of single-walled carbon nanotube bundles as bulk materials. *Journal of the Mechanics and Physics of Solids*, 53:123–142, 2005.

[262] Juan J. Vilatela, James A. Elliott, and Alan H. Windle. A model for the strength of yarn-like carbon nanotube fibers. *ACS Nano*, 5:1921–1927, 2011.

[263] J. Tersoff and R. S. Ruoff. Structural properties of a carbon-nanotube crystal. *Physical Review Letters*, 73:676–679, 1994.

[264] Jean-Paul Salvetat, G. Andrew D. Briggs, Jean-Marc Bonard, Revathi R. Bacsa, and Andrzej Kulik. Elastic and shear moduli of single-walled carbon nanotube ropes. *Physical Review Letters*, 82:944–947, 1999.

[265] Min-Feng Yu, Bradley S. Files, Sivaram Arepalli, and Rodney S. Ruoff. Tensile loading of ropes of single-wall carbon nanotubes and their mechanical properties. *Physical Review Letters*, 84:5552–5555, 2000.

[266] T. Filleter, R. Bernal, S. Li, and H. D. Espinosa. Ultrahigh strength and stiffness in cross-linked hierarchical carbon nanotube bundles. *Advanced Materials*, 23:2855–2860, 2011.

[267] Mohammad Naraghi, Tobin Filleter, Alexander Moravsky, Mark Locascio, Raouf O. Loutfy, and Horacio D. Espinosa. A multiscale study of high performance double-walled nanotube-polymer fibers. *ACS Nano*, 4:6463–6476, 2010.

[268] Surinder M. Sharma, S. Karmakar, S. K. Sikka, Pallavi V. Teredesai, A. K. Sood, A. Govindaraj, and C. N. R. Rao. Pressure-induced phase transformation and structural resilience of single-wall carbon nanotube bundles. *Physical Review B*, 63:205417, 2001.

[269] Jie Tang, Lu-Chang Qin, Taizo Sasaki, Masako Yudasaka, Akiyuki Matsushita, and Sumio Iijima. Compressibiity and polygonization of single-walled carbon nanotubes under hydrostatic pressure. *Physical Review Letters*, 85:1887–1889, 2000.

[270] M. J. Peters, L. E. McNeil, Jian Ping Lu, and Daniel Kahn. Structural phase transition in carbon nanotube bundles under pressure. *Physical Review B*, 61:5939–5944, 2000.

[271] U. D. Venkateswaran, A. M. Rao, E. Richter, M. Menon, A. Rinzler, R. E. Smalley, and P. C. Eklund. Probing the single-wall carbon nanotube bundle: Raman scattering under high pressure. *Physical Review B*, 59:10928–10934, 1999.

[272] Jian Ping Lu. Elastic properties of carbon nanotubes and nanoropes. *Physical Review Letters*, 79:1297–1300, 1997.

[273] E. Saether, S. J. V. Frankland, and R. B. Pipes. Transverse mechanical properties of single-walled carbon nanotube crystals: Part i: determination of elastic moduli. *Composites Science and Technology*, 63:1543–1550, 2003.

[274] V. N. Popov, V. E. Van Doren, and M. Balkanski. Elastic properties of crystals of single-walled carbon nanotubes. *Solid State Communications*.

[275] A. Kis, G. Csányi, J.-P. Salvetat, Thien-Nga Lee, E. Couteau, A. J. Kulik, W. Benoit, J. Brugger, and L. Forró. Reinforcement of single-walled carbon nanotube bundles by intertube bridging. *Nature Materials*, 3:153–157, 2004.

[276] A. Kis, K. Jensen, S. Aloni, W. Mickelson, and A. Zettl. Interlayer forces and ultralow sliding friction in multiwalled carbon nanotubes. *Physical Review Letters*, 97:025501, 2006.

[277] Osamu Suekane, Atsuko Nagataki, Hideki Mori, and Yoshikazu Nakayama. Static friction force of carbon nanotube surfaces. *Applied Physics Express*, 1:064001, 2008.

[278] Mohammad Naraghi, Graham H. Bratzel, Tobin Filleter, Zhi An, Xiaoding Wei, Son-Bihn T. Nguyen, Markus J. Buehler, and Horacio D. Espinosa. Atomistic investigation of load transfer between dwnt bundles "crosslinked" by pmma oligomers. *Advanced Functional Materials*, 23:1883–1892, 2013.

[279] X. Wei, T. Filleter, and H. D. Espinosa. Optimal length scales emerging from shear load transfer in natural materials: application to carbon-based nanocomposite design. *ACS Nano*, 6:2333–2344, 2012.

[280] Jeffrey T. Paci, Al'ona Furmanchuk, Horacio D. Espinosa, and George C. Schatz. Shear and friction between carbon nanotubes in bundles and yarns. *Nano Letters*, 14:6138–6147, 2014.

[281] Bharat Bhushan, Xiang Ling, Alain Jungen, and Christopher Hierold. Adhesion and friction of a multiwalled carbon nanotube sliding against a single-walled carbon nanotube. *Physical Review B*, 77:165428, 2008.

[282] Bharat Bhushan and Xiang Ling. Adhesion and friction between individual carbon nanotubes measured using force-versus-distance curves in atomic force microscopy. *Physical Review B*, 78:045429, 2008.

[283] John Cumings and A. Zettl. Low-friction nanoscale linear bearing realized from multiwall carbon nanotubes. *Science*, 289:602–604, 2000.

[284] Min-Feng Yu, Boris I. Yakobson, and Rodney S. Ruoff. Controlled sliding and pullout of nested shells in individual multiwalled carbon nanotubes. *Journal of Physical Chemistry B*, 104:8764–8767, 2000.

[285] B. T. Kelly. *Physics of Graphite*. Applied Science Publishers, London, United Kingdom, 1981.

[286] Ze Liu, Jiarui Yang, Francois Grey, Jefferson Zhe Liu, Yilun Liu, Yibing Wang, Yanlian Yang, Yao Cheng, and Quanshui Zheng. Observation of microscale superlubricity in graphite. *Physical Review Letters*, 108:205503, 2012.

[287] Rufan Zhang, Zhiyuan Ning, Yingying Zhang, Quanshui Zheng, Qing Chen, Huanhuan Xie, Qian Zhang, Weizhong Qian, and Fei Wei. Superlubricity in centimeters-long double-walled carbon nanotubes under ambient conditions. *Nature Nanotechnology*, 8:912–916, 2013.

[288] D. E. Soule and C. W. Nezbeda. Direct basal-plane shear in single-crystal graphite. *Journal of Applied Physics*, 11:5122–5139, 1968.

[289] M. R. Falvo, R. M. Taylor II, A. Helser, V. Chi, F. P. Brooks Jr, S. Washburn, and R. Superfine. Nanometre-scale rolling and sliding of carbon nanotubes. *Nature*, 397:236–238, 1999.

[290] Tobin Filleter, Scott Yockel, Mohammad Naraghi, Jeffrey T. Paci, Owen C. Compton, Maricris L. Mayes, SonBinh T. Nguyen, George C. Schatz, and Horacio D. Espinosa. Experimental-computational study of shear interactions within double-walled carbon nanotube bundles. *Nano Letters*, 12:732–742, 2012.

[291] J. Israelachvili. *Intermolecular & surface forces*. Academic Press Ltd., Cambridge, Massachusetts, USA, 1991.

[292] Boris V. Derjaguin. The force between molecules. *Scientific American*, 203:47–53, 1960.

[293] René M. Overney Lakshmi S. Kocherlakota, Brad A. Krajina. Communication: local energetic analysis of the interfacial and surface energies of graphene from the single layer to graphite. *Journal of Chemical Physics*, 143:241105, 2015.

[294] Michael R. Roenbeck, Xiaoding Wei, Allison M. Beese, Mohammad Naraghi, Al'ona Furmanchuk, Jeffrey T. Paci, George C. Schatz, and Horacio D. Espinosa. In situ scanning electron microscope peeling to quantify surface energy between multiwalled carbon nanotubes and graphene. *ACS Nano*, 8:124–138, 2014.

[295] Christian. D. Van Engers, Nico E. A. Cousens, Vitaliy Babenko, Jude Britton, Bruno Zappone, Nicole Grobert, and Susan Perkin. Direct measurement of the surface energy of graphene. *Nano Letters*, 17:3815–3821, 2017.

[296] R. H. S. Winterton D. Tabor. Surface forces: direct measurement of normal and retarded van der waals forces. *Nature*, 219:1120–1121, 1969.

[297] L. A. Girifalco. *Ph.D. thesis*. University of Cincinnati, 1954.

[298] L. A. Girifalco and R. A. Lad. Energy of cohesion, compressibility, and the potential energy functions of the graphite system. *Journal of Chemical Physics*, 25:693–698, 1956.

[299] Lorin X. Benedict, Nasreen G. Chopra, Marvin L. Cohen, A. Zettl, Steven G. Louie, and Vincent H. Crespi. Microscopic determination of the interlayer binding energy in graphite. *Chemical Physics Letters*, 286:490–496, 1998.

[300] Renju Zacharia, Hendrik Ulbricht, and Tobias Hertel. Interlayer cohesive energy from thermal desorption of polyaromatic hydrocarbons. *Physical Review B*, 69:155406, 2004.

[301] Ze Liu, Jefferson Zhe Liu, Yao Cheng, Zhihong Li, Li Wang, and Quanshui Zheng. Interlayer binding energy of graphite: a mesoscopic determination from deformation. *Physical Review B*, 85:205418, 2012.

[302] Minggang Xia, Chunping Liang, Zhaofeng Chen, Ruixue Hu, and Shiru Liu. The adhesion energy measured by a stress accumulation-peeling mechanism in the exfoliation of graphite. *Physical Chemistry Chemical Physics*, 21:1217–1223, 2019.

[303] Wen Wang, Shuyang Dai, Xide Li, Jiarui Yang, David J. Srolovitz, and Quanshui Zheng. Measurement of the cleavage energy of grahite. *Nature Communications*, 6:7853, 2015.

[304] Elad Koren, Emanuel Lörtscher, Colin Rawlings, Armin W. Knoll, and Urs Duerig. Adhesion and friction in mesoscopic graphite contacts. *Science*, 348, 2015.

[305] Peng Li, Zheng You, and Tianhong Cui. Adhesion energy of few layer graphene characterized by atomic force microscope. *Sensors and Actuators A: Physical*, 217:56–61, 2014.

[306] Jun Wang, Dan C. Sorescu, Seokmin Jeon, Alexei Balianinov, Sergei V. Kalinin, Arthur P. Baddorf, and Petro Maksymovych. Atomic intercalation to measure adhesion of graphene on graphite. *Nature Communications*, 7:13263, 2016.

[307] B. A. Krajina, L. J. Kocherlakota, and R. M. Overney. Direct determination of the local hamaker constant of inorganic surfaces based on scanning force microscopy. *Journal of Chemical Physics*, 141:164707, 2014.

[308] Eric Pop, Vikas Varshney, and Ajit K. Roy. Thermal properties of graphene: fundamentals and applications. *MRS Bulletin*, 37:1273–1281, 2012.

[309] Qunfeng Cheng, Jianwen Bao, JinGyu Park, Zhiyong Liang, Chuck Zhang, and Ben Wang. High mechanical performance composite conductor: multi-walled carbon nanotube sheet/bismaleimide nanocomposites. *Advanced Functional Materials*, 19:3219–3225, 2009.

[310] Rebekah Downes, Shakai Wang, David Haldane, Andrew Moench, and Richard Liang. Strain-induced alignment mechanisms of carbon nanotube networks. *Advanced Engineering Materials*, 17:349–358, 2015.

[311] Yuanyuan Shang, Ying Wang, Shuhui Li, Chunfei Hua, and Mingchu Zou. High-strength carbon nanotube fibers by twist-induced self-strengthening. *Carbon*, 119:47–55, 2017.

[312] Juan J. Vilatela and Alan H. Windle. Yarn-like carbon nanotube fibers. *Advanced Materials*, 22:4959–4963, 2010.

[313] J. P. Attwood, N. A. Fleck, H. N. G. Wadley, and V. S. Deshpande. The compressive response of ultra-high molecular weight polyethylene fibres and composites. *International Journal of Solids and Structures*, 71:141–155, 2015.

[314] Allison M. Beese, Xiaoding Wei, Sourangsu Sarkar, Rajaprakash Ramacandramoorthy, Michael R. Roenbeck, Alexander Moravsky, Matthew Ford, Fazel Yavari, Denis T. Keane, Raouf O. Loufty, SonBinh T. Nguyen, and Horacio D. Espinosa. Key factors limiting carbon nanotube yarn strength: exploring processing-structure-property relationships. *ACS Nano*, 8:11454–11466, 2014.

[315] V. S. Deshpande, M. F. Ashby, and N. A. Fleck. Foam topology bending versus stretching dominated architectures. *Acter Materialia*, 49:1035–1040, 2001.

[316] C. P. Broedersz and F. C. Mackintosh. Modeling semiflexible polymer networks. *Reviews of Modern Physics*, 86:995–1036, 2014.

[317] L. Berhan, Y. B. Yi, A. M. Sastry, E. Munoz, M. Selvidge, and R. Baughman. Mechanical properties of nanotube sheets: alterations in joint morphology and achievable moduli in manufacturable materials. *Journal of Applied Physics*, 95:4335, 2004.

[318] D. A. Head, A. J. Levine, and F. C. MacKintosh. Distinct regimes of elastic response and deformation modes of cross-linked cytoskeletal and semiflexible polymer networks. *Physical Review E*, 68:061907, 2003.

[319] Mark Bathe, Claus Heussinger, Mireille M. A. E. Claessens, Andreas R. Bausch, and Erwin Frey. Cytoskeletal bundle mechanics. *Biophysical Journal*, 94:2955–2964, 2008.

[320] L. Berhan, Y. B. Li, and A. M. Sastry. Effect of nanorope waviness on the effective moduli of nanotube sheets. *Journal of Applied Physics*, 95:5027, 2004.

[321] Kerstyn Comley and Norman A. Fleck. A micromechanical model for the young's modulus of adipose tissue. *International Journal of Solids and Structures*, 47:2982–2990, 2010.

[322] Digby D. Symons and Norman A. Fleck. The imperfection sensitivity of isotropic two-dimensional elastic lattices. *Journal of Applied Mechanics*, page 051011, 2008.

[323] Bo Xie, Yilun Liu, Yiting Ding, Quanshui Zheng, and Zhiping Xu. Mechanics of carbon nanotube networks: microstructural evolution and optimal design. *Soft Matter*, 7:10039, 2007.

[324] Linda Vaisman, H. Daniel Wagner, and Gad Marom. The role of surfactants in dispersion of carbon nanotubes. *Advances in Colloid and Interface Science*, 128-130:37–46, 2006.

[325] Yan Yan Huang and Eugene M. Terentjev. Dispersion of carbon nanotubes: mixing, sonication, stabilization and composite properties. *Polymers*, 4:275–295, 2012.

[326] J. B. Bai and A. Allaoui. Effect of the length and the aggregate size of mwnts on the improvement efficiency of the mechanical and electrical properties of nanocomposites – experimental investigation. *Composites: Part A*, 34:689–694, 2003.

[327] Kevin P. Ryan, Martin Cadek, Valeria Nicolosi, David Blond, Manuel Ruether, Gordon Armstrong, Harry Swan, Antonio Fonseca, Janos B. Nagy, Wolfgang K. Maser, Werner J. Blau, and Jonathan N. Coleman. Carbon nanotubes for reinforcement of plastics? a case study with poly(vinyl alcohol). *Composites Science and Technology*, 67:1640–1649, 2007.

[328] Jing Zhu, JongDae Kim, Haiqing Peng, John L. Margrave, Valery N. Khabashesku, and Enrique V. Barrera. Improving the dispersion and integration of single-wall carbon nanotubes in epoxy composites through functionalization. *Nano Letters*, 3:1107–1113, 2003.

[329] P. Miaudet, S. Badaire, M. Maugey, A. Derré, V. Pichot, P. Launois, P. Poulin, and C. Zakri. Hot-drawing of single and multiwall carbon nanotube fibers for high toughness and alignment. *Nano Letters*, 5:2212–2215, 2005.

[330] Jiangsha Meng, Yiying Zhang, Kenan Song, and Marilyn L. Minus. Forming crystalline polymer-nano interphase structures for high-modulus and high-tensile/strength composite fibers. *Macromolecular Materials and Engineering*, 299:144–153, 2013.

[331] Jonathan N. Coleman, Werner J. Blau, Alan B. Dalton, Edgar Muñoz, Steve Collins, Bog G. Kim, Joselito Razel, Miles Selvidge, Guillermo Vieiro, and Ray H. Baughman. Improving the mechanical properties of single-walled carbon nanotube sheets by intercalation of polymeric adhesives. *Applied Physics Letters*, 82:1682–1684, 2003.

[332] Giang T. Pham, Young-Bin Park, Shiren Wang, Zhiyong Liang, Ben Wang, Chuck Zhang, Percy Funchess, and Leslie Kramer. Mechanical and electrical properties of polycarbonate nanotube buckypaper composite sheets. *Nanotechnology*, 19:325705, 2008.

[333] Paulo E. Lopes, Ferrie van Hattum, Celeste M. C. Pereira, Paulo J. R. O. Nóvoa, Sefan Forero, Felicitas Hepp, and Laurent Pambaguian. High cnt content composites with cnt buckypaper and epoxy resin matrix: impregnation behaviour composite production and characterization. *Composites Structures*, 92:1291–1298, 2010.

[334] Ana Díez-Pascual, Jingwen Guan, Benoit Simard, and Marián A. Gómez-Fatou. Poly(phenylene sulphide) and poly(ether ether ketone) composites reinforced with single-walled carbon nanotube buckypaper: ii – mechanical properties, electrical and thermal conductivity. *Composites: Part A*, 43:1007–1015, 2012.

[335] Qunfeng Cheng, Ben Wang, Chuck Zhang, and Zhiyong Liang. Functionalized carbon-nanotube sheet/bismaleimide nanocomposites: mechanical and electrical performance beyond carbon-fiber composites. *Small*, 6:763–767, 2010.

[336] H. S. Kim. Processing and characterization of carbon nanotube mat/epoxy composites. *Metals and Materials International*, 17:697–704, 2011.

[337] Brian L. Wardle, Diego S. Saito, Enrique J. García, A. John Hart, Roberto Guzmán de Villoria, and Eric A. Verploegen. Fabrication and characterization of ultrahigh-volume-fraction aligned carbon nanotube-polymer composites. *Advanced Materials*, 20:2707–2714, 2008.

[338] Philip D. Bradford, Xin Wang, Haibo Zhao, Jon-Paul Maria, Quanxi Jia, and Y. T. Zhu. A novel approach to fabricate high volume fraction nanocomposites with long aligned carbon nanotubes. *Composites Science and Technology*, 70:1980–1985, 2010.

[339] Matthias Mecklenburg, Daisuke Mizushima, Naoto Ohtake, Wolfgang Bauhofer, Bodo Fiedler, and Karl Schulte. On the manufacturing and electrical and mechanical properties of ultra-high wt.% fraction aligned mwcnt and randomly oriented cnt epoxy composites. *Carbon*, 91:275–290, 2015.

[340] Q. F. Cheng, J. P. Wang, J. J. Wen, C. H. Liu, K. L. Jiang, Q. Q. Li, and S. S. Fan. Carbon nanotube/epoxy composites fabricated by resin transfer molding. *Carbon*, 48:260–266, 2010.

[341] Ya-Nan Liu, Min Li, Yizhou Gu, Yongyi Zhang, Qingwen Li, and Zuoguang Zhang. Ultrastrong carbon nanotube/bismaleimide composite film with super-aligned and tightly packing structure. *Composites Science and Technology*, 117:176–182, 2015.

[342] Qunfeng Cheng, Jiaping Wang, Kaili Jiang, Qunqing Li, and Shoushan Fan. Fabrication and properties of aligned multiwall carbon nanotube-reinforced epoxy composites. *Journal of Materials Research*, 23:2975–2983, 2008.

[343] Wei Liu, Xiaohua Zhang, Geng Xu, Philip D. Bradford, Xin Wang, Haibo Zhao, Yingying Zhang, Quanxi Jia, Fuh-Gwo Yuan, Qingwen Li, Yiping Qiu, and Yuntian Zhu. Producing superior composites by winding carbon nanotubes onto a mandrel under a poly(vinyl alcohol) spray. *Carbon*, 49:4786–4791, 2011.

[344] X. Yao, B. G. Falzon, S. C. Hawkins, and S. Tsantzalis. Aligned carbon nanotube webs embedded in a composite laminate: a route towards a highly tunable electro-thermal system. *Carbon*, 129:486–494, 2018.

[345] Xin Wang, Qian Jiang, Weizong Xu, Wei Cai, Yoku Inoue, and Yuntian Zhu. Effect of carbon nanotube length on thermal, electrical and mechanical properties of cnt/bismalemidime composites. *Carbon*, 53:145–152, 2013.

[346] Erik T. Thostenson, Zhifeng Ren, and Tsu-Wei Chou. Advances in the science and technology of carbon nanotubes and their composites: a review. *Composites Science and Technology*, 61:1899–1912, 2001.

[347] Nitilaksha Hiremath, Jimmy Mays, and Gajanan Bhat. Recent developments in carbon fibers and carbon nanotube-based fibers: a review. *Polymer Reviews*, 57:339–368, 2017.

[348] Yaodong Liu and Satish Kumar. Polymer/carbon nanotube nano composite fibers – a review. *ACS Applied Materials & Interfaces*, 6:6069–6087, 2014.

[349] J-H. Du, J. Bai, and H-M. Cheng. The present status and key problems of carbon nanotube based polymer composites. *eXPRESS Polymer Letters*, 1:253–273, 2007.

[350] F. T. Fisher, R. D. Bradshaw, and L. C. Brinson. Fiber waviness in nanotube-reinforced polymer composites – i: Modulus predictions using effective nanotube properties. *Composites Science and Technology*, 63:1689–1703, 2003.

[351] Xiao Zhang, Wei Tan, Fiona Smail, Michael De Volder, Norman Fleck, and Adam Boies. High-fedelity characterization on anisotropic thermal conductivity of carbon nanotube sheets and on their effects of thermal enhancement of nanocomposites. *Nanotechnology*, 29:365708, 2018.

[352] Frank Gardea and Dimitris C. Lagoudas. Characterization of electrical and thermal properties of carbon nanotube/epoxy composites. *Composites: Part B*, 56:611–620, 2014.

[353] Lei Gao, Xiaofeng Zhou, and Yulong Ding. Effective thermal and electrical conductivity of carbon nanotube composites. *Chemical Physics Letters*, 434:297–300, 2007.

[354] Wei Cui, Feipeng Du, Jinchao Zhao, Wei Zhang, Yingkui Yang, Xiaolin Xie, and Yiu-Wing Mai. Improving thermal conductivity while retaining high electrical resistivity of epoxy composites by incorporating silica-coated multi-walled carbon nanotubes. *Carbon*, 49:495–500, 2011.

[355] Jin Gyu Park, Qunfeng Cheng, Jun Lu, Jianwen Bao, Shu Li, Ying Tian, Zhiyong Liang, Chuck Zhang, and Ben Wang. Thermal conductivity of mwcnt/epoxy composites: the effects of length, alignment and functionalization. *Carbon*, 50:2083–2090, 2012.

[356] Qian Jiang, Xin Wang, Yuntian Zhu, David Hui, and Yiping Qiu. Mechanical, electrical and thermal properties of aligned carbon nanotube/polyimide composites. *Composites: Part B*, 56:408–412, 2014.

[357] A. Moisala, Q. Li, I. A. Kinloch, and A. H. Windle. Thermal and electrical conductivity of single- and multi-walled carbon nanotube-epoxy composites. *Composites Science and Technology*, 66:1285–1288, 2006.

[358] Florian H. Gojny, Malte H. G. Wichmann, Bodo Fiedler, Ian A. Kinloch, Wolfgang Bauhofer, Alan H. Windle, and Karl Schulte. Evaluation and identification of electrical and thermal conduction mechanisms in carbon nanotube/epoxy composites. *Polymer*, 47:2036–2045, 2006.

[359] Juan J. Vilatela, Rupesh Khare, and Alan H. Windle. The hierarchical structure and properties of multifunctional carbon nanotube fibre composites. *Carbon*, 50:1227–1234, 2012.

[360] E. S. Choi, J. S. Brooks, D. L. Eaton, M. S. Al-Haik, M. Y. Hussaini, H. Garmestani, D. Li, and K. Dahmen. Enhancement of thermal and electrical properties of carbon nanotube polymer composites by magnetic field processing. *Journal of Applied Physics*, 94:6034–6039, 2003.

[361] G. D. Dean and P. Turner. The elastic properties of carbon fibres and their composites. *Composites*, 4:174–180, 1973.

[362] Thomas Bru, Peter Hellström, Renaud Gutkin, Dimitra Ramantani, and Göran Peterson. Characterisation of the mechanical and fracture properties of a uni-weave carbon fibre/epoxy non-crimp fabric composite. *Data in Brief*, 6:680–695, 2016.

[363] C. Qian, L. T. Harper, T. A. Turner, and N. A. Warrior. Notched behaviour of discontinuous carbon fibre composites: comparison with quasi-isotropic non-crimp fabric. *Composites: Part A*, 42:293–302, 2011.

[364] S. Hernández, F. Sket, C. González, and J. LLorca. Optimization of curing cycle in carbon fiber-reinforced laminates: void distribution and mechanical properties. *Composites Science and Technology*, 85:73–82, 2013.

[365] Mohsen M. Sohi, Thomas H. Hahn, and Jerry G. Williams. Effect of resin toughness and modulus on compressive failure modes of quasi-isotropic graphite/epoxy laminates. *ASTM Special Technical Publication*, pages 37–60, 1987.

[366] Wei Tan and Brian G. Falzon. Modelling the crush behaviour of thermoplastic composites. *Composites Science and Technology*, 134:57–71, 2016.

[367] Erik T. Thostenson and Tsu-Wei Chou. On the elastic properties of carbon nanotube-based composites: modelling and characterization. *Journal of Physics D: Applied Physics*, 36:573–582, 2003.

[368] Tran Huu Nam, Ken Goto, Yudai Yamaguchi, E. V. A. Premalal, Yoshinobu Shimamura, Yoku Inoue, Shuichi Arikawa, Satoru Yoneyama, and Shinji Ogihara. Improving mechanical properties of high volume fraction aligned multi-walled carbon nanotube/epoxy composites by stretching and pressing. *Composites Part B*, 85:15–23, 2016.

[369] W. A. Curtin. The tough' to brittle transition in brittle matrix composites. *Journal of the Mechanics and Physics of Solids*, 41:217–245, 1993.

[370] F. Barthelat, H. Tang, P. D. Zavattieri, C.-M. Li, and H. D. Espinosa. On the mechanics of mother-of-pearl: a key feature in the material hierarchical structure. *Journal of the Mechanics and Physics of Solids*, 55:306–337, 2007.

[371] Xiaoming Chen, Liuyang Zhang, Meng Zheng, Cheol Park, Xianqiao Wang, and Changhong Ke. Quantitative nanomechanical characterization of the van der waals interfaces between carbon nanotubes and epoxy. *Carbon*, 82:214–228, 2015.

[372] Yogeeswaran Ganesan, Cheng Peng, Yang Lu, Phillip E. Loya, Padraig Moloney, Enrique Barrera, Boris I. Yakobson, James M. Tour, Roberto Ballarini, and Jun Lou. Interface toughness of carbon nanotube reinforced epoxy composites. *ACS Applied Materials & Interfaces*, 3:129–134, 2011.

[373] Carole A. Cooper, Sidney R. Cohen, Asa H. Barber, and H. Daniel Wagner. Detachment of nanotubes from a polymer matrix. *Applied Physics Letters*, 81:3873–3875, 2002.

[374] Asa H. Barber, Sidney R. Cohen, Ami Eitan, Linda S. Schadler, and H. Daniel Wanger. Fracture transitions at a carbon nanotube/polymer interface. *Advanced Materials*, 18:83–87, 2006.

[375] Asa H. Barber, Sidney R. Cohen, Shmuel King, and H. Daniel Wagner. Interfacial fracture energy measurements for multi-walled carbon nanotubes pulled from a polymer matrix. *Composites Science and Technology*, 64:2283–2289, 2004.

[376] Asa H. Barber, Sidney R. Cohen, and H. Daniel Wagner. Measurement of carbon nanotube-polymer interfacial strength. *Applied Physics Letters*, 82:4140–4142, 2003.

[377] Terumasa Tsuda, Toshio Ogasawara, Fei Deng, and Nobuo Takeda. Direct measurements of interfacial shear strength of multi-walled carbon nanotube/peek composite using a nano-pullout method. *Composites Science and Technology*, 71:1295–1300, 2011.

[378] Xiaoming Chen, Ming Zheng, Cheol Park, and Changhong Ke. Direct measurements of the mechanical strength of carbon nanotube-poly(methyl methacrylate) interfaces. *Small*, 9:3345–3351, 2013.

[379] Shanju Zhang, Marilyn Minus, Lingbo Zhu, Ching-Ping Wong, and Satish Kumar. Polymer transcrystallinity induced by carbon nanotubes. *Polymer*, 49:1356–1364, 2008.

[380] W. Ding, A. Eitan, F. T. Fisher, X. Chen, D. A. Dikin, R. Andrews, L. C. Brinson, L. S. Schadler, and R. S. Ruoff. Direct observation of polymer sheathing in carbon nanotube-polycarbonate composites. *Nano Letters*, 3:1593–1597, 2003.

[381] Yue Han, Xiaohua Zhang, Xueping Yu, Jingna Zhao, Shan Li, Feng Liu, Peng Gao, Yongyi Zhang, Tong Zhao, and Qingwen Li. Bio-inspired aggregation control of carbon nanotubes for ultra-strong composites. *Scientific Reports*, 5:11533, 2015.

[382] E. W. Washburn. The dynamics of capillary flow. *Physics Review*, 17:525–531, 1921.

[383] M. Whitby and N. Quirke. Fluid flow in carbon nanotubes and nanopipes. *Nature Nanotechnology*, 2:87–94, 2007.

[384] Davide Mattia and Yury Gogotsi. Review: static and dynamic behaviour of liquids inside carbon nanotubes. *Microfluid Nanofluid*, 5:289–305, 2008.

[385] P. A. Ajayan and Sumio Iijima. Capillarity-induced filling of carbon nanotubes. *Nature*, 361:333–334, 1993.

[386] J. Y. Chen, A. Kutana, C. P. Collier, and K. P. Giapis. Electrowetting in carbon nanotubes. *Science*, 310:1480–1483, 2005.

[387] E. Dujardin, T. W. Ebbesen, H. Hiura, and K. Tanigaki. Capillarity and wetting of carbon nanotubes. *Science*, 265:1850–1852, 1994.

[388] Erik Dujardin, Thomas W. Ebbesen, Ajit Krishnan, and Michael M. J. Treacy. Wetting of single shell carbon nanotubes. *Advanced Materials*, 10:1472–1475, 1998.

[389] M. Pía Rossi, Haihui Ye, Yury Gogotsi, Sundar Babu, Patrick Ndungu, and Jean-Claude Bradley. Environmental scanning electron microscopy study of water in carbon nanopipes. *Nano Letters*, 4:989–993, 2004.

[390] Mark Majumder, Nitin Chopra, Rodney Andrews, and Bruce J. Hinds. Enhanced flow in carbon nanotubes. *Nature*, 483:44, 2005.

[391] Jason K. Holt, Hyung Gyu Park, Yinmin Wang, Michael Stadermann, Alexander B. Artyukhin, Costas P. Grigoropoulos, Alekxander Noy, and Olgica Bakajin. Fast mass transport through sub-2-nanometer carbon nanotubes. *Science*, 312:1034–1037, 2006.

[392] D. Mattia, M. P. Rossi, B. M. Kim, G. Korneva, H. H. Bau, and Y. Gogotsi. Effect of graphitization on the wettability and electrical conductivity of cvd-carbon nanotubes and films. *Journal of Physical Chemistry B*, 110:9850–9855, 2006.

[393] Jing Qiu, Jeronimo Terrones, Juan J. Vilatela, Mary E. Vickers, James A. Elliott, and Alan H. Windle. Liquid infiltration into carbon nanotube fibers: effect on structure and electrical properties. *ACS Nano*, 7:8412–8422, 2013.

[394] Jan P. F. Lagerwall and Giusy Scaia. Carbon nanotubes in liquid crystals. *Journal of Materials Chemistry*, 18:2890–2898, 2008.

[395] Virginia A. Davis, A. Nicholas G. Parra-Vasquez, Micah J. Green, Pradeep K. Rai, Natnael Behabtu, Valentin Prieto, Richard D. Booker, Judith Schmidt, Ellina Kesselman, Wei Zhou, Hua Fan, W. Wade Adams, Robert H. Hauge, John E. Fischer, Yachin Cohen, Yeshayahu Talmon, Richard E. Smalley, and Matteo Pasquali. True solutions of single-walled carbon nanotubes for assembly into macroscopic materials. *Nature Nanotechnology*, 4:830–834, 2009.

[396] Yan Y. Huang, Tuomas P. J. Knowles, and Eugene M. Terentjev. Strength of nanotubes, filaments and nanowires from sonication-induced scission. *Advanced Materials*, 21:3945–3948, 2009.

[397] Howard Wang. Dispersing carbon nanotubes using surfactant. *Current Opinion in Colloid & Interface Science*, 14:364–371, 2009.

[398] Jonathan N. Coleman. Liquid-phase exfoliation of nanotubes and graphene. *Advanced Functional Materials*, 19:3680–3695, 2009.

[399] Sang Won Kim, Taehoon Kim, Yern Seung Kim, Hong Soo Choi, Heyong Jun Lim, Seung Jae Yang, and Chong Rae Park. Surface modifications for the effective dispersion of carbon nanotubes in solvents and polymers. *Carbon*, 50:3–33, 2012.

[400] Shane D. Bergin, Zhenyu Sun, David Rickard, Philip V. Streich, James P. Hamilton, and Jonathan N. Coleman. Multicomponent solubility parameters for single-walled carbon nanotube-solvent mixtures. *ACS Nano*, 3:2340–2350, 2009.

[401] Shane D. Bergin, Valeria Nicolosi, Philip V. Streich, Silvia Giordani, Zhenyu Sun, Alan H. Windle, Peter Ryan, N. Peter P. Niraj, Zhi-Tao T. Wang, Leslie Carpenter, Werner J. Blau, John J. Boland, James P. Hamilton, and Jonathan N. Coleman. Towards solutions of single-walled carbon nanotubes in common solvents. *Advanced Materials*, 20:1876–1881, 2008.

[402] Stéphane Badaire, Cécile Zakri, Maryse Maugey, Alain Derré, Joseph N. Barisci, Gordon Wallace, and Philippe Poulin. Liquid crystals of dna-stabilized carbon nanotubes. *Advanced Materials*, 17:1673–1676, 2005.

[403] Cécile Zakri and Philippe Poulin. Phase behaviour of nanotube suspensions: from attraction induced percolation to liquid crystalline phases. *Journal of Materials Chemistry*, 16:4095–4098, 2006.

[404] Christopher A. Dyke and James M. Tour. Overcoming the insolubility of carbon nanotubes through high degrees of sidewall functionalization. *Chemistry – A European Journal*, 10:812–817, 2004.

[405] A. Nicholas G. Parra-Vasquez, Natnael Behabtu, Micah J. Green, Cary L. Pint, Colin C. Young, Judith Schmidt, Ellina Kesselman, Anubha Goyal, Pulickel M. Ajayan, Yachin Cohen, Yeshayahu Talmon, Robert H. Hauge, and Matteo Pasquali. Spontaneous dissolution of ultralong single- and multiwalled carbon nanotubes. *ACS Nano*, 4:3969–3978, 2010.

[406] Sivarajan Ramesh, Lars M. Ericson, Virginia A. Davis, Rajesh K. Saini, Carter Kittrell, Matteo Pasquali, W. E. Billups, W. Wade Adams, Robert H. Hauge, and Richard E. Smalley. Dissolution of pristine single walled carbon nanotubes in superacids by direct protonation. *Journal of Physical Chemistry B*, 108:8794–8798, 2004.

[407] Silvia Giordani, Shane D. Bergin, Valeria Nicolosi, Sergei Lebedkin, Manfred M. Kappes, Werner J. Blau, and Jonathan N. Coleman. Debundling of single-walled nanotubes by dilution: observation of large populations of individual nanotubes in amide solvent dispersions. *Journal of Physical Chemistry B*, 110:15708–15718, 2006.

[408] Jeffrey L. Bahr, Edward T. Mickelson, Michael J. Bronikowski, Richard E. Smalley, and James M. Tour. Dissolution of small diameter single-wall carbon nanotubes in organic solvents? *Chemical Communications*, pages 193–194, 2001.

[409] Brian J. Landi, Herbert J. Ruf, James J. Worman, and Ryne P. Raffaelle. Effects of alkyl amide solvents on the dispersion of single-wall carbon nanotubes. *Journal of Physical Chemistry B*, 108:17089–17095, 2004.

[410] Jie Liu, Michael J. Casavant, Michael Cox, D. A. Walters, P. Boul, Wei Lu, A. J. Rimberg, K A. Smith, Daniel T. Colbert, and Richard E. Smalley. Controlled deposition of individual single-walled carbon nanotubes on functionalized templates. *Chemical Physics Letters*, 303:125–129, 1999.

[411] Michael J. O'Connell, Sergei M. Bachilo, Chad B. Huffman, Valerie C. Moore, Michael S. Strano, Erik H. Haroz, Kirsty L. Rialon, Peter J. Boul, William H. Noon, Carter Kittrell, Jianpeng Ma, Robert H. Hauge, R. Bruce Weisman, and Richard E. Smalley. Band gap fluorescence from individual single-walled carbon nanotubes. *Science*, 297:593–596, 2002.

[412] Yutaka Maeda, Shin inchi Kimura, Yuya Hirashima, Makoto Kanda, Yongfu Lian, Takatsugu Wakahera, Takeshi Akasaka, Tadashi Hasegawa, Hiroshi Tokumoto, Tetsuo Shimizu, Hiromichi Kataura, Yuhei Miyauchi, Shigeo Maruyama, Kaoru Kobayashi, and Shigeru Nagase. Dispersion of single-walled carbon nanotube bundles in nanaqueous solution. *Journal of Physical Chemistry B*, 108:18395–18397, 2004.

[413] M. F. Islam, E. Rojas, D. M. Bergey, A. T. Johnson, and A. G. Yodh. High weight fraction surfactant solubilisation of single-wall carbon nanotubes in water. *Nano Letters*, 3:269–273, 2003.

[414] Zhenyu Sun, Valeria Nicolosi, David Rickard, Shane D. Bergin, Damian Aherne, and Jonathan N. Coleman. Quantitative evaluation of surfactant-stabilized single-walled carbon nanotubes: dispersion quality and its correlation with zeta potential. *Journal of Physical Chemistry C*, 112:10692–10699, 2008.

[415] Howard Wang, Wei Zhou, Derek L. Ho, Karen I. Winey, John E. Fischer, Charles J. Glinka, and Erik K. Hobbie. Dispersing single-walled carbon nanotubes with surfactants: a small angle neutron scattering study. *Nano Letters*, 4:1789–1793, 2004.

[416] Dhriti Nepal, Jung-Inn Sohn, Wilhelm K. Aicher, Seonghoon Lee, and Kurt E. Geckeler. Supramolecular conjugates of carbon nanotubes and dna by a solid-state reaction. *Biomacromolecules*, 6:2919–2922, 2005.

[417] Atsushi Ikeda, Kentaro Hayashi, Toshifumi Konishi, and Jun ichi Kikuchi. Solubilization and debundling of purified single-walled carbon nanotubes using solubilizing agents in an aqueous solution by high-speed vibration milling technique. *Chemical Communications*, pages 1334–1335, 2004.

[418] Wei Zhao, Yi-Tao Liu, Qing-Ping Feng, Xu-Ming Xie, Xiao-Hao Wang, and Xiong-Ying Ye. Dispersion and noncovalent modifications of multiwalled carbon nanotubes by various polystyrene-based polymers. *Journal of Applied Polymer Science*, 109:3525–3532, 2008.

[419] Yehai Yan, Jian Cui, Petra Pötschke, and Brigitte Voit. Dispersion of pristine single-walled carbon nanotubes using pyrene-capped polystyrene and its application for preparation of polystyrene matrix composites. *Carbon*, 48:2603–2612, 2010.

[420] Jianhua Zou, Liwei Liu, Hui Chen, Saiful I. Kohandaker, Richard D. McCullough, Qun Huo, and Lei Zhai. Dispersion of pristine carbon nanotubes using conjugated block copolymers. *Advanced Materials*, 20:2055–2060, 2008.

[421] Qing-Yuan Tang, Jie Chen, and C. Y. Chung. Effect of carbon nanotubes and their dispersion on thermal curing of polyimide precursors. *Polymer Degradation and Stability*, 95:1672–1678, 2010.

[422] Rina Shvartzman-Cohen, Ivonne Monje, Marc Florent, Veronica Frydman, Daniella Goldfarb, and Rachel Yerushalmi-Rozen. Self-assembly of amphilic block copolymers in dispersions of multiwalled carbon nanotubes as reported by spin probe electron paramagnetic resonance spectroscopy. *Macromolecules*, 43:606–614, 2010.

[423] Richa Rastogi, Rahul Kaushal, S. K. Tripathi, Amit L. Sharma, Inderpreet Kaur, and Lalit M. Bharadwaj. Comparative study of carbon nanotube dispersion using surfactants. *Journal of Colloid and Interface Science*, 328:421–428, 2008.

[424] Junrong Yu, Nadia Grissiord, Cor E. Koning, and Joachim Loos. Controlling the dispersion of multi-wall carbon nanotubes in aqueous surfactant solution. *Carbon*, 45:618–623, 2007.

[425] Olga Matarredona, Heather Rhoads, Zhongrui Li, Jeffrey H. Harwell, Leandro Balzano, and Daniel E. Resasco. Dispersion of single-walled carbon nanotubes in aqueous solutions of the anionic surfactant naddbs. *Journal of Physical Chemistry B*, 107:13357–13367, 2003.

[426] Hoon Hyung, John D. Fortner, Joseph B. Hughes, and Jae-Hong Kim. Natural organic matter stabilizes carbon nanotubes in the aqueous phase. *Environmental Science Technology*, 41:179–184, 2007.

[427] Valerie S. Moore, Michael S. Strano, Erik H. Haroz, Robert H. Hauge, and Richard E. Smalley. Individually suspended single-walled carbon nanotubes in various surfactants. *Nano Letters*, 3:1379–1382, 2003.

[428] Simon E. Moulton, Maryse Maugey, Philippe Poulin, and Gordon G. Wallace. Liquid crystal behaviour of single-walled carbon nanotubes dispersed in biological hyaluronic acid solutions. *Journal of the American Chemical Society*, 129:9452–9457, 2007.

[429] Jian Chen, Mark A. Hamon, Hui Hu, Yongsheng Chen, Apparao M. Rao, Peter C. Eklund, and Robert C. Haddon. Solution properties of single-walled carbon nanotubes. *Science*, 282:95–98, 1998.

[430] Hemg Li, Jia Cai Nie, and Sándor Kunsági-Máté. Modified dispersion of functionalized multi-walled carbon nanotubes in acetonitrile. *Chemical Physics Letters*, 492:258–262, 2010.

[431] Bin Zhao, Hui Hu, Aiping Yu, Daniel Perea, and Robert C. Haddon. Synthesis and characterization of water soluble single-walled carbon nanotube graft copolymers. *Journal of the American Chemical Society*, 127:8197–8203, 2005.

[432] Atsushi Ikeda, Tomoe Hamano, Kentaro Hayashi, and Jun ichi Kikuchi. Water-solubilization of nucleotitdes-coated single-walled carbon nanotubes using a high-speed vibration milling technique. *Organic letters*, 8:1153–1156, 2006.

[433] Hualong Pan, Liqi Liu, Zhi-Xin Guo, Liming Dai, Fushi Zhang, Daoben Zhu, Richard Czerw, and David L. Carroll. Carbon nanotubols from mechanochemical reaction. *Nano Letters*, 3:29–32, 2003.

[434] Lifei Chen, Huaqing Xie, Yang Li, and Wei Yu. Carbon nanotubes with hydrophilic surfaces produced by a wet-mechanochemical reaction with potassium hydroxide using ethanol as a solvent. *Materials Letters*, 63:45–47, 2009.

[435] Xudong Lou, Cristophe Detrembleur, Cristophe Pagnoulle, Robert Jérôme, Vera Bocharova, Anton Kiriy, and Manfred Stamm. Surface modification of multiwalled carbon nanotubes by poly(2-vinylpyridine): dispersion, selective deposition, and decoration of the nanotubes. *Advanced Materials*, 16:2123–2127, 2004.

[436] Shanju Zhang, Ian A. Kinloch, and Alan H. Windle. Mesogenicity drives fractionation in lyotropic aqueous suspensions of multiwall carbon nanotubes. *Nano Letters*, 6:568–572, 2006.

[437] Wenhui Song and Alan H. Windle. Isotropic-nematic phase transition of dispersions of multiwall carbon nanotubes. *Macromolecules*, 38:6181–6188, 2005.

[438] Wenhui Song, Ian A. Kinloch, and Alan H. Windle. Nematic liquid crystallinity of multiwall carbon nanotubes. *Science*, 302:1363, 2003.

[439] Virginia A. Davis, Lars M. Ericson, A. Nicholas G. Parra-Vasquez, Hua Fan, Yuhuang Wang, Valentin Prieto, Jason A. Longoria, Sivarajan Ramesh, Rajesh K. Saini, Carter Kittrell, W. E. Billups, W. Wade Adams, Robert H. Hauge, Richard E. Smalley, and Matteo Pasquali. Phase behaviour and rheology of swnts in superacids. *Macromolecules*, 37:154–160, 2004.

[440] ASTM International. *Standard Test Method for Tear-Propagation Resistance (Trouser Tear) of Plastic Film and Thin Sheeting by a Single-Tear Method*. ASTM D1938-14, ASTM International, West Conshohocken, PA, USA., 2014.

[441] H. W. Greensmith and A. G. Thomas. Rupture of rubber. iii. determination of tear properties. *Journal of Polymer Science*, 18:189–200, 1955.

[442] ASTM International. *Standard Test Method for Peel Resistance of Adhesives (T-Peel Test)*. ASTM D1876-08, ASTM International, West Conshohocken, PA, USA., 2014.

[443] A. Jorio, M. A. Pimenta, A. G. Souza Filho, R. Saito, G. Dresselhaus, and M. S. Dresselhaus. Characterizing carbon nanotube samples with resonance raman scattering. *New Journal of Physics*, 5:139, 2003.

[444] A. C. Ferrari and J. Robertson. Interpretation of raman spectra of disordered and amorphous cabon. *Physical Review B*, 61:14095–14107, 2000.

[445] S. Timoshenko and J. N. Goodier. *Theory of Elasticity*. McGraw-Hill, New York, 1970.

[446] J. C. Lasjaunias, K. Biljakovic, P. Monceau, and J. L. Sauvajol. Low-energy vibrational excitations in carbon nanotubes studied by heat capacity. *Nanotechnology*, 14:998–1003, 2003.

[447] B. I. Prenitzer, L. A. Giannuzzi, K. Newman, S. R. Brown, R. B. Irwin, F. A. Stevie, and T. L. Shofner. Transmission electron microscope specimen preparation of zn powders using the focused ion beam lift-out technique. *Metallurgical and Materials Transactions A*, 29:2399–2406, 1998.

[448] Oxana V. Kharissova and Boris I. Kharisov. Variations of interlayer spacing in carbon nanotubes. *RSC Advances*, 4:30807–30815, 2014.

[449] R. Hill. A theory of the yielding and plastic flow of anisotropic metals. *Proceedings of the Royal Society A*, pages 281–297, 1948.

[450] Jonathan N. Coleman, Martin Cadek, Rowan Blake, Valeria Nicolosi, Kevin P. Ryan, Colin Belton, Antonio Fonseca, Janos B. Nagy, Yurii K. Gun'ko, and Werner J. Blau. High-performance nanotube-reinforced plastics: understanding the mechanism of strength increase. *Advanced Functional Materials*, 14:791–798, 2004.

[451] Toray Carbon Fibers Ltd. T300 data sheet. *Santa Ana, C.A. USA*.

[452] T. Hertel, R. E. Walkup, and P. Avouris. Deformation of carbon nanotubes by surface van der waals forces. *Physical Review B*, 58:870–873, 1998.

[453] X. Wei, T. Filleter, and H. D. Espinosa. Statistical shear lag model- unravelling the size effect in hierarchical composites. *Acta Biomaterialia*, 18:206–212, 2015.

[454] C. Wang, X. He, L. Tong, Q. Luo, Y. Li. Q. Song, X. Lv, Y. Shang, Q. Peng, and J. Li. Tensile failure mechanisms of individual junctions assembled by two carbon nanotubes. *Composites Science and Technology*, 110:159–163, 2015.

[455] K. L. Johnson, K. Kendall, and A. D. Roberts. Surface energy and the contact of elastic solids. *Proceedings of the Royal Society A*, 324:301–313, 1971.

[456] Nasreen G Chopra, Lorin X. Benedict, Vincent H. Crespi, Marvin L. Cohen, Steven G. Louie, and A. Zettl. Fully collapsed carbon nanotubes. *Nature*, 377:135–138, 1995.

[457] O. L. Blakslee, D. G. Proctor, E. J. Seldin, G. B Spence, and T. Wang. Elastic constants of compression-annealed pyrolytic graphite. *Journal of Applied Physics*, 41:3373–3382, 1970.

[458] G. Savini, Y. J. Dappe, S. Ölberg, J. –C. Charlier, M. I. Katsnelson, and A. Fasolino. Bending modes, elastic constants and mechanical stability of graphitic systems. *Carbon*, 49:62–69, 2011.

[459] R. D. Henshell and K. G. Shaw. Crack tip finite elements are unnecessary. *Numerical Methods in Engineering*, 9:495–507, 1975.

[460] J. R. Rice. A path-dependant integral and the approximate analysis of strain concentration by notches and cracks. *Journal of Applied Mechanics*, 36:397–386, 1968.

[461] Francesca Mirri, Rana Ashkar, Vida Jamali, Lucy Liberman, Robert A. Pinnick, Paul van der Schoot, Yeshayahu Talmon, Paul D. Butler, and Matteo Pasquali. Quantification of carbon nanotube liquid crystal morphology via neutron scattering. *Macromolecules*, 51:6892–6900, 2018.

[462] D. G. Gilbert, M. F. Ashby, and P. W. R. Beaumont. Modulus-maps for amorphous polymers. *Journal of Materials Science*, 21:3194–3210, 1996.

[463] P. Puech, T. Hu, A. Sapelkin, I. Gerber, V. Tishkova, E. Pavlenko, B. Levine, E. Flahaut, and W. Bacsa. Charge transfer between carbon nanotubes and sulphuric acid as determined by raman spectroscopy. *Physical Review B*, 85:205412, 2012.

[464] M. Elimelech, J. Gregory, X. Jia, and R. Williams. *Particle deposition & aggregation: measurement, modelling and simulation*. Butterworth-Heinemann, Oxford, UK, 1995.

[465] E. J. W. Verwey and J. Th. G. Overbeek. *Theory of the stability of Lyophobic Colloids*. Elsevier, Amsterdam, Netherlands, 1948.

[466] B. V. Derjaguin and L. D. Landau. Theory of the stability of strongly charged lyophobic sols and of the adhesion of strongly charged particles in solutions of electrolytes. *Acta Physiochim, URSS*, 14:733–762, 1941.

[467] R. M. Cremlyn. *Chlorosulfonic acid; a versatile reagent*. The Royal Society of Chemisty, Cambridge, UK, 2014.

[468] M. A. Gebbie, A. M. Smith, H. A. Dobbs, A. A. Lee, G. C. Warr, X. Banquy, M. Valtiner, M. W. Rutland, J. N. Israelachivili, S. Perkin, and R. Atkin. Long-range electrostatic forces in ionic liquids. *Chemical Communications*, 53:1214–1224, 2017.

[469] A. A. Lee, C. S. Perez-Martinez, A. M. Smith, and S. Perkin. Scaling analysis of the screening length in concentrated electrolytes. *Physical Review Letters*, 119:026002, 2017.

[470] Micah J. Green, A. Nicholas G. Parra-Vasquez, Natnael Behabtu, and Matteo Pasquali. Modeling the phase behaviour of polydisperse rigid rods with attractive interactions with applications to single-walled carbon nanotubes in superacids. *Journal of Chemical Physics*, 131:084901, 2009.

[471] U. G. K. Wegst and M. F. Ashby. The mechanical efficiency of natural materials. *Philosophical Magazine*, 84:2167–2181, 2004.

[472] Sanjit Bhowmick, Horacio Espinosa, Katherine Jungjohann, Thomas Pardoen, and Oliver Pierron. Advanced microelectromechanical systems-based nanomechanical testing: beyond stress and strain measurements. *Advances in In Situ Nanomechanical Testing*, 44:487–493, 2019.

[473] T. Tsuzuku K. Matsubara, K. Sugihara. Electrical resistance in the c direction of graphite. *Physical Review B*, 41:969–974, 1990.

[474] B. Budiansky and N. A. Fleck. Compressive failure of fibre composites. *Journal of the Mechanics and Physics of Solids*, 41:183–211, 1993.

[475] E.A. Robinson and J.A. Ciruna. The chlorosulfuric acid solvent system. part i. electrical conductivity, transport number, and density measurements of solutions of simple bases. *Canadian Journal of Chemistry*, 46:1719–1725, 1968.

Appendix A

Axial elastic modulus of carbon fibres

The value of reinforcement Young's modulus E_R used in normalisation of the principal carbon fibre composite modulus is given in Table A.1

Table A.1 Axial Young's modulus of carbon fibres

CFRP Laminate	Carbon fibre	Resin	E_R (GPa)	Reference
Unidirectional laminates	Modmor type I	LY558 Epoxy	410	[361]
	Modmor type II	LY558 Epoxy	240	[361]
	Rolls-Royce fibres	LY558 Epoxy	200	[361]
	Tenax HS45 fibre	LY556 Epoxy	240	[362]
Quasi-isotropic	Sigmatex 450 gsm	Gurit Prime 20LV	212	[363]
	AS4	PEKK 8552	231	[364, 366]
	T300	S208, BP907, 4901/(m)MDA	230	[365]
	T700	S208, BP907, 4901/(m)MDA	230	[365]

Appendix B

Real time measurement of sample resistance during tensile testing

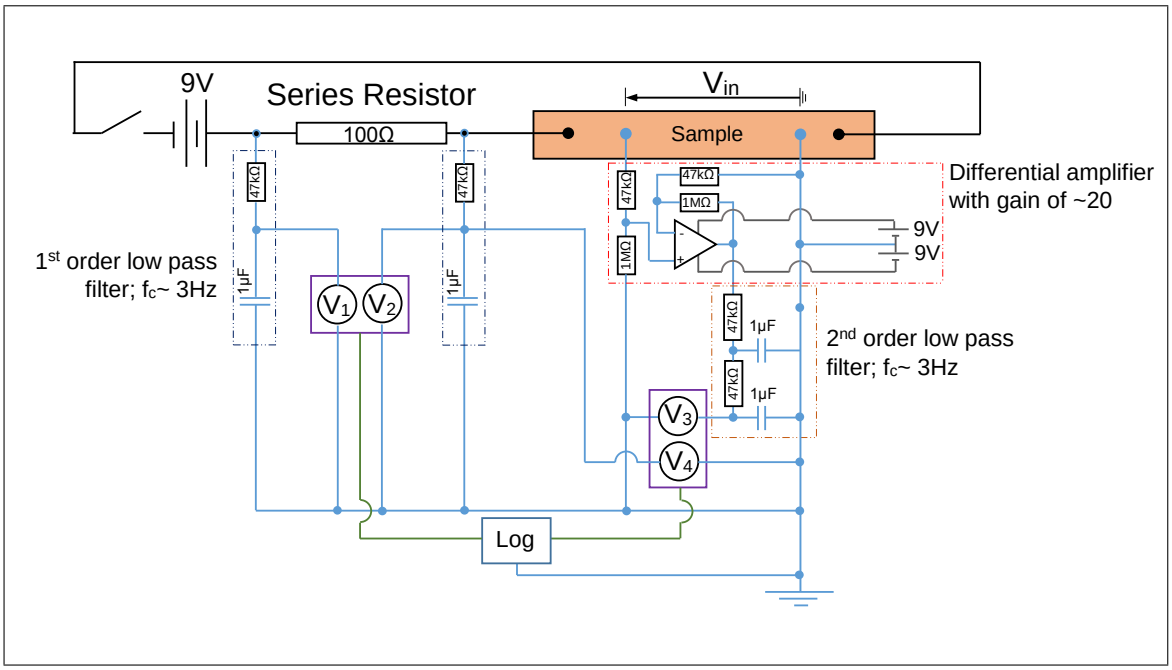

Fig. B.1 Measurement circuit for real time measurement of sample resistance during tensile testing

Appendix C

Out-of-plane stress-strain and piezoresistive response of direct-spun CNT mat

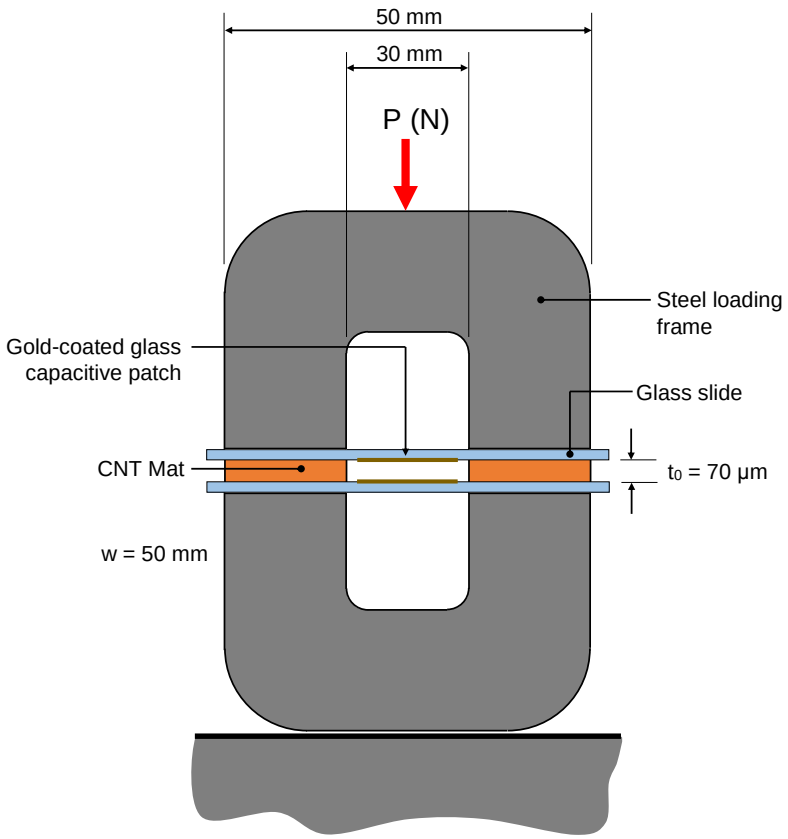

Fig. C.1 Measurement of the out-of-plane stress-strain response of direct-spun CNT mat.

Two direct-spun CNT mat samples of width 10 mm, length 50 mm and thickness 70 µm were placed between glass slides. Compressive stress was applied to the slides by an external steel frame, see Figure C.1. The central portion of the glass slides was coated with an electro-deposited gold layer; the capacitance measured between the plates was recorded during compression testing, from which the distances between the plates and compressive strain was deduced.

The piezoresistive out-of-plane behaviour was recorded by monitoring the through thickness resistance upon the application of compressive stress to the experimental apparatus of Figure 3.2b.

The compressive stress-strain reponse and piezoresistive response are presented in Figure C.2a and C.2b respectively. The out-of-plane stress versus strain response implies a Young's modulus of approximately 0.7 MPa.

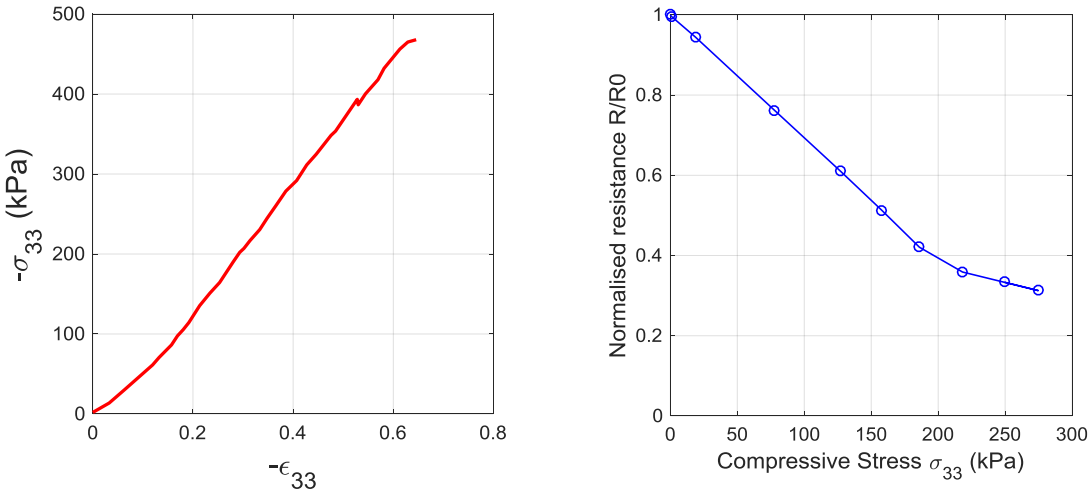

(a) (b)

Fig. C.2 (a) The compressive stress-strain response of direct-spun CNT mat in the through-thickness direction, (b) the sample resistance measured in the through-thickness direction versus applied compressive stress.

Appendix D

Finite element analysis of honeycomb unit cell model

To verify the applicability of beam theory, finite element simulations were performed, with elastic constants as outlined in Chapter 4. The simulation boundary conditions are illustrated in Figure D.1.

The volume fraction of the unit cell was varied, and its macroscopic modulus is plotted as a function of its relative density $\bar{\rho}$ and shear modulus G_{12} in Figure D.2. Beam theory with or without inclusion of axial stretch predicts the macroscopic modulus closely for relative densities of less than 0.3, and is a useful prediction of the effect of shear modulus G_{12} upon the macroscopic modulus.

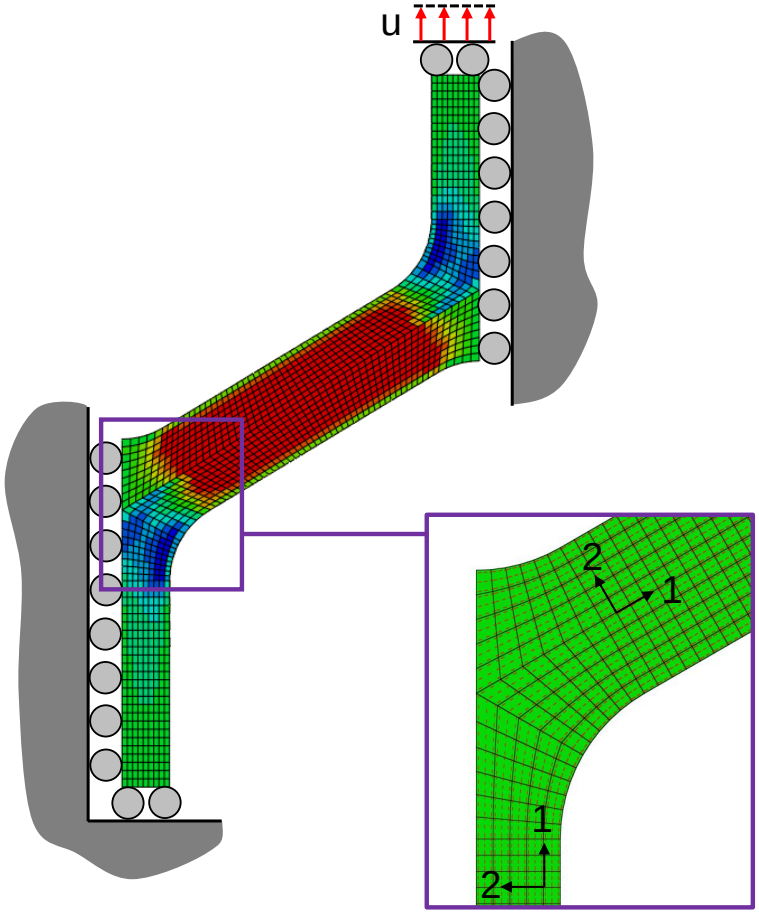

Fig. D.1 Boundary conditions for the finite element analysis of a honeycomb unit cell.

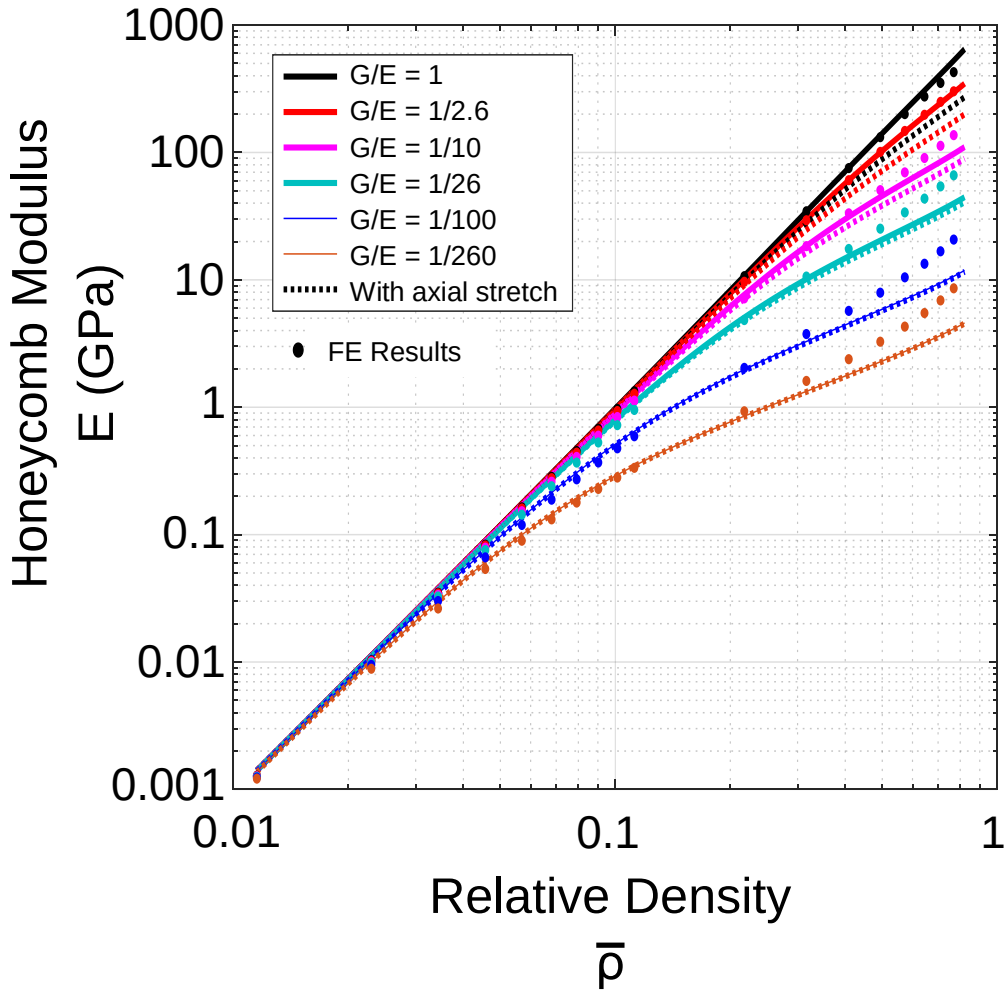

Fig. D.2 Predicted modulus from finite element simulation compared with Timoshenko beam theory.

Appendix E

Determination of bulk ion number concentration n_0

The specific conductance of chlosulfonic acid was measured with the 4-point probe conductivity cell illustrated in Figure E.1. The cell resistance was determined by passing an alternating current through the two outer probes, and recording the potential difference across the two central probes — variation of the current established that the solutions were linear, and resistance was calculated from the current-voltage relationship. The cell was calibrated with measurements of dilute solutions of sodium chloride in distilled water, of known specific conductance [86]. The measured specific conductance of the chlorosulfonic acid was $K = 0.135$ S/m — a little under three times that reported in literature [475]. Ions in chlorosulfonic acid are present as a consequence of the protonation of impurities (bases) according to the reaction of equation 5.5, and due to self-disassociation of chlorosulfonic acid via the following reaction [475],

$$\mathrm{HSO_3Cl} \leftrightarrows \mathrm{SO_3Cl^-} + \mathrm{H^+}. \tag{E.1}$$

Now, consider the relationship between the specific conductance K and chlorosulfate ion concentration n_0. The proportion of chlorosulfonic acid molecules α which are disassociated at any one time and facilitate electrical transport relates to the molar conductivity $\Lambda_C = K/\left(\rho_{CSA}/M_{CSA}\right)$ and limiting molar conductivity Λ_0 of the ions in solution at infinite dilution, as follows:

$$\alpha = \frac{\Lambda_C}{\Lambda_0} \tag{E.2}$$

The limiting molar conductivity is the sum of the limiting molar conductivity λ of each constituent ion i present in solution, and number of ions in each formula unit m_i, which is unity here according to equation 5.5.

$$\Lambda_0 = \sum_i m_i \lambda_i \tag{E.3}$$

Transport measurements in literature on dilute solutions of bases in chlorosulfonic acid have revealed that the chlorosulfate ion dominates the electrical conductivity of chlorosulfonic acid, with average mobility $\lambda = 6.95 \times 10^{-3}$ Sm^2 mol^{-1} [475]. Taking the mobility of other ions as null, it follows that $\alpha = 1.29 \times 10^{-3}$ from equation E.2, and the bulk ion number concentration n_0 is as below,

$$n_0 = \alpha \frac{\rho_{CSA} N_A}{M_{CSA}} \tag{E.4}$$

Hence an estimate of the bulk chlorosulfate ion number density is determined, $n_0 = 1.2 \times 10^{25}$ m^{-3}.

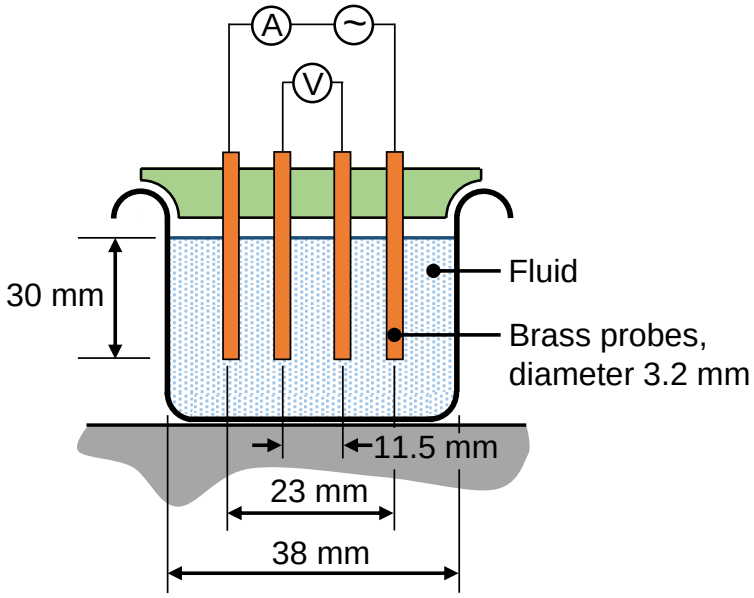

Fig. E.1 Measurement of the specific conductance of chlorosulfonic acid.

Appendix F

Calculation of double layer and van der Waals potential between two CNTs via the Derjaguin approximation

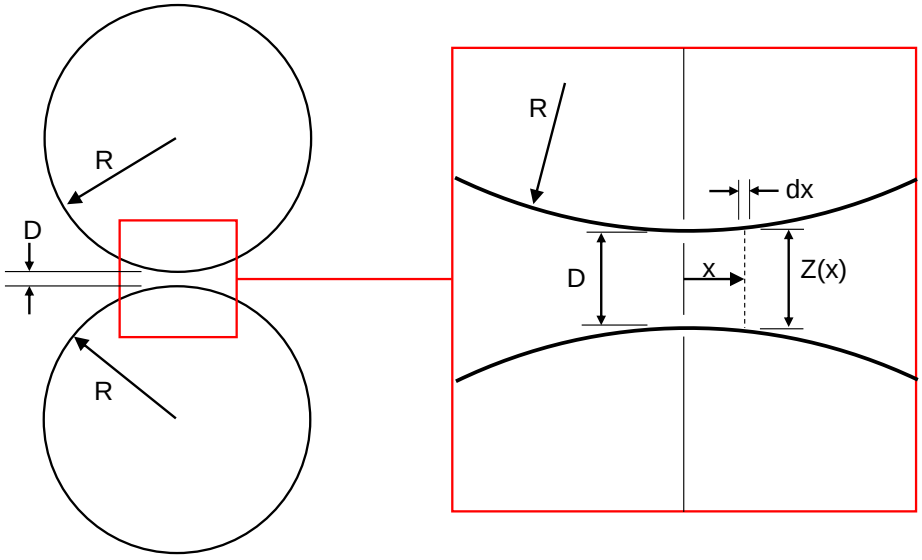

Fig. F.1 The Derjaguin approximation for interaction energy between two parallel cylinders.

Consider two CNTs, both of radius R, with a closest separation distance between their outer walls of D, see Figure F.1. The gap between the walls $Z(x)$ varies as a function of position x according to the chord theorem, as follows:

$$Z(x) = D + \frac{x^2}{R} \tag{F.1}$$

The interaction energy per unit area U locally between the two walls at position x is a function of $Z(x)$ [291], as below:

$$U = -\frac{A}{12\pi \left(Z(x)\right)^2} \tag{F.2}$$

The total interaction energy is obtained by integration of U over all x:

$$U_{VDW} = -\frac{A}{6\pi} \int_{x=0}^{x=\infty} \frac{A}{\left(D + \frac{x^2}{R}\right)^2} \tag{F.3}$$

$$= -\frac{AR^2}{6\pi} \int_{x=0}^{x=\infty} \frac{1}{\left(DR + x^2\right)^2} \tag{F.4}$$

$$= -\frac{A}{24} R^{\frac{1}{2}} D^{-\frac{3}{2}} \tag{F.5}$$

Now, consider the double layer interaction energy. The local energy as a function of distance $Z(x)$ is given by the least-squares-approximation:

$$U_{LSA} = \frac{64 n_0 kT}{\kappa} \gamma^2 \exp(-\kappa Z(x)) \tag{F.6}$$

where the Debye-Hückel parameter $\kappa = 1/\lambda_D$. Again by integration,

$$U_{DL} = 2 \int_{x=0}^{x=\infty} \frac{64 n_0 kT}{\kappa} \gamma^2 \exp\left(-\kappa Z(x)\right) dx \tag{F.7}$$

$$= \frac{128 n_0 kT \gamma^2}{\kappa} \exp(-\kappa D) \int_{x=0}^{x=\infty} \exp\left(-\left(\frac{\kappa}{R}\right) x^2\right) dx \tag{F.8}$$

$$= \frac{\left(64\sqrt{\pi R}\right) n_0 kT}{\kappa^{\frac{3}{2}}} \gamma^2 \exp\left(-\kappa D\right) \tag{F.9}$$